

Inclusive Jet Production in γp and $\gamma\gamma$ Processes: Direct and Resolved Photon Cross Sections in Next-To-Leading Order QCD

M. Klasen^a, T. Kleinwort^b, G. Kramer^c

^a Deutsches Elektronen-Synchrotron DESY, Notkestraße 85,
D-22607 Hamburg, Germany, e-mail: klasens@mail.desy.de

and

High Energy Physics Division*, Argonne National Laboratory,
Argonne, IL 60439-4815, U.S.A., email: klasens@hep.anl.gov

^b DESY-IfH Zeuthen, Platanenallee 6,
D-15738 Zeuthen, Germany, e-mail: tkleinw@ifh.de

^c II. Institut für Theoretische Physik[†], Universität Hamburg,
Luruper Chaussee 149, D-22761 Hamburg, Germany,
e-mail: kramer@desy.de

Abstract

The production of jets in low Q^2 ep scattering (photoproduction) and in low Q^2 e^+e^- scattering ($\gamma\gamma$ scattering) allows for testing perturbative QCD and for measuring the proton and photon structure functions. This requires exact theoretical predictions for one- and two-jet cross sections. We describe the theoretical formalism, giving sufficient details, for calculating the direct and resolved processes in γp and $\gamma\gamma$ reactions in next-to-leading order QCD. We present the complete analytical results for the Born terms, the virtual, and the real corrections. To separate singular and regular regions of phase space we use the phase space slicing method with an invariant mass cut-off. In this way, all soft and collinear singularities are either canceled or absorbed into the structure functions. Using a flexible Monte Carlo program, we evaluate the cross sections numerically and perform various tests and comparisons with other calculations. We consider the scale dependence of our results and compare them to data from the experiments H1 and ZEUS at HERA and OPAL at LEP.

*Supported by the U.S. Department of Energy, Division of High Energy Physics, Contracts W-31-109-ENG-38 and DEFG05-86-ER-40272.

[†]Supported by Bundesministerium für Bildung und Wissenschaft, Forschung und Technologie, Bonn, Germany under Contract 05 7HH92P(0) and EU Program "Human Capital and Mobility" through Network "Physics at High Energy Colliders" under Contract CHRX-CT93-0357 (DG12 COMA).

1 Introduction

The analysis of jet production in various high energy processes has become a major field for testing perturbative QCD. Recently jet production in $\gamma\gamma$ processes, where the two photons of very small virtuality are produced in the collision of electrons and positrons, has come into focus after data have been collected at the TRISTAN [1] and LEP [2] colliders. In addition jet production in deep inelastic (high Q^2) [3] and low Q^2 ep scattering (equivalent to photoproduction) has been measured at the two HERA experiments H1 [4] and ZEUS [5].

Jet production in $\gamma\gamma$ and γp collisions has several similarities. At very small Q^2 , where q ($Q^2 = -q^2$) is the four-momentum transfer of the electron (positron) producing the virtual photons in the $\gamma\gamma$ or γp initial state, the emission of the photon can be described in the Equivalent Photon Approximation. The spectrum of the virtual photons is approximated by the Weizsäcker-Williams (WWA) formula, which depends only on $y = E_\gamma/E_e$, the fraction of the initial electron (positron) energy E_e transferred to the photon with energy E_γ , and on Q_{\max}^2 (or θ_{\max}), which is the maximal virtuality (or the maximal electron scattering angle) allowed in the experimental set-up.

Concerning the hard scattering reactions both processes have so-called direct and resolved components. Thus, in leading order (LO) QCD the cross section $\sigma(\gamma\gamma \rightarrow \text{jets})$ receives contributions from three distinct parts: (i) the direct contribution (DD), in which the two photons couple directly to quarks, (ii) the single-resolved contribution (DR), where one of the photons interacts with the partonic constituents of the other photon, (iii) the double-resolved contribution (RR), where both photons are resolved into partonic constituents before the hard scattering subprocess takes place. In the DD component (in LO) we have only two high- p_T jets in the final state and no additional spectator jets. In the DR contribution one spectator jet originating from low transverse momentum fragments of one of the photons is present, and in the RR component we have two such spectator or photon remnant jets. In the case of γp collisions one of the photons is replaced by the proton which has no direct interaction. Then we have only the DR and RR components which are usually referred to as the direct and the resolved contribution. This means that the DR component for $\gamma\gamma \rightarrow \text{jets}$ has the same structure as the direct contribution of $\gamma p \rightarrow \text{jets}$ and the RR part for $\gamma\gamma \rightarrow \text{jets}$ is calculated in the same way as the resolved cross section for $\gamma p \rightarrow \text{jets}$.

Of course, to calculate the resolved cross sections we need a description of the partonic constituents of the photon. These parton distributions of the photon are partly perturbative and non-perturbative quantities. To fix the non-perturbative part one needs information from experimental measurements to determine the fractional momentum dependence at a reference scale M_0^2 . The change with the factorization scale $M^2 \gtrsim M_0^2$ is obtained from perturbative evolution equations. Most of the information on the parton distribution functions (PDF) of the photon comes from photon structure function (F_2^γ) measurements in deep inelastic $e\gamma$ scattering, where, however, mainly the quark distribution function can be determined. In $\gamma\gamma$ and γp high- p_T jet production also the gluon distribution of the photon enters which can be constrained by these processes.

When we want to proceed to next-to-leading order (NLO) QCD the following steps must be taken: (i) The hard scattering cross section for the direct and resolved photon processes are calculated up to NLO. (ii) NLO constructions for the PDF's of the proton and the photon are used and are evolved in NLO up to the chosen factorization scale via the Altarelli-Parisi equations and convoluted with the NLO hard-scattering cross sections. (iii) To calculate jet cross sections we must choose a jet definition which may be either a cluster or a cone algorithm in accordance with the choice made in the experimental analysis.

There exist several methods for calculating NLO corrections of jet cross sections in high energy reactions [6]. As in our previous work we apply the phase space slicing method with invariant mass slicing to separate infrared and collinear singular phase space regions. In this approach the contributions from the singular regions are calculated analytically with the approximation that terms of the order of the slicing cut are neglected. In the non-singular phase space regions the cross section is

obtained numerically. This method allows the application of different clustering procedures, the use of different variables for describing the final state together with cuts on these variables as given by the measurement of the jet cross sections. This method has been used for the calculation of the NLO DD and DR cross sections in the case of $\gamma\gamma \rightarrow \text{jets}$ [7] and for the calculation of the direct cross section in the case of $\gamma p \rightarrow \text{jets}$ [8]. It is obvious that the NLO calculation of the DR cross section for the $\gamma\gamma$ case is the same as of the NLO direct cross section for the γp case.

In the calculation of the $\gamma\gamma$ DD and DR or γp direct cross section one encounters the photon-quark collinear singularity. This is subtracted and absorbed into the quark distribution of the photon in accord with the factorization theorem. This subtraction at the factorization scale M^2 produces an interdependence of the three components in the $\gamma\gamma$ and the two components in the γp reaction, so that a unique separation in DD, DR, and RR (for $\gamma\gamma$) and in direct and resolved (for γp) contributions is valid only in LO. The calculation of these subtraction terms and of the contributions from the other singular regions has been presented with sufficient details in [7, 8]. The phase space slicing method was applied also for the calculation of the NLO correction of the $\gamma\gamma$ RR contribution [9] and the resolved γp cross section [10]. Results for the inclusive two-jet cross sections together with a comparison to recent experimental data were presented for $\gamma\gamma \rightarrow \text{jets}$ in [11] and for $\gamma p \rightarrow \text{jets}$ in [12], respectively. In these two papers the specific calculations of the corresponding resolved cross sections in NLO were not explicitly outlined, in particular it was not shown, how the different infrared and collinear singularities cancel between virtual and real contributions and after the subtraction of collinear initial state singularities. In this work we want to fill this gap. We describe the analytic calculation of the various resolved terms in the specific singular regions needed for the NLO corrections. Furthermore we check the analytical results by comparing with results obtained with other methods. In order to have a complete presentation we include also the calculation of the NLO correction to the $\gamma\gamma$ DD cross section already presented in [7]. We also include the details of the DR contributions in the form of the direct γp cross section taken from [8]. Details of other material, as for example, various jet definitions, which were only mentioned in our previous work and which now become more and more relevant in the analysis of the experimental data, will also be presented. Since the calculation of the RR (DR) cross section for $\gamma\gamma \rightarrow \text{jets}$ is the same as the calculation of the $\gamma p \rightarrow \text{jets}$ resolved (direct) cross section we concentrate on the γp case when we present the details of the calculations. So for the $\gamma\gamma$ case we present only the DD contribution which has no analogy in the γp case. We come back to the $\gamma\gamma$ case when we show the numerical results for specific cases including all three components.

We organize this work in seven main sections: After this introduction we relate the experimental ep scattering to photon parton scattering in section 2. We describe the Weizsäcker-Williams approximation, discuss the proton and photon PDF's and explain the experimental and theoretical properties of various jet definitions. Furthermore, section 2 contains the master formulæ for one- and two-jet cross sections. These will be calculated in section 3 in LO and in section 4 in NLO. In both sections, we calculate the relevant phase space for $2 \rightarrow 2$ and $2 \rightarrow 3$ scattering, respectively. The Born matrix elements are contained in section 3. In section 4 we present the virtual one-loop matrix elements and the tree-level $2 \rightarrow 3$ matrix elements, which are then integrated over singular regions of phase space. Next, we demonstrate how all ultraviolet and infrared poles in the NLO calculation cancel or are removed through renormalization and factorization into PDF's. A detailed numerical evaluation of jet cross sections in γp scattering with the purpose to compare with results of other work and to make consistency checks is contained in section 5. We study the renormalization and factorization scale dependence of one- and two-jet cross sections including the direct and resolved components. We also show results for some specific inclusive one- and two-jet cross sections and compare them with experimental data, in case they are available, to demonstrate the usefulness of our methods. Section 6 contains the corresponding numerical studies and comparisons to data for $\gamma\gamma$ scattering. The final conclusions are left for section 7.

2 Photoproduction of Jets at HERA

In this section we set up the general framework for theoretical predictions of the photoproduction of jets in electron-proton scattering. This includes the separation of the perturbatively calculable parts from the non-perturbative parts of the cross section and linking the electron-proton to photon-proton scattering. This link will be discussed first in section 2.1 and consists in the Weizsäcker-Williams or Equivalent Photon Approximation.

The framework of the QCD improved parton model for protons will shortly be discussed in section 2.2. This is necessary, since protons are not pointlike but composed of three valence quarks and sea quarks and gluons. Perturbative QCD is not applicable at distances comparable to the size of the proton, but only at small partonic scales due to the asymptotic freedom of QCD. Therefore, the parton content of the proton is the domain of non-perturbative QCD and has to be described with universal distribution functions. The scale dependence of these functions is governed by the Altarelli-Parisi equations.

A similar concept applies for resolved photons, which are discussed in section 2.3. Contrary to direct photons, which are obviously pointlike, resolved photons can be considered to have a complicated hadronic structure like protons. However, they have a different valence structure than protons. Furthermore, a complex relationship between direct and resolved photons will show up in next-to-leading order of QCD.

Having related the initial state particles electron and proton in the experiment to the photons and partons in perturbative QCD, we can turn our attention to the final state particles. Section 2.4 describes how the interpretation of partons as jets changes from leading to next-to-leading order of QCD. Several jet definition schemes are discussed with respect to their theoretical and experimental behavior.

The last section 2.5 summarizes the different ingredients of the calculation and contains the master formulæ for one- and two-jet photoproduction. Also, the numerous analytical contributions in leading and next-to-leading order of QCD are organized in a tabular form for transparency.

2.1 Photon Spectrum in the Electron

In photoproduction, one would like to study the hard scattering of real photon beams off nuclear targets. This has been done in fixed target experiments, like NA14 at CERN [13] or E683 at Fermilab [14], where real photons are produced e.g. in pion decay with energies of up to 400 GeV [15]. If higher energies are required, one must resort to spacelike, almost real photons radiated from electrons. This method is employed at the electron-proton collider HERA. There, electrons of energy $E_e = 26.7$ GeV and recently positrons of energy $E_e = 27.5$ GeV produce photons with small virtuality Q^2 , which then collide with a proton beam of energy $E_p = 820$ GeV. This corresponds to photon energies of up to 50 TeV in fixed target experiments.

On the theoretical side, the calculation of the electron-proton cross section can be considerably simplified by using the Weizsäcker-Williams or Equivalent Photon Approximation. Here, one uses current conservation and the small photon virtuality to factorize the electron-proton cross section into a broad-band photon spectrum in the electron and the hard photon-proton cross section. Already in 1924, Fermi discovered the equivalence between the perturbation of distant atoms by the field of charged particles flying by and the one due to incident electromagnetic radiation [16]. His semi-classical treatment was then extended to high-energy electrodynamics in 1933-1935 by Weizsäcker [17] and Williams [18] independently, who used a Fourier analysis to unravel the predominance of transverse over longitudinal photons radiated from a relativistic charged particle. In the fifties, Curtis [19] and Dalitz and Yennie [20] gave the first field-theoretical derivations and applied the approximation to meson production in electron-nucleon collisions. Chen and Zerwas used infinite-momentum-frame techniques for an extension to photon bremsstrahlung and photon splitting processes [21]. For a recent review of the various approximations see [22] and for the application to $\gamma\gamma$ processes see [23].

Let us consider the electroproduction process

$$\text{electron}(k) + \text{proton}(p) \rightarrow \text{electron}(k') + X \quad (2.1)$$

as shown in figure 1, where k , k' , and p are the four-momenta of the incoming and outgoing electron

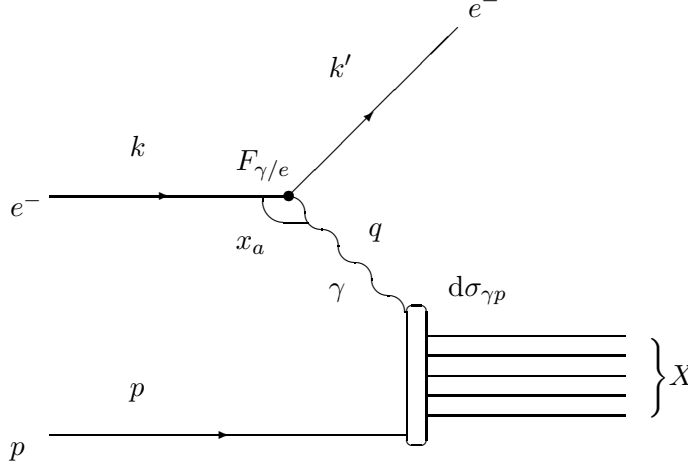


Figure 1: *Electron-proton scattering with single photon exchange.*

and the proton, respectively. X denotes a generic hadronic system not specified here. $q = k - k'$ is the momentum transfer of the electron to the photon with virtuality $Q^2 = -q^2 \simeq 0$, and the center-of-mass energy of the process is $\sqrt{s_H} = \sqrt{(k + p)^2} = 295.9 \text{ GeV}$ ($= 300.3 \text{ GeV}$ for the positron beam). We restrict ourselves to one-photon exchange without electroweak Z^0 admixture. Two-photon exchange is suppressed by an additional order of α , and Z^0 exchange is suppressed by the pole in the Z^0 mass $1/m_{Z^0}^2$.

The cross section of this process is

$$d\sigma_{ep}(ep \rightarrow eX) = \int \frac{1}{8k \cdot p} \frac{e^2 W^{\mu\nu} T_{\mu\nu}}{Q^4} \frac{d^3 k'}{(2\pi)^3 2E'_e}, \quad (2.2)$$

where $W^{\mu\nu}$ and $T_{\mu\nu}$ are the usual hadron and lepton tensors. Exploiting current conservation and the small photon virtuality, we find

$$W^{\mu\nu} T_{\mu\nu} = 4W_1(Q^2 = 0, q \cdot p) \left[Q^2 \frac{1 + (1 - x_a)^2}{x_a^2} - 2m_e^2 \right], \quad (2.3)$$

where

$$x_a = \frac{q \cdot p}{k \cdot p} = 1 - \frac{k' \cdot p}{k \cdot p} \in [0, 1] \quad (2.4)$$

is the fraction of longitudinal momentum carried by the photon. Next, we have to calculate the phase space for the scattered electron. Using

$$k' = (E'_e, 0, E'_e \beta' \sin \theta, E'_e \beta' \cos \theta) \quad , \quad k = (E_e, 0, 0, E_e \beta), \quad (2.5)$$

$$\beta' = \sqrt{1 - \frac{m_e^2}{E_e'^2}} \quad , \quad \beta = \sqrt{1 - \frac{m_e^2}{E_e^2}}, \quad (2.6)$$

and integrating over the azimuthal angle, we find

$$\begin{aligned}\frac{d^3k'}{E'_e} &= 2\pi\beta'^2 E'_e dk' d\cos\theta \\ &= \pi dq^2 dx_a.\end{aligned}\tag{2.7}$$

Combining eq. (2.3) and (2.7) and integrating over the photon virtuality, we can factorize the electron-proton cross section into

$$d\sigma_{ep}(ep \rightarrow eX) = \int_0^1 dx_a F_{\gamma/e}(x_a) d\sigma_{\gamma p}(\gamma p \rightarrow X),\tag{2.8}$$

where

$$F_{\gamma/e}(x_a) = \frac{\alpha}{2\pi} \left[\frac{1 + (1 - x_a)^2}{x_a} \ln \frac{Q_{\max}^2}{Q_{\min}^2} + 2m_e^2 x_a \left(\frac{1}{Q_{\min}^2} - \frac{1}{Q_{\max}^2} \right) \right]\tag{2.9}$$

is the renowned Weizsäcker-Williams approximation and where

$$\sigma_{\gamma p}(\gamma p \rightarrow X) = -\frac{g_{\mu\nu} W^{\mu\nu}}{8q \cdot p} = \frac{W_1(Q^2 = 0, q \cdot p)}{4q \cdot p}\tag{2.10}$$

is the photon-proton cross section. We will only use the leading logarithmic contribution and neglect the second term in eq. (2.9), also calculated by Frixione et al. [24].

There exist two fundamentally different experimental situations. At HERA, the scattered electron is anti-tagged and must disappear into the beam pipe. For such small scattering angles of the electron, the integration bounds Q_{\min} and Q_{\max} can be calculated from the equation

$$Q^2 = \frac{m_e^2 x_a^2}{1 - x_a} + \frac{E_e(1 + \beta)(A^2 - m_e^2)^2}{4A^3} \theta^2 + \mathcal{O}(\theta^4),\tag{2.11}$$

where $A = E_e(1 + \beta)(1 - x_a)$. Using the minimum scattering angle $\theta = 0$, we obtain

$$Q_{\min}^2 = \frac{m_e^2 x_a^2}{1 - x_a},\tag{2.12}$$

which leads us to the final form of the Weizsäcker-Williams approximation used here:

$$F_{\gamma/e}(x_a) = \frac{\alpha}{2\pi} \frac{1 + (1 - x_a)^2}{x_a} \ln \left(\frac{Q_{\max}^2(1 - x_a)}{m_e^2 x_a^2} \right).\tag{2.13}$$

At H1 and ZEUS, the maximum virtualities of the photon are given directly as $Q_{\max}^2 = 0.01 \text{ GeV}^2$ and 4 GeV^2 , respectively. If only the maximum scattering angle of the electron is known, we obtain

$$Q_{\max}^2 = E_e^2(1 - x_a)\theta_{\max}^2\tag{2.14}$$

with θ_{\max} being of the order of 5° . This form of Q_{\max}^2 will be used for the calculation of the $\gamma\gamma$ cross sections in accordance with experimental choices of θ_{\max} at LEP. Except in equation (2.13), we will assume all particles to be massless in this paper. Therefore, all results are only valid in the high-energy limit.

When no information about the scattered electron is available, one has to integrate over the whole phase space thus allowing large transverse momenta and endangering the factorization property of the cross section. Then, one only knows that the invariant mass of the produced hadronic system X has to be bounded from below, e.g. by minimal transverse momenta or heavy quark mass thresholds, which constrains the maximum virtuality of the photon only weakly. Possible choices are

$$Q_{\max} = \frac{\sqrt{s_H}}{2}, \frac{\sqrt{x_a s_H}}{2}, E_e, \dots\tag{2.15}$$

At e^+e^- colliders, bremsstrahlung of electrons is not the only source of almost real photons. The particles in one bunch experience rapid acceleration when they enter the electromagnetic field of the opposite bunch producing beamstrahlung which depends sensitively on the machine parameters. Even higher luminosities can be achieved by colliding the electron beam at some distance from the interaction point with a dense laser beam [25].

2.2 Parton Distributions in the Proton

The first evidence that the proton has a substructure came from deep inelastic electron-proton scattering $ep \rightarrow eX$. Together with muon- and neutrino-scattering, this process provides us with information on the distribution of partons (quarks and gluons) in the proton. In the parton model, scattering off hadrons is interpreted as an incoherent superposition of scattering off massless and pointlike partons. This is shown in figure 2, where p_b is the four-momentum of the scattered parton b . If the scale M_b ,

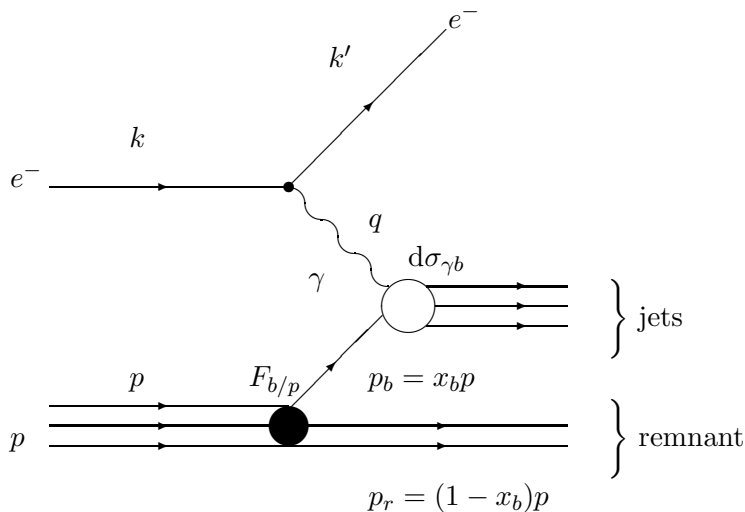


Figure 2: *Electron-proton scattering in the parton model.*

at which the proton is probed, is large enough, the transverse momentum of the parton will be small and its phase space can be described by a single variable

$$x_b = \frac{qp_b}{qp} \in [0, 1], \quad (2.16)$$

the longitudinal momentum fraction of the proton carried by the parton. The other partons in the proton will then not notice the interaction but form a so-called remnant or spectator jet. Multiple scattering is suppressed by factors of $1/M_b^2$, and only the leading twist contributes for large M_b^2 . The proton remnant carries the four-momentum p_r , which again depends only on x_b and the proton momentum p . The proton remnant will not be counted as a jet in the following.

We can now factorize the photon-proton cross section into

$$d\sigma_{\gamma p}(\gamma p \rightarrow \text{jets} + \text{remnant}) = \sum_b \int_0^1 dx_b F_{b/p}(x_b, M_b^2) d\sigma_{\gamma b}(\gamma b \rightarrow \text{jets}), \quad (2.17)$$

where $F_{b/p}(x_b, M_b^2)$ is the probability of finding a parton b (where b may be a quark, an antiquark, or a gluon) within the proton carrying a fraction x_b of its momentum when probed at the hard scale M_b .

The usual choice for deep inelastic scattering, $M_b = Q$, is not possible for photoproduction, as $Q^2 \simeq 0$ here. Instead, one takes $M_b = \xi E_T$ with E_T being the transverse energy of the outgoing parton or observed jet and ξ being of order 1. Contrary to the hard photon-parton scattering cross section $d\sigma_{\gamma b}$, the parton densities $F_{b/p}(x_b, M_b^2)$ are not calculable in perturbative QCD and have to be taken from experiment.

In the leading twist approximation, the parton densities extracted from deep inelastic scattering can be used for any other process with incoming nucleons like photoproduction or proton-antiproton scattering – they are universal. As stated above, they have to be determined by experiment at some scale $Q^2 = Q_0^2$, where one parametrizes the x dependence before evolving up to any value of Q^2 according to the Altarelli-Parisi (AP) equations [26]. The input parameters are then determined by a global fit to the data. The u , d , and s quark densities are rather well known today from muon scattering (BCDMS, NMC, E665) and neutrino scattering (CCFR) experiments, and the c quark is constrained by open charm production at EMC. The small- x region, where the gluon and the sea quarks become important, could, however, not be studied by these experiments. This is mainly the domain of the HERA experiments H1 and ZEUS in DIS as well as in photoproduction.

There exist many different sets of parton density functions. Most of them are easily accessible in the CERN library PDFLIB kept up to date by Plathow-Besch [27]. We will now briefly compare the three parametrizations mainly in use today: CTEQ [28], MRS [29], and GRV [30]. The first two are very similar to each other, and both take $Q_0^2 = 4 \text{ GeV}^2$. Very recently, CTEQ and MRS presented new parametrizations (set 4 and set R, respectively) including new HERA and TEVATRON inclusive jet data [31, 32]. The GRV approach is rather different from the two mentioned above. In order to avoid any free additional parameters, their original version was based on the assumption that all gluon and sea distributions are generated dynamically from measured valence quark densities at a very low scale $Q_0 \simeq \mathcal{O}(\Lambda)$. The QCD coupling scale Λ is fitted to the data and ranges from 200 to 344 MeV for the parametrizations considered here and for four quark flavors.

2.3 Parton Distributions in the Photon

Although the photon is the fundamental gauge boson of quantum electrodynamics (QED), which is the most accurately tested field theory, many reactions involving photons are much less well understood. This is due to the fact that the photon can fluctuate into $q\bar{q}$ pairs which in turn evolve into a complicated hadronic structure. At HERA, the photon radiated from the electron can thus interact either directly with a parton in the proton (direct component) or act as a hadronic source of partons which collide with the partons in the proton (resolved component, see figure 3). In the latter case, one does not test the proton structure alone but also the photon structure.

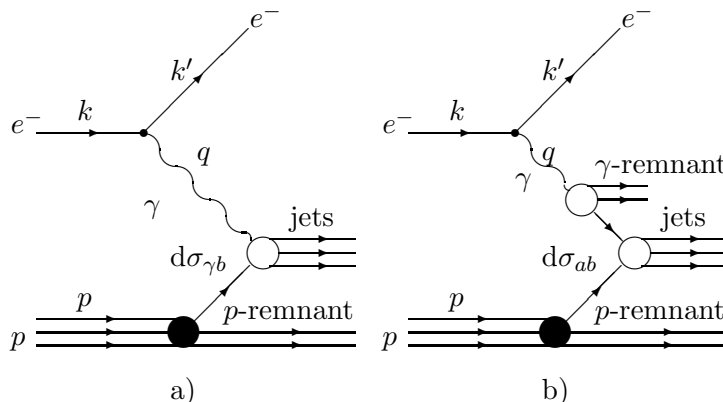


Figure 3: *Generic diagrams for a) direct and b) resolved photoproduction.*

Using the factorization theorem, the cross section for photon-parton scattering can be written as

$$d\sigma_{\gamma b}(\gamma b \rightarrow \text{jets}) = \sum_a \int_0^1 dy_a F_{a/\gamma}(y_a, M_a^2) d\sigma_{ab}(ab \rightarrow \text{jets}). \quad (2.18)$$

Here, $F_{a/\gamma}(y_a, M_a^2)$ stands for the probability of finding a parton a with momentum fraction y_a in the photon, which has to be universal in all processes. The scale M_a is a measure for the hardness of the parton-parton cross section $d\sigma_{ab}$ calculable in perturbative QCD and is again taken to be of $\mathcal{O}(E_T)$. The particle a can also be a direct photon. Then, $F_{\gamma/\gamma}(y_a, M_a^2)$ is simply given by the δ -function $\delta(1 - y_a)$ and does not depend on the hard scale M_a .

Before HERA started taking data, information on the hadronic structure of the photon came almost exclusively from deep inelastic $\gamma^* \gamma$ scattering at e^+e^- colliders. Similarly to deep inelastic ep scattering, this is a totally inclusive process well suited to define a photon structure function. Using $y = Q^2/(x_B s_H)$, where Q^2 denotes the virtuality of the probing photon γ^* , and replacing F_1 by the longitudinal structure function $F_L(x_B, Q^2) = F_2(x_B, Q^2) - 2x_B F_1(x_B, Q^2)$, we can write the deep inelastic scattering (DIS) cross section in the following form

$$\frac{d^2\sigma}{dx_B dy} = \frac{2\pi\alpha^2 s_H}{Q^4} \left\{ [1 + (1 - y)^2] F_2^\gamma(x_B, Q^2) - y^2 F_L^\gamma(x_B, Q^2) \right\}, \quad (2.19)$$

where in LO $F_2^\gamma(x_B, Q^2)$ is related to the singlet quark parton density in the photon similarly as in deep inelastic ep scattering

$$F_2^\gamma(x_B, Q^2) = \sum_q x_B e_q^2 (F_{q/\gamma}(x_B, Q^2) + F_{\bar{q}/\gamma}(x_B, Q^2)). \quad (2.20)$$

Fitting the input parameters to data is not as easy as in the proton case. First, no momentum sum rule applies for the photonic parton densities as they are all of LO in QED. This and the subleading nature of the gluonic process makes a determination of the gluon from F_2^γ very difficult. However, a momentum sum rule exists for mesons so that the VMD part of the gluon is constrained. Second, the cross section for F_2^γ is quite small and falls rapidly with increasing Q^2 (see eq. (2.19)) leading to large statistical errors.

Presently, over 20 different parton distributions exist for the photon, and most of them are available in the PDFLIB [27]. The VMD input is insufficient to fit the data at higher Q^2 offering two alternatives: GRV [33], AFG [34], and SaS [35] follow the same ‘‘dynamical’’ philosophy as in the GRV proton case starting from a simple valence-like input at a low scale $Q_0^2 = 0.25 \dots 0.36 \text{ GeV}^2$. On the other hand, LAC [36] and GS [37] take a larger value for $Q_0^2 = 4 \dots 5.3 \text{ GeV}^2$, assume a more complicated ansatz there, and fit the free parameters to F_2^γ data. LAC intended to demonstrate the poor constraints on the gluon assuming a very soft gluon (fits 1 and 2) as well as a very hard one (fit 3). However, LAC 3 is ruled out now by recent e^+e^- and HERA data. In their latest parametrization, GS lowered their input scale to $Q_0^2 = 3 \text{ GeV}^2$, included all available data on F_2^γ , and constrained the gluon from jet production at TRISTAN [38].

The distinction between direct and resolved photon is only meaningful in LO of perturbation theory. In NLO, collinear singularities arise from the photon initial state that have to be absorbed into the photon structure function (cf. sections 4.2.5 and 4.2.7) and produce a factorization scheme dependence as in the proton case. If one requires approximately the same F_2^γ in LO and NLO, the quark distributions in the $\overline{\text{MS}}$ -scheme have quite different shapes in LO and NLO. This is not the case if the DIS $_\gamma$ -scheme of GRV is used, where the direct-photon contribution to F_2^γ is absorbed into the photonic quark distributions. This allows for perturbative stability between LO and NLO results. Therefore, the separation between direct and resolved process is an artifact of finite order perturbation theory and depends on the factorization scheme and scale M_a . Experimentally, one tries to get a handle on this by introducing kinematical cuts, e.g. on the photon energy fraction taking part in the hard cross section.

2.4 Jet Definitions

Due to the confinement of color charge, neither incoming nor outgoing partons can be observed directly in experiment, but rather transform into colorless hadrons. This transformation is a long-distance process and is not calculable in perturbative QCD. For the incoming particles, we have already described how the ignorance of universal parton distributions in hadrons is parametrized. A similar method can be used for the final state partons, employing so-called fragmentation functions for the inclusive production of single hadrons [39]. The transformation of partons into individual hadrons forming part of the total final state was first studied by [40]. Alternatively, one can observe beams of many hadrons going approximately into the same direction without the need to specify individual hadrons. The hadrons are then combined into so-called jets by cluster algorithms, where one starts from an initial cluster in phase space and ends at stable fixed points for the jet coordinates. These jet definitions should fulfill a number of important properties. They should [41]

- be simple to implement in the experimental analysis,
- be simple to implement in the theoretical calculation,
- be defined at any order of perturbation theory,
- yield a finite cross section at any order of perturbation theory,
- yield a cross section that is relatively insensitive to hadronization.

Although, in principle, hadronization of the final state should be factorizable from the hard cross section and the initial state, jets do indeed look quite different in e^+e^- and in, at least partly, hadronic collisions like ep scattering. This can be attributed to the “underlying event” of remnant jet production from the initial state, which can interfere with the hard jets in the final state. The main problem here is the determination of the true jet energy and the subtraction of the remnant pedestal.

In LO QCD, there is a one-to-one correspondence between partons and jets. This results in a complete insensitivity of theory to the experimentally used algorithm or to the resolution parameters. The experimental results depend, however, on these parameters as well as on detector properties and have to be corrected stepwise from detector level to hadron level to parton level. The situation can only be improved by going to NLO in perturbation theory. Here, the emission of one additional soft or collinear parton is calculable with correct treatment of the occurring singularities. A hadron jet can then consist not only of one, but also of two partons. It acquires a certain substructure, and will depend on the experimental algorithm and resolution.

Historically, the first resolution criterion was proposed by Serman and Weinberg [42]. It adds a particle to a jet if its energy is smaller than ϵM or its angle with the jet is less than 2δ , which provides a close link to the radiation of secondary partons. The energy cut handles the soft divergencies and the angular cut the collinear divergencies. There is some freedom in the choice for M . Usually, one takes the hard scale of the process, e.g. Q in e^+e^- annihilation.

The PETRA experiments used this (ϵ, δ) algorithm and the so-called JADE cluster algorithm [43], which has the advantage of being invariant. Two particles are combined into a cluster, if their invariant mass $s_{ij} = (p_i + p_j)^2$ is smaller than yM^2 [44], where M^2 is again a typical scale and y is of $\mathcal{O}(10^{-2})$. In this way, the soft and collinear divergencies can be described by a single cut-off y . There exist a number of different schemes for this algorithm regarding the invariant mass of the combination of the two particles and the combination of the particle four-momenta (JADE-, E -, $E0$ -, P -, and $P0$ -scheme).

At hadron colliders, cluster algorithms tend to include hadrons from the remnant jet, which is not present in e^+e^- collisions, into the current jet. Therefore, algorithms are preferred here which use a cone in rapidity-azimuth $(\eta - \phi)$ space, quite similar to the δ -condition of Serman and Weinberg. The (pseudo-)rapidity $\eta = -\ln[\tan(\theta/2)]$ parametrizes the polar angle θ between the hard jet and the beam

axis, and ϕ is the azimuthal angle of the jet around the beam axis. In the case of cone algorithms, only inclusive cross sections are infrared safe, where an arbitrary number of particles outside the jet cone can be radiated as long as they are softer than the observed jets. According to the standardization of the Snowmass meeting in 1990, calorimeter cells or partons i may have a distance R_i from the jet center provided that

$$R_i = \sqrt{(\eta_i - \eta_J)^2 + (\phi_i - \phi_J)^2} \leq R, \quad (2.21)$$

where η_i and ϕ_i are the coordinates of the parton or the center of the calorimeter cell [45]. Typical values for the resolution parameter R range from 0.7 to 1, where the effects of hadronization and the underlying event are minimized. The transverse energy of the combined jet E_{T_J} is calculated from the sum of the particle E_{T_i}

$$E_{T_J} = \sum_{R_i \leq R} E_{T_i}, \quad (2.22)$$

and the jet axis is defined by the weighted averages

$$\eta_J = \frac{1}{E_{T_J}} \sum_{R_i \leq R} E_{T_i} \eta_i, \quad (2.23)$$

$$\phi_J = \frac{1}{E_{T_J}} \sum_{R_i \leq R} E_{T_i} \phi_i. \quad (2.24)$$

In perturbative QCD, the final state consists of a limited number of partons. For a single isolated parton i , the partonic and jet parameters agree ($(E_{T_i}, \eta_i, \phi_i) = (E_{T_J}, \eta_J, \phi_J)$) as shown in figure 4a), whereas two neighboring partons i, j will form a combined jet as shown in figure 4b). Equation (2.21)

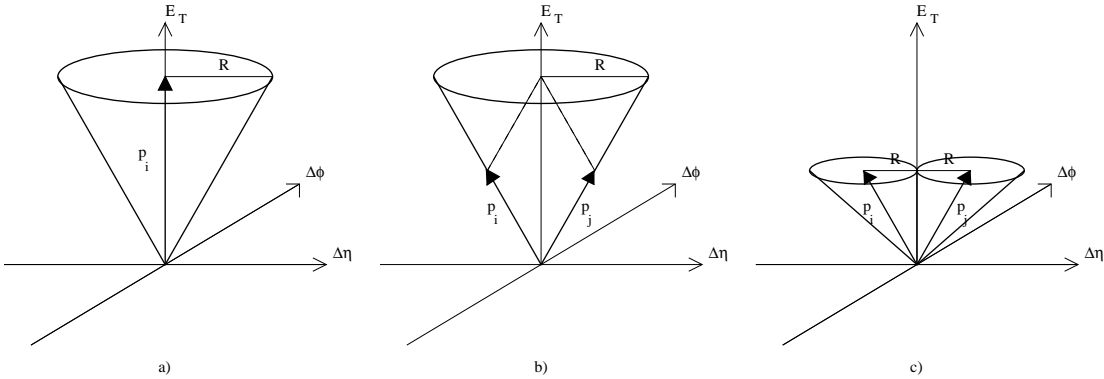


Figure 4: *Jet cone definition according to the Snowmass convention for a) a single parton, b) two combined partons with distance R from the jet axis, and c) two single partons.*

only defines the distances R_i, R_j of each parton from the jet axis so that the two partons may be separated from each other by

$$R_{ij} = \sqrt{(\eta_i - \eta_j)^2 + (\phi_i - \phi_j)^2} \leq \frac{E_{T_i} + E_{T_j}}{\max(E_{T_i}, E_{T_j})} R. \quad (2.25)$$

If both partons have equal transverse energy, they may then be separated by as much as $2R$. As parton j does not lie inside a cone of radius R around parton i and vice versa, one might with some justification also count the two partons separately as shown in figure 4c). If one wants to study only the highest- E_T jet, this “double counting” must be excluded.

The selection of the initiating cluster, before a cone is introduced (“seed-finding”), is not fixed by the Snowmass convention, and different approaches are possible. The ZEUS collaboration at HERA

uses two different cone algorithms: EUCELL takes the calorimeter cells in a window in $\eta - \phi$ space as seeds to find a cone with the highest E_T . The cells in this cone are then removed, and the algorithm continues. On the other hand, PUCELL was adapted from CDF and starts with single calorimeter cells. It then iterates cones around each of them, until the set of enclosed cells is stable. In this case it may happen that two stable jets overlap. If the overlapping transverse energy amounts to a large fraction of the jets, they are merged, otherwise the overlapping energy is split. Alternatively, the overlap could be attributed to the nearest, to the largest, or to both jets. The question of overlapping jets cannot be addressed in a next-to-leading order calculation of photoproduction. There, we only have up to three partons in the final state, which can form at most one recombined jet and no overlap.

Experimentally, jets of type b) in figure 4 are hard to find because of the missing seed in the jet center. This is a problem in particular with the PUCELL algorithm, which relies on initial clusters and does indeed find smaller cross sections than the less affected EUCELL algorithm [46]. One possibility to model this theoretically is to introduce an additional parameter R_{sep} [85] to restrict the distance of two partons from each other:

$$R_{ij} \leq \min \left[\frac{E_{T_i} + E_{T_j}}{\max(E_{T_i}, E_{T_j})} R, R_{\text{sep}} \right]. \quad (2.26)$$

$R_{\text{sep}} = 2R$ means no restriction. In figure 5, we can see that for two partons of similar or equal

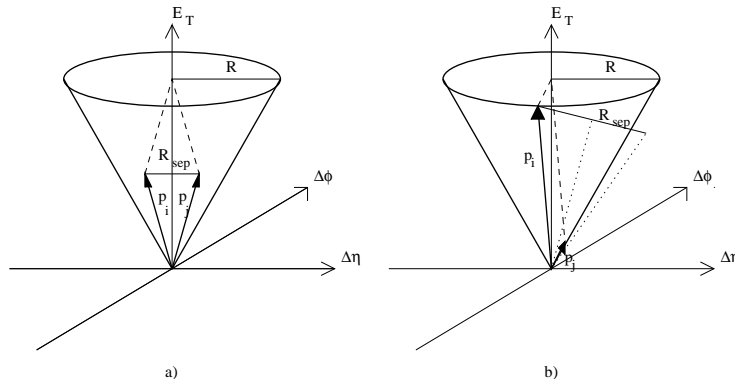


Figure 5: *Jet cone definition with an additional parameter for parton-parton separation R_{sep} : a) two partons with similar or equal transverse energies E_T , b) two partons with large E_T imbalance.*

transverse energies E_T , R_{sep} is the limiting parameter, whereas it is the parton-jet distance R for two partons with large E_T imbalance. Numerical studies of the R and R_{sep} dependences will be given in sections 5.3 and 5.5 [46].

The JADE algorithm clusters soft particles regardless of how far apart in angle they are, because only the invariant mass of the clusters is used. This is improved in the k_T or Durham clustering algorithm of Catani et al. [47], where one defines the closeness of two particles by

$$d_{ij} = \min(E_{T_i}, E_{T_j})^2 R_{ij}^2. \quad (2.27)$$

R_{ij} is again defined in $(\eta - \phi)$ space. For small opening angles, $R_{ij} \ll 1$, eq. (2.27) reduces to

$$\min(E_{T_i}, E_{T_j})^2 R_{ij}^2 \simeq \min(E_i, E_j)^2 \Delta\theta^2 \simeq k_T^2, \quad (2.28)$$

the relative transverse momentum squared of the two particles in the jet. Similarly, one can define a closeness to the remnant jet particles b , if they are present:

$$d_{ib} = E_{T_i}^2 R_{ib}^2. \quad (2.29)$$

Particles are clustered into jets as long as they are closer than

$$d_{\{ij,ib\}} \leq d_i^2 = E_{T_i}^2 R^2, \quad (2.30)$$

where R is an adjustable parameter of $\mathcal{O}(1)$ analogous to the cone size parameter in the cone algorithm. Also, one chooses the same recombination scheme. Consequently, the k_T algorithm produces jets that are very similar to those produced by the cone algorithm with $R = R_{\text{sep}}$.

2.5 Hard Photoproduction Cross Sections

We have now established the links between the experimentally observed initial and final states at HERA (electron, proton, and jets) and the partonic subprocess calculable in perturbative QCD. Formally, we can combine eqs. (2.8), (2.17), and (2.18) into

$$\begin{aligned} d\sigma_{ep}(ep \rightarrow e + \text{jets} + \text{remnants}) &= \\ &= \sum_{a,b} \int_0^1 dx_a F_{\gamma/e}(x_a) \int_0^1 dy_a F_{a/\gamma}(y_a, M_a^2) \int_0^1 dx_b F_{b/p}(x_b, M_b^2) d\sigma_{ab}^{(n)}(ab \rightarrow \text{jets}), \end{aligned} \quad (2.31)$$

where x_a , y_a , and x_b denote the longitudinal momentum fractions of the photon in the electron, the parton in the photon, and the parton in the proton, respectively. From now on, we will use the variable x_a as the variable for the *parton in the electron* with the consequence that the incoming partons have momenta $p_a = x_a k$ and $p_b = x_b p$ and eq. (2.31) becomes

$$\begin{aligned} d\sigma_{ep}(ep \rightarrow e + \text{jets} + \text{remnants}) &= \\ &= \sum_{a,b} \int_0^1 dx_a F_{\gamma/e}\left(\frac{x_a}{y_a}\right) \int_{x_a}^1 \frac{dy_a}{y_a} F_{a/\gamma}(y_a, M_a^2) \int_0^1 dx_b F_{b/p}(x_b, M_b^2) d\sigma_{ab}^{(n)}(ab \rightarrow \text{jets}). \end{aligned} \quad (2.32)$$

Next, one has to fix the kinematics for the photoproduction of jets. All particles are considered to be massless. In the HERA laboratory system, the positive z -axis is taken along the proton direction such that $k = E_e(1, 0, 0, -1)$ and $p = E_p(1, 0, 0, 1)$. For the hard jets, we choose the decomposition of four-momenta into transverse energies, rapidities, and azimuthal angles $p_i = E_{T_i}(\cosh \eta_i, \cos \phi_i, \sin \phi_i, \sinh \eta_i)$. The boost from the HERA laboratory system into the ep center-of-mass system is then simply mediated by a shift in rapidity $\eta_{\text{boost}} = 1/2 \ln(E_e/E_p)$. Through energy and momentum conservation $p_a + p_b = \sum_i p_i$, the final partons are related kinematically to the invariant scaling variables x_a and x_b

$$x_a = \frac{1}{2E_e} \sum_i E_{T_i} e^{-\eta_i}, \quad (2.33)$$

$$x_b = \frac{1}{2E_p} \sum_i E_{T_i} e^{\eta_i}. \quad (2.34)$$

The cross section for the production of an n -parton final state from two initial partons a, b ,

$$d\sigma_{ab}^{(n)}(ab \rightarrow \text{jets}) = \frac{1}{2s} \overline{|\mathcal{M}|^2} d\text{PS}^{(n)}, \quad (2.35)$$

depends on the flux factor $1/(2s)$, where $s = x_a x_b s_H$ is the partonic center-of-mass energy, the n -particle phase space

$$d\text{PS}^{(n)} = \int (2\pi)^d \prod_{i=1}^n \frac{d^d p_i \delta(p_i^2)}{(2\pi)^{d-1}} \delta^d \left(p_a + p_b - \sum_{j=1}^n p_j \right), \quad (2.36)$$

where $d = 4 - 2\varepsilon$ is the space-time dimension, and on the squared matrix element $\overline{|\mathcal{M}|^2}$. The latter is averaged over initial and summed over final spin and color states. Since we study almost-real photons with $Q^2 \simeq 0$ and treat quarks and gluons as massless, only transverse polarizations are possible giving spin average factors of $1/2$ for photons and quarks and $1/(2(1 - \varepsilon))$ for gluons in dimensional regularization. The quarks form the fundamental representation of the SU(3) color symmetry group and can therefore carry $N_C = 3$ different colors. The gluons belong to the adjoint representation of dimension $2N_C C_F = N_C^2 - 1 = 8$. This is the defining equation for the so-called color factor C_F . We therefore average the initial colors with factors of $1/N_C$ for quarks and $1/(2N_C C_F)$ for gluons.

In leading order QCD, the phase space for two partons $\text{dPS}^{(2)}$ in the final state and the Born matrix elements T have to be computed as displayed in the first line of table 1. In next-to-leading order QCD, new contributions arise. Whereas the virtual corrections V also have a two-particle phase space (second line in table 1), the real corrections of the final state F , of the photon initial state I , and of the proton initial state J require the inclusion of a third outgoing parton into the phase space $\text{dPS}^{(3)}$ (lines three to five in table 1). We will distinguish between direct and resolved photoproduction in the subsequent chapters and treat the two contributions in a completely parallel way.

Order	Phase Space $\text{dPS}^{(n)}$	Direct Matrix Element $ \mathcal{M} ^2$	Resolved Matrix Element $ \mathcal{M} ^2$
LO	$\text{dPS}^{(2)}$, sect. 3.1	$T_{\gamma b \rightarrow 12}$, sect. 3.2	$T_{ab \rightarrow 12}$, sect. 3.3
NLO	$\text{dPS}^{(3)}$, sect. 4.2.1	$V_{\gamma b \rightarrow 12}$, sect. 4.1.1	$V_{ab \rightarrow 12}$, sect. 4.1.2
		$F_{\gamma b \rightarrow 123}$, sect. 4.2.2	$F_{ab \rightarrow 123}$, sect. 4.2.3
	$\text{dPS}^{(3)}$, sect. 4.2.4	$I_{\gamma b \rightarrow 123}$, sect. 4.2.5	$I_{ab \rightarrow 123}$, sect. 4.2.7
		$J_{\gamma b \rightarrow 123}$, sect. 4.2.6	$J_{ab \rightarrow 123}$, sect. 4.2.8

Table 1: *Summary of phase space parametrizations and matrix elements needed for this NLO calculation of direct and resolved photoproduction.*

The two final state partons produced in a LO process have to balance their transverse energies $E_{T_1} = E_{T_2} = E_T$, so that relations (2.33) and (2.34) simplify to

$$x_a = \frac{E_T}{2E_e} (e^{-\eta_1} + e^{-\eta_2}), \quad (2.37)$$

$$x_b = \frac{E_T}{2E_p} (e^{\eta_1} + e^{\eta_2}). \quad (2.38)$$

The rapidity η_2 of the second jet is kinematically fixed by E_T , η_1 , and x_a through the relation

$$\eta_2 = -\ln \left(\frac{2x_a E_e}{E_T} - e^{-\eta_1} \right). \quad (2.39)$$

In the HERA experiments, x_a is restricted to a fixed interval $x_{a,\min} \leq x_a \leq x_{a,\max} < 1$. We shall disregard this constraint and allow x_a to vary in the kinematically allowed range $x_{a,\min} \leq x_a \leq 1$, where

$$x_{a,\min} = \frac{E_p E_T e^{-\eta_1}}{2E_e E_p - E_e E_T e^{\eta_1}} \quad (2.40)$$

except when we compare to experimental data. There we shall include the correct limits on x_a dictated by the experimental analysis. From eqs. (2.37) and (2.38), we can express x_b as a function of E_T , η_1 , and x_a :

$$x_b = \frac{x_a E_e E_T e^{\eta_1}}{2x_a E_e E_p - E_p E_T e^{-\eta_1}}. \quad (2.41)$$

The inclusive two-jet cross section for $ep \rightarrow e + \text{jet}_1 + \text{jet}_2 + X$ is obtained from

$$\frac{d^3\sigma}{dE_T^2 d\eta_1 d\eta_2} = \sum_{a,b} x_a F_{a/e}(x_a, M_a^2) x_b F_{b/p}(x_b, M_b^2) \frac{d\sigma}{dt}(ab \rightarrow \text{jets}), \quad (2.42)$$

where

$$F_{a/e}(x_a, M_a^2) = \int_{x_a}^1 \frac{dy_a}{y_a} F_{a/\gamma}(y_a, M_a^2) F_{\gamma/e}\left(\frac{x_a}{y_a}\right) \quad (2.43)$$

defines the parton content in the electron. $d\sigma/dt$ stands for the differential cross section of the partonic subprocess $ab \rightarrow \text{jets}$. The invariants of this process are $s = (p_a + p_b)^2$, $t = (p_a - p_1)^2$, and $u = (p_a - p_2)^2$. They can be expressed by the final state variables E_T , η_1 , and η_2 and the initial state momentum fractions x_a and x_b :

$$s = 4x_a x_b E_e E_p, \quad (2.44)$$

$$t = -2x_a E_e E_T e^{\eta_1} = -2x_b E_p E_T e^{-\eta_2}, \quad (2.45)$$

$$u = -2x_a E_e E_T e^{\eta_2} = -2x_b E_p E_T e^{-\eta_1}. \quad (2.46)$$

For the inclusive one-jet cross section, we must integrate over one of the rapidities in (2.42). We integrate over η_2 and transform to the variable x_a using (2.37). The result is the cross section for $ep \rightarrow e + \text{jet} + X$, which depends on E_T and η :

$$\frac{d^2\sigma}{dE_T d\eta} = \sum_{a,b} \int_{x_{a,\min}}^1 dx_a x_a F_{a/e}(x_a, M_a^2) x_b F_{b/p}(x_b, M_b^2) \frac{4E_e E_T}{2x_a E_e - E_T e^{-\eta}} \frac{d\sigma}{dt}(ab \rightarrow \text{jet}). \quad (2.47)$$

Here, x_b is given by (2.41) with $\eta_1 = \eta$.

3 Leading Order Cross Sections

In this section, we consider the leading order contributions to the photoproduction cross section $d\sigma/dt$. The leading order direct hard scattering process is of $\mathcal{O}(\alpha\alpha_s)$, and the leading order resolved hard scattering process is of $\mathcal{O}(\alpha_s^2)$. Since the latter has to be multiplied with the photon structure function of $\mathcal{O}(\alpha/\alpha_s)$, both contributions are of the same order $\mathcal{O}(\alpha\alpha_s)$. To this order, it is necessary to calculate the phase space of two-particle final states, the tree-level matrix elements for direct photons $\gamma b \rightarrow 12$, and those for resolved photons $ab \rightarrow 12$. The two particles produced in the hard scattering then correspond directly to the two jets that can at most be observed. Either particle can be in jet one or jet two, so that the cross sections $d\sigma/dt$ have to be considered in their given form and with $(t \leftrightarrow u)$ to give the complete cross section $d\sigma/dt(s, t, u) + d\sigma/dt(s, u, t)$. Furthermore, one has to add symmetry factors of $1/n!$ for n identical particles in the final state. As we will later go from four to $d = 4 - 2\varepsilon$ dimensions to regularize the singularities showing up in next-to-leading order, we already give the results in this section in d dimensions. If one is only interested in leading order results, one can always set ε to zero in this section.

Section 3.1 contains the phase space for $2 \rightarrow 2$ scattering in d dimensions. It is calculated in the center-of-mass system of the incoming or equivalently outgoing particles. The matrix elements for direct photons are presented in section 3.2. Only one master diagram for the so-called QCD Compton scattering process $\gamma q \rightarrow gq$ contributes. The gluon initiated process is obtained by crossing. For resolved photons, we have four parton-parton master diagrams. The corresponding matrix elements are given in section 3.3. In addition, we show a table from which the matrix elements for all other processes can be deduced. Section 3.4 contains the direct $\gamma\gamma$ Born matrix element.

3.1 Phase Space for Two-Particle Final States

We give here a brief sketch of the phase space calculation for the scattering of two initial into two final particles in $d = 4 - 2\varepsilon$ dimensions. We start from the general expression [48]

$$d\text{PS}^{(2)} = \int (2\pi)^d \prod_{i=1}^2 \frac{d^d p_i \delta(p_i^2)}{(2\pi)^{d-1}} \delta^d \left(p_a + p_b - \sum_{j=1}^2 p_j \right). \quad (3.1)$$

The dijet and single-jet cross sections in eqs. (2.42) and (2.47) require partonic cross sections differential in the Mandelstam variable t . We therefore insert an additional δ -function with respect to t

$$\frac{d\text{PS}^{(2)}}{dt} = \int (2\pi)^d \prod_{i=1}^2 \frac{d^d p_i \delta(p_i^2)}{(2\pi)^{d-1}} \delta^d \left(p_a + p_b - \sum_{j=1}^2 p_j \right) \delta(t + 2p_a p_1), \quad (3.2)$$

before we integrate over the d -dimensional δ -function leading to

$$\frac{d\text{PS}^{(2)}}{dt} = \int \frac{d^d p_1 \delta(p_1^2)}{(2\pi)^{d-2}} \delta((p_a + p_b - p_1)^2) \delta(t + 2p_a p_1). \quad (3.3)$$

Next, we choose the center-of-mass system of the incoming partons a, b as shown in figure 6, where

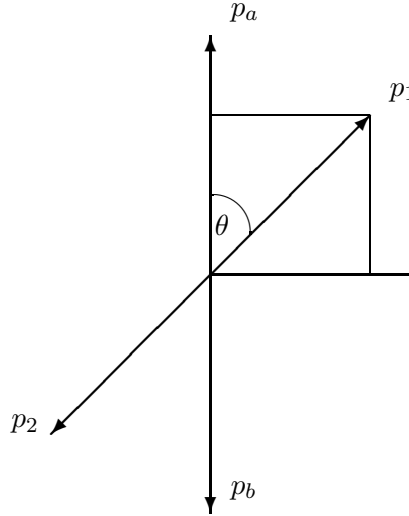


Figure 6: *Center-of-mass system for the scattering of two initial into two final partons.*

the outgoing partons are of the same energy and can be described by a single polar angle θ between p_1 and p_a . We integrate over the azimuthal angle ϕ

$$\frac{d\text{PS}^{(2)}}{dt} = \int \frac{dE_1 E_1^{d-3} d \cos \theta (1 - \cos^2 \theta)^{\frac{d-4}{2}}}{2^{d-2} \pi^{\frac{d-2}{2}} \Gamma\left(\frac{d-2}{2}\right)} \delta(s - 2\sqrt{s} E_1) \delta(t + \sqrt{s} E_1 (1 - \cos \theta)) \quad (3.4)$$

and over the remaining δ -functions. The final result is [49, 50, 51]

$$\frac{d\text{PS}^{(2)}}{dt} = \frac{1}{\Gamma(1 - \varepsilon)} \left(\frac{4\pi s}{tu} \right)^\varepsilon \frac{1}{8\pi s}. \quad (3.5)$$

3.2 Born Matrix Elements for Direct Photons

For direct photoproduction of two partons, there is only one generic Feynman diagram $\gamma q \rightarrow gq$ as displayed in figure 7. Unlike deep inelastic scattering, the leading order process already includes the

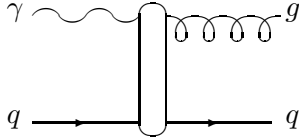


Figure 7: $2 \rightarrow 2$ Feynman diagram for direct photoproduction.

production of a hard gluon, which balances the transverse momentum of the scattered quark. This can either happen in the initial state (left diagram in figure 8) or in the final state (right diagram in figure 8) of this so-called ‘‘QCD Compton Scattering’’. Both diagrams have to be added and squared

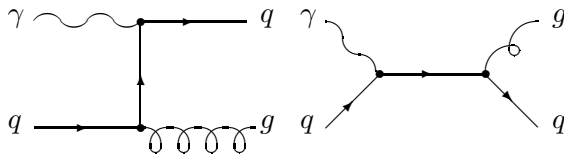


Figure 8: Born diagrams for direct photoproduction.

to give the full matrix element squared. In d dimensions, the result is

$$|\mathcal{M}|_{\gamma q \rightarrow gq}^2(s, t, u) = e^2 e_q^2 g^2 \mu^{4\epsilon} T_{\gamma q \rightarrow gq}(s, t, u), \quad (3.6)$$

where the renormalization scale μ keeps the couplings dimensionless and where

$$T_{\gamma q \rightarrow gq}(s, t, u) = 8N_C C_F (1 - \epsilon) \left[(1 - \epsilon) \left(-\frac{u}{s} - \frac{s}{u} \right) + 2\epsilon \right]. \quad (3.7)$$

Note that the DIS interference term of the two diagrams is missing as it is proportional to $Q^2 \simeq 0$. As discussed in section 2.2, the proton not only consists of quarks but also of gluons giving rise to a ‘‘Boson Gluon Fusion’’ process $\gamma g \rightarrow q\bar{q}$ not shown here. The corresponding matrix element is obtained from eq. (3.6) by simply crossing the initial quark with the final gluon, or ($s \leftrightarrow t$), and multiplying by (-1) for crossing a fermion line. Similarly, the contribution for incoming anti-quarks $\gamma \bar{q} \rightarrow g\bar{q}$ can be calculated by crossing ($s \leftrightarrow u$). The LO direct matrix elements have been known for quite some time [49, 52, 53] and are summarized in table 2.

Process	Matrix Element $ \mathcal{M} ^2$
$\gamma q \rightarrow gq$	$[\mathcal{M} _{\gamma q \rightarrow gq}^2(s, t, u)]/[4N_C]$
$\gamma \bar{q} \rightarrow g\bar{q}$	$[\mathcal{M} _{\gamma q \rightarrow gq}^2(u, t, s)]/[4N_C]$
$\gamma g \rightarrow q\bar{q}$	$-[\mathcal{M} _{\gamma q \rightarrow gq}^2(t, s, u)]/[8(1 - \epsilon)N_C C_F]$

Table 2: Summary of $2 \rightarrow 2$ squared matrix elements for direct photoproduction.

3.3 Born Matrix Elements for Resolved Photons

For resolved photoproduction of two partons, we have to calculate the four generic parton-parton scattering processes $qq' \rightarrow qq'$, $qq \rightarrow qq$, $q\bar{q} \rightarrow gg$, and $gg \rightarrow gg$. The corresponding Feynman diagrams are displayed in figure 9. The first process for the scattering of two non-identical quarks

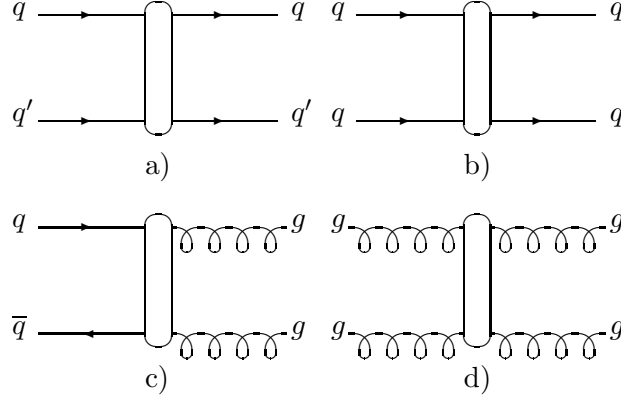


Figure 9: $2 \rightarrow 2$ Feynman diagrams for resolved photoproduction.

q and q' has already been calculated in 1978 by Cutler and Sivers [54], shortly prior to the other processes [55], and was compared to inclusive jet and hadron production at ISR energies.

Figure 10a) shows that for $qq' \rightarrow qq'$ only the one-gluon exchange between the different quarks in the t -channel contributes. The matrix element squared is given by

$$|\mathcal{M}|_{qq' \rightarrow qq'}^2(s, t, u) = g^4 \mu^{4\epsilon} T_{qq' \rightarrow qq'}(s, t, u) \quad (3.8)$$

with

$$T_{qq' \rightarrow qq'}(s, t, u) = 4N_C C_F \left(\frac{s^2 + u^2}{t^2} - \epsilon \right). \quad (3.9)$$

We will split off the coupling constants for the other Born matrix elements $|\mathcal{M}|^2$ as in eq. (3.8).

Equal quark flavors cannot be distinguished in the final state so that both diagrams in figure 10b) have to be added. In addition to the squares of the individual diagrams already present in the case of different quark flavors, the interference term

$$T_{qq \rightarrow qq}(s, t, u) = -8C_F(1 - \epsilon) \left(\frac{s^2}{ut} + \epsilon \right) \quad (3.10)$$

also contributes to the process $qq \rightarrow qq$.

Final gluons are also undistinguishable and can even couple in a non-abelian way as shown in figure 10c). The resulting matrix element for the process $q\bar{q} \rightarrow gg$ is

$$T_{q\bar{q} \rightarrow gg}(s, t, u) = 4C_F(1 - \epsilon) \left(\frac{2N_C C_F}{ut} - \frac{2N_C^2}{s^2} \right) (t^2 + u^2 - \epsilon s^2). \quad (3.11)$$

The diagrams for the process $gg \rightarrow gg$ in figure 10d) give

$$T_{gg \rightarrow gg}(s, t, u) = 32N_C^3 C_F(1 - \epsilon)^2 \left(3 - \frac{ut}{s^2} - \frac{us}{t^2} - \frac{st}{u^2} \right). \quad (3.12)$$

All other diagrams can be obtained from the above by simple crossing relations. The complete result in d dimensions can be found in [56] and is summarized in table 3.

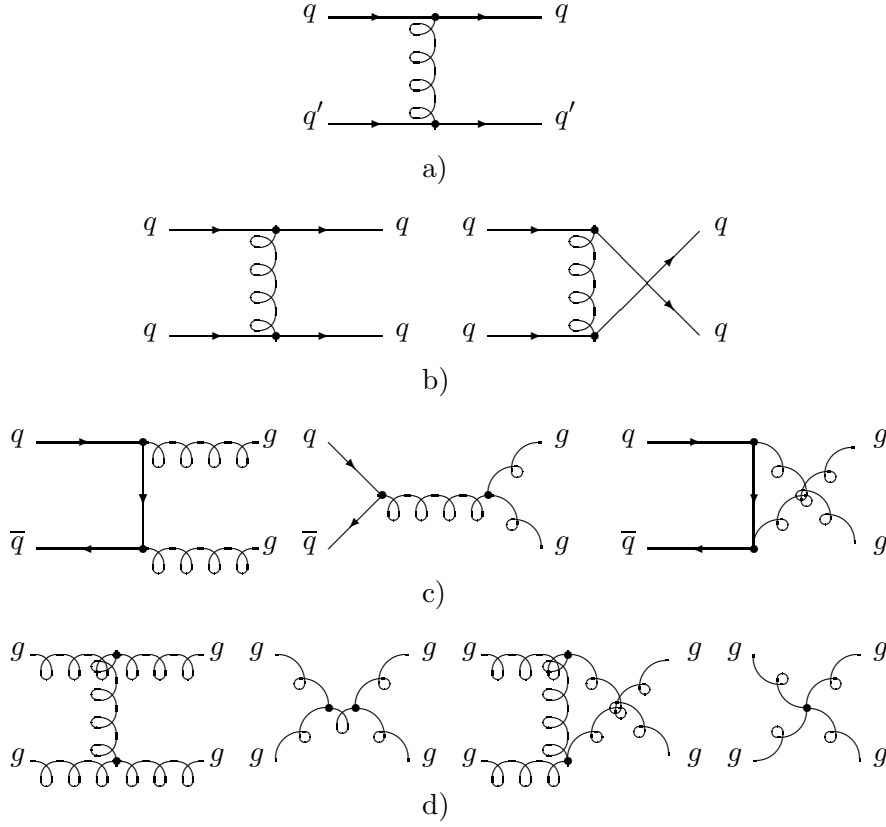


Figure 10: *Born diagrams for resolved photoproduction.*

Process	Matrix Element $ \mathcal{M} ^2$
$qq' \rightarrow qq'$	$[\mathcal{M} _{qq' \rightarrow qq'}^2(s, t, u)]/[4N_C^2]$
$q\bar{q}' \rightarrow q\bar{q}'$	$[\mathcal{M} _{qq' \rightarrow qq'}^2(u, t, s)]/[4N_C^2]$
$q\bar{q} \rightarrow \bar{q}'q'$	$[\mathcal{M} _{qq' \rightarrow qq'}^2(t, s, u)]/[4N_C^2]$
$qq \rightarrow qq$	$[\mathcal{M} _{qq' \rightarrow qq'}^2(s, t, u) + \mathcal{M} _{qq' \rightarrow qq'}^2(s, u, t) + \mathcal{M} _{qq \rightarrow qq}^2(s, t, u)]/[4N_C^2]/2!$
$q\bar{q} \rightarrow q\bar{q}$	$[\mathcal{M} _{qq' \rightarrow qq'}^2(u, t, s) + \mathcal{M} _{qq' \rightarrow qq'}^2(u, s, t) + \mathcal{M} _{qq \rightarrow qq}^2(u, t, s)]/[4N_C^2]$
$q\bar{q} \rightarrow gg$	$[\mathcal{M} _{q\bar{q} \rightarrow gg}^2(s, t, u)]/[4N_C^2]/2!$
$qg \rightarrow qg$	$-[\mathcal{M} _{q\bar{q} \rightarrow gg}^2(t, s, u)]/[8(1 - \varepsilon)N_C^2 C_F]$
$\bar{q}g \rightarrow \bar{q}g$	$-[\mathcal{M} _{q\bar{q} \rightarrow gg}^2(t, u, s)]/[8(1 - \varepsilon)N_C^2 C_F]$
$gg \rightarrow q\bar{q}$	$[\mathcal{M} _{q\bar{q} \rightarrow gg}^2(s, t, u)]/[16(1 - \varepsilon)^2 N_C^2 C_F^2]$
$gg \rightarrow gg$	$[\mathcal{M} _{qq \rightarrow qq}^2(s, t, u)]/[16(1 - \varepsilon)^2 N_C^2 C_F^2]/2!$

Table 3: *Summary of $2 \rightarrow 2$ squared matrix elements for resolved photoproduction.*

3.4 Born Matrix Element for Direct $\gamma\gamma$ Scattering

Since the gluon has no electromagnetic charge, direct $\gamma\gamma$ scattering can only proceed through the process $\gamma\gamma \rightarrow q\bar{q}$ as shown in figure 11. The corresponding matrix element is given by

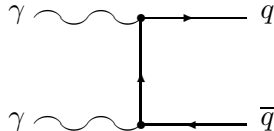


Figure 11: *Born diagram for direct $\gamma\gamma$ scattering.*

$$|\mathcal{M}|_{\gamma\gamma \rightarrow q\bar{q}}^2(s, t, u) = e^4 e_q^4 \mu^{4\epsilon} T_{\gamma\gamma \rightarrow q\bar{q}}(s, t, u), \quad (3.13)$$

where

$$T_{\gamma\gamma \rightarrow q\bar{q}}(s, t, u) = 8N_C(1 - \epsilon) \left[(1 - \epsilon) \left(\frac{u}{t} + \frac{t}{u} \right) - 2\epsilon \right]. \quad (3.14)$$

It can be obtained from the direct photoproduction matrix element for $\gamma q \rightarrow qg$ in 3.6 through crossing of $s \rightarrow t$, multiplication with (-1) for the crossing of a fermion line, and replacing the strong coupling constant g^2 by $e^2 e_q^2$ and the color factor C_F by 1.

4 Next-To-Leading Order Cross Sections

As in any calculation of next-to-leading order cross sections, we have to calculate two types of corrections in photoproduction: virtual and real corrections. For the direct case, these corrections are of $\mathcal{O}(\alpha\alpha_s^2)$, and for the resolved case, they are of $\mathcal{O}(\alpha_s^3)$. Throughout this section, direct and resolved photon results will be presented separately, but in a completely parallel way. Whereas the direct contributions have already been published [57, 8], the resolved contributions are presented here for the first time.

The virtual corrections consist of the interference terms of one-loop graphs with the Born graphs calculated in section 3 and will be given in section 4.1. We can still use the same phase space for two final partons as in the last section. The direct matrix elements are contained in section 4.1.1, those for resolved photons in section 4.1.2. Again, we display only the relevant master diagrams, from which all subprocesses can be deduced through crossing. Section 4.1.3 contains the virtual corrections for direct $\gamma\gamma$ scattering.

The real corrections are derived from the integration of diagrams with a third parton in the final state over regions of phase space, where this third parton causes singularities in the matrix elements. Different methods can be employed here. We choose the phase space slicing method with an invariant mass cut [44] in section 4.2. Alternatively, the subtraction method could be used [62, 58, 6]. We calculate the three particle phase space in two different versions for final state singularities (section 4.2.1) and initial state singularities (section 4.2.4). These sections are followed by the calculation of the matrix elements for final state (sections 4.2.2 through 4.2.3) and initial state corrections (sections 4.2.5 through 4.2.8). The real corrections for direct $\gamma\gamma$ scattering are presented in section 4.2.9.

Finally, we demonstrate the cancellation of the infrared and collinear singularities, that show up in the virtual and real corrections separately, in section 4.3. The ultraviolet singularities in the virtual corrections are removed by counter terms in the renormalization procedure. Remaining collinear singularities in the initial states can be absorbed into the photon and proton structure functions.

4.1 Virtual Corrections

The central blobs in figures 7 and 9 can also contain loop corrections to the leading order matrix elements in figures 8 and 10. Up to $\mathcal{O}(\alpha_s^2)$, the interference terms between the direct Born diagrams T and the direct one-loop diagrams V have to be taken into account according to

$$\begin{aligned} |\mathcal{M}|^2(\mathcal{O}(\alpha_s^2)) &= |\sqrt{\alpha_s T} + \sqrt{\alpha_s^3 V}|^2 \\ &= \alpha_s T + 2\alpha_s^2 \sqrt{V^* T} + \mathcal{O}(\alpha_s^3). \end{aligned} \quad (4.1)$$

Similarly, the interference terms between the resolved Born diagrams T and the resolved one-loop diagrams V have to be taken into account up to $\mathcal{O}(\alpha_s^3)$.

The inner loop momenta are unconstrained from the outer $2 \rightarrow 2$ scattering process. We can therefore still make use of the phase space calculated in section 3.1, but have to integrate over the inner degrees of freedom. At the lower and upper integration bounds, we encounter infrared (IR) and ultraviolet (UV) divergencies. Using the dimensional regularization scheme of t'Hooft and Veltman [59], we integrate in $d = 4 - 2\varepsilon$ dimensions, thus rendering the integrals finite and keeping the theory Lorentz and gauge invariant. The IR and UV poles show up as terms $\propto 1/\varepsilon^2$ and $1/\varepsilon$. As a consequence, the complete higher order cross sections have to be calculated in d dimensions up to $\mathcal{O}(\varepsilon^2)$ to ensure that no finite terms are missing.

The ultraviolet divergencies coming from infinite loop momenta can be removed by renormalizing the fields, couplings, gauge parameters, and masses in the Lagrangian, since QCD is a renormalizable field theory. This is done by multiplying the divergent parameters in the Lagrangian with renormalization constants Z_i and expanding up to the required order in the coupling constant g . The resulting counter terms then render the physical Green's functions finite. In addition to the $1/\varepsilon$ poles, universal finite contributions

$$\frac{1}{\varepsilon} - \gamma_E + \ln(4\pi) \quad (4.2)$$

are included into the counter terms according to the modified minimal subtraction ($\overline{\text{MS}}$) scheme [60], which we employ here. The coupling constant g is kept dimensionless by multiplying it with the renormalization scale μ

$$g \rightarrow g\mu^\varepsilon. \quad (4.3)$$

If eq. (4.3) is expanded in powers of ε and combined with single poles of the type in eq. (4.2), the renormalization procedure will produce an explicit logarithmic dependence on the renormalization scale μ

$$\frac{1}{\varepsilon} \left(\frac{4\pi\mu^2}{s} \right)^\varepsilon \doteq \frac{1}{\varepsilon} + \ln \frac{4\pi\mu^2}{s}, \quad (4.4)$$

that cancels the first term of the expansion of the running coupling constant

$$\alpha_s(\mu^2) = \frac{12\pi}{(33 - 2N_f) \ln \frac{\mu^2}{\Lambda^2}} \left(1 - \frac{6(153 - 19N_f) \ln(\ln \frac{\mu^2}{\Lambda^2})}{(33 - 2N_f)^2 \ln \frac{\mu^2}{\Lambda^2}} \right) + \dots \quad (4.5)$$

α_s is given here in two-loop approximation as appropriate in NLO QCD, and N_f is the number of flavors in the $q\bar{q}$ loops. We choose $\mu = \mathcal{O}(E_T)$ as for the factorization scales.

Infrared divergencies arise from small loop momenta in the virtual corrections. They have to cancel eventually against the divergencies from the emission of real soft and collinear partons according to the Kinoshita-Lee-Nauenberg theorem [61]. Finally, one obtains finite physical results in the limit $d \rightarrow 4$.

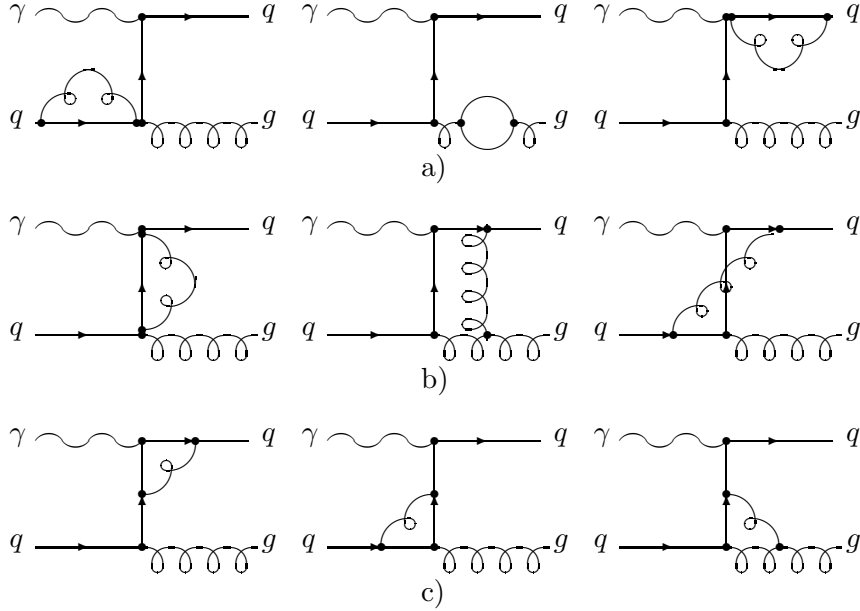


Figure 12: *Virtual diagrams for direct photoproduction. The circle in diagram a) denotes a quark, gluon, and ghost loop.*

4.1.1 Virtual Corrections for Direct Photons

The one-loop corrections to the left diagram of figure 8 are shown in figure 12 and can be classified into a) self-energy diagrams, b) propagator corrections and box diagrams, and c) vertex corrections. They contain an additional virtual gluon, which leads to an extra factor α_s . Similar diagrams are obtained for the right diagram of figure 8. As in leading order, the diagrams for the process $\gamma g \rightarrow q\bar{q}$ can be obtained from figure 12 by crossing the initial quark and the final gluon or equivalently ($s \leftrightarrow t$) and multiplying by (-1) for the crossing of a fermion line. However, the virtual corrections can in general contain logarithms $\ln(x/s - i\eta)$ and dilogarithms $\text{Li}_2(x/s)$, where x denotes different Mandelstam variables before and after crossing. The $i\eta$ -prescription for Feynman propagators then takes care of additional terms of π^2 , that arise in the quadratic logarithms with negative argument.

The virtual contributions have been well known for many years from $e^+e^- \rightarrow q\bar{q}g$ higher order QCD calculations [62, 63]. For the corresponding photoproduction cross section, one substitutes $Q^2 = 0$ and performs the necessary crossings. The result can be found in [49, 53, 57]. We have also compared with the results in [51] for deep inelastic scattering $eq \rightarrow e'gq$ and $eg \rightarrow e'q\bar{q}$, which can be expressed by the invariants s , t , and u after setting $Q^2 = 0$. For completeness and for later use, we write the final result in the form

$$|\mathcal{M}|_{\gamma b \rightarrow 12}^2(s, t, u) = e^2 e_q^2 g^2 \mu^{4\epsilon} \frac{\alpha_s}{2\pi} \left(\frac{4\pi\mu^2}{s} \right)^\epsilon \frac{\Gamma(1-\epsilon)}{\Gamma(1-2\epsilon)} V_{\gamma b \rightarrow 12}(s, t, u) \quad (4.6)$$

The expression $V_{\gamma q \rightarrow gq}(s, t, u)$ is given by

$$\begin{aligned} V_{\gamma q \rightarrow gq}(s, t, u) = & \left[C_F \left(-\frac{2}{\epsilon^2} + \frac{1}{\epsilon} \left(2 \ln \frac{-t}{s} - 3 \right) + \frac{2\pi^2}{3} - 7 + \ln^2 \frac{t}{u} \right) \right. \\ & - \frac{N_C}{2} \left(\frac{2}{\epsilon^2} + \frac{1}{\epsilon} \left(\frac{11}{3} + 2 \ln \frac{-t}{s} - 2 \ln \frac{-u}{s} \right) + \frac{\pi^2}{3} + \ln^2 \frac{t}{u} + \frac{11}{3} \ln \frac{s}{\mu^2} \right) \\ & \left. + \frac{N_f}{3} \left(\frac{1}{\epsilon} + \ln \frac{s}{\mu^2} \right) \right] T_{\gamma q \rightarrow gq}(s, t, u) \end{aligned} \quad (4.7)$$

$$\begin{aligned}
& +8N_C C_F^2 \left(-2 \ln \frac{-u}{s} + 4 \ln \frac{-t}{s} - 3 \frac{s}{u} \ln \frac{-u}{s} - \left(2 + \frac{u}{s} \right) \left(\pi^2 + \ln^2 \frac{t}{u} \right) \right. \\
& - \left. \left(2 + \frac{s}{u} \right) \ln^2 \frac{-t}{s} \right) \\
& -4N_C^2 C_F \left(4 \ln \frac{-t}{s} - 2 \ln \frac{-u}{s} - \left(2 + \frac{u}{s} \right) \left(\pi^2 + \ln^2 \frac{t}{u} \right) - \left(2 + \frac{s}{u} \right) \ln^2 \frac{-t}{s} \right).
\end{aligned}$$

The contributions for incoming anti-quarks and gluons $\gamma \bar{q} \rightarrow g \bar{q}$ and $\gamma g \rightarrow q \bar{q}$ could be obtained according to table 2, if the imaginary parts were included above. The result for anti-quarks turns out to be identical to eq. (4.7), and for the gluon initiated process one obtains

$$\begin{aligned}
V_{\gamma g \rightarrow q \bar{q}}(s, t, u) &= \left[C_F \left(-\frac{2}{\varepsilon^2} - \frac{3}{\varepsilon} + \frac{2\pi^2}{3} - 7 + \ln^2 \frac{-t}{s} + \ln^2 \frac{-u}{s} \right) \right. \\
& - \frac{N_C}{2} \left(\frac{2}{\varepsilon^2} + \frac{1}{\varepsilon} \left(\frac{11}{3} - 2 \ln \frac{-t}{s} - 2 \ln \frac{-u}{s} \right) + \frac{\pi^2}{3} + \ln^2 \frac{tu}{s^2} + \frac{11}{3} \ln \frac{s}{\mu^2} \right) \\
& \left. + \frac{N_f}{3} \left(\frac{1}{\varepsilon} + \ln \frac{s}{\mu^2} \right) \right] T_{\gamma g \rightarrow q \bar{q}}(s, t, u) \\
& + 8N_C C_F^2 \left(2 \ln \frac{-t}{s} + 2 \ln \frac{-u}{s} + 3 \frac{u}{t} \ln \frac{-t}{s} + 3 \frac{t}{u} \ln \frac{-u}{s} + \left(2 + \frac{u}{t} \right) \ln^2 \frac{-u}{s} \right. \\
& \left. + \left(2 + \frac{t}{u} \right) \ln^2 \frac{-t}{s} \right) \\
& - 4N_C^2 C_F \left(2 \ln \frac{-t}{s} + 2 \ln \frac{-u}{s} + \left(2 + \frac{u}{t} \right) \ln^2 \frac{-u}{s} + \left(2 + \frac{t}{u} \right) \ln^2 \frac{-t}{s} \right).
\end{aligned} \tag{4.8}$$

All UV poles have been canceled by counter terms through the renormalization procedure, and the remaining IR poles are contained in the first three lines of eqs. (4.7) and (4.8). Contrary to some of the finite terms, they are proportional to the LO Born matrix elements $T_{\gamma q \rightarrow gq}$ and $T_{\gamma g \rightarrow q \bar{q}}$. The explicit dependence of the virtual corrections on the renormalization scale μ is contained in the logarithms proportional to the Born matrix elements and N_C and N_f , respectively. All terms of $\mathcal{O}(\varepsilon)$ and higher have been omitted since they do not contribute in the physical limit $d \rightarrow 4$.

4.1.2 Virtual Corrections for Resolved Photons

For the resolved virtual corrections, we show in figure 13 only the one-loop diagrams for $qq' \rightarrow qq'$ and classify them again into a) self-energy diagrams, b) propagator corrections and box diagrams, and c) vertex corrections. Due to the additional gluon, these contributions are again one order higher in α_s than the Born terms as in the direct case. The complete set of diagrams can be found in [56] as well as the results

$$|\mathcal{M}|_{ab \rightarrow 12}^2(s, t, u) = g^4 \mu^{4\varepsilon} \frac{\alpha_s}{2\pi} \left(\frac{4\pi\mu^2}{Q^2} \right)^\varepsilon \frac{\Gamma(1-\varepsilon)}{\Gamma(1-2\varepsilon)} V_{ab \rightarrow 12}(s, t, u), \tag{4.9}$$

where Q^2 denotes now an arbitrary scale. For the diagrams in figure 13, we obtain

$$\begin{aligned}
V_{qq' \rightarrow qq'}(s, t, u) &= \left[C_F \left(-\frac{4}{\varepsilon^2} - \frac{1}{\varepsilon} (6 + 8l(s) - 8l(u) - 4l(t)) \right. \right. \\
& - \frac{2\pi^2}{3} - 16 - 2l^2(t) + l(t)(6 + 8l(s) - 8l(u)) \\
& - 2 \frac{s^2 - u^2}{s^2 + u^2} (2\pi^2 + (l(t) - l(s))^2 + (l(t) - l(u))^2) \\
& \left. \left. + 2 \frac{s+u}{s^2 + u^2} ((s+u)(l(u) - l(s)) + (u-s)(2l(t) - l(s) - l(u))) \right) \right]
\end{aligned} \tag{4.10}$$

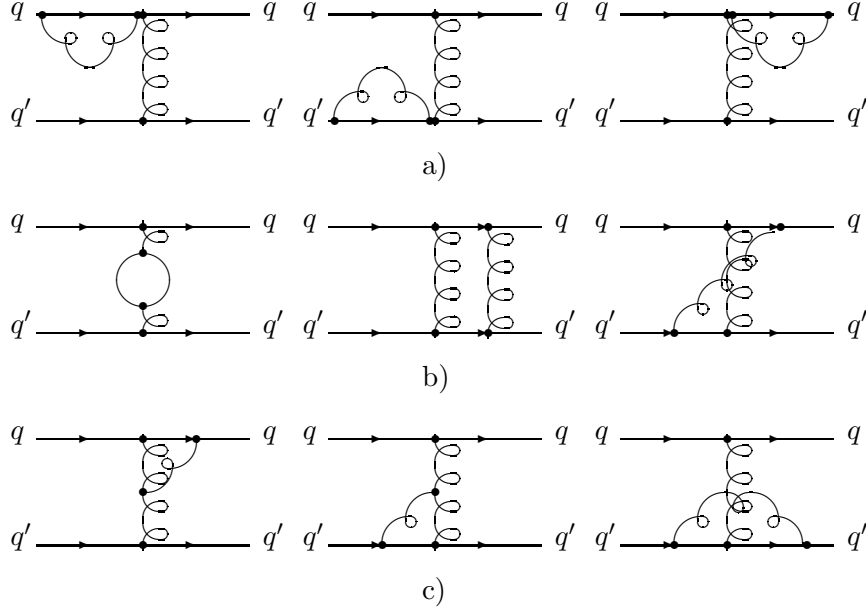


Figure 13: *Virtual diagrams for resolved photoproduction. Only the one-loop corrections to $qq' \rightarrow qq'$ are shown. The circle in diagram b) denotes a quark, gluon, and ghost loop.*

$$\begin{aligned}
& +N_C \left(\frac{1}{\varepsilon} (4l(s) - 2l(u) - 2l(t)) + \frac{85}{9} + \pi^2 + 2l(t)(l(t) + l(u) - 2l(s)) \right. \\
& + \frac{s^2 - u^2}{2(s^2 + u^2)} (3\pi^2 + 2(l(t) - l(s))^2 + (l(t) - l(u))^2) \\
& \left. - \frac{st}{s^2 + u^2} (l(t) - l(u)) + \frac{2ut}{s^2 + u^2} (l(t) - l(s)) + \frac{11}{3} (l(-\mu^2) - l(t)) \right) \\
& + \frac{N_f}{2} \left(\frac{4}{3} (l(t) - l(-\mu^2)) - \frac{20}{9} \right) \Big] T_{qq' \rightarrow qq'}(s, t, u).
\end{aligned}$$

The contributions for incoming quarks and anti-quarks of different flavor can be obtained from table 3 as well as the contribution for identical quark flavors. There one also has to include the interference term

$$\begin{aligned}
V_{qq \rightarrow qq}(s, t, u) = & \left[C_F \left(-\frac{4}{\varepsilon^2} - \frac{1}{\varepsilon} (6 + 4l(s) - 4l(t) - 4l(u)) - \frac{7\pi^2}{6} - 16 \right. \right. \\
& \left. \left. - \frac{3}{2} (l(t) + l(u))^2 + 2l(s)(l(t) + l(u)) + 2(l(t) + l(u)) \right) \right. \\
& + N_C \left(\frac{1}{\varepsilon} (4l(s) - 2l(t) - 2l(u)) + \frac{85}{9} + \frac{5}{4} (l(t) + l(u))^2 \right. \\
& \left. - l(t)l(u) - 2l(s)(l(t) + l(u)) - \frac{4}{3} (l(t) + l(u)) + \frac{5}{4} \pi^2 + \frac{11}{3} l(-\mu^2) \right) \\
& + \frac{N_f}{2} \left(-\frac{20}{9} + \frac{2}{3} (l(t) + l(u) - 2l(-\mu^2)) \right) \\
& \left. + \frac{1}{N_C} \left((\pi^2 + (l(t) - l(u))^2) \frac{ut}{2s^2} + \frac{u}{s} l(t) + \frac{t}{s} l(u) \right) \right] T_{qq \rightarrow qq}(s, t, u).
\end{aligned} \tag{4.11}$$

For incoming antiquarks, the Mandelstam variables ($s \leftrightarrow u$) have to be crossed. The first lines proportional to the color factors C_F and N_C contain the IR singular terms in the two processes

discussed above. Furthermore, the complete virtual corrections are proportional to the Born matrix elements. This is not true for the case $q\bar{q} \rightarrow gg$, where the virtual corrections are given by

$$\begin{aligned}
V_{q\bar{q} \rightarrow gg}(s, t, u) = & \left[C_F \left(-\frac{2}{\varepsilon^2} - \frac{3}{\varepsilon} - 7 - \frac{\pi^2}{3} \right) \right. \\
& + N_C \left(-\frac{2}{\varepsilon^2} - \frac{11}{3\varepsilon} + \frac{11}{3} l(-\mu^2) - \frac{\pi^2}{3} \right) \\
& + \frac{N_f}{2} \left(\frac{4}{3\varepsilon} - \frac{4}{3} l(-\mu^2) \right) \left. \right] T_{q\bar{q} \rightarrow gg}(s, t, u) \\
& + \frac{l(s)}{\varepsilon} \left(\left(4N_C^3 C_F + \frac{4C_F}{N_C} \right) \frac{t^2 + u^2}{ut} - 16N_C^2 C_F^2 \frac{t^2 + u^2}{s^2} \right) \\
& + \frac{8N_C^3 C_F}{\varepsilon} \left(l(t) \left(\frac{u}{t} - \frac{2u^2}{s^2} \right) + l(u) \left(\frac{t}{u} - \frac{2t^2}{s^2} \right) \right) \\
& - \frac{8N_C C_F}{\varepsilon} \left(\frac{u}{t} + \frac{t}{u} \right) (l(t) + l(u)) \\
& + f^c(s, t, u) + f^c(s, u, t).
\end{aligned} \tag{4.12}$$

Here, only parts of the IR singular terms are proportional to the Born matrix element $T_{q\bar{q} \rightarrow gg}$. The finite contributions have been put into the function

$$\begin{aligned}
f^c(s, t, u) = & 8N_C^2 C_F \left[\frac{l(t)l(u)}{N_C} \frac{t^2 + u^2}{2tu} \right. \\
& + l^2(s) \left(\frac{1}{4N_C^3} \frac{s^2}{tu} + \frac{1}{4N_C} \left(\frac{1}{2} + \frac{t^2 + u^2}{tu} - \frac{t^2 + u^2}{s^2} \right) - \frac{N_C}{4} \frac{t^2 + u^2}{s^2} \right) \\
& + l(s) \left(\left(\frac{5C_F}{4} - \frac{1}{2N_C} - \frac{1}{N_C^3} \right) - \left(N_C + \frac{1}{N_C^3} \right) \frac{t^2 + u^2}{2tu} - \frac{C_F}{2} \frac{t^2 + u^2}{s^2} \right) \\
& + \pi^2 \left(\frac{1}{8N_C} + \frac{1}{N_C^3} \left(\frac{3(t^2 + u^2)}{8tu} + \frac{1}{2} \right) + N_C \left(\frac{t^2 + u^2}{8tu} - \frac{t^2 + u^2}{2s^2} \right) \right) \\
& + \left(N_C + \frac{1}{N_C} \right) \left(\frac{1}{8} - \frac{t^2 + u^2}{4s^2} \right) \\
& + l^2(t) \left(N_C \left(\frac{s}{4t} - \frac{u}{s} - \frac{1}{4} \right) + \frac{1}{N_C} \left(\frac{t}{2u} - \frac{u}{4s} \right) + \frac{1}{N_C^3} \left(\frac{u}{4t} - \frac{s}{2u} \right) \right) \\
& + l(t) \left(N_C \left(\frac{t^2 + u^2}{s^2} + \frac{3t}{4s} - \frac{5u}{4t} - \frac{1}{4} \right) - \frac{1}{N_C} \left(\frac{u}{4s} + \frac{2s}{u} + \frac{s}{2t} \right) - \frac{1}{N_C^3} \left(\frac{3s}{4t} + \frac{1}{4} \right) \right) \\
& \left. + l(s)l(t) \left(N_C \left(\frac{t^2 + u^2}{s^2} - \frac{u}{2t} \right) + \frac{1}{N_C} \left(\frac{u}{2s} - \frac{t}{u} \right) + \frac{1}{N_C^3} \left(\frac{s}{u} - \frac{u}{2t} \right) \right) \right]
\end{aligned} \tag{4.13}$$

Finally, the process $gg \rightarrow gg$ gives

$$\begin{aligned}
V_{gg \rightarrow gg}(s, t, u) = & \left[N_C \left(-\frac{4}{\varepsilon^2} - \frac{22}{3\varepsilon} - \frac{67}{9} + \frac{11}{3} l(-\mu^2) + \frac{\pi^2}{3} \right) \right. \\
& + \frac{N_f}{2} \left(\frac{8}{3\varepsilon} + \frac{20}{9} - \frac{4}{3} l(-\mu^2) \right) \left. \right] T_{gg \rightarrow gg}(s, t, u) \\
& + \frac{32N_C^4 C_F}{\varepsilon} l(s) \left(3 - \frac{2tu}{s^2} + \frac{t^4 + u^4}{t^2 u^2} \right)
\end{aligned} \tag{4.14}$$

$$\begin{aligned}
& + \frac{32N_C^4 C_F}{\varepsilon} l(t) \left(3 - \frac{2us}{t^2} + \frac{u^4 + s^4}{u^2 s^2} \right) \\
& + \frac{32N_C^4 C_F}{\varepsilon} l(u) \left(3 - \frac{2st}{u^2} + \frac{s^4 + t^4}{s^2 t^2} \right) \\
& + 8N_C^3 C_F (f^d(s, t, u) + f^d(t, u, s) + f^d(u, s, t)),
\end{aligned}$$

where, once more, not all IR singularities are proportional to the complete Born matrix element and the finite terms are given by the function

$$\begin{aligned}
f^d(s, t, u) = & N_C \left[\left(\frac{2(t^2 + u^2)}{tu} \right) l^2(s) + \left(\frac{4s(t^3 + u^3)}{t^2 u^2} - 6 \right) l(t)l(u) \right. \\
& + \left. \left(\frac{4tu}{3s^2} - \frac{14}{3} \frac{t^2 + u^2}{tu} - 14 - 8 \left(\frac{t^2}{u^2} + \frac{u^2}{t^2} \right) \right) l(s) - 1 - \pi^2 \right] \\
& + \frac{N_f}{2} \left[\left(\frac{10}{3} \frac{t^2 + u^2}{tu} + \frac{16}{3} \frac{tu}{s^2} - 2 \right) l(s) - \frac{s^2 + tu}{tu} l^2(s) \right. \\
& \left. - 2 \frac{t^2 + u^2}{tu} l(t)l(u) + 2 - \pi^2 \right].
\end{aligned} \tag{4.15}$$

All UV singularities have already been absorbed into the Lagrangian, and terms of $\mathcal{O}(\varepsilon)$ and higher have been neglected.

As mentioned previously, the crossing of Mandelstam variables according to table 3 may change the signs of the arguments in the logarithms. This is accounted for in the definition of

$$l(x) = \ln \left| \frac{x}{Q^2} \right|, \tag{4.16}$$

where x may be any of the variables s , t , or u and is normalized to $Q^2 = \max(s, t, u)$. Due to the $i\eta$ -prescription in the propagators, terms bilinear in the logarithms may give an extra π^2 :

$$l^2(x) = \ln^2 \left(\frac{x}{Q^2} \right) - \pi^2, \quad \text{if } x > 0, \tag{4.17}$$

$$l^2(x) = \ln^2 \left(-\frac{x}{Q^2} \right), \quad \text{if } x < 0. \tag{4.18}$$

4.1.3 Virtual Corrections for Direct $\gamma\gamma$ Scattering

The virtual diagrams contributing to direct $\gamma\gamma$ scattering are shown in figure 14. As has already been seen in the Born case, direct $\gamma\gamma \rightarrow q\bar{q}$ scattering is intimately related to $\gamma g \rightarrow q\bar{q}$ scattering. Again, we have to replace the strong coupling constant by its electromagnetic counterpart resulting in

$$|\mathcal{M}|_{\gamma\gamma \rightarrow 12}^2(s, t, u) = e^4 e_q^4 \mu^{4\varepsilon} \frac{\alpha_s}{2\pi} \left(\frac{4\pi\mu^2}{s} \right)^\varepsilon \frac{\Gamma(1-\varepsilon)}{\Gamma(1-2\varepsilon)} V_{\gamma\gamma \rightarrow 12}(s, t, u). \tag{4.19}$$

The expression $V_{\gamma\gamma \rightarrow q\bar{q}}(s, t, u)$ is given by

$$\begin{aligned}
V_{\gamma\gamma \rightarrow q\bar{q}}(s, t, u) = & C_F \left(-\frac{2}{\varepsilon^2} - \frac{3}{\varepsilon} + \frac{2\pi^2}{3} - 7 + \ln^2 \frac{-t}{s} + \ln^2 \frac{-u}{s} \right) T_{\gamma\gamma \rightarrow q\bar{q}}(s, t, u) \\
& + 8N_C C_F \left(2 \ln \frac{-t}{s} + 2 \ln \frac{-u}{s} + 3 \frac{u}{t} \ln \frac{-t}{s} + 3 \frac{t}{u} \ln \frac{-u}{s} + \left(2 + \frac{u}{t} \right) \ln^2 \frac{-u}{s} \right. \\
& \left. + \left(2 + \frac{t}{u} \right) \ln^2 \frac{-t}{s} \right).
\end{aligned} \tag{4.20}$$

Note that due to the abelian structure of QED, the color class N_C , which is present in eq. (4.8) and arises there from the triple-gluon vertex, does not appear here.

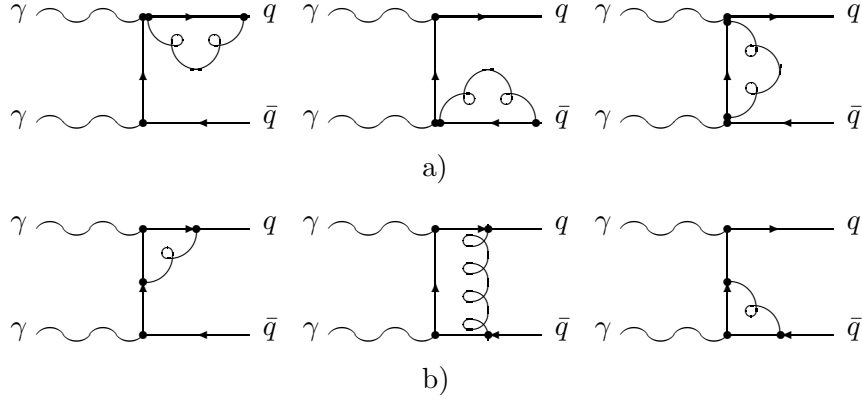


Figure 14: *Virtual diagrams for direct $\gamma\gamma$ scattering.*

4.2 Real Corrections

For the calculation of the hard scattering cross section in next-to-leading order, we must include all diagrams with an additional parton in the final state. The four-vectors of these subprocesses will be labeled by $p_a p_b \rightarrow p_1 p_2 p_3$, where p_a is the momentum of the incoming photon or parton in the photon and p_b is the momentum of the incoming parton in the proton. The invariants will be denoted by $s_{ij} = (p_i + p_j)^2$ and the previously defined Mandelstam variables s , t , and u . For massless partons, the $2 \rightarrow 3$ contributions can contain singularities at $s_{ij} = 0$. They can be extracted with the dimensional regularization method and canceled against those associated with the one-loop contributions.

In order to achieve this, we go through the following steps. First, we calculate the phase space for $2 \rightarrow 3$ scattering in d dimensions and factorize it into a regular part corresponding to $2 \rightarrow 2$ scattering and a singular part corresponding to the unresolved two-parton subsystem. Next, the matrix elements for the $2 \rightarrow 3$ subprocesses are calculated in d dimensions as well. They are squared and averaged/summed over initial/final state spins and colors and can be used for incoming quarks, antiquarks, and gluons with the help of crossing.

One can distinguish three classes of singularities in photoproduction ($Q^2 \simeq 0$) depending on which propagators in the squared matrix elements vanish. Examples for these three classes are shown in figure 15. The X marks the propagator leading to the divergence. In the first graph, it is the invariant

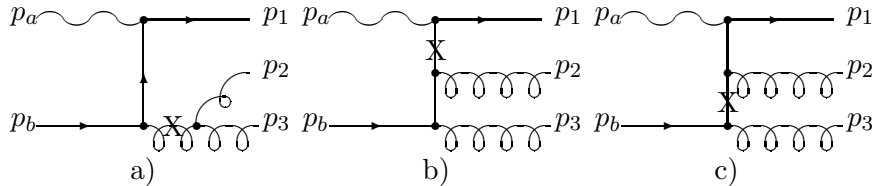


Figure 15: *Three-body diagrams with a) final state, b) photon initial state and c) proton initial state singularities.*

s_{23} given by momenta of the final state, which causes the singularity. Therefore, this divergence will be called final state singularity. The second graph becomes singular for $-t_{a1} = s_{a1} = (p_a + p_1)^2 = 0$, when the photon and the final quark momentum are parallel. This is the class of photon initial state singularities. In the third graph, the singularity occurs at $-t_{b3} = s_{b3} = (p_b + p_3)^2$, where p_b is the initial parton momentum in the proton. This stands for proton initial state singularity. Since resolved

photons behave like hadrons, they produce similar initial state divergencies. The first class is familiar from calculations for jet production in e^+e^- annihilation [63], the third class from jet production in deep inelastic ep scattering ($Q^2 \neq 0$) [51]. The second class occurs only for direct photoproduction [53].

When squaring the sum of all relevant $2 \rightarrow 3$ matrix elements, we encounter terms, where more than one of the invariants become singular, e.g. when one of the gluon momenta $p_3 \rightarrow 0$ so that $s_{23} = 0$ and $-t_{b3} = s_{b3} = 0$. These infrared singularities are disentangled by a partial fractioning decomposition, so that every term has only one vanishing denominator. This also allows the separation of the different classes of singularities in figure 15.

It turns out that the results for direct photoproduction are always proportional to the LO cross sections involved in the hard scatter

$$F, I, J_{\gamma b \rightarrow 123} = KT_{\gamma b \rightarrow 12}, \quad (4.21)$$

where F , I , and J denote final state, photon initial state and proton initial state contributions. For resolved photoproduction, this is no more true in general but only for the quark-quark scattering subprocesses with a less complicated color structure than those involving real gluons. For gluonic processes, only parts of the leading order cross sections can be factorized

$$F, I, J_{ab \rightarrow 123} = \sum_i K^{(i)} T_{ab \rightarrow 12}^{(i)}, \quad (4.22)$$

where

$$T_{ab \rightarrow 12} = \sum_i T_{ab \rightarrow 12}^{(i)} \quad (4.23)$$

is again the full Born matrix element.

As the last step, the decomposed matrix elements have to be integrated up to $s_{ij} \leq ys$. y characterizes the region, where the two partons i and j cannot be resolved. Then, the singular kernels K and $K^{(i)}$ produce terms $\propto 1/\varepsilon^2$ and $1/\varepsilon$, which will cancel against those in the virtual diagrams or be absorbed into structure functions, and finite corrections proportional to $\ln^2 y$, $\ln y$, and y^0 . For small values of y , terms of $\mathcal{O}(y)$ can be neglected. In the following, we shall give the results for the different classes of singularities separately.

4.2.1 Phase Space for Three-Particle Final States

For the real corrections, we have to consider all subprocesses, which have an additional third parton in the final state attached to the $2 \rightarrow 2$ scattering process. We therefore calculate the phase space for $2 \rightarrow 3$ scattering in this section and choose as the coordinate system the center-of-mass system of partons 1 and 3 as shown in figure 16. The angle between p_a and p_1 is called θ , the azimuthal angle between the planes defined by p_a and p_1 and p_a and p_2 is called ϕ , and the angle χ^* between p_a and p_2 is defined in the overall center-of-mass system of the incoming partons a and b denoted by an asterisk (*). As we have to accommodate a third final particle in the scattering process, the Mandelstam variables in this section

$$s = (p_a + p_b)^2, \quad (4.24)$$

$$t = (p_a - p_1 - p_3)^2 - 2p_1 p_3, \quad (4.25)$$

$$u = (p_a - p_2)^2 \quad (4.26)$$

differ slightly from the previously used ones, but still satisfy the relation $s + t + u = 0$ for massless partons. In the limit of soft ($p_3 = 0$) or collinear ($p_3 \parallel p_1$) particle emission, they can however be written in a form similar to $2 \rightarrow 2$ scattering as $t = (p_a - \bar{p}_1)^2$ and $u = (p_a - p_2)^2$. Here $\bar{p}_1 = p_1 + p_3$ represents the four-momentum of the recombined jet, and p_2 is the four-momentum of the second jet.

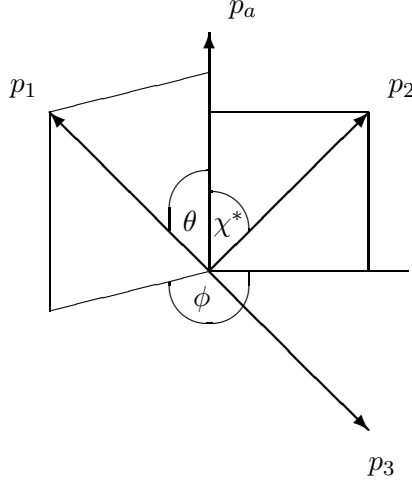


Figure 16: *Center-of-mass system of partons 1 and 3 defining the kinematic variables for the scattering of two initial into three final partons. χ^* is defined in the overall center-of-mass system of partons a and b.*

We start again from the general expression [48]

$$d\text{PS}^{(3)} = \int (2\pi)^d \prod_{i=1}^3 \frac{d^d p_i \delta(p_i^2)}{(2\pi)^{d-1}} \delta^d \left(p_a + p_b - \sum_{j=1}^3 p_j \right) \quad (4.27)$$

and describe the final state singularity with the new variable

$$z' = \frac{p_1 p_3}{p_a p_b}. \quad (4.28)$$

We can then insert two additional δ -functions with respect to t and z'

$$\frac{d\text{PS}^{(3)}}{dt dz'} = \int (2\pi)^d \prod_{i=1}^3 \frac{d^d p_i \delta(p_i^2)}{(2\pi)^{d-1}} \delta^d \left(p_a + p_b - \sum_{j=1}^3 p_j \right) \delta(t + s + (p_a - p_2)^2) \delta \left(z' - \frac{2p_1 p_3}{s} \right), \quad (4.29)$$

before we integrate over the $\delta(p_i^2)$ and the space-like components of the d -dimensional δ -function to eliminate p_3 . The resulting expression is

$$\frac{d\text{PS}^{(3)}}{dt dz'} = \int \frac{d^{d-1} p_1 d^{d-1} p_2}{(2\pi)^{2d-3} 2E_1 2E_2 2E_3} \delta \left(E_a + E_b - \sum_{j=1}^3 E_j \right) \delta(t + s + (p_a - p_2)^2) \delta \left(z' - \frac{2p_1 p_3}{s} \right). \quad (4.30)$$

We now decompose p_1 into its energy E_1 and angular components θ and ϕ in the center-of-mass system of partons 1 and 3, and p_2 into its components E_2^* , χ^* , and ϕ_2^* in the overall center-of-mass system with the result

$$\begin{aligned} \frac{d\text{PS}^{(3)}}{dt dz'} &= \int \frac{1}{(2\pi)^{2d-3} 8E_3} \frac{2\pi^{\frac{d-3}{2}}}{\Gamma\left(\frac{d-3}{2}\right)} E_1^{d-3} dE_1 \sin^{d-3} \theta d\theta \sin^{d-4} \phi d\phi \frac{\pi^{\frac{d-4}{2}}}{\Gamma\left(\frac{d-2}{2}\right)} E_2^{*d-3} dE_2^* \quad (4.31) \\ &\sin^{d-3} \chi^* d\chi^* d\phi_2^* \delta \left(E_a + E_b - \sum_{j=1}^3 E_j \right) \delta(t + s - 2E_a^* E_2^* (1 - \cos \chi^*)) \delta \left(z' - \frac{4E_1^2}{s} \right). \end{aligned}$$

Integrating over the remaining δ -functions and the trivial azimuthal angle ϕ_2^* up to 2π , we arrive at

$$\frac{d\text{PS}^{(3)}}{dt dz'} = \int \frac{(16\pi^2)^\varepsilon}{128\pi^3\Gamma(2-2\varepsilon)} z'^{-\varepsilon} u^{-\varepsilon} (t + sz')^{-\varepsilon} (b(1-b))^{-\varepsilon} \frac{db}{N_b} \sin^{-2\varepsilon} \phi \frac{d\phi}{N_\phi}, \quad (4.32)$$

where we have substituted the polar angle θ by

$$b = \frac{1}{2}(1 - \cos \theta), \quad (4.33)$$

and N_b and N_ϕ are the normalization factors

$$N_b = \int_0^1 db (b(1-b))^{-\varepsilon} = \frac{\Gamma^2(1-\varepsilon)}{\Gamma(2-2\varepsilon)}, \quad (4.34)$$

$$N_\phi = \int_0^\pi \sin^{-2\varepsilon} \phi d\phi = \frac{\pi 4^\varepsilon \Gamma(1-2\varepsilon)}{\Gamma^2(1-\varepsilon)}. \quad (4.35)$$

Finally, we can factorize this three particle phase space into

$$d\text{PS}^{(3)} = d\text{PS}^{(2)} d\text{PS}^{(r)}, \quad (4.36)$$

where

$$\frac{d\text{PS}^{(2)}}{dt} = \frac{1}{\Gamma(1-\varepsilon)} \left(\frac{4\pi s}{tu} \right)^\varepsilon \frac{1}{8\pi s} \quad (4.37)$$

is the phase space for the two observed jets with momenta \bar{p}_1 and p_2 already calculated in section 3.1 and

$$d\text{PS}^{(r)} = \left(\frac{4\pi}{s} \right)^\varepsilon \frac{\Gamma(1-\varepsilon)}{\Gamma(1-2\varepsilon)} \frac{s}{16\pi^2} \frac{1}{1-2\varepsilon} d\mu_F \quad (4.38)$$

is the phase space of the unresolved subsystem of partons 1 and 3. The integration measure is

$$d\mu_F = dz' z'^{-\varepsilon} \left(1 + \frac{z's}{t} \right)^{-\varepsilon} \frac{db}{N_b} b^{-\varepsilon} (1-b)^{-\varepsilon} \frac{d\phi}{N_\phi} \sin^{-2\varepsilon} \phi. \quad (4.39)$$

The full range of integration in $d\text{PS}^{(r)}$ is given by $z' \in [0, -t/s]$, $b \in [0, 1]$, and $\phi \in [0, \pi]$. The singular region is defined by the requirement that partons p_1 and p_3 are recombined, i.e. $p_3 = 0$ or p_3 parallel to p_1 , so that $s_{13} = (p_1 + p_3)^2 = 0$. We integrate over this region up to $s_{13} \leq ys$, which restricts the range of z' to $0 \leq z' \leq \min\{-t/s, y\} \equiv y_F$.

4.2.2 Final State Corrections for Direct Photons

The real corrections to the QCD Compton Scattering process of figure 7 arise from two different mechanisms. Either an additional gluon can be radiated from the quark or the gluon leading to the left diagram in figure 17, or a quark-antiquark pair is emitted by a gluon as shown in the right diagram

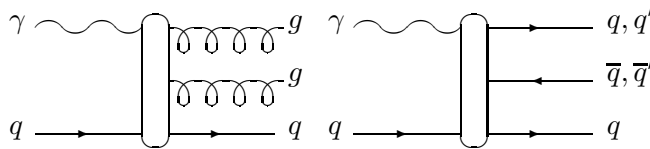


Figure 17: $2 \rightarrow 3$ Feynman diagrams for direct photoproduction.

of figure 17. Both cases lead to an extra factor of α_s , when the matrix elements are squared, so that

Process	Matrix Element $ \mathcal{M} ^2$
$\gamma q \rightarrow qgg$	$[\mathcal{M} _{\gamma q \rightarrow qgg}^2(s, t, u)]/[4N_C]/2!$
$\gamma \bar{q} \rightarrow \bar{q}gg$	$[\mathcal{M} _{\gamma \bar{q} \rightarrow \bar{q}gg}^2(s, t, u)]/[4N_C]/2!$
$\gamma q \rightarrow qq\bar{q}$	$[\mathcal{M} _{\gamma q \rightarrow qq\bar{q}}^2(s, t, u)]/[4N_C]$
$\gamma g \rightarrow gq\bar{q}$	$[\mathcal{M} _{\gamma g \rightarrow gq\bar{q}}^2(s, t, u)]/[8(1 - \varepsilon)N_C C_F]$

Table 4: *Summary of 2 \rightarrow 3 squared matrix elements for direct photoproduction.*

all real corrections discussed in the following are of $\mathcal{O}(\alpha_s^2)$. The outgoing quark-antiquark pair can be of the same or different flavor than the incoming quark. The diagrams for incoming anti-quarks or gluons can be obtained from figure 17 by crossing a final quark or gluon line with the incoming quark line. The corresponding matrix elements can then be obtained from table 4.

All possible topologies and orders of outgoing particles have to be considered for the full matrix elements of the processes, although they are not shown here explicitly. The complete result in d dimensions can be found in [49] in a very compact notation not suitable to isolate the singularities. We therefore re-calculate the matrix elements with the help of REDUCE [64], check their sums with the results in [49], and keep only those that have singularities in a final state invariant $s_{ij} = (p_i + p_j)^2$. This can either be a soft or collinear gluon leading to a quadratic pole (left diagram of figure 17) or a collinear quark-antiquark pair leading only to a single pole (right diagram of figure 17). With the help of the singular invariant

$$z' = \frac{p_1 p_3}{p_a p_b}, \quad (4.40)$$

we can approximate the nine other invariants describing the 2 \rightarrow 3 scattering process and express them through the 2 \rightarrow 2 Mandelstam variables s , t , and u and the variable $b = 1/2(1 - \cos \theta)$ as defined in section 4.2.1:

$$p_a p_b = \frac{s}{2} \quad (4.41)$$

$$p_a p_1 = \frac{s-t}{2} b \quad (4.42)$$

$$p_a p_2 = \frac{s-u}{2} \quad (4.43)$$

$$p_a p_3 = \frac{s-t}{2} (1-b) \quad (4.44)$$

$$p_b p_1 = \frac{s-u}{2} b \quad (4.45)$$

$$p_b p_2 = \frac{s-t}{2} \quad (4.46)$$

$$p_b p_3 = \frac{s-u}{2} (1-b) \quad (4.47)$$

$$p_1 p_2 = \frac{s}{2} b \quad (4.48)$$

$$p_1 p_3 = \frac{s}{2} z' \quad (4.49)$$

$$p_2 p_3 = \frac{s}{2} (1-b) \quad (4.50)$$

For the subprocess $\gamma q \rightarrow qgg$, where a gluon becomes soft or collinear to the other outgoing gluon or the quark, the approximated matrix element takes the form

$$|\mathcal{M}|_{\gamma q \rightarrow qgg}^2(s, t, u) = e^2 e_q^2 g^4 \mu^{6\varepsilon} \frac{1}{s z'} \left[4C_F \left((1-b)(1-\varepsilon) - 2 + \frac{-2t/s}{z' - t/s(1-b)} \right) \right] \quad (4.51)$$

$$-4N_C \left(\frac{-t/s}{z' - t/s(1-b)} - \frac{-u/s}{z' - u/s(1-b)} - \frac{2}{z' + (1-b)} + 2 - b + b^2 \right) \Big] T_{\gamma q \rightarrow gq}(s, t, u)$$

with an identical result for incoming anti-quarks. The four-fermion diagram only produces a divergence from the collinear quark-antiquark pair, which can have N_f flavors

$$|\mathcal{M}|_{\gamma q \rightarrow qq\bar{q}}^2(s, t, u) = e^2 e_q^2 g^4 \mu^{6\epsilon} \frac{1}{sz'} N_f [1 - 2b(1-b)(1+\epsilon)] T_{\gamma q \rightarrow gq}(s, t, u), \quad (4.52)$$

and the gluon-initiated process $\gamma g \rightarrow gq\bar{q}$ can have a gluon that becomes soft or collinear to the quark or anti-quark

$$|\mathcal{M}|_{\gamma g \rightarrow gq\bar{q}}^2(s, t, u) = e^2 e_q^2 g^4 \mu^{6\epsilon} \frac{1}{sz'} \left[4C_F \left((1-b)(1-\epsilon) - 2 + \frac{2}{z' + (1-b)} \right) - 2N_C \left(\frac{2}{z' + (1-b)} - \frac{-t/s}{z' - t/s(1-b)} - \frac{-u/s}{z' - u/s(1-b)} \right) \right] T_{\gamma g \rightarrow q\bar{q}}(s, t, u). \quad (4.53)$$

Finally, we integrate the above matrix elements over the singular phase space $\text{dPS}^{(r)}$ given in section 4.2.1. The necessary integrals are given in appendix A. The integration over ϕ in $\text{dPS}^{(r)}$ is trivial, as the matrix elements do not depend on this variable. This is true for all direct and resolved photoproduction processes and for all final and initial state contributions, contrary to the case of deep-inelastic scattering. The result is

$$\int \text{dPS}^{(r)} |\mathcal{M}|_{\gamma b \rightarrow 123}^2(s, t, u) = e^2 e_q^2 g^2 \mu^{4\epsilon} \frac{\alpha_s}{2\pi} \left(\frac{4\pi\mu^2}{s} \right)^\epsilon \frac{\Gamma(1-\epsilon)}{\Gamma(1-2\epsilon)} F_{\gamma b \rightarrow 123}(s, t, u). \quad (4.54)$$

The functions $F_{\gamma b \rightarrow 123}$ are given by

$$F_{\gamma q \rightarrow qgg}(s, t, u) = \left[2C_F \left(\frac{1}{\epsilon^2} - \frac{1}{2\epsilon} \left(2 \ln \frac{-t}{s} - 3 \right) - \frac{\pi^2}{3} + \frac{7}{2} - \frac{1}{2} \ln^2 \frac{-t}{s} + 2 \ln y_F \ln \frac{-t}{s} - 2 \text{Li}_2 \left(\frac{y_F s}{t} \right) - \ln^2 y_F - \frac{3}{2} \ln y_F \right) - N_C \left(-\frac{2}{\epsilon^2} - \frac{1}{\epsilon} \left(\frac{11}{3} + \ln \frac{-t}{s} - \ln \frac{-u}{s} \right) - \frac{1}{2} \ln^2 \frac{-t}{s} + 2 \ln y_F \ln \frac{-t}{s} - 2 \text{Li}_2 \left(\frac{y_F s}{t} \right) - \frac{67}{9} + \frac{11}{3} \ln y_F + \ln^2 y_F + \ln^2 \frac{y_F s}{-u} - \frac{1}{2} \ln^2 \frac{-u}{s} + \frac{2\pi^2}{3} + 2 \text{Li}_2 \left(\frac{y_F s}{u} \right) \right) \right] T_{\gamma q \rightarrow gq}(s, t, u), \quad (4.55)$$

$$F_{\gamma q \rightarrow qq\bar{q}}(s, t, u) = N_f \left[-\frac{1}{3\epsilon} + \frac{1}{3} \ln y_F - \frac{5}{9} \right] T_{\gamma q \rightarrow gq}(s, t, u), \quad (4.56)$$

$$F_{\gamma g \rightarrow gq\bar{q}}(s, t, u) = \left[C_F \left(\frac{2}{\epsilon^2} + \frac{3}{\epsilon} - \frac{2\pi^2}{3} + 7 - 2 \ln^2 y_F - 3 \ln y_F \right) - \frac{N_C}{2} \left(\frac{1}{\epsilon} \left(\ln \frac{-t}{s} + \ln \frac{-u}{s} \right) + \ln^2 \frac{y_F s}{-t} + \ln^2 \frac{y_F s}{-u} - 2 \ln^2 y_F - \frac{1}{2} \ln^2 \frac{-t}{s} - \frac{1}{2} \ln^2 \frac{-u}{s} + 2 \text{Li}_2 \left(\frac{y_F s}{t} \right) + 2 \text{Li}_2 \left(\frac{y_F s}{u} \right) \right) \right] T_{\gamma g \rightarrow q\bar{q}}(s, t, u). \quad (4.57)$$

Terms of $\mathcal{O}(\epsilon)$ and of $\mathcal{O}(y_F)$ have been neglected. The Spence-functions or dilogarithms Li_2 resulting from the calculation are written down explicitly even though they are also of $\mathcal{O}(y_F)$. The complete approximated $2 \rightarrow 3$ matrix elements are proportional to the corresponding Born matrix elements $T_{\gamma b \rightarrow 12}$. This is also true for the exact matrix elements in four dimensions as calculated by Berends et al. [65], but not for the exact d -dimensional matrix elements [49].

4.2.3 Final State Corrections for Resolved Photons

For the four different generic Born diagrams of resolved photoproduction in figure 9, the real corrections all arise from an additional gluon in the final state as shown in figure 18. They are of $\mathcal{O}(\alpha_s^3)$. All

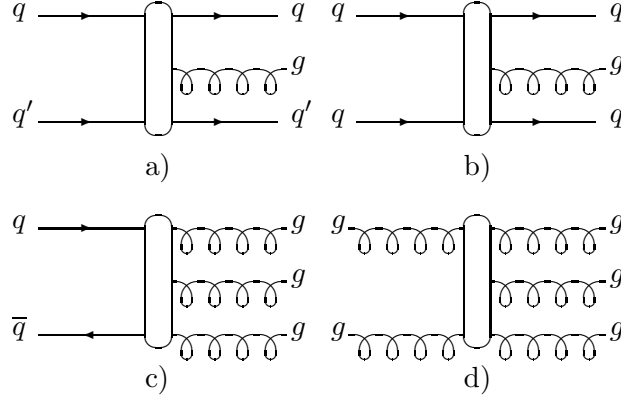


Figure 18: $2 \rightarrow 3$ Feynman diagrams for resolved photoproduction.

other diagrams can be obtained from figure 18 by crossing one or two outgoing gluon lines into the initial state, which leads to the gluon initiated processes with quarks in the final state, or by crossing an incoming and an outgoing quark line, which leads to the processes with incoming anti-quarks. Process c) is symmetric under the interchange of the three gluons and under the interchange of the quark and anti-quark. Process d) is completely symmetric under the interchange of any of the five gluons. The complete list of matrix elements is written down in table 5.

Process	Matrix Element $ \mathcal{M} ^2$
$qq' \rightarrow qq'g$	$[\mathcal{M} _{qq' \rightarrow qq'g}^2(s, t, u)]/[4N_C^2]$
$q\bar{q}' \rightarrow q\bar{q}'g$	$[\mathcal{M} _{q\bar{q}' \rightarrow q\bar{q}'g}^2(u, t, s)]/[4N_C^2]$
$q\bar{q} \rightarrow \bar{q}'q'g$	$[\mathcal{M} _{q\bar{q}' \rightarrow qq'g}^2(t, s, u) + \mathcal{M} _{q\bar{q} \rightarrow q\bar{q}g}^2(s, t, u)]/[4N_C^2]$
$qg \rightarrow qq'\bar{q}'$	$-[\mathcal{M} _{q\bar{q} \rightarrow q\bar{q}g}^2(t, s, u)]/[8(1 - \varepsilon)N_C^2C_F]$
$qq \rightarrow qqg$	$[\mathcal{M} _{qq' \rightarrow qq'g}^2(s, t, u) + \mathcal{M} _{qq' \rightarrow qq'g}^2(s, u, t) + \mathcal{M} _{qq \rightarrow qqg}^2(s, t, u)]/[4N_C^2]/2!$
$q\bar{q} \rightarrow q\bar{q}g$	$[\mathcal{M} _{qq' \rightarrow qq'g}^2(u, t, s) + \mathcal{M} _{qq' \rightarrow qq'g}^2(u, s, t) + \mathcal{M} _{qq \rightarrow qqg}^2(u, t, s) + \mathcal{M} _{q\bar{q} \rightarrow q\bar{q}g}^2(s, t, u)]/[4N_C^2]$
$qg \rightarrow qq\bar{q}$	$-[2 \mathcal{M} _{q\bar{q} \rightarrow q\bar{q}g}^2(t, s, u)]/[8(1 - \varepsilon)N_C^2C_F]/2!$
$q\bar{q} \rightarrow ggg$	$[\mathcal{M} _{q\bar{q} \rightarrow ggg}^2(s, t, u)]/[4N_C^2]/3!$
$qg \rightarrow qgg$	$[- \mathcal{M} _{q\bar{q} \rightarrow qqg}^2(t, s, u)]/3 + \mathcal{M} _{qq \rightarrow qqg}^2(s, t, u)]/[8(1 - \varepsilon)N_C^2C_F]/2!$
$\bar{q}g \rightarrow \bar{q}gg$	$[- \mathcal{M} _{q\bar{q} \rightarrow qqg}^2(t, u, s)]/3 + \mathcal{M} _{qq \rightarrow qqg}^2(u, t, s)]/[8(1 - \varepsilon)N_C^2C_F]/2!$
$gg \rightarrow q\bar{q}g$	$[- \mathcal{M} _{qq \rightarrow qqg}^2(t, s, u) + \mathcal{M} _{gg \rightarrow q\bar{q}g}^2(s, t, u)]/[16(1 - \varepsilon)^2N_C^2C_F^2]$
$gg \rightarrow ggg$	$[\mathcal{M} _{qq \rightarrow qqg}^2(s, t, u)]/[16(1 - \varepsilon)^2N_C^2C_F^2]/3!$

Table 5: Summary of $2 \rightarrow 3$ squared matrix elements for resolved photoproduction.

In four dimensions, these matrix elements were first calculated by Gottschalk and Sivers [66] and by Kunszt and Pietarinen [67]. The result in d dimensions was given in a compact form by Ellis and Sexton [56]. We calculate the matrix elements again with the help of REDUCE [64], check with the result in [56], and keep only terms singular in the final state invariant z' . The result can be expressed through this variable z' , b , and the Mandelstam variables s , t , and u . For quark-quark scattering of

different flavors in diagram 18a), we can have a soft or collinear gluon in the final state

$$|\mathcal{M}|_{qq' \rightarrow qq'g}^2(s, t, u) = g^6 \mu^{6\epsilon} \frac{4}{sz'} \left[(2C_F - N_C) \left(\frac{-2}{z' + (1-b)} + \frac{-t/s}{z' - t/s(1-b)} + \frac{-u/s}{z' - u/s(1-b)} \right) + C_F \left((1-b)(1-\epsilon) - 2 + \frac{-2u/s}{z' - u/s(1-b)} \right) \right] T_{qq' \rightarrow qq'}(s, t, u). \quad (4.58)$$

For equal flavors, there is additionally the interference contribution

$$|\mathcal{M}|_{qq \rightarrow qqg}^2(s, t, u) = g^6 \mu^{6\epsilon} \frac{4}{sz'} \left[(2C_F - N_C) \left(\frac{-2}{z' + (1-b)} + \frac{-t/s}{z' - t/s(1-b)} + \frac{-u/s}{z' - u/s(1-b)} \right) + C_F \left((1-b)(1-\epsilon) - 2 + \frac{2}{z' + (1-b)} \right) \right] T_{qq \rightarrow qq}(s, t, u) \quad (4.59)$$

as the final quark lines in diagram 18b) are undistinguishable and can be interchanged. The crossed diagram of quark-antiquark annihilation has an additional singularity, if the final quark-antiquark pair with N_f possible flavors becomes collinear

$$|\mathcal{M}|_{q\bar{q} \rightarrow q\bar{q}g}^2(s, t, u) = g^6 \mu^{6\epsilon} \frac{1}{sz'} N_f [1 - 2b(1-b)(1+\epsilon)] T_{q\bar{q} \rightarrow gg}(s, t, u). \quad (4.60)$$

The complete matrix elements given above are proportional to the corresponding Born matrix elements $T_{ab \rightarrow 12}$. Quarks and anti-quarks can, of course, also annihilate into three final gluons as shown in figure 18c), where any pair of two gluons can produce a soft or collinear singularity:

$$|\mathcal{M}|_{q\bar{q} \rightarrow ggg}^2(s, t, u) = g^6 \mu^{6\epsilon} \frac{12}{sz'} \left[-N_C(b^2 - b + 2) T_{q\bar{q} \rightarrow gg}(s, t, u) + 4N_C C_F \left(\frac{-u/s}{z' - u/s(1-b)} (1-\epsilon) \left(\frac{t^2 + u^2 - \epsilon s^2}{tu} \right) \left(2N_C C_F - 2N_C^2 \frac{tu}{s^2} - N_C^2 \frac{u^2}{s^2} \right) + \frac{1}{z' + (1-b)} (1-\epsilon) \left(\frac{t^2 + u^2 - \epsilon s^2}{tu} \right) \left(N_C^2 \frac{t^2 + u^2}{s^2} \right) + \frac{-t/s}{z' - t/s(1-b)} (1-\epsilon) \left(\frac{t^2 + u^2 - \epsilon s^2}{tu} \right) \left(2N_C C_F - 2N_C^2 \frac{tu}{s^2} - N_C^2 \frac{t^2}{s^2} \right) \right]. \quad (4.61)$$

Here, only parts of the Born matrix element $T_{q\bar{q} \rightarrow gg}$ can be factorized. The process $qg \rightarrow qgg$ can be obtained by crossing a final gluon with the incoming anti-quark or ($s \leftrightarrow t$). In this case, either of the outgoing gluons can also be radiated from the outgoing quark leading to

$$|\mathcal{M}|_{qg \rightarrow qgg}^2(s, t, u) = g^6 \mu^{6\epsilon} \frac{4}{sz'} \left[C_F ((1-b)(1-\epsilon) - 2) T_{qg \rightarrow qg}(s, t, u) - 4N_C C_F \left(\frac{-t/s}{z' - t/s(1-b)} (1-\epsilon) \left(\frac{s^2 + u^2 - \epsilon t^2}{su} \right) \left(\left(2N_C C_F - 2N_C^2 \frac{su}{t^2} \right) \left(-2 + 2\frac{C_F}{N_C} \right) + N_C^2 \frac{s^2 + u^2}{t^2} \right) + \frac{-u/s}{z' - u/s(1-b)} (1-\epsilon) \left(\frac{s^2 + u^2 - \epsilon t^2}{su} \right) \left(2N_C C_F - 2N_C^2 \frac{su}{t^2} - N_C^2 \frac{u^2}{t^2} \right) + \frac{1}{z' + (1-b)} (1-\epsilon) \left(\frac{s^2 + u^2 - \epsilon t^2}{su} \right) \left(2N_C C_F - 2N_C^2 \frac{su}{t^2} - N_C^2 \frac{s^2}{t^2} \right) \right], \quad (4.62)$$

where again only parts of the Born matrix element $T_{qg \rightarrow qg}$ can be factorized. If also the incoming quark is crossed into the final state, the resulting quark-antiquark pair in the final state with N_f flavors can produce the collinear singularity

$$|\mathcal{M}|_{gg \rightarrow q\bar{q}g}^2(s, t, u) = g^6 \mu^{6\epsilon} \frac{1}{sz'} N_f [1 - 2b(1-b)(1+\epsilon)] T_{gg \rightarrow gg}(s, t, u) \quad (4.63)$$

proportional to the full Born matrix element. Finally, the five-gluon process in figure 18d) can have three different pairs of soft or collinear gluons in the final state with the result

$$\begin{aligned} |\mathcal{M}|_{gg \rightarrow ggg}^2(s, t, u) &= g^6 \mu^{6\epsilon} \frac{12}{sz'} \left[-N_C(b^2 - b + 2) T_{gg \rightarrow gg}(s, t, u) \right. \\ &\quad + 16N_C^4 C_F \\ &\quad \left(\frac{-t/s}{z' - t/s(1-b)} (1-\epsilon)^2 \left(3 - \frac{2su}{t^2} + \frac{s^4 + u^4}{s^2 u^2} \right) \right. \\ &\quad + \frac{-u/s}{z' - u/s(1-b)} (1-\epsilon)^2 \left(3 - \frac{2st}{u^2} + \frac{s^4 + t^4}{s^2 t^2} \right) \\ &\quad \left. \left. + \frac{1}{z' + (1-b)} (1-\epsilon)^2 \left(3 - \frac{2tu}{s^2} + \frac{t^4 + u^4}{t^2 u^2} \right) \right) \right]. \quad (4.64) \end{aligned}$$

Only parts of the leading-order matrix element $T_{gg \rightarrow gg}$ can be factorized.

Next, the approximated matrix elements have to be integrated over the final state singularity z' in phase space up to the invariant mass cut y_F . Terms of order $\mathcal{O}(y_F)$ can be neglected if y_F is chosen sufficiently small. We use the phase space for the unobserved subsystem $\text{dPS}^{(r)}$ from section 4.2.1 and find

$$\int \text{dPS}^{(r)} |\mathcal{M}|_{ab \rightarrow 123}^2(s, t, u) = g^4 \mu^{4\epsilon} \frac{\alpha_s}{2\pi} \left(\frac{4\pi\mu^2}{Q^2} \right)^\epsilon \frac{\Gamma(1-\epsilon)}{\Gamma(1-2\epsilon)} F_{ab \rightarrow 123}(s, t, u) \quad (4.65)$$

similar to the direct case. The functions $F_{ab \rightarrow 123}$ are given by

$$\begin{aligned} F_{qq' \rightarrow qq'g}(s, t, u) &= \left[2(2C_F - N_C) \left(-\frac{1}{2\epsilon} (-2l(s) + l(t) + l(u)) - \frac{1}{2} \left(-2l^2 \left(\frac{s}{y_F} \right) \right. \right. \right. \\ &\quad \left. \left. + l^2 \left(\frac{t}{y_F} \right) + l^2 \left(\frac{u}{y_F} \right) \right) + \frac{1}{4} (-2l^2(s) + l^2(t) + l^2(u)) + 2\text{Li}_2 \left(-\left| \frac{y_F Q^2}{s} \right| \right) \right. \\ &\quad \left. - \text{Li}_2 \left(-\left| \frac{y_F Q^2}{t} \right| \right) - \text{Li}_2 \left(-\left| \frac{y_F Q^2}{u} \right| \right) \right) \\ &\quad + 2C_F \left(\frac{1}{\epsilon^2} + \frac{1}{2\epsilon} (3 - 2l(u)) + \frac{1}{2} l^2(u) + \frac{7}{2} - l^2 \left(\frac{u}{y_F} \right) - \frac{3}{2} \ln y_F \right. \\ &\quad \left. - \frac{\pi^2}{3} - 2\text{Li}_2 \left(-\left| \frac{y_F Q^2}{u} \right| \right) \right) \right] T_{qq' \rightarrow qq'g}(s, t, u), \quad (4.66) \end{aligned}$$

$$\begin{aligned} F_{qq \rightarrow qqg}(s, t, u) &= \left[2(2C_F - N_C) \left(-\frac{1}{2\epsilon} (-2l(s) + l(t) + l(u)) - \frac{1}{2} \left(-2l^2 \left(\frac{s}{y_F} \right) \right. \right. \right. \\ &\quad \left. \left. + l^2 \left(\frac{t}{y_F} \right) + l^2 \left(\frac{u}{y_F} \right) \right) + \frac{1}{4} (-2l^2(s) + l^2(t) + l^2(u)) + 2\text{Li}_2 \left(-\left| \frac{y_F Q^2}{s} \right| \right) \right. \\ &\quad \left. - \text{Li}_2 \left(-\left| \frac{y_F Q^2}{t} \right| \right) - \text{Li}_2 \left(-\left| \frac{y_F Q^2}{u} \right| \right) \right) \\ &\quad + 2C_F \left(\frac{1}{\epsilon^2} + \frac{1}{2\epsilon} (3 - 2l(s)) + \frac{1}{2} l^2(s) + \frac{7}{2} - l^2 \left(\frac{s}{y_F} \right) - \frac{3}{2} \ln y_F \right. \\ &\quad \left. - \frac{\pi^2}{3} - 2\text{Li}_2 \left(-\left| \frac{y_F Q^2}{s} \right| \right) \right) \right] T_{qq \rightarrow qqg}(s, t, u), \quad (4.67) \end{aligned}$$

$$F_{q\bar{q} \rightarrow q\bar{q}g}(s, t, u) = N_f \left[-\frac{1}{3\varepsilon} + \frac{1}{3} \ln y_F - \frac{5}{9} \right] T_{q\bar{q} \rightarrow gg}(s, t, u), \quad (4.68)$$

$$\begin{aligned} F_{q\bar{q} \rightarrow ggg}(s, t, u) = & \left[3N_C \left(\frac{2}{\varepsilon^2} + \frac{11}{3\varepsilon} - \frac{11}{3} \ln y_F + \frac{67}{9} - \frac{2\pi^2}{3} \right) \right] T_{q\bar{q} \rightarrow gg}(s, t, u) \\ & + 6N_C C_F \left[\left(-\frac{2}{\varepsilon} l(u) + 2l(u) - 2l^2 \left(\frac{u}{y_F} \right) + l^2(u) - 4\text{Li}_2 \left(-\left| \frac{y_F Q^2}{u} \right| \right) \right) \right. \\ & \left(N_C^2 \left(\frac{t}{u} - \frac{2t^2}{s^2} \right) - \frac{u}{t} - \frac{t}{u} \right) \\ & + \left(-\frac{2}{\varepsilon} l(s) + 2l(s) - 2l^2 \left(\frac{s}{y_F} \right) + l^2(s) - 4\text{Li}_2 \left(-\left| \frac{y_F Q^2}{s} \right| \right) \right) \\ & \left(N_C^2 \frac{(t^2 + u^2)^2}{uts^2} \right) \\ & + \left(-\frac{2}{\varepsilon} l(t) + 2l(t) - 2l^2 \left(\frac{t}{y_F} \right) + l^2(t) - 4\text{Li}_2 \left(-\left| \frac{y_F Q^2}{t} \right| \right) \right) \\ & \left(N_C^2 \left(\frac{u}{t} - \frac{2u^2}{s^2} \right) - \frac{u}{t} - \frac{t}{u} \right) \\ & + \left(2l(u) \left(N_C^2 \frac{t}{u} - \frac{s^2}{tu} \right) + 2l(s) N_C^2 \left(\frac{t}{u} + \frac{u}{t} \right) \right. \\ & \left. + 2l(t) \left(N_C^2 \frac{u}{t} - \frac{s^2}{tu} \right) \right) \Big], \quad (4.69) \end{aligned}$$

$$\begin{aligned} F_{qg \rightarrow qgg}(s, t, u) = & \left[C_F \left(\frac{1}{\varepsilon^2} + \frac{3}{2\varepsilon} - \frac{3}{2} \ln y_F + \frac{7}{2} - \frac{\pi^2}{3} \right) \right] T_{qg \rightarrow qg}(s, t, u) \\ & - N_C C_F \left[\left(-\frac{2}{\varepsilon} l(u) + 2l(u) - 2l^2 \left(\frac{u}{y_F} \right) + l^2(u) - 4\text{Li}_2 \left(-\left| \frac{y_F Q^2}{u} \right| \right) \right) \right. \\ & \left(N_C^2 \left(\frac{s}{u} - \frac{2s^2}{t^2} \right) - \frac{u}{s} - \frac{s}{u} \right) \\ & + \left(-\frac{2}{\varepsilon} l(s) + 2l(s) - 2l^2 \left(\frac{s}{y_F} \right) + l^2(s) - 4\text{Li}_2 \left(-\left| \frac{y_F Q^2}{s} \right| \right) \right) \\ & \left(N_C^2 \left(\frac{u}{s} - \frac{2u^2}{t^2} \right) - \frac{u}{s} - \frac{s}{u} \right) \\ & + \left(-\frac{2}{\varepsilon} l(t) + 2l(t) - 2l^2 \left(\frac{t}{y_F} \right) + l^2(t) - 4\text{Li}_2 \left(-\left| \frac{y_F Q^2}{t} \right| \right) \right) \\ & \left(2 \frac{s^2 + u^2}{t^2} + \frac{1}{N_C^2} \left(\frac{u}{s} + \frac{s}{u} \right) \right) \\ & + \left(2l(u) \left(N_C^2 \frac{s}{u} - \frac{t^2}{su} \right) + 2l(s) \left(N_C^2 \frac{u}{s} - \frac{t^2}{su} \right) \right. \\ & \left. + 2l(t) \left(2 + \frac{1}{N_C^2} \frac{t^2}{su} \right) \right) \Big], \quad (4.70) \end{aligned}$$

$$F_{gg \rightarrow q\bar{q}g}(s, t, u) = N_f \left[-\frac{1}{3\varepsilon} + \frac{1}{3} \ln y_F - \frac{5}{9} \right] T_{gg \rightarrow gg}(s, t, u), \quad (4.71)$$

$$\begin{aligned}
F_{gg \rightarrow ggg}(s, t, u) = & \left[3N_C \left(\frac{2}{\varepsilon^2} + \frac{11}{3\varepsilon} - \frac{11}{3} \ln y_F + \frac{67}{9} - \frac{2\pi^2}{3} \right) \right] T_{gg \rightarrow gg}(s, t, u) \\
& + 48N_C^4 C_F \left[\left(-\frac{1}{\varepsilon} l(t) + 2l(t) - l^2 \left(\frac{t}{y_F} \right) + \frac{1}{2} l^2(t) - 2\text{Li}_2 \left(- \left| \frac{y_F Q^2}{t} \right| \right) \right) \right. \\
& \left(3 - \frac{2us}{t^2} + \frac{u^4 + s^4}{u^2 s^2} \right) \\
& + \left(-\frac{1}{\varepsilon} l(u) + 2l(u) - l^2 \left(\frac{u}{y_F} \right) + \frac{1}{2} l^2(u) - 2\text{Li}_2 \left(- \left| \frac{y_F Q^2}{u} \right| \right) \right) \\
& \left(3 - \frac{2ts}{u^2} + \frac{t^4 + s^4}{t^2 s^2} \right) \\
& + \left(-\frac{1}{\varepsilon} l(s) + 2l(s) - l^2 \left(\frac{s}{y_F} \right) + \frac{1}{2} l^2(s) - 2\text{Li}_2 \left(- \left| \frac{y_F Q^2}{s} \right| \right) \right) \\
& \left. \left(3 - \frac{2tu}{s^2} + \frac{t^4 + u^4}{t^2 u^2} \right) \right]. \tag{4.72}
\end{aligned}$$

All terms of $\mathcal{O}(\varepsilon)$ have been omitted since they do not contribute in the physical limit $d \rightarrow 4$.

As in the virtual corrections, we account for sign-changing arguments in the logarithms before and after crossing with the definition of

$$l(x) = \ln \left| \frac{x}{Q^2} \right|, \tag{4.73}$$

where x is any of the Mandelstam variables s , t , and u and Q^2 is an arbitrary scale chosen to be $Q^2 = \max(s, t, u)$. However, there are no additional terms of π^2 in the real corrections so that

$$l^2(x) = \ln^2 \left| \frac{x}{Q^2} \right| \tag{4.74}$$

for $x > 0$ as well as for $x < 0$.

4.2.4 Phase Space for Three-Particle Final States Revisited

Having calculated all real corrections coming from final state singularities, where the singular variable was $s_{13} = (p_1 + p_3)^2$, we now turn to the singularities that arise in the photon and proton initial states in the variables $-t_{a3} = s_{a3} = (p_a + p_3)^2$ and $-t_{b3} = s_{b3} = (p_b + p_3)^2$. The singular variables are then defined as

$$z'' = \frac{p_a p_3}{p_a p_b} \text{ and } z''' = \frac{p_b p_3}{p_a p_b}, \tag{4.75}$$

respectively. It is convenient to calculate the three-body phase space in the same center-of-mass system of the two final state particles *now called 1 and 2* as in the case of final state corrections (see figure 16), where now p_3 is defined in the overall center-of-mass system of partons a and b . However, we will not choose the angle θ between the hard jet and the incoming photon or the related variable $b = 1/2(1 - \cos \theta)$ as the second independent variable. Instead it is more convenient to choose the fraction of the center-of-mass energy going into the hard subprocess $ab \rightarrow 12$

$$z_a = \frac{p_1 p_2}{p_a p_b} \in [X_a, 1] \text{ and } z_b = \frac{p_1 p_2}{p_a p_b} \in [X_b, 1], \tag{4.76}$$

respectively. In this way, the variables z_a and z_b describe the momentum of the third unobserved particle $p_3 = (1 - z_a)p_a$ and $p_3 = (1 - z_b)p_b$. They are bounded from below through the fractions of the initial electron and proton energies transferred to the partons with momenta $z_a p_a$ and $z_b p_b$ in the hard scattering

$$X_a = \frac{p_1 p_2}{k p_b} \text{ and } X_b = \frac{p_1 p_2}{p_a p}. \tag{4.77}$$

As the three-particle phase space can be calculated for photon and proton initial state singularities in exactly the same manner, we only consider the case of the photon initial state in the following. The Mandelstam variables differ slightly from those used in $2 \rightarrow 2$ scattering and final state corrections in order to accommodate the third unobserved particle radiated from the initial state

$$s = (z_a p_a + p_b)^2 = (p_1 + p_2)^2, \quad (4.78)$$

$$t = (z_a p_a - p_1)^2, \quad (4.79)$$

$$u = (z_a p_a - p_2)^2. \quad (4.80)$$

In the limit of soft ($p_3 = 0$) or collinear ($p_3 \parallel p_a$) particle emission, they satisfy the relation $s + t + u = sz'' \rightarrow 0$ for massless partons.

The calculation proceeds as follows: We insert three additional δ -functions with respect to t , z'' , and z_a into the general expression

$$d\text{PS}^{(3)} = \int (2\pi)^d \prod_{i=1}^3 \frac{d^d p_i \delta(p_i^2)}{(2\pi)^{d-1}} \delta^d \left(p_a + p_b - \sum_{j=1}^3 p_j \right) \quad (4.81)$$

giving

$$\begin{aligned} \frac{d\text{PS}^{(3)}}{dt dz'' dz_a} &= \int (2\pi)^d \prod_{i=1}^3 \frac{d^d p_i \delta(p_i^2)}{(2\pi)^{d-1}} \delta^d \left(p_a + p_b - \sum_{j=1}^3 p_j \right) \\ &\quad \delta(t - (z_a p_a - p_1)^2) \delta \left(z'' - \frac{p_a p_3}{p_a p_b} \right) \delta \left(z_a - \frac{p_1 p_2}{p_a p_b} \right). \end{aligned} \quad (4.82)$$

Next, we integrate over the $\delta(p_i^2)$ and the space-like components of the d -dimensional δ -function to eliminate p_2 . In the resulting expression

$$\begin{aligned} \frac{d\text{PS}^{(3)}}{dt dz'' dz_a} &= \int \frac{d^{d-1} p_1 d^{d-1} p_3}{(2\pi)^{2d-3} 2E_1 2E_2 2E_3} \delta \left(E_a + E_b - \sum_{j=1}^3 E_j \right) \\ &\quad \delta(t - (z_a p_a - p_1)^2) \delta \left(z'' - \frac{p_a p_3}{p_a p_b} \right) \delta \left(z_a - \frac{p_1 p_2}{p_a p_b} \right), \end{aligned} \quad (4.83)$$

we now decompose p_1 into its energy and angular components in the center-of-mass system of partons 1 and 2 and p_3 in the overall center-of-mass system

$$\begin{aligned} \frac{d\text{PS}^{(3)}}{dt dz'' dz_a} &= \int \frac{1}{(2\pi)^{2d-3} 8E_2} \frac{2\pi^{\frac{d-3}{2}}}{\Gamma\left(\frac{d-3}{2}\right)} E_1^{d-3} dE_1 \sin^{d-3} \theta d\theta \sin^{d-4} \phi d\phi \frac{\pi^{\frac{d-4}{2}}}{\Gamma\left(\frac{d-2}{2}\right)} E_3^{d-3} dE_3^* \\ &\quad \sin^{d-3} \chi^* d\chi^* d\phi_3^* \delta \left(E_a + E_b - \sum_{j=1}^3 E_j \right) \delta(t + 2z_a E_a E_1 (1 - \cos \theta)) \\ &\quad \delta \left(z'' - \frac{2z_a E_a^* E_3^*}{s} (1 - \cos \chi^*) \right) \delta \left(z_a - \frac{4z_a E_1^2}{s} \right). \end{aligned} \quad (4.84)$$

Integrating over the remaining δ -functions and the trivial azimuthal angle ϕ_2^* up to 2π , we arrive at

$$\frac{d\text{PS}^{(3)}}{dt dz'' dz_a} = \int \frac{(16\pi^2)^\varepsilon}{128\pi^3 \Gamma^2(1-\varepsilon)} z''^{-\varepsilon} (ut)^{-\varepsilon} (1-z'')^{-1+2\varepsilon} (1-z_a-z'')^{-\varepsilon} z_a^{-1+\varepsilon} \sin^{-2\varepsilon} \phi \frac{d\phi}{N_\phi}, \quad (4.85)$$

where N_ϕ is the normalization factor given in eq. (4.35). Finally, we can factorize this three particle phase space into

$$d\text{PS}^{(3)} = d\text{PS}^{(2)} d\text{PS}^{(r)}, \quad (4.86)$$

where $d\text{PS}^{(2)}$ is the usual phase space for the two observed jets 1 and 2 from section 3.1 and

$$d\text{PS}^{(r)} = \left(\frac{4\pi}{s}\right)^\varepsilon \frac{\Gamma(1-\varepsilon)}{\Gamma(1-2\varepsilon)} \frac{s}{16\pi^2} H(z'') d\mu_I \quad (4.87)$$

is the phase space of the unresolved subsystem of partons a and 3. The integration measure is

$$d\mu_I = dz'' z''^{-\varepsilon} \frac{dz_a}{z_a} \left(\frac{z_a}{1-z_a}\right)^\varepsilon \frac{d\phi}{N_\phi} \sin^{-2\varepsilon} \phi \frac{\Gamma(1-2\varepsilon)}{\Gamma^2(1-\varepsilon)}, \quad (4.88)$$

and the function

$$H(z'') = (1-z'')^{-1+2\varepsilon} \left(1 - \frac{z''}{1-z_a}\right)^{-\varepsilon} = 1 + \mathcal{O}(z'') \quad (4.89)$$

can be approximated by 1 as it leads only to negligible terms of $\mathcal{O}(y)$. The integration of $d\text{PS}^{(r)}$ over $z'' \in [0, -u/s]$, $z_a \in [X_a, 1]$, and $\phi \in [0, \pi]$ is restricted to the singular region of z'' , when partons p_a and p_3 are recombined, such that $0 \leq z'' \leq \min\{-u/s, y\} \equiv y_I$.

4.2.5 Photon Initial State Corrections for Direct Photons

Singularities from the initial direct photon arise from diagrams of type b) in figure 15. The photon here splits up into a quark-antiquark pair, and one of the two becomes a part of the photon remnant. If the (anti-)quark is collinear to the incoming photon, a simple $1/\varepsilon$ pole is produced. Quadratic $1/\varepsilon^2$ poles corresponding to soft *and* collinear singularities do not exist, since there is no direct coupling to a gluon line. In this specific case, it is therefore not necessary to perform a partial fractioning decomposition.

The matrix elements for the $2 \rightarrow 3$ processes $\gamma q \rightarrow qgg$ and $\gamma q \rightarrow qq\bar{q}$ are computed from the generic diagrams in figure 17 as in the case of final state corrections in section 4.2.2. Those for the processes with incoming anti-quarks and gluons are obtained by simple crossing of the diagrams or Mandelstam variables according to table 4. We keep only terms that are singular in the variable

$$z'' = \frac{p_a p_3}{p_a p_b} \quad (4.90)$$

and express the ten invariants for $2 \rightarrow 3$ scattering through z'' , the longitudinal momentum fraction z_a transferred from the photon to the parton entering the hard subprocess, and the variables s , t , and u defined in section 4.2.4:

$$p_a p_b = \frac{s}{2z_a} \quad (4.91)$$

$$p_a p_1 = \frac{s-t}{2z_a s} \quad (4.92)$$

$$p_a p_2 = \frac{s-u}{2z_a s} \quad (4.93)$$

$$p_a p_3 = \frac{s}{2z_a} z'' \quad (4.94)$$

$$p_b p_1 = \frac{s-u}{2z_a s} z_a \quad (4.95)$$

$$p_b p_2 = \frac{s-t}{2z_a s} z_a \quad (4.96)$$

$$p_b p_3 = \frac{s}{2z_a} (1-z_a) \quad (4.97)$$

$$p_1 p_2 = \frac{s}{2z_a} z_a \quad (4.98)$$

$$p_1 p_3 = \frac{s-t}{2z_a s} (1-z_a) \quad (4.99)$$

$$p_2 p_3 = \frac{s-u}{2z_a s} (1-z_a) \quad (4.100)$$

Under these approximations, a singular kernel can be factorized out, which is universal for all processes of the type $\gamma b \rightarrow 123$ and describes the splitting of a boson (in this case the photon) into two fermions (i.e. the quark-antiquark pair). Consequently, a parton from the photon scatters now off the parton in the proton and the relevant parton-parton Born matrix elements show up. In the case of

$$|\mathcal{M}|_{\gamma q \rightarrow qgg}^2(s, t, u) = e^2 e_q^2 g^4 \mu^{6\varepsilon} \frac{1}{sz''} \left[z_a^2 + (1 - z_a)^2 - \varepsilon \right] T_{q\bar{q} \rightarrow gg}(s, t, u), \quad (4.101)$$

it is the quark-antiquark annihilation process into two gluons. For

$$|\mathcal{M}|_{\gamma q \rightarrow qq\bar{q}}^2(s, t, u) = e^2 e_q^2 g^4 \mu^{6\varepsilon} \frac{1}{sz''} \left[z_a^2 + (1 - z_a)^2 - \varepsilon \right] T_{q\bar{q} \rightarrow q\bar{q}}(s, t, u), \quad (4.102)$$

it is the process $q\bar{q} \rightarrow q\bar{q}$. The result for

$$|\mathcal{M}|_{\gamma g \rightarrow gq\bar{q}}^2(s, t, u) = e^2 e_q^2 g^4 \mu^{6\varepsilon} \frac{1}{sz''} \left[z_a^2 + (1 - z_a)^2 - \varepsilon \right] T_{qg \rightarrow qg}(s, t, u) \quad (4.103)$$

is easily obtained by crossing ($s \leftrightarrow t$) in the first process and multiplying by (-1) .

As the matrix elements do not depend on the variable ϕ , the integration over ϕ in $d\text{PS}^{(r)}$ is as trivial as before. In addition, the integration over the simple pole in z'' can also be carried out easily. However, the integration over the momentum fraction z_a involves a convolution with the photon spectrum in the electron. Since these exist only in a parametrized form too complicated to integrate, the z_a -integration has to be done numerically and is written down explicitly in the final result

$$\int d\text{PS}^{(r)} |\mathcal{M}|_{\gamma b \rightarrow 123}^2(s, t, u) = \int_{X_a}^1 \frac{dz_a}{z_a} e^2 g^2 \mu^{4\varepsilon} \frac{\alpha_s}{2\pi} \left(\frac{4\pi\mu^2}{s} \right)^\varepsilon \frac{\Gamma(1-\varepsilon)}{\Gamma(1-2\varepsilon)} I_{\gamma b \rightarrow 123}(s, t, u). \quad (4.104)$$

The functions $I_{\gamma b \rightarrow 123}$ are given by

$$I_{\gamma q \rightarrow qgg}(s, t, u) = \left[-\frac{1}{\varepsilon} \frac{1}{2N_C} P_{q\leftarrow\gamma}(z_a) + \frac{1}{2N_C} P_{q\leftarrow\gamma}(z_a) \ln \left(y_I \frac{1-z_a}{z_a} \right) + \frac{e_q^2}{2} \right] T_{q\bar{q} \rightarrow gg}(s, t, u), \quad (4.105)$$

$$I_{\gamma q \rightarrow qq\bar{q}}(s, t, u) = \left[-\frac{1}{\varepsilon} \frac{1}{2N_C} P_{q\leftarrow\gamma}(z_a) + \frac{1}{2N_C} P_{q\leftarrow\gamma}(z_a) \ln \left(y_I \frac{1-z_a}{z_a} \right) + \frac{e_q^2}{2} \right] T_{q\bar{q} \rightarrow q\bar{q}}(s, t, u), \quad (4.106)$$

$$I_{\gamma g \rightarrow gq\bar{q}}(s, t, u) = \left[-\frac{1}{\varepsilon} \frac{1}{2N_C} P_{q\leftarrow\gamma}(z_a) + \frac{1}{2N_C} P_{q\leftarrow\gamma}(z_a) \ln \left(y_I \frac{1-z_a}{z_a} \right) + \frac{e_q^2}{2} \right] T_{qg \rightarrow qg}(s, t, u). \quad (4.107)$$

Terms of $\mathcal{O}(\varepsilon)$ and $\mathcal{O}(y)$ have been omitted as before.

The collinear $1/\varepsilon$ poles are proportional to the splitting function

$$P_{q\leftarrow\gamma}(z_a) = 2N_C e_q^2 P_{q\leftarrow g}(z_a) \quad (4.108)$$

for photons into quarks, where e_q is the fractional charge of the quark coupling to the photon and

$$P_{q\leftarrow g}(z_a) = \frac{1}{2} \left[z_a^2 + (1 - z_a)^2 \right] \quad (4.109)$$

is the Altarelli-Parisi splitting function for gluons into quarks. This function appears in the evolution equation of the photon structure function as an inhomogeneous or so-called point-like term (see section 2.3). Therefore, the photon initial state singularities can be absorbed into the photon structure function. The necessary steps are well known [53, 68]. We define the renormalized distribution function of a parton a in the electron $F_{a/e}(X_a, M_a^2)$ as

$$F_{a/e}(X_a, M_a^2) = \int_{X_a}^1 \frac{dz_a}{z_a} \left[\delta_a \gamma \delta(1 - z_a) + \frac{\alpha}{2\pi} R_{q\leftarrow\gamma}(z_a, M_a^2) \right] F_{\gamma/e} \left(\frac{X_a}{z_a} \right), \quad (4.110)$$

where R has the general form

$$R_{a\leftarrow\gamma}(z_a, M_a^2) = -\frac{1}{\varepsilon} P_{q\leftarrow\gamma}(z_a) \frac{\Gamma(1-\varepsilon)}{\Gamma(1-2\varepsilon)} \left(\frac{4\pi\mu^2}{M_a^2}\right)^\varepsilon + C_{q\leftarrow\gamma}(z_a) \quad (4.111)$$

with $C = 0$ in the $\overline{\text{MS}}$ scheme. The renormalized partonic cross section for $\gamma b \rightarrow \text{jets}$ is then calculated from

$$d\sigma(\gamma b \rightarrow \text{jets}) = d\bar{\sigma}(\gamma b \rightarrow \text{jets}) - \frac{\alpha}{2\pi} \int dz_a R_{q\leftarrow\gamma}(z_a, M_a^2) d\sigma(ab \rightarrow \text{jets}). \quad (4.112)$$

$d\bar{\sigma}(\gamma b \rightarrow \text{jets})$ is the higher order cross section before the subtraction procedure, and $d\sigma(ab \rightarrow \text{jets})$ contains the LO parton-parton scattering matrix elements $T_{ab\rightarrow 12}(s, t, u)$. The factor $4\pi\mu^2/M_a^2$ in eq. (4.111) is combined with the factor $4\pi\mu^2/s$ in eq. (4.104) and leads to M_a^2 dependent terms of the form

$$-\frac{1}{\varepsilon} P_{q\leftarrow\gamma}(z_a) \left[\left(\frac{4\pi\mu^2}{s}\right)^\varepsilon - \left(\frac{4\pi\mu^2}{M_a^2}\right)^\varepsilon \right] = -P_{q\leftarrow\gamma}(z_a) \ln\left(\frac{M_a^2}{s}\right), \quad (4.113)$$

so that the cross section after subtraction in eq. (4.112) will depend on the factorization scale M_a^2 .

4.2.6 Proton Initial State Corrections for Direct Photons

Initial state singularities cannot only show up on the direct photon side, but also on the proton side. The parton from the proton, which undergoes the hard scattering, will then radiate a soft or collinear secondary parton. A quark can, e.g., radiate a gluon as in figure 15c), which will then not be observed but contributes to the proton remnant. As we can now have soft gluons, we find not only single but also quadratic poles in ε . After singling out the matrix elements for the diagrams in figure 17 singular in the variable

$$z''' = \frac{p_b p_3}{p_a p_b}, \quad (4.114)$$

we therefore have to decompose them with partial fractioning using REDUCE [64]. The invariants are approximated quite similarly to the photon initial state corrections and are given by

$$p_a p_b = \frac{s}{2z_b} \quad (4.115)$$

$$p_a p_1 = \frac{s-t}{2z_b} z_b \quad (4.116)$$

$$p_a p_2 = \frac{s-u}{2z_b} z_b \quad (4.117)$$

$$p_a p_3 = \frac{s}{2z_b} (1-z_b) \quad (4.118)$$

$$p_b p_1 = \frac{s-u}{2z_b} \frac{s}{s} \quad (4.119)$$

$$p_b p_2 = \frac{s-t}{2z_b} \frac{s}{s} \quad (4.120)$$

$$p_b p_3 = \frac{s}{2z_b} z''' \quad (4.121)$$

$$p_1 p_2 = \frac{s}{2z_b} z_b \quad (4.122)$$

$$p_1 p_3 = \frac{s-u}{2z_b} \frac{s}{s} (1-z_b) \quad (4.123)$$

$$p_2 p_3 = \frac{s-t}{2z_b} \frac{s}{s} (1-z_b) \quad (4.124)$$

The result for the first subprocess $\gamma q \rightarrow qgg$ turns out to be

$$|\mathcal{M}|_{\gamma q \rightarrow qgg}^2(s, t, u) = e^2 e_q^2 g^4 \mu^{6\varepsilon} \frac{1}{sz''' } \left[4C_F \left((1-z_b)(1-\varepsilon) - 2 + \frac{-2t/s}{z''' - t/s(1-z_b)} \right) - 4N_C \left(\frac{-t/s}{z''' - t/s(1-z_b)} - \frac{-u/s}{z''' - u/s(1-z_b)} \right) \right] T_{\gamma q \rightarrow qg}(s, t, u). \quad (4.125)$$

Since the initial quark has to couple to the photon, it cannot vanish in the beam pipe. The singular kernel only describes the radiation of a gluon from the quark, factorizing the leading-order QCD Compton process $\gamma q \rightarrow gq$. According to table 4, we find the same result for incoming anti-quarks. In the four-fermion process

$$|\mathcal{M}|_{\gamma q \rightarrow qq\bar{q}}^2(s, t, u) = e^2 e_q^2 g^4 \mu^{6\varepsilon} \frac{1}{sz''' } \left[\frac{1 + (1-z_b)^2}{z_b} - \varepsilon z_b \right] T_{\gamma g \rightarrow q\bar{q}}(s, t, u), \quad (4.126)$$

the initial quark necessarily produces a collinear final state quark. Thus, we have a non-diagonal transition of the quark-initiated process $\gamma q \rightarrow qq\bar{q}$ into the gluon-initiated process $\gamma g \rightarrow q\bar{q}$. The other non-diagonal transition shows up in

$$|\mathcal{M}|_{\gamma g \rightarrow gq\bar{q},1}^2(s, t, u) = e^2 e_q^2 g^4 \mu^{6\varepsilon} \frac{2}{sz''' } C_F \left[(z_b^2 + (1-z_b)^2)(1+\varepsilon) - \varepsilon \right] T_{\gamma q \rightarrow gq}(s, t, u), \quad (4.127)$$

where the gluon-initiated process $\gamma g \rightarrow gq\bar{q}$ is transformed into the quark-initiated process $\gamma q \rightarrow gq$. The splitting of a gluon into a collinear quark-antiquark pair is analogous to the splitting of the direct photon in the last section. However, the gluon also possesses a non-abelian coupling to other gluons, which can become soft or collinear in

$$|\mathcal{M}|_{\gamma g \rightarrow gq\bar{q},2}^2(s, t, u) = e^2 e_q^2 g^4 \mu^{6\varepsilon} \frac{2}{sz''' } N_C \left[2 \left(\frac{1}{z_b} + z_b(1-z_b) - 2 \right) + \frac{-t/s}{z''' - t/s(1-z_b)} - \frac{-u/s}{z''' - u/s(1-z_b)} \right] T_{\gamma g \rightarrow q\bar{q}}(s, t, u) \quad (4.128)$$

and factorizes the photon-gluon fusion process $\gamma g \rightarrow q\bar{q}$.

The complete list of proton initial state corrections given above has to be integrated over the phase space region, where parton 3 is an unobserved part of the proton remnant. The phase space for three-particle final states is taken from section 4.2.4, where $(z'' \leftrightarrow z''')$ and $(z_a \leftrightarrow z_b)$ have to be interchanged. The relevant integrals are calculated in appendix B. The result is

$$\int d\text{PS}^{(r)} |\mathcal{M}|_{\gamma b \rightarrow 123}^2(s, t, u) = \int_{X_b}^1 \frac{dz_b}{z_b} e^2 e_q^2 g^2 \mu^{4\varepsilon} \frac{\alpha_s}{2\pi} \left(\frac{4\pi\mu^2}{s} \right)^\varepsilon \frac{\Gamma(1-\varepsilon)}{\Gamma(1-2\varepsilon)} J_{\gamma b \rightarrow 123}(s, t, u), \quad (4.129)$$

where the functions $J_{\gamma b \rightarrow 123}$ are given by

$$\begin{aligned} J_{\gamma q \rightarrow qgg}(s, t, u) = & \left[2C_F \left(-\frac{1}{\varepsilon} \frac{1}{C_F} P_{q \leftarrow q}(z_b) + \delta(1-z_b) \left(\frac{1}{\varepsilon^2} + \frac{1}{2\varepsilon} \left(3 - 2 \ln \frac{-t}{s} \right) + \frac{1}{2} \ln^2 \frac{-t}{s} + \pi^2 \right) \right. \right. \\ & + 1 - z_b + (1-z_b) \ln \left(y_J \frac{1-z_b}{z_b} \right) + 2R_+ \left(\frac{-t}{s} \right) - 2 \ln \left(\frac{-t}{s} \left(\frac{1-z_b}{z_b} \right)^2 \right) \\ & \left. \left. - 2 \frac{z_b}{1-z_b} \ln \left(1 + \frac{-t}{y_J s} \frac{1-z_b}{z_b} \right) \right) \right. \\ & - N_C \left(\delta(1-z_b) \left(\frac{1}{\varepsilon} \ln \frac{u}{t} + \frac{1}{2} \ln^2 \frac{-t}{s} - \frac{1}{2} \ln^2 \frac{-u}{s} \right) + 2R_+ \left(\frac{-t}{s} \right) - 2R_+ \left(\frac{-u}{s} \right) \right. \\ & \left. \left. - 2 \ln \left(\frac{-t}{s} \left(\frac{1-z_b}{z_b} \right)^2 \right) + 2 \ln \left(\frac{-u}{s} \left(\frac{1-z_b}{z_b} \right)^2 \right) \right) \right] \end{aligned}$$

$$-2\frac{z_b}{1-z_b}\ln\left(1+\frac{-t}{y_J s}\frac{1-z_b}{z_b}\right)+2\frac{z_b}{1-z_b}\ln\left(1+\frac{-u}{y_J s}\frac{1-z_b}{z_b}\right)\Bigg] T_{\gamma q\rightarrow gq}(s,t,u), \quad (4.130)$$

$$J_{\gamma q\rightarrow qq\bar{q}}(s,t,u) = \frac{1}{2}\left[-\frac{1}{\varepsilon}P_{g\leftarrow q}(z_b)+\frac{1}{C_F}P_{g\leftarrow q}(z_b)\left(\ln\left(y_J\frac{1-z_b}{z_b}\right)+1\right)-2\frac{1-z_b}{z_b}\right]T_{\gamma g\rightarrow q\bar{q}}(s,t,u), \quad (4.131)$$

$$J_{\gamma g\rightarrow gq\bar{q},1}(s,t,u) = 2C_F\left[-\frac{1}{\varepsilon}P_{q\leftarrow g}(z_b)+P_{q\leftarrow g}(z_b)\left(\ln\left(y_J\frac{1-z_b}{z_b}\right)-1\right)+\frac{1}{2}\right]T_{\gamma q\rightarrow gq}(s,t,u), \quad (4.132)$$

$$J_{\gamma g\rightarrow gq\bar{q},2}(s,t,u) = N_C\left[-\frac{1}{\varepsilon}P_{g\leftarrow g}(z_b)+\delta(1-z_b)\left(\frac{1}{\varepsilon^2}+\frac{1}{\varepsilon}N_C\left(\frac{11}{6}N_C-\frac{1}{3}N_f\right)-\frac{1}{2\varepsilon}\ln\frac{tu}{s^2}+\frac{1}{4}\ln^2\frac{-t}{s}+\frac{1}{4}\ln^2\frac{-u}{s}+\pi^2\right)-2R_+\left(\frac{-t}{s}\right)-2R_+\left(\frac{-u}{s}\right)+2\ln\left(\frac{-t}{s}\left(\frac{1-z_b}{z_b}\right)^2\right)+2\ln\left(\frac{-u}{s}\left(\frac{1-z_b}{z_b}\right)^2\right)+2\frac{z_b}{1-z_b}\ln\left(1+\frac{-t}{y_J s}\frac{1-z_b}{z_b}\right)+2\frac{z_b}{1-z_b}\ln\left(1+\frac{-u}{y_J s}\frac{1-z_b}{z_b}\right)-4\left(\frac{1-z_b}{z_b}+z_b(1-z_b)\right)\ln\left(y_J\frac{1-z_b}{z_b}\right)\right]\left(-\frac{N_C}{4}\right)T_{\gamma g\rightarrow q\bar{q}}(s,t,u). \quad (4.133)$$

Here, we have used the function

$$R_+(x) = \left(\frac{\ln\left(x\left(\frac{1-z_b}{z_b}\right)^2\right)}{1-z_b}\right)_+ \quad (4.134)$$

as an abbreviation. As the integration over z_b in eq. (4.129) runs from X_b to 1, the $+$ -distributions [69] are defined as

$$D_+[g] = \int_{X_b}^1 dz_b D(z_b)g(z_b) - \int_0^1 dz_b D(z_b)g(1), \quad (4.135)$$

where

$$g(z_b) = \frac{1}{z_b}F_{b'/p}\left(\frac{X_b}{z_b}\right)h(z_b), \quad (4.136)$$

and $h(z_b)$ is a regular function of z_b [70]. This leads to additional terms not given here explicitly when eq. (4.135) is transformed so that both integrals are calculated in the range $[X_b, 1]$.

Some of the $J_{\gamma b\rightarrow 123}$ contain infrared singularities $\propto 1/\varepsilon^2$, which must cancel against the corresponding singularities in the virtual contributions. The singular parts are decomposed in such a way that the Altarelli-Parisi kernels in four dimensions

$$P_{q\leftarrow q}(z_b) = C_F\left[\frac{1+z_b^2}{(1-z_b)_+}+\frac{3}{2}\delta(1-z_b)\right], \quad (4.137)$$

$$P_{g\leftarrow q}(z_b) = C_F\left[\frac{1+(1-z_b)^2}{z_b}\right], \quad (4.138)$$

$$P_{g\leftarrow g}(z_b) = 2N_C\left[\frac{1}{(1-z_b)_+}+\frac{1}{z_b}+z_b(1-z_b)-2\right]+\left[\frac{11}{6}N_C-\frac{1}{3}N_f\right]\delta(1-z_b), \quad (4.139)$$

$$P_{q\leftarrow g}(z_b) = \frac{1}{2}\left[z_b^2+(1-z_b)^2\right] \quad (4.140)$$

proportional to $1/\varepsilon$ are split off. They also appear in the evolution equations for the parton distribution functions in the proton in section 2.2. The singular terms proportional to these kernels are absorbed as usual into the scale dependent structure functions

$$F_{b/p}(X_b, M_b^2) = \int_{X_b}^1 \frac{dz_b}{z_b} \left[\delta_{bb'} \delta(1 - z_b) + \frac{\alpha_s}{2\pi} R'_{b \leftarrow b'}(z_b, M_b^2) \right] F_{b'/p} \left(\frac{X_b}{z_b} \right), \quad (4.141)$$

where $F_{b'/p}(X_b/z_b)$ is the LO structure function before absorption of the collinear singularities and

$$R'_{b \leftarrow b'}(z_b, M_b^2) = -\frac{1}{\varepsilon} P_{b \leftarrow b'}(z_b) \frac{\Gamma(1 - \varepsilon)}{\Gamma(1 - 2\varepsilon)} \left(\frac{4\pi\mu^2}{M_b^2} \right)^\varepsilon + C'_{b \leftarrow b'}(z_b) \quad (4.142)$$

with $C' = 0$ in the $\overline{\text{MS}}$ scheme. Then, the renormalized higher order hard scattering cross section $d\sigma(\gamma b \rightarrow \text{jets})$ is calculated from

$$d\sigma(\gamma b \rightarrow \text{jets}) = d\bar{\sigma}(\gamma b \rightarrow \text{jets}) - \frac{\alpha_s}{2\pi} \int dz_b R'_{b \leftarrow b'}(z_b, M_b^2) d\sigma(\gamma b' \rightarrow \text{jets}). \quad (4.143)$$

$d\bar{\sigma}(\gamma b \rightarrow \text{jets})$ is the higher order cross section before the subtraction procedure, and $d\sigma(\gamma b' \rightarrow \text{jets})$ contains the lowest order matrix elements $T_{\gamma q \rightarrow gq}(s, t, u)$ and $T_{\gamma g \rightarrow q\bar{q}}(s, t, u)$ in d dimensions. This well known factorization prescription [68, 71, 50] removes finally all remaining collinear singularities. It is universal and leads for all processes to the same definition of structure functions if the choice concerning the regular function C' in (4.142) is kept fixed. Similar to the case of photon initial state singularities, the higher order cross sections in (4.143) will depend on the factorization scale M_b due to terms of the form $P_{b \leftarrow b'}(z_b) \ln(M_b^2/s)$.

4.2.7 Photon Initial State Corrections for Resolved Photons

We now turn back to the case of resolved photons and consider their initial state corrections. We start with the singularities on the photonic side of the hard scattering cross section. For direct photons, there was only one possible singularity coming from the splitting of the photon into a quark-antiquark pair as shown in figure 15b). However, resolved photons contribute to the hard scattering like hadrons through their partonic structure. Therefore they produce similar poles to the proton initial state singularities as in figure 15c) or those in section 4.2.6. These poles can be of quadratic strength due to the radiation of soft and collinear gluons off the quarks in the photon.

We use the same $\mathcal{O}(\alpha_s^3)$ matrix elements that were already calculated for the final state corrections of resolved photons in section 4.2.3. The relevant diagrams are those for parton-parton scattering in figure 18. As stated before, these diagrams show only the generic types and have also to be used in their crossed forms for the complete set of diagrams. All possible processes are listed in table 6 together with their matrix elements, initial spin and color averages, and statistical factors. Only the matrix elements singular in the variable $z''_a = p_a p_3 / p_a p_b$ are kept, where p_3 is the momentum of the parton soft or collinear to the original parton in the photon with momentum p_a . Parton 3 will then be a part of the photon remnant. The matrix elements are expressed through the ten approximated invariants given in eqs. (4.91)-(4.100) and decomposed with the help of partial fractioning. It is then possible to factorize them into singular kernels and parts of the leading-order parton-parton matrix elements.

Let us start with the process $qq' \rightarrow qq'g$ in figure 18a). Here, the final gluon can be soft or collinear to the incoming quark a

$$\begin{aligned} |\mathcal{M}|_{qq' \rightarrow qq'g,1}^2(s, t, u) &= g^6 \mu^{6\varepsilon} \frac{2}{s z''} \\ &\left[(2C_F - N_C) \left(\frac{-2}{z'' + (1 - z_a)} + \frac{-t/s}{z'' - t/s(1 - z_a)} + \frac{-u/s}{z'' - u/s(1 - z_a)} \right) \right. \\ &\left. + C_F \left((1 - z_a)(1 - \varepsilon) - 2 + \frac{-2u/s}{z'' - u/s(1 - z_a)} \right) \right] T_{qq' \rightarrow qq'}(s, t, u), \quad (4.144) \end{aligned}$$

Process	Matrix Element $ \mathcal{M} ^2$
$qq' \rightarrow qq'g$	$[\mathcal{M}_{qq' \rightarrow qq'g,1}^2(s, t, u) + \mathcal{M}_{qq' \rightarrow qq'g,2}^2(s, t, u)]/[4N_C^2]$
$q\bar{q}' \rightarrow q\bar{q}'g$	$[\mathcal{M}_{qq' \rightarrow qq'g,1}^2(u, t, s) + \mathcal{M}_{qq' \rightarrow qq'g,2}^2(u, t, s)]/[4N_C^2]$
$q\bar{q} \rightarrow \bar{q}'q'g$	$[\mathcal{M}_{qq' \rightarrow qq'g,1}^2(t, s, u)]/[4N_C^2]$
$qg \rightarrow qq'\bar{q}'$	$[\mathcal{M}_{qg \rightarrow qq'\bar{q}'}^2(s, t, u) + \mathcal{M}_{qg \rightarrow qq'\bar{q}'}^2(u, t, s) + \mathcal{M}_{qg \rightarrow qq'\bar{q}'}^2(t, s, u) - \mathcal{M}_{qq' \rightarrow qq'g,2}^2(t, s, u)]/[8(1 - \varepsilon)N_C^2C_F]$
$qq \rightarrow qqg$	$[\mathcal{M}_{qq' \rightarrow qq'g,1}^2(s, t, u) + \mathcal{M}_{qq' \rightarrow qq'g,1}^2(s, u, t) + \mathcal{M}_{qq \rightarrow qqg}^2(s, t, u) + 2 \mathcal{M}_{qq' \rightarrow qq'g,2}^2(s, t, u)]/[4N_C^2]/2!$
$q\bar{q} \rightarrow q\bar{q}g$	$[\mathcal{M}_{qq' \rightarrow qq'g,1}^2(u, t, s) + \mathcal{M}_{qq' \rightarrow qq'g,1}^2(u, s, t) + \mathcal{M}_{qq \rightarrow qqg}^2(u, t, s) + \mathcal{M}_{qq' \rightarrow qq'g,2}^2(u, t, s)]/[4N_C^2]$
$qg \rightarrow qq\bar{q}$	$[\mathcal{M}_{qg \rightarrow qq'\bar{q}'}^2(s, t, u) + \mathcal{M}_{qg \rightarrow qq'\bar{q}'}^2(s, u, t) + \mathcal{M}_{qg \rightarrow qq\bar{q}}^2(s, t, u) + \mathcal{M}_{qg \rightarrow qq'\bar{q}'}^2(u, t, s) + \mathcal{M}_{qg \rightarrow qq'\bar{q}'}^2(t, u, s) + \mathcal{M}_{qg \rightarrow qq\bar{q}}^2(u, t, s) + \mathcal{M}_{qg \rightarrow qq'\bar{q}'}^2(t, s, u) + \mathcal{M}_{qg \rightarrow qq'\bar{q}'}^2(u, s, t) + \mathcal{M}_{qg \rightarrow qq\bar{q}}^2(t, s, u) - 2 \mathcal{M}_{qq' \rightarrow qq'g,2}^2(t, s, u)]/[8(1 - \varepsilon)N_C^2C_F]/2!$
$q\bar{q} \rightarrow ggg$	$[\mathcal{M}_{q\bar{q} \rightarrow ggg}^2(s, t, u)]/[4N_C^2]/3!$
$qg \rightarrow qgg$	$[- \mathcal{M}_{q\bar{q} \rightarrow qgg}^2(t, s, u)/3 + \mathcal{M}_{qq \rightarrow qgg,1}^2(s, t, u) + \mathcal{M}_{qq \rightarrow qgg,2}^2(s, t, u)]/[8(1 - \varepsilon)N_C^2C_F]/2!$
$\bar{q}g \rightarrow \bar{q}gg$	$[- \mathcal{M}_{q\bar{q} \rightarrow ggg}^2(t, u, s)/3 + \mathcal{M}_{qq \rightarrow qgg,1}^2(u, t, s) + \mathcal{M}_{qq \rightarrow qgg,2}^2(u, t, s)]/[8(1 - \varepsilon)N_C^2C_F]/2!$
$gg \rightarrow q\bar{q}g$	$[- \mathcal{M}_{qg \rightarrow qgg,1}^2(t, s, u) + \mathcal{M}_{qg \rightarrow q\bar{q}g}^2(s, t, u)]/[16(1 - \varepsilon)^2N_C^2C_F^2]$
$gg \rightarrow ggg$	$[\mathcal{M}_{qg \rightarrow ggg}^2(s, t, u)]/[16(1 - \varepsilon)^2N_C^2C_F^2]/3!$

Table 6: Summary of $2 \rightarrow 3$ squared matrix elements for resolved photoproduction.

so that the original quark will also participate in the Born process $qq' \rightarrow qq'$. However, the quark can also go into the photon remnant. It will then radiate a gluon that scatters from the quark b with different flavor

$$|\mathcal{M}_{qq' \rightarrow qq'g,2}^2(s, t, u) = g^6 \mu^{6\varepsilon} \frac{1}{sz''} \left[\frac{1 + (1 - z_a)^2}{z_a} - \varepsilon z_a \right] T_{qg \rightarrow qg}(s, t, u). \quad (4.145)$$

For equal flavors in figure 18b), the interference contribution

$$\begin{aligned} |\mathcal{M}_{qq \rightarrow qqg}^2(s, t, u) &= g^6 \mu^{6\varepsilon} \frac{2}{sz''} \\ &\left[(2C_F - N_C) \left(\frac{-2}{z'' + (1 - z_a)} + \frac{-t/s}{z'' - t/s(1 - z_a)} + \frac{-u/s}{z'' - u/s(1 - z_a)} \right) \right. \\ &\left. + C_F \left((1 - z_a)(1 - \varepsilon) - 2 + \frac{2}{z'' + (1 - z_a)} \right) \right] T_{qq \rightarrow qq}(s, t, u) \end{aligned} \quad (4.146)$$

has the same kernel for the color factor $(2C_F - N_C)$, but a crossed version for the color factor C_F , and is proportional to the Born interference contribution $T_{qq \rightarrow qq}$. If the final gluon is crossed into the initial state for the processes $qg \rightarrow qq'\bar{q}'$ and $qg \rightarrow qq\bar{q}$ with unlike and like quark flavors, it can split up into a collinear quark-antiquark pair quite similar to the splitting of direct photons in section 4.2.5. Consequently, the singular kernels in

$$|\mathcal{M}_{qg \rightarrow qq'\bar{q}'}^2(s, t, u) = g^6 \mu^{6\varepsilon} \frac{2}{sz''} C_F \left[(z_a^2 + (1 - z_a)^2)(1 + \varepsilon) - \varepsilon \right] T_{qq' \rightarrow qq'}(s, t, u) \quad (4.147)$$

and

$$|\mathcal{M}_{qg \rightarrow qq\bar{q}}^2(s, t, u) = g^6 \mu^{6\varepsilon} \frac{4}{sz''} C_F \left[(z_a^2 + (1 - z_a)^2)(1 + \varepsilon) - \varepsilon \right] T_{qq \rightarrow qq}(s, t, u) \quad (4.148)$$

are the same as in eqs. (4.101)-(4.103), and we have the quark-quark scattering processes $qq' \rightarrow qq'$ and $qq \rightarrow qq$ on the tree level. The additional factor of $(1 + \varepsilon)$ is due to the averaging of initial gluon spins with $1/(2(1 - \varepsilon)) \simeq 1/2(1 + \varepsilon)$, whereas the photons were averaged just by $1/2$. The third process to be considered is taken from figure 18c). Obviously, only a gluon can go into the photon remnant so that in

$$\begin{aligned}
|\mathcal{M}|_{q\bar{q} \rightarrow ggg}^2(s, t, u) &= g^6 \mu^{6\varepsilon} \frac{6}{sz''} [C_F ((1 - z_a)(1 - \varepsilon) - 2) T_{q\bar{q} \rightarrow gg}(s, t, u) \\
&+ 4N_C C_F \\
&\left(\frac{-u/s}{z'' - u/s(1 - z_a)} (1 - \varepsilon) \left(\frac{t^2 + u^2 - \varepsilon s^2}{tu} \right) \left(2N_C C_F - 2N_C^2 \frac{tu}{s^2} - N_C^2 \frac{u^2}{s^2} \right) \right. \\
&+ \frac{1}{z'' + (1 - z_a)} (1 - \varepsilon) \left(\frac{t^2 + u^2 - \varepsilon s^2}{tu} \right) \left(\left(2N_C C_F - 2N_C^2 \frac{ut}{s^2} \right) \left(-2 + 2\frac{C_F}{N_C} \right) \right. \\
&\left. \left. + N_C^2 \frac{t^2 + u^2}{s^2} \right) \right. \\
&\left. + \frac{-t/s}{z'' - t/s(1 - z_a)} (1 - \varepsilon) \left(\frac{t^2 + u^2 - \varepsilon s^2}{tu} \right) \left(2N_C C_F - 2N_C^2 \frac{tu}{s^2} - N_C^2 \frac{t^2}{s^2} \right) \right]
\end{aligned} \tag{4.149}$$

we find the same simple pole for the color factor C_F as in eq. (4.144) and still have quark-antiquark annihilation into gluons in the Born process. The double poles are, however, more complicated and factorize only parts of the Born matrix elements. If a final gluon is crossed into the initial state, a soft or collinear gluon can also be radiated from the initial gluon

$$\begin{aligned}
|\mathcal{M}|_{qg \rightarrow qgg,1}^2(s, t, u) &= g^6 \mu^{6\varepsilon} \frac{8}{sz''} \left[N_C \left(\frac{1}{z_a} + z_a(1 - z_a) - 2 \right) T_{qg \rightarrow qg}(s, t, u) \right. \\
&- 2N_C C_F \\
&\left(\frac{-u/s}{z'' - u/s(1 - z_a)} (1 - \varepsilon) \left(\frac{s^2 + u^2 - \varepsilon t^2}{su} \right) \left(2N_C C_F - 2N_C^2 \frac{su}{t^2} - N_C^2 \frac{u^2}{t^2} \right) \right. \\
&+ \frac{1}{z'' + (1 - z_a)} (1 - \varepsilon) \left(\frac{s^2 + u^2 - \varepsilon t^2}{su} \right) \left(2N_C C_F - 2N_C^2 \frac{us}{t^2} - N_C^2 \frac{s^2}{t^2} \right) \\
&\left. \left. + \frac{-t/s}{z'' - t/s(1 - z_a)} (1 - \varepsilon) \left(\frac{s^2 + u^2 - \varepsilon t^2}{su} \right) \left(N_C^2 \frac{s^2 + u^2}{t^2} \right) \right] ,
\end{aligned} \tag{4.150}$$

leaving a new kernel and a partly factorizable $qg \rightarrow qg$ scattering process behind. Alternatively, the quark can go into the photon remnant

$$|\mathcal{M}|_{qg \rightarrow qgg,2}^2(s, t, u) = g^6 \mu^{6\varepsilon} \frac{1}{sz''} \left[\frac{1 + (1 - z_a)^2}{z_a} - \varepsilon z_a \right] T_{gg \rightarrow gg}(s, t, u), \tag{4.151}$$

which leads to a $gg \rightarrow gg$ Born process. For collinear quarks, only a single divergence is possible. The next kernel for $qg \rightarrow q\bar{q}g$ is already known from $qg \rightarrow qq'\bar{q}'$ and $qg \rightarrow qq\bar{q}$

$$|\mathcal{M}|_{qg \rightarrow q\bar{q}g}^2(s, t, u) = g^6 \mu^{6\varepsilon} \frac{2}{sz''} C_F \left[(z_a^2 + (1 - z_a)^2)(1 + \varepsilon) - \varepsilon \right] T_{qg \rightarrow qg}(s, t, u), \tag{4.152}$$

where a gluon splits into a quark-antiquark pair, but now with a different leading-order matrix element $qg \rightarrow qg$. Finally in

$$\begin{aligned}
|\mathcal{M}|_{gg \rightarrow ggg}^2(s, t, u) &= g^6 \mu^{6\varepsilon} \frac{12}{sz''} \left[N_C \left(\frac{1}{z_a} + z_a(1 - z_a) - 2 \right) T_{gg \rightarrow gg}(s, t, u) \right. \\
&\left. + 8N_C^4 C_F \right]
\end{aligned}$$

$$\begin{aligned}
& \left(\frac{-t/s}{z'' - t/s(1 - z_a)} (1 - \varepsilon)^2 \left(3 - \frac{2su}{t^2} + \frac{s^4 + u^4}{s^2 u^2} \right) \right. \\
& + \frac{-u/s}{z'' - u/s(1 - z_a)} (1 - \varepsilon)^2 \left(3 - \frac{2st}{u^2} + \frac{s^4 + t^4}{s^2 t^2} \right) \\
& \left. + \frac{1}{z'' + (1 - z_a)} (1 - \varepsilon)^2 \left(3 - \frac{2tu}{s^2} + \frac{t^4 + u^4}{t^2 u^2} \right) \right), \quad (4.153)
\end{aligned}$$

it is clear that the Born process must also be completely gluonic and we can only have the gluon splitting into two gluons as in $gg \rightarrow qgg$. All these contributions have to be considered several times and also in crossed forms according to table 6.

What remains to be done is the integration over the phase space of particle 3 in a region, where it can be considered a part of the photon remnant. We do so with the help of the phase space $d\text{PS}^{(r)}$ calculated in section 4.2.4 and leave the z_a -integration for numerics. Again, the reason is the analytically not integrable form of the photonic parton densities that have to be convoluted with the matrix elements. The result is

$$\int d\text{PS}^{(r)} |\mathcal{M}|_{ab \rightarrow 123}^2(s, t, u) = \int_{X_a}^1 \frac{dz_a}{z_a} g^4 \mu^{4\varepsilon} \frac{\alpha_s}{2\pi} \left(\frac{4\pi\mu^2}{Q^2} \right)^\varepsilon \frac{\Gamma(1 - \varepsilon)}{\Gamma(1 - 2\varepsilon)} I_{ab \rightarrow 123}(s, t, u). \quad (4.154)$$

The integrated matrix elements are put into the functions $I_{ab \rightarrow 123}$:

$$\begin{aligned}
I_{qq' \rightarrow qq'g,1}(s, t, u) &= \left[(2C_F - N_C) \left(\delta(1 - z_a) \left(-\frac{1}{2\varepsilon} (-2l(s) + l(t) + l(u)) \right. \right. \right. \\
& + \frac{1}{4} (-2l^2(s) + l^2(t) + l^2(u)) \left. \left. \right) + \frac{z_a}{(1 - z_a)_+} (-2l(s) + l(t) + l(u)) \right. \\
& + 2 \frac{z_a}{1 - z_a} \ln \left(1 + \frac{|s|}{y_I Q^2} \frac{1 - z_a}{z_a} \right) - \frac{z_a}{1 - z_a} \ln \left(1 + \frac{|t|}{y_I Q^2} \frac{1 - z_a}{z_a} \right) \\
& - \frac{z_a}{1 - z_a} \ln \left(1 + \frac{|u|}{y_I Q^2} \frac{1 - z_a}{z_a} \right) \left. \right) \\
& + C_F \left(-\frac{1}{\varepsilon} \frac{1}{C_F} P_{q \leftarrow q}(z_a) + \delta(1 - z_a) \left(\frac{1}{\varepsilon^2} + \frac{1}{2\varepsilon} (3 - 2l(u)) \right. \right. \\
& + \frac{1}{2} l^2(u) + \pi^2 \left. \left. \right) + 1 - z_a + (1 - z_a) \ln \left(y_I \frac{1 - z_a}{z_a} \right) + 2R_+ \left(\left| \frac{u}{Q^2} \right| \right) \right. \\
& \left. - 2l \left(u \left(\frac{1 - z_a}{z_a} \right)^2 \right) - 2 \frac{z_a}{1 - z_a} \ln \left(1 + \frac{|u|}{y_I Q^2} \frac{1 - z_a}{z_a} \right) \right) \left. \right] \\
& T_{qq' \rightarrow qq'}(s, t, u), \quad (4.155)
\end{aligned}$$

$$\begin{aligned}
I_{qq' \rightarrow qq'g,2}(s, t, u) &= \frac{1}{2} \left[-\frac{1}{\varepsilon} \frac{1}{C_F} P_{g \leftarrow q}(z_a) + \frac{1}{C_F} P_{g \leftarrow q}(z_a) \left(\ln \left(y_I \frac{1 - z_a}{z_a} \right) + 1 \right) \right. \\
& \left. - 2 \frac{1 - z_a}{z_a} \right] T_{qq \rightarrow qq}(s, t, u), \quad (4.156)
\end{aligned}$$

$$\begin{aligned}
I_{qq \rightarrow qqg}(s, t, u) &= \left[(2C_F - N_C) \left(\delta(1 - z_a) \left(-\frac{1}{2\varepsilon} (-2l(s) + l(t) + l(u)) \right. \right. \right. \\
& + \frac{1}{4} (-2l^2(s) + l^2(t) + l^2(u)) \left. \left. \right) + \frac{z_a}{(1 - z_a)_+} (-2l(s) + l(t) + l(u)) \right. \\
& + 2 \frac{z_a}{1 - z_a} \ln \left(1 + \frac{|s|}{y_I Q^2} \frac{1 - z_a}{z_a} \right) - \frac{z_a}{1 - z_a} \ln \left(1 + \frac{|t|}{y_I Q^2} \frac{1 - z_a}{z_a} \right) \\
& - \frac{z_a}{1 - z_a} \ln \left(1 + \frac{|u|}{y_I Q^2} \frac{1 - z_a}{z_a} \right) \left. \right)
\end{aligned}$$

$$\begin{aligned}
& +C_F \left(-\frac{1}{\varepsilon} \frac{1}{C_F} P_{q \leftarrow q}(z_a) + \delta(1-z_a) \left(\frac{1}{\varepsilon^2} + \frac{1}{2\varepsilon} (3-2l(s)) \right. \right. \\
& \left. \left. + \frac{1}{2} l^2(s) + \pi^2 \right) + 1 - z_a + (1-z_a) \ln \left(y_I \frac{1-z_a}{z_a} \right) + 2R_+ \left(\left| \frac{s}{Q^2} \right| \right) \right. \\
& \left. - 2l \left(s \left(\frac{1-z_a}{z_a} \right)^2 \right) - 2 \frac{z_a}{1-z_a} \ln \left(1 + \frac{|s|}{y_I Q^2} \frac{1-z_a}{z_a} \right) \right) \Big] \\
& T_{qq \rightarrow qq}(s, t, u), \tag{4.157}
\end{aligned}$$

$$\begin{aligned}
I_{qg \rightarrow qq' \bar{q}'}(s, t, u) &= 2C_F \left[-\frac{1}{\varepsilon} P_{q \leftarrow g}(z_a) + P_{q \leftarrow g}(z_a) \left(\ln \left(y_I \frac{1-z_a}{z_a} \right) - 1 \right) + \frac{1}{2} \right] \\
& T_{qq' \rightarrow qq'}(s, t, u), \tag{4.158}
\end{aligned}$$

$$\begin{aligned}
I_{qg \rightarrow qq \bar{q}}(s, t, u) &= 4C_F \left[-\frac{1}{\varepsilon} P_{q \leftarrow g}(z_a) + P_{q \leftarrow g}(z_a) \left(\ln \left(y_I \frac{1-z_a}{z_a} \right) - 1 \right) + \frac{1}{2} \right] \\
& T_{qq \rightarrow qq}(s, t, u), \tag{4.159}
\end{aligned}$$

$$\begin{aligned}
I_{q\bar{q} \rightarrow ggg}(s, t, u) &= \left[3C_F \left(-\frac{1}{\varepsilon} \frac{1}{C_F} P_{q \leftarrow q}(z_a) + \delta(1-z_a) \left(\frac{1}{\varepsilon^2} + \frac{3}{2\varepsilon} + \pi^2 \right) \right. \right. \\
& \left. \left. + 1 - z_a + (1-z_a) \ln \left(y_I \frac{1-z_a}{z_a} \right) \right) \right] T_{q\bar{q} \rightarrow gg}(s, t, u) \\
& + 3N_C C_F \left[\left(\delta(1-z_a) \left(-\frac{2}{\varepsilon} l(t) + 2l(t) + l^2(t) \right) + 4R_+ \left(\left| \frac{t}{Q^2} \right| \right) \right. \right. \\
& \left. \left. - 4l \left(t \left(\frac{1-z_a}{z_a} \right)^2 \right) - 4 \frac{z_a}{1-z_a} \ln \left(1 + \frac{|t|}{y_I Q^2} \frac{1-z_a}{z_a} \right) \right) \right. \\
& \left. \left(N_C^2 \left(\frac{u}{t} - \frac{2u^2}{s^2} \right) - \frac{u}{t} - \frac{t}{u} \right) \right. \\
& \left. + \left(\delta(1-z_a) \left(-\frac{2}{\varepsilon} l(s) + 2l(s) + l^2(s) \right) + 4R_+ \left(\left| \frac{s}{Q^2} \right| \right) \right. \right. \\
& \left. \left. - 4l \left(s \left(\frac{1-z_a}{z_a} \right)^2 \right) - 4 \frac{z_a}{1-z_a} \ln \left(1 + \frac{|s|}{y_I Q^2} \frac{1-z_a}{z_a} \right) \right) \right. \\
& \left. \left(2 \frac{t^2 + u^2}{s^2} + \frac{1}{N_C^2} \left(\frac{u}{t} + \frac{t}{u} \right) \right) \right. \\
& \left. + \left(\delta(1-z_a) \left(-\frac{2}{\varepsilon} l(u) + 2l(u) + l^2(u) \right) + 4R_+ \left(\left| \frac{u}{Q^2} \right| \right) \right. \right. \\
& \left. \left. - 4l \left(u \left(\frac{1-z_a}{z_a} \right)^2 \right) - 4 \frac{z_a}{1-z_a} \ln \left(1 + \frac{|u|}{y_I Q^2} \frac{1-z_a}{z_a} \right) \right) \right. \\
& \left. \left(N_C^2 \left(\frac{t}{u} - \frac{2t^2}{s^2} \right) - \frac{u}{t} - \frac{t}{u} \right) \right. \\
& \left. + \delta(1-z_a) \left(2l(t) \left(N_C^2 \frac{u}{t} - \frac{s^2}{tu} \right) + 2l(s) \left(2 + \frac{1}{N_C^2} \frac{s^2}{tu} \right) \right. \right. \\
& \left. \left. + 2l(u) \left(N_C^2 \frac{t}{u} - \frac{s^2}{tu} \right) \right) \right], \tag{4.160}
\end{aligned}$$

$$\begin{aligned}
I_{qg \rightarrow qgg,1}(s, t, u) &= \left[2N_C \left(-\frac{1}{\varepsilon} \frac{1}{N_C} P_{g \leftarrow g}(z_a) \right. \right. \\
& \left. \left. + \delta(1-z_a) \left(\frac{1}{\varepsilon^2} + \frac{1}{\varepsilon} \frac{1}{N_C} \left(\frac{11}{6} N_C - \frac{1}{3} N_f \right) + \pi^2 \right) \right. \right. \\
& \left. \left. + 2 \ln \left(y_I \frac{1-z_a}{z_a} \right) \left(\frac{1}{z_a} + z_a(1-z_a) - 1 \right) \right) \right] T_{qg \rightarrow qg}(s, t, u)
\end{aligned}$$

$$\begin{aligned}
& -2N_C C_F \left[\left(\delta(1-z_a) \left(-\frac{2}{\varepsilon} l(t) + 2l(t) + l^2(t) \right) + 4R_+ \left(\left| \frac{t}{Q^2} \right| \right) \right. \right. \\
& -4l \left(t \left(\frac{1-z_a}{z_a} \right)^2 \right) - 4 \frac{z_a}{1-z_a} \ln \left(1 + \frac{|t|}{y_I Q^2} \frac{1-z_a}{z_a} \right) \\
& \left. \left(N_C^2 \frac{(s^2+u^2)^2}{ust^2} \right) \right. \\
& + \left(\delta(1-z_a) \left(-\frac{2}{\varepsilon} l(s) + 2l(s) + l^2(s) \right) + 4R_+ \left(\left| \frac{s}{Q^2} \right| \right) \right. \\
& -4l \left(s \left(\frac{1-z_a}{z_a} \right)^2 \right) - 4 \frac{z_a}{1-z_a} \ln \left(1 + \frac{|s|}{y_I Q^2} \frac{1-z_a}{z_a} \right) \\
& \left. \left(N_C^2 \left(\frac{u}{s} - \frac{2u^2}{t^2} \right) - \frac{u}{s} - \frac{s}{u} \right) \right. \\
& + \left(\delta(1-z_a) \left(-\frac{2}{\varepsilon} l(u) + 2l(u) + l^2(u) \right) + 4R_+ \left(\left| \frac{u}{Q^2} \right| \right) \right. \\
& -4l \left(u \left(\frac{1-z_a}{z_a} \right)^2 \right) - 4 \frac{z_a}{1-z_a} \ln \left(1 + \frac{|u|}{y_I Q^2} \frac{1-z_a}{z_a} \right) \\
& \left. \left(N_C^2 \left(\frac{s}{u} - \frac{2s^2}{t^2} \right) - \frac{u}{s} - \frac{s}{u} \right) \right. \\
& + \delta(1-z_a) \left(2l(t) N_C^2 \left(\frac{u}{s} + \frac{s}{u} \right) + 2l(s) \left(N_C^2 \frac{u}{s} - \frac{t^2}{su} \right) \right. \\
& \left. \left. + 2l(u) \left(N_C^2 \frac{s}{u} - \frac{t^2}{su} \right) \right) \right], \tag{4.161}
\end{aligned}$$

$$\begin{aligned}
I_{qg \rightarrow qgg,2}(s, t, u) &= \frac{1}{2} \left[-\frac{1}{\varepsilon} \frac{1}{C_F} P_{g \leftarrow q}(z_a) + \frac{1}{C_F} P_{g \leftarrow q}(z_a) \left(\ln \left(y_I \frac{1-z_a}{z_a} \right) + 1 \right) \right. \\
& \left. - 2 \frac{1-z_a}{z_a} \right] T_{gg \rightarrow gg}(s, t, u), \tag{4.162}
\end{aligned}$$

$$\begin{aligned}
I_{gg \rightarrow q\bar{q}g}(s, t, u) &= 2C_F \left[-\frac{1}{\varepsilon} P_{q \leftarrow g}(z_a) + P_{q \leftarrow g}(z_a) \left(\ln \left(y_I \frac{1-z_a}{z_a} \right) - 1 \right) + \frac{1}{2} \right] \\
& T_{qg \rightarrow qg}(s, t, u), \tag{4.163}
\end{aligned}$$

$$\begin{aligned}
I_{gg \rightarrow ggg}(s, t, u) &= \left[3N_C \left(-\frac{1}{\varepsilon} \frac{1}{N_C} P_{g \leftarrow g}(z_a) \right) \right. \\
& + \delta(1-z_a) \left(\frac{1}{\varepsilon^2} + \frac{1}{\varepsilon} \frac{1}{N_C} \left(\frac{11}{6} N_C - \frac{1}{3} N_f \right) + \pi^2 \right) \\
& \left. + 2 \ln \left(y_I \frac{1-z_a}{z_a} \right) \left(\frac{1}{z_a} + z_a(1-z_a) - 1 \right) \right] T_{gg \rightarrow gg}(s, t, u) \\
& + 12N_C^4 C_F \left[\left(\delta(1-z_a) \left(-\frac{2}{\varepsilon} l(t) + 4l(t) + l^2(t) \right) + 4R_+ \left(\left| \frac{t}{Q^2} \right| \right) \right. \right. \\
& -4l \left(t \left(\frac{1-z_a}{z_a} \right)^2 \right) - 4 \frac{z_a}{1-z_a} \ln \left(1 + \frac{|t|}{y_I Q^2} \frac{1-z_a}{z_a} \right) \\
& \left. \left(3 - \frac{2us}{t^2} + \frac{u^4+s^4}{u^2s^2} \right) \right. \\
& \left. + \left(\delta(1-z_a) \left(-\frac{2}{\varepsilon} l(u) + 4l(u) + l^2(u) \right) + 4R_+ \left(\left| \frac{u}{Q^2} \right| \right) \right) \right]
\end{aligned}$$

$$\begin{aligned}
& -4l\left(u\left(\frac{1-z_a}{z_a}\right)^2\right) - 4\frac{z_a}{1-z_a}\ln\left(1 + \frac{|u|}{y_I Q^2}\frac{1-z_a}{z_a}\right) \\
& \left(3 - \frac{2ts}{u^2} + \frac{t^4 + s^4}{t^2 s^2}\right) \\
& + \left(\delta(1-z_a)\left(-\frac{2}{\varepsilon}l(s) + 4l(s) + l^2(s)\right) + 4R_+\left(\left|\frac{s}{Q^2}\right|\right)\right) \\
& -4l\left(s\left(\frac{1-z_a}{z_a}\right)^2\right) - 4\frac{z_a}{1-z_a}\ln\left(1 + \frac{|s|}{y_I Q^2}\frac{1-z_a}{z_a}\right) \\
& \left(3 - \frac{2tu}{s^2} + \frac{t^4 + u^4}{t^2 u^2}\right) \Big]. \tag{4.164}
\end{aligned}$$

The absorption of the collinear poles $1/\varepsilon$ proportional to the different Altarelli-Parisi splitting functions is handled in a completely analogous way as in section 4.2.6 for proton initial state corrections. The only difference is that the poles are absorbed into the photon structure function and not the proton structure function. As always, we omit terms of higher order in ε and the invariant mass cut-off y .

4.2.8 Proton Initial State Corrections for Resolved Photons

Finally, the next-to-leading order $\mathcal{O}(\alpha_s^3)$ resolved photoproduction cross section receives also initial state corrections on the proton side. It is, however, not necessary to calculate these contributions again. The relevant diagrams in figure 18 are the same as in the last section as is the singularity structure in figure 15c). This is due to the fact that resolved photons behave like hadrons.

The proton initial state formulæ are obtained from those in section 4.2.7 by interchanging ($z'' \leftrightarrow z'''$) and ($z_a \leftrightarrow z_b$), so that we consider matrix elements that are singular in the variable

$$z''' = \frac{pbp_3}{p_a p_b}. \tag{4.165}$$

The parton b in the proton gives a fraction

$$z_b = \frac{p_1 p_2}{p_a p_b} \tag{4.166}$$

of its momentum to the $2 \rightarrow 2$ hard scattering process and the rest of $(1 - z_b)$ to particle 3 in the proton remnant. The list of approximated invariants is the same as in section 4.2.6 for proton initial state corrections of direct photons, and the list of contributing matrix elements is the same as in table 6.

The integration over the singular region of phase space gives

$$\int d\text{PS}^{(r)} |\mathcal{M}|_{ab \rightarrow 123}^2(s, t, u) = \int_{X_b}^1 \frac{dz_b}{z_b} g^4 \mu^{4\varepsilon} \frac{\alpha_s}{2\pi} \left(\frac{4\pi\mu^2}{Q^2}\right)^\varepsilon \frac{\Gamma(1-\varepsilon)}{\Gamma(1-2\varepsilon)} J_{ab \rightarrow 123}(s, t, u), \tag{4.167}$$

where the z_b -integration is done numerically to allow for inclusion of the proton structure function. The functions

$$J_{ab \rightarrow 123}(s, t, u) = I_{ab \rightarrow 123}(s, t, u) \tag{4.168}$$

are identical to those from the last chapter. For the IR singularities and finite contributions proportional to the $\delta(1 - z_b)$ -function, the integration can of course be carried out trivially. Thus, these singularities cancel against those from the virtual corrections for resolved photoproduction. The collinear singularities proportional to the Altarelli-Parisi splitting functions are now absorbed into the proton structure functions and not the photon structure functions as before.

4.2.9 Real Corrections for Direct $\gamma\gamma$ Scattering

Real corrections to direct $\gamma\gamma$ scattering arise through the radiation of a gluon off one of the quark lines in the underlying Born process $\gamma\gamma \rightarrow q\bar{q}$. This can be inferred from figure 19. The calculation

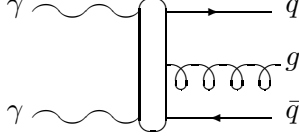


Figure 19: $2 \rightarrow 3$ Feynman diagram for direct $\gamma\gamma$ scattering.

of the final and initial state singular parts proceeds along the same lines as for direct and resolved photoproduction.

Let us first consider the final state singularity. There, the approximated matrix element

$$|\mathcal{M}|_{\gamma\gamma \rightarrow q\bar{q}g}^2(s, t, u) = e^4 e_q^4 g^2 \mu^{6\varepsilon} \frac{1}{sz'} 4C_F \left((1-b)(1-\varepsilon) - 2 + \frac{2}{z' + (1-b)} \right) T_{\gamma\gamma \rightarrow q\bar{q}}(s, t, u) \quad (4.169)$$

is integrated over the singular phase space to give

$$\int d\text{PS}^{(r)} |\mathcal{M}|_{\gamma\gamma \rightarrow 123}^2(s, t, u) = e^4 e_q^4 \mu^{4\varepsilon} \frac{\alpha_s}{2\pi} \left(\frac{4\pi\mu^2}{s} \right)^\varepsilon \frac{\Gamma(1-\varepsilon)}{\Gamma(1-2\varepsilon)} F_{\gamma\gamma \rightarrow 123}(s, t, u) \quad (4.170)$$

with

$$F_{\gamma\gamma \rightarrow q\bar{q}g}(s, t, u) = C_F \left(\frac{2}{\varepsilon^2} + \frac{3}{\varepsilon} - \frac{2\pi^2}{3} + 7 - 2\ln^2 y_F - 3\ln y_F \right) T_{\gamma\gamma \rightarrow q\bar{q}}(s, t, u). \quad (4.171)$$

Turning to the initial state, we find the approximated matrix element

$$|\mathcal{M}|_{\gamma\gamma \rightarrow q\bar{q}g}^2(s, t, u) = e^4 e_q^4 g^2 \mu^{6\varepsilon} \frac{1}{sz''} \left[z_a^2 + (1-z_a)^2 - \varepsilon \right] T_{\gamma q \rightarrow gq}(s, t, u). \quad (4.172)$$

After integration, this yields

$$\int d\text{PS}^{(r)} |\mathcal{M}|_{\gamma\gamma \rightarrow 123}^2(s, t, u) = \int_{X_a} \frac{dz_a}{z_a} e^4 e_q^2 \mu^{4\varepsilon} \frac{\alpha_s}{2\pi} \left(\frac{4\pi\mu^2}{s} \right)^\varepsilon \frac{\Gamma(1-\varepsilon)}{\Gamma(1-2\varepsilon)} I_{\gamma\gamma \rightarrow 123}(s, t, u) \quad (4.173)$$

with

$$I_{\gamma\gamma \rightarrow q\bar{q}g}(s, t, u) = \left[-\frac{1}{\varepsilon} \frac{1}{2N_C} P_{q\leftarrow\gamma}(z_a) + \frac{1}{2N_C} P_{q\leftarrow\gamma}(z_a) \ln \left(y_I \frac{1-z_a}{z_a} \right) + \frac{e_q^2}{2} \right] T_{\gamma q \rightarrow gq}(s, t, u). \quad (4.174)$$

The pole is proportional to the Altarelli-Parisi splitting function and is absorbed into the photon parton density.

4.3 Finite Next-To-Leading Order Cross Sections

We conclude this section with a summary of all singularities that appeared in the next-to-leading order cross section of jet photoproduction. There were three types of singularities:

- UV singularities in the virtual corrections

- IR singularities in the virtual and real corrections
- Collinear singularities in the initial state real corrections

All of them were regularized dimensionally by going from four to $d = 4 - 2\varepsilon$ dimensions, where the regulator ε had a positive sign for the ultraviolet (UV) and a negative sign for the infrared (IR) divergencies.

The ultraviolet divergencies were encountered in the calculation of the virtual diagrams in section 4.1. The diagrams had an additional inner “virtual” particle and were classified into self-energy diagrams, propagator corrections, box diagrams, and vertex corrections. The inner loop momenta could not be observed and had to be integrated up to infinity. The resulting UV singularities could be removed by renormalizing the fields, couplings, gauge parameters, and masses in the Lagrangian through multiplicative renormalization constants Z_i , which show up in perturbation theory as counter terms order by order in the strong coupling α_s . The counter terms were not given explicitly, so that all matrix element formulæ in section 4.1 are already UV-divergence free and all fields, couplings etc. have to be considered physical and renormalized. As an example, the counter term for the QCD Compton graph $\gamma q \rightarrow gq$ has the form

$$\begin{aligned}
|\mathcal{M}|_{\gamma q \rightarrow gq, CT}^2(s, t, u) &= e^2 e_q^2 g^2 \mu^{4\varepsilon} \frac{\alpha_s}{2\pi} \left(\frac{4\pi\mu^2}{s} \right)^\varepsilon \frac{\Gamma(1-\varepsilon)}{\Gamma(1-2\varepsilon)} \\
&\quad \left(\frac{1}{\varepsilon} + \ln \frac{s}{\mu^2} \right) \left(\frac{1}{3} N_f - \frac{11}{6} N_C \right) T_{\gamma q \rightarrow gq}(s, t, u)
\end{aligned} \tag{4.175}$$

in the $\overline{\text{MS}}$ scheme and leads to a logarithmic dependence of the cross section on the renormalization scale μ .

The second type of singularities, IR divergencies, were produced at the lower end of the loop integration in the virtual corrections and through soft or collinear real particle emission in the real corrections. They were written down explicitly throughout the last sections and have to cancel according to the Kinoshita-Lee-Nauenberg theorem [61]. We demonstrate this cancellation separately for direct and resolved photoproduction in tables 7 and 8 and for direct $\gamma\gamma$ scattering in table 9.

Process	Color Factor	NLO Correction	Singular Parts of Matrix Elements
$\gamma q \rightarrow gq$	C_F	Virtual Corr.	$\left[-\frac{2}{\varepsilon^2} - \frac{1}{\varepsilon}(3 - 2l(t)) \right] T_{\gamma q \rightarrow gq}(s, t, u)$
		Final State	$\left[+\frac{1}{\varepsilon^2} + \frac{1}{2\varepsilon}(3 - 2l(t)) \right] T_{\gamma q \rightarrow gq}(s, t, u)$
		Initial State	$\left[+\frac{1}{\varepsilon^2} + \frac{1}{2\varepsilon}(3 - 2l(t)) \right] T_{\gamma q \rightarrow gq}(s, t, u)$
	N_C	Virtual Corr.	$\left[-\frac{1}{\varepsilon^2} - \frac{1}{2\varepsilon} \left(\frac{11}{3} - 2l(s) + 2l(t) - 2l(u) \right) \right] T_{\gamma q \rightarrow gq}(s, t, u)$
		Final State	$\left[+\frac{1}{\varepsilon^2} + \frac{1}{2\varepsilon} \left(\frac{11}{3} - l(s) + l(t) - l(u) \right) \right] T_{\gamma q \rightarrow gq}(s, t, u)$
		Initial State	$\left[+\frac{1}{2\varepsilon} \left(-l(s) + l(t) - l(u) \right) \right] T_{\gamma q \rightarrow gq}(s, t, u)$
	N_f	Virtual Corr.	$+ \frac{1}{3\varepsilon} T_{\gamma q \rightarrow gq}(s, t, u)$
		Final State	$- \frac{1}{3\varepsilon} T_{\gamma q \rightarrow gq}(s, t, u)$

Table 7: Cancellation of IR singularities from virtual, final state, and initial state NLO corrections for the direct partonic subprocesses and different color factors.

There is only one generic $2 \rightarrow 2$ diagram $\gamma q \rightarrow gq$ in direct photoproduction as shown in figure 7, from which the photon-gluon fusion process can be deduced with the help of crossing relations. Therefore we show only this process in table 7, but for the three contributing color factors C_F , N_C , and N_f . The real corrections for the first two classes come from the process $\gamma q \rightarrow qgg$ and are equally

divided among final and initial state singularities. The last class, however, occurs only in the splitting of the final gluon into an additional quark-antiquark pair with N_f flavors. This is the reason why no initial state singularity is present here.

For resolved photoproduction, we have the four generic processes in figure 9. They are presented in table 8 and divided further into color factor classes. All other processes can be obtained through crossing. The real corrections for quark-quark scattering with different and like flavors arise simply from the emission of an additional gluon and factorize the complete Born matrix element. Final and initial state corrections contribute at equal parts. For processes involving more gluons, the situation is more complex. In $q\bar{q} \rightarrow gg$, an additional gluon leads to different color factors depending on whether it is radiated in the initial state (C_F) or the final state (N_C). A final gluon can also split up into N_f flavors accounting for half of the real corrections in the class N_f . The other half comes from the process $qg \rightarrow qgg$, where the initial gluon splits up into a quark-antiquark pair with N_f flavors. So far, the factorization property of $q\bar{q} \rightarrow gg$ holds. However, the logarithmic contributions to the emission of a third initial or final gluon in the color classes 1, $8N_C^3C_F$, and $8N_CN_C$ only factorize parts of the leading order cross section. In the completely gluonic process $gg \rightarrow gg$ it does not matter where the third gluon is radiated (color class N_C). Still, a final gluon can split up into N_f flavors or an initial gluon can have come from N_f different quarks. Finally, the logarithmic contributions proportional to $32N_C^4C_F$ only factorize parts of the Born cross section, but are symmetric under cyclic permutations of the Mandelstam variables as a completely symmetric process must be.

For direct $\gamma\gamma$ scattering, there is only one Born matrix element $\gamma\gamma \rightarrow q\bar{q}$ and only one color class C_F . The virtual singularities are canceled by the final state singularities alone as shown in table 9.

The third and last class of singularities are those in the initial state from collinear real particle emission. Although they are generally classified as infrared singularities as well, they are not included in the tables 7, 8, and 9 above. These single poles proportional to the Altarelli-Parisi splitting functions $P_{q\leftarrow q}(z)$, $P_{g\leftarrow q}(z)$, $P_{q\leftarrow g}(z)$, and $P_{g\leftarrow g}(z)$ do not cancel against similar poles from virtual corrections. They are absorbed into the renormalized photon and proton structure functions according to the $\overline{\text{MS}}$ scheme and leave behind a logarithmic dependence of the hard cross section on the factorization scales M_a and M_b .

The finite next-to-leading order cross section for the photoproduction of two jets was given in section 2.5 as

$$\frac{d^3\sigma}{dE_T^2 d\eta_1 d\eta_2} = \sum_b x_a F_{a/e}(x_a, M_a^2) x_b F_{b/p}(x_b, M_b^2) \frac{d\sigma}{dt}(ab \rightarrow p_1 p_2) \quad (4.176)$$

with the partonic cross section

$$\frac{d\sigma}{dt}(ab \rightarrow p_1 p_2) = \frac{1}{2s} |\mathcal{M}|^2 \frac{d\text{PS}^{(2)}}{dt}. \quad (4.177)$$

We can now return to the physical four dimensions letting $\varepsilon \rightarrow 0$ everywhere in the calculation. The strong coupling constant α_s and the parton densities in the electron $F_{a/e}(x_a, M_a^2)$ and in the proton $F_{b/p}(x_b, M_b^2)$ are renormalized and defined in the $\overline{\text{MS}}$ scheme.

5 Numerical Results for Photoproduction

In this section we present numerical results first for single and dijet NLO cross sections in complete photoproduction, as they were defined in section 2.5. We use the analytical results that have been calculated in leading order in section 3 and in next-to-leading order in section 4. All UV, IR, and collinear initial state singularities canceled or could be removed through a renormalization procedure, leading to finite results in four dimensions. Equivalent numerical results for single and dijet NLO cross sections in complete $\gamma\gamma$ collision are presented in the next chapter.

The cross section formulæ are implemented in a FORTRAN computer program, which consists of four main parts as explained in table 10. The first part contains the analytical results of sections

Process	Color Factor	NLO Correction	Singular Parts of Matrix Elements
$qq' \rightarrow qq'$	C_F	Virtual Corr. Final State Initial State	$\left. \begin{array}{l} -\frac{4}{\varepsilon^2} - \frac{1}{\varepsilon}(6 + 8l(s) - 8l(u) - 4l(t)) \\ +\frac{2}{\varepsilon^2} + \frac{1}{\varepsilon}(3 + 4l(s) - 4l(u) - 2l(t)) \\ +\frac{2}{\varepsilon^2} + \frac{1}{\varepsilon}(3 + 4l(s) - 4l(u) - 2l(t)) \end{array} \right\} \begin{array}{l} T_{qq' \rightarrow qq'}(s, t, u) \\ T_{qq' \rightarrow qq'}(s, t, u) \\ T_{qq' \rightarrow qq'}(s, t, u) \end{array}$
	N_C	Virtual Corr. Final State Initial State	$\left. \begin{array}{l} +\frac{1}{\varepsilon}(4l(s) - 2l(u) - 2l(t)) \\ -\frac{1}{\varepsilon}(2l(s) - l(u) - l(t)) \\ -\frac{1}{\varepsilon}(2l(s) - l(u) - l(t)) \end{array} \right\} \begin{array}{l} T_{qq' \rightarrow qq'}(s, t, u) \\ T_{qq' \rightarrow qq'}(s, t, u) \\ T_{qq' \rightarrow qq'}(s, t, u) \end{array}$
$qq \rightarrow qq$	C_F	Virtual Corr. Final State Initial State	$\left. \begin{array}{l} -\frac{4}{\varepsilon^2} - \frac{1}{\varepsilon}(6 + 4l(s) - 4l(t) - 4l(u)) \\ +\frac{2}{\varepsilon^2} + \frac{1}{\varepsilon}(3 + 2l(s) - 2l(t) - 2l(u)) \\ +\frac{2}{\varepsilon^2} + \frac{1}{\varepsilon}(3 + 2l(s) - 2l(t) - 2l(u)) \end{array} \right\} \begin{array}{l} T_{qq \rightarrow qq}(s, t, u) \\ T_{qq \rightarrow qq}(s, t, u) \\ T_{qq \rightarrow qq}(s, t, u) \end{array}$
	N_C	Virtual Corr. Final State Initial State	$\left. \begin{array}{l} +\frac{2}{\varepsilon}(2l(s) - l(t) - l(u)) \\ -\frac{1}{\varepsilon}(2l(s) - l(t) - l(u)) \\ -\frac{1}{\varepsilon}(2l(s) - l(t) - l(u)) \end{array} \right\} \begin{array}{l} T_{qq \rightarrow qq}(s, t, u) \\ T_{qq \rightarrow qq}(s, t, u) \\ T_{qq \rightarrow qq}(s, t, u) \end{array}$
$q\bar{q} \rightarrow gg$	C_F	Virtual Corr. Initial State	$\left. \begin{array}{l} -\frac{2}{\varepsilon^2} - \frac{3}{\varepsilon} \\ +\frac{2}{\varepsilon^2} + \frac{3}{\varepsilon} \end{array} \right\} \begin{array}{l} T_{q\bar{q} \rightarrow gg}(s, t, u) \\ T_{q\bar{q} \rightarrow gg}(s, t, u) \end{array}$
	N_C	Virtual Corr. Final State	$\left. \begin{array}{l} -\frac{2}{\varepsilon^2} - \frac{11}{3\varepsilon} \\ +\frac{2}{\varepsilon^2} + \frac{11}{3\varepsilon} \end{array} \right\} \begin{array}{l} T_{q\bar{q} \rightarrow gg}(s, t, u) \\ T_{q\bar{q} \rightarrow gg}(s, t, u) \end{array}$
	N_f	Virtual Corr. Final State Initial State	$\begin{array}{l} +\frac{2}{3\varepsilon} T_{q\bar{q} \rightarrow gg}(s, t, u) \\ -\frac{1}{3\varepsilon} T_{q\bar{q} \rightarrow gg}(s, t, u) \\ -\frac{1}{3\varepsilon} T_{q\bar{q} \rightarrow gg}(s, t, u) \end{array}$
	1	Virtual Corr. Final State Initial State	$\begin{array}{l} +\frac{1}{\varepsilon} l(s) \left(\left(4N_C^3 C_F + \frac{4C_F}{N_C} \right) \frac{t^2+u^2}{tu} - 16N_C^2 C_F^2 \frac{t^2+u^2}{s^2} \right) \\ -\frac{1}{2\varepsilon} l(s) \left(\left(4N_C^3 C_F + \frac{4C_F}{N_C} \right) \frac{t^2+u^2}{tu} - 16N_C^2 C_F^2 \frac{t^2+u^2}{s^2} \right) \\ -\frac{1}{2\varepsilon} l(s) \left(\left(4N_C^3 C_F + \frac{4C_F}{N_C} \right) \frac{t^2+u^2}{tu} - 16N_C^2 C_F^2 \frac{t^2+u^2}{s^2} \right) \end{array}$
	$8N_C^3 C_F$	Virtual Corr. Final State Initial State	$\begin{array}{l} +\frac{1}{\varepsilon} \left(l(t) \left(\frac{u}{t} - \frac{2u^2}{s^2} \right) + l(u) \left(\frac{t}{u} - \frac{2t^2}{s^2} \right) \right) \\ -\frac{1}{2\varepsilon} \left(l(t) \left(\frac{u}{t} - \frac{2u^2}{s^2} \right) + l(u) \left(\frac{t}{u} - \frac{2t^2}{s^2} \right) \right) \\ -\frac{1}{2\varepsilon} \left(l(t) \left(\frac{u}{t} - \frac{2u^2}{s^2} \right) + l(u) \left(\frac{t}{u} - \frac{2t^2}{s^2} \right) \right) \end{array}$
	$8N_C C_F$	Virtual Corr. Final State Initial State	$\begin{array}{l} -\frac{1}{\varepsilon} \left(\frac{u}{t} + \frac{t}{u} \right) (l(t) + l(u)) \\ +\frac{1}{2\varepsilon} \left(\frac{u}{t} + \frac{t}{u} \right) (l(t) + l(u)) \\ +\frac{1}{2\varepsilon} \left(\frac{u}{t} + \frac{t}{u} \right) (l(t) + l(u)) \end{array}$
$gg \rightarrow gg$	N_C	Virtual Corr. Final State Initial State	$\left. \begin{array}{l} -\frac{4}{\varepsilon^2} - \frac{22}{3\varepsilon} \\ +\frac{2}{\varepsilon^2} + \frac{11}{3\varepsilon} \\ +\frac{2}{\varepsilon^2} + \frac{11}{3\varepsilon} \end{array} \right\} \begin{array}{l} T_{gg \rightarrow gg}(s, t, u) \\ T_{gg \rightarrow gg}(s, t, u) \\ T_{gg \rightarrow gg}(s, t, u) \end{array}$
	N_f	Virtual Corr. Final State Initial State	$\begin{array}{l} +\frac{4}{3\varepsilon} T_{gg \rightarrow gg}(s, t, u) \\ -\frac{2}{3\varepsilon} T_{gg \rightarrow gg}(s, t, u) \\ -\frac{2}{3\varepsilon} T_{gg \rightarrow gg}(s, t, u) \end{array}$
	$32N_C^4 C_F$	Virtual Corr. Final State Initial State	$\begin{array}{l} +\frac{1}{\varepsilon} \left(l(s) \left(3 - 2\frac{tu}{s^2} + \frac{t^4+u^4}{t^2u^2} \right) + \text{cycl. perm.} \right) \\ -\frac{1}{2\varepsilon} \left(l(s) \left(3 - 2\frac{tu}{s^2} + \frac{t^4+u^4}{t^2u^2} \right) + \text{cycl. perm.} \right) \\ -\frac{1}{2\varepsilon} \left(l(s) \left(3 - 2\frac{tu}{s^2} + \frac{t^4+u^4}{t^2u^2} \right) + \text{cycl. perm.} \right) \end{array}$

Table 8: Cancellation of IR singularities from virtual, final state, and initial state NLO corrections for the resolved partonic subprocesses and different color factors.

Process	Color Factor	NLO Correction	Singular Parts of Matrix Elements
$\gamma\gamma \rightarrow q\bar{q}$	C_F	Virtual Corr.	$-\frac{2}{\varepsilon^2} - \frac{1}{\varepsilon}(3 - 2l(t))$
		Final State	$+\frac{2}{\varepsilon^2} + \frac{1}{\varepsilon}(3 - 2l(t))$

Table 9: *Cancellation of IR singularities from virtual and final state NLO corrections for direct $\gamma\gamma$ scattering.*

Part No.	Number of Jets	Contributions
1	2	Analytical contributions in LO and NLO
2	2	Numerical contributions in jet cone 1
3	2	Numerical contributions in jet cone 2
4	3	Numerical contributions outside jet cones

Table 10: *Organization of the FORTRAN program into four main parts.*

3 and 4, and the numerical parts are needed for an implementation of the Snowmass jet definition (see section 5.1). Obviously, the third part is only needed for two-jet cross sections. For one-jet cross sections, this region of phase space is included in part four.

The main task of the computer program is to integrate over different parameters. For example, total or partly differential cross sections are integrated over E_T , η_1 and/or η_2 . Furthermore, the momentum fractions of the initial photon in the electron x_a , the parton in the photon y_a , and the parton in the proton x_b have to be integrated. Additional momentum fractions z_a and z_b appear in the initial state corrections. Finally, the numerical contributions have to be integrated over the phase space of the third parton E_{T_3} , η_3 , and ϕ_3 . The two δ -functions for the momentum fractions of the partons going into the hard $2 \rightarrow 2$ scattering X_a and X_b ,

$$\delta\left(X_a - \frac{1}{2E_e} \sum_i E_{T_i} e^{-\eta_i}\right) \text{ and } \delta\left(X_b - \frac{1}{2E_p} \sum_i E_{T_i} e^{\eta_i}\right), \quad (5.1)$$

reduce the total number of integrations by two. The non-trivial task of computing up to seven-dimensional integrals is solved with the Monte Carlo routine VEGAS written by G.P. Lepage [72], which adapts the spacing of the integration bins to the size of the integrand in the bin.

The input parameters for our predictions will be kept constant throughout this chapter, if not stated otherwise. All cross sections are for HERA conditions, where electrons of energy $E_e = 26.7$ GeV collide with protons of energy $E_p = 820$ GeV. Positive rapidities η correspond to the proton direction. We use the Weizsäcker-Williams approximation of eq. (2.13) with $Q_{\max}^2 = 4$ GeV² as in the ZEUS experiment, but do not restrict the range of longitudinal photon momentum x_a in the electron. For the parton densities in the proton, we choose the next-to-leading order parametrization CTEQ3 in the $\overline{\text{MS}}$ scheme, which already includes HERA deep inelastic scattering data. The corresponding Λ value of $\Lambda^{(4)} = 239$ MeV is also used in the two-loop calculation of the strong coupling constant α_s with four flavors. We do not use the one-loop approximation for leading order calculations, because the effects of the next-to-leading order hard scattering contributions are then isolated. The parton densities in the photon are taken from the NLO fit of GRV and transformed from the DIS_γ into the $\overline{\text{MS}}$ scheme. The renormalization and factorization scales are equal to E_T . We use the Snowmass jet definition with $R = 1$, no jet double counting, and no R_{sep} parameter. This makes the cross sections independent of the phase space slicing parameter y , which is fixed at $y = 10^{-3}$. This value is sufficiently small to justify the omission of $\mathcal{O}(y)$ terms in the analytical calculation (see section 5.1).

In section 5.1, we check our analytical results with respect to y -cut independence and with two different existing programs for direct and resolved one-jet production. Section 5.2 contains studies of the dependence of the cross sections on renormalization and factorization scales and on various cancellation mechanisms. Theoretical predictions for one- and two-jet cross sections are presented in sections 5.3 and 5.4, before we conclude this section with a comparison of our calculation to data from the H1 and ZEUS collaborations in section 5.5.

5.1 Check of the Analytical Results

The first check of our analytical results for the photoproduction of jets in next-to-leading order of QCD has already been given in section 4.3. There it has been shown that all infrared divergencies cancel in a consistent way between the virtual and the real corrections, giving a finite cross section in four dimensions. We have therefore missed none of the singular terms. This cancellation mechanism could only work since we integrated the $2 \rightarrow 3$ matrix elements over regions, where two final state particles or an initial and a final state particle had an invariant mass $s_{ij} = (p_i + p_j)^2$ smaller than a fraction $y_{F,I,J}$ of the center-of-mass energy s . Naturally, this leads to a dependence of the cross sections on these phase space slicing parameters $y_{F,I,J}$. We choose $y_{\text{cut}} = y_F = y_I = y_J$ in the following.

One possibility to deal with the dependence of the cross section on the invariant mass cut-off y_{cut} is to use it as a definition for the experimentally observed jets. As we noted already in section 2.4, the experimental jet definition has only a correspondence in theory beyond the leading order. Furthermore, we mentioned a special kind of algorithm, i.e. the JADE cluster algorithm, which uses exactly the invariant mass criterion to cluster hadrons into jets. For e^+e^- -experiments, one can then identify the theoretical (partonic) with the experimental (hadronic) cut-off

$$y_{\text{cut}}^{\text{theory}} = y_{\text{cut}}^{\text{experiment}}. \quad (5.2)$$

In this case, the corresponding cross sections are for *exclusive* dijet production.

The numerical value of y_{cut} is constrained in a two-fold manner. First, the real corrections contain simple and quadratic logarithmic terms $\ln y_{\text{cut}}$, $\ln^2 y_{\text{cut}}$, coming from the single and quadratic $1/\varepsilon$ poles, which force the cross section to become negative for $y_{\text{cut}} < 10^{-2}$. Therefore one should choose $y_{\text{cut}} \geq 10^{-2}$. Second, we have always assumed the singular region to be small in the real corrections. This means we have omitted terms like $y_{\text{cut}} \ln y_{\text{cut}}$, y_{cut} , ... This forces us to take $y_{\text{cut}} \ll 1$. The typical value for the JADE algorithm is therefore given by $y_{\text{cut}} \simeq 10^{-2}$.

The omitted terms of $\mathcal{O}(y_{\text{cut}})$ can be calculated numerically to improve the precision of the calculation. This makes it necessary to include the full and un-approximated $2 \rightarrow 3$ matrix elements in the FORTRAN program, which are then integrated numerically in the region between the analytical cut-off $y_{\text{cut}}^{\text{theory}}$ and the experimental cut-off $y_{\text{cut}}^{\text{experiment}}$. It is important to note that the full $2 \rightarrow 3$ matrix elements have to be integrated *after partial fractioning*. Regions, where a single invariant is small but is not a pole in the matrix element, cannot be neglected. The theoretical invariant mass cut is then reduced to a purely technical variable, on which the physical prediction will no more depend. If one integrates over the phase space outside the experimental cut-off as well, one arrives at *inclusive* dijet cross sections. In this case, the full $2 \rightarrow 3$ matrix elements contribute as a leading-order process through the production of three jets, where the third jet is unobserved.

At HERA, we have to deal with a partly hadronic process, for which cluster algorithms are not so well suited. We will therefore follow the two experiments H1 and ZEUS and use the Snowmass cone algorithm, where hadrons i are combined into a single jet, if they lie inside a cone in azimuth-rapidity space from the jet center. The experimental cone size R was already defined in section 2.4

$$R_i = \sqrt{(\eta_i - \eta_J)^2 + (\phi_i - \phi_J)^2} \leq R \quad (5.3)$$

and will be chosen to be $R = 1$ in the following. As R takes the role of $y_{\text{cut}}^{\text{experiment}}$, we expect the sum of the analytical two-body and numerical three-body cross sections to be independent of $y_{\text{cut}}^{\text{theory}}$. This is the second decisive test of our analytical results.

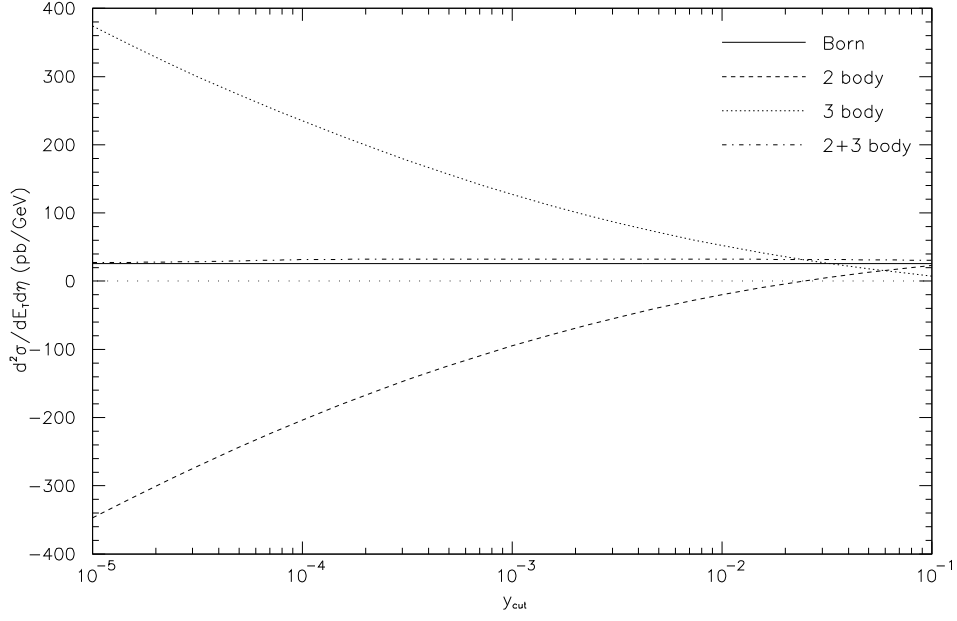


Figure 20: *Inclusive single-jet cross section $d^2\sigma/dE_T d\eta$ for direct photons at $E_T = 20$ GeV and $\eta = 1$, as a function of y_{cut} . The analytical (dashed) and numerical (dotted) contributions have a quadratic logarithmic dependence on y_{cut} , which cancels in the full next-to-leading order result (dot-dashed curve).*

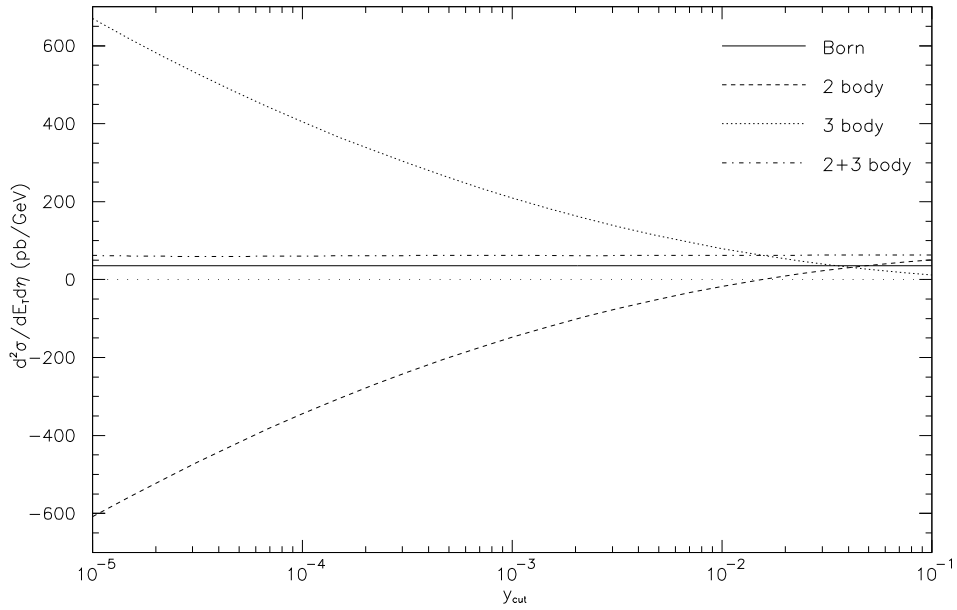


Figure 21: *Inclusive single-jet cross section $d^2\sigma/dE_T d\eta$ for resolved photons at $E_T = 20$ GeV and $\eta = 1$, as a function of y_{cut} . Again the sum of two-body (dashed) and three-body (dotted) curves is y_{cut} -independent (dot-dashed curve) like the leading order (full) curve.*

In figure 20 we plot the inclusive single-jet cross section $d^2\sigma/dE_T d\eta$ for direct photons at $E_T = 20$ GeV and $\eta = 1$ as a function of y_{cut} . The leading order prediction (full curve) is trivially independent of y_{cut} . The analytical two-body contributions (dashed curve) exhibit a quadratic logarithmic dependence on y_{cut} and turn negative below $y_{\text{cut}} = 2.3 \cdot 10^{-2}$. We add the numerical contributions inside and outside the jet cone into the three-body contributions (dotted curve), which are also quadratically logarithmically dependent on y_{cut} , but positive. The sum of two- and three-body contributions is the full inclusive next-to-leading order result (dot-dashed curve) and is independent of y_{cut} . This proves that the y_{cut} -dependent finite terms in our analytical results are correct. Towards very small values of $y_{\text{cut}} \simeq 10^{-5}$, the dot-dashed curve drops slightly. This is due to the limited accuracy in the numerical integration of the three-body contributions and can be remedied with increased computer power.

Figure 21 is the analogue to figure 20 for resolved photoproduction. The two-body curve turns negative at a slightly smaller value of $y_{\text{cut}} = 1.5 \cdot 10^{-2}$. As the number of contributing partonic subprocesses is much larger than in the direct case, more computer time was needed for similar statistical accuracy.

The ultimate test for our analytical and numerical results consists in the comparison of our prediction with existing predictions, that were obtained by Bödeker [53] (direct case) and by Salesch [73] (resolved case) with different methods. This can only be done for the single-jet inclusive cross section $d^2\sigma/dE_T d\eta$, since dijet cross sections are not available. Bödeker's results are obtained with the subtraction method of Ellis et al. [58] to cancel soft and collinear singularities. Salesch calculated finite cone corrections in addition to the results by Aversa et al. [74], who used the so-called small cone approximation. Here, a small jet cone radius δ is used to slice the phase space and isolate the final state divergencies. The dependence on δ cancels, when the finite cone corrections are added. We take exactly the same parameters in our calculation and in the reference calculations. Furthermore, we choose $y_{\text{cut}} = 10^{-3}$ to ensure that we are not sensitive to the omission of terms of $\mathcal{O}(y_{\text{cut}})$.

The E_T dependence is checked in figure 22 with Bödeker for direct photons and in figure 23 with Salesch for resolved photons at $\eta = 1$. Our prediction (full curve) agrees with the older calculations (open circles) at a level better than 1%. The numerical statistics are so good that the error bars in Bödeker's and Salesch's programs are not seen. For comparison, we include the leading order dotted curves, where the predictions are identical.

We compare the same inclusive single-jet cross section as a rapidity distribution for $E_T = 20$ GeV. We choose now a linear scale for the ordinate in figures 24 for direct and 25 for resolved photoproduction. This makes it possible to see the error bars in the reference calculations (open circles) which are at the same level as the agreement between the different programs. Errors of $\sim 1\%$ present in our program are not shown. With more computer time, the agreement would certainly be even better.

From these comparisons, we conclude that also the cut-independent finite terms in our analytical results and in our numerical FORTRAN program are correct. Even more, it was possible to check the transverse energy, rapidity, and other distributions not shown here for every single direct and resolved partonic subprocess. We found perfect agreement everywhere.

It is clear that the results presented in this work can also be applied to the calculation of inclusive jet cross sections in $p\bar{p}$ collisions by just replacing the photon parton distributions with those of the antiproton and considering only the resolved case. We could have extended our tests further by comparing with published results for the $p\bar{p}$ case. Such results have been given in [58] using the subtraction method and in [96] based on the phase-space slicing method. In connection with work on the large transverse momentum production of single inclusive jets in $p\bar{p}$ collisions [97], in which the program based on [73] was used, we compared with results from [58] and found good agreement. A comparison with the two-jet results in [96] has not been attempted.

After completion of this work, two new complete calculations of jet production in low Q^2 ep collisions have been presented. In [98], the subtraction method for canceling infrared and collinear singularities was applied to obtain various inclusive one- and two-jet cross sections. These authors compared inclusive single-jet and two-jet cross sections with our published results [12] and found good

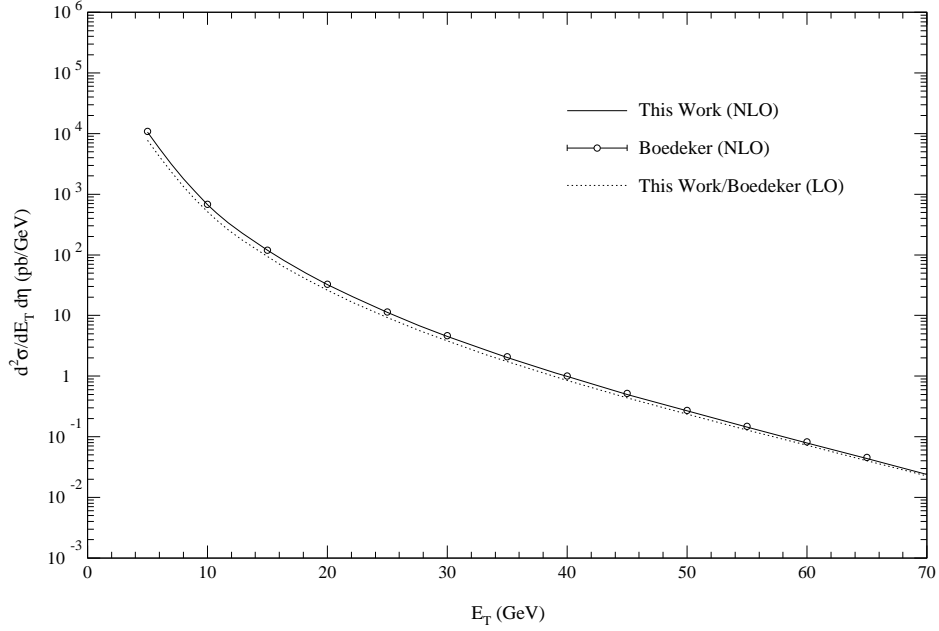


Figure 22: *Inclusive single-jet cross section $d^2\sigma/dE_T d\eta$ for direct photons at $\eta = 1$, as a function of E_T . The subtraction method results (open circles) agree with our phase space slicing prediction (full curve).*

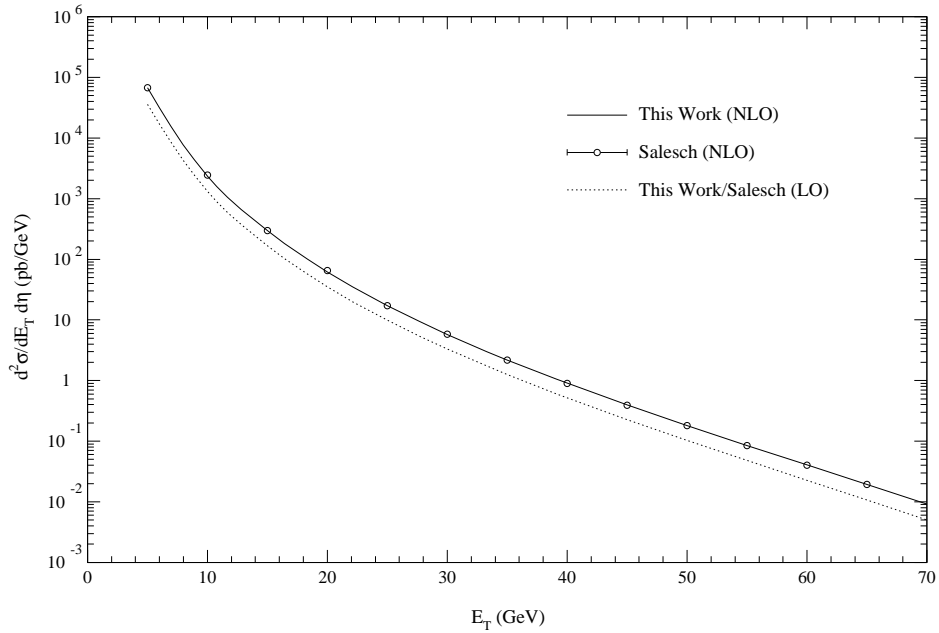


Figure 23: *Inclusive single-jet cross section $d^2\sigma/dE_T d\eta$ for resolved photons at $\eta = 1$, as a function of E_T . The small cone approximation and finite cone corrections (open circles) agree with our invariant mass cut method (full curve). The leading order (dotted) curve is shown for comparison.*

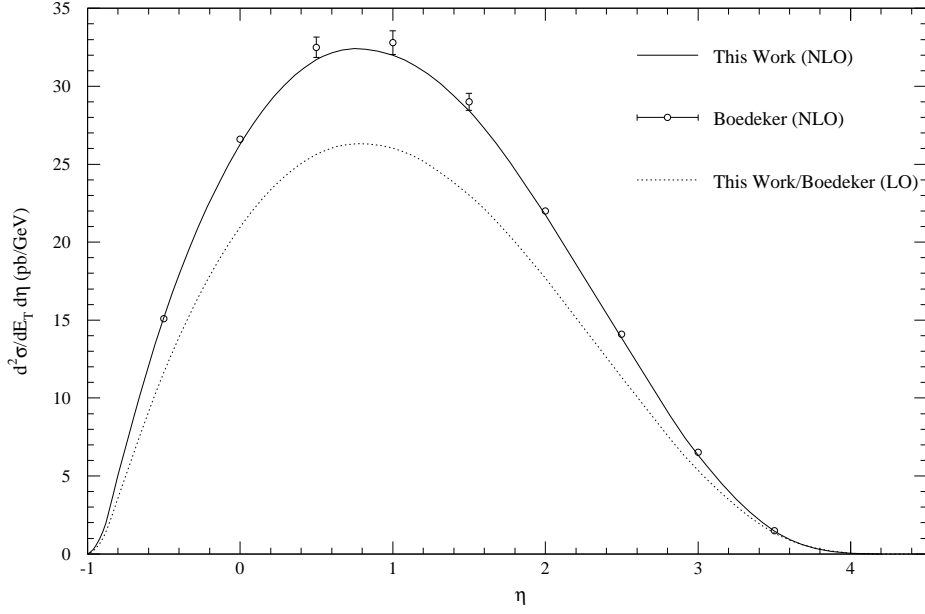


Figure 24: *Inclusive single-jet cross section $d^2\sigma/dE_T d\eta$ for direct photons at $E_T = 20$ GeV, as a function of η . Our predictions (full curve) agree with Bödeker's predictions (open circles).*

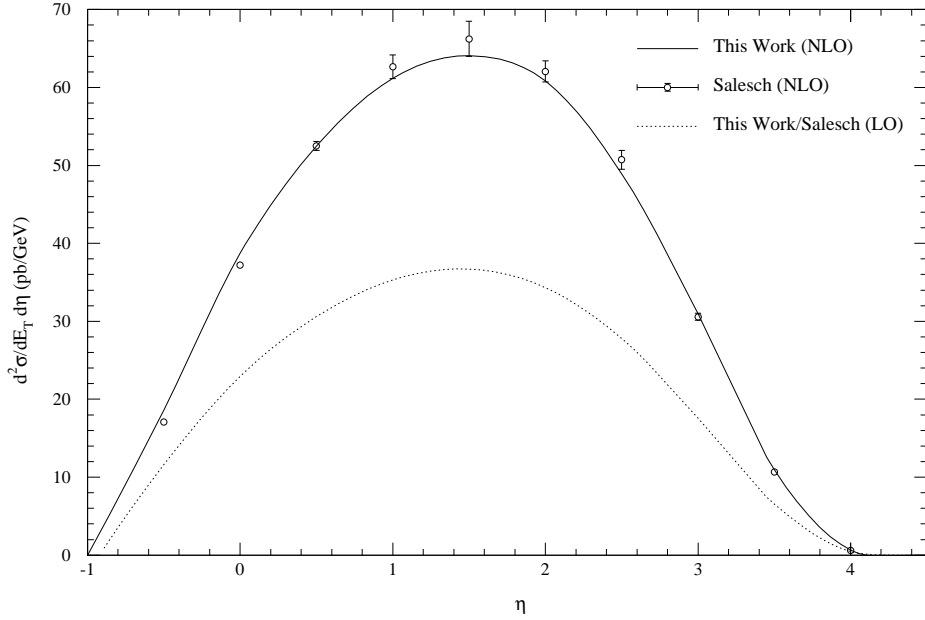


Figure 25: *Inclusive single-jet cross section $d^2\sigma/dE_T d\eta$ for resolved photons at $E_T = 20$ GeV, as a function of η . Good agreement is seen for Salesch's (open circles) and our calculation (full curve). The leading order (dotted) curve is shown for comparison.*

agreement [98]. Another work [99] uses also the phase-space slicing method, but with two separate parameters for the infrared and the collinear singular regions as in their earlier work [52]. Their results compare to our results in [12]. A direct thorough comparison of the results obtained with the same input has not been done yet.

5.2 Renormalization- and Factorization-Scale Dependences

From the numerical checks in section 5.1, we can now be sure to have a reliable computer program for the calculation of jet cross sections in photoproduction. We will use this program here to study the dependence of these cross sections on the three relevant scales:

- the renormalization scale μ
- the factorization scale for the photon M_a
- the factorization scale for the proton M_b

We expect a reduced dependence in next-to-leading order for all three scales with respect to the leading order. As stated in sections 4.1, 2.2, and 2.3, we take μ , M_a , and M_b to be of $\mathcal{O}(E_T)$. Therefore, we will always plot the single-jet inclusive cross section $d^2\sigma/dE_T d\eta$ as a function of scale/E_T in the following. Direct and resolved photoproduction will be presented separately at a fixed transverse jet energy of $E_T = 20$ GeV and at a rapidity of $\eta = 1$, where the cross sections are at their maximum.

We start with the dependence on the renormalization scale μ . Leading order $\mathcal{O}(\alpha\alpha_s)$ cross sections depend on μ only through the running of the strong coupling constant $\alpha_s(\mu^2)$, which has to be implemented in the one-loop approximation

$$\alpha_s(\mu^2) = \frac{12\pi}{(33 - 2N_f) \ln \frac{\mu^2}{\Lambda^2}} \quad (5.4)$$

for consistency. The results are shown as dotted curves in figures 26 and 27. For direct photons, the curve drops by one half when going from $\mu = 1/4E_T$ to $\mu = 4E_T$. The resolved photon hard cross section is one order higher in α_s ($\mathcal{O}(\alpha_s^2)$) and therefore drops even by a factor of four. This strong $1/\ln(\mu^2)$ -behavior is slightly weakened in the two-loop approximation

$$\alpha_s(\mu^2) = \frac{12\pi}{(33 - 2N_f) \ln \frac{\mu^2}{\Lambda^2}} \left(1 - \frac{6(153 - 19N_f) \ln(\ln \frac{\mu^2}{\Lambda^2})}{(33 - 2N_f)^2 \ln \frac{\mu^2}{\Lambda^2}} \right), \quad (5.5)$$

where one adds further logarithmic terms in μ^2 . These curves are shown in dashed form in figures 26 and 27. However, going from one-loop to two-loop α_s affects not so much the shape but the overall normalization. The cross sections are reduced by 20% in the direct and by almost 40% in the resolved case. Although not physically relevant, the dashed curves can be compared to the full curves and enable us to see solely the effect of the explicit logarithmic terms

$$\frac{1}{\varepsilon} \left(\frac{4\pi\mu^2}{s} \right)^\varepsilon \doteq \frac{1}{\varepsilon} + \ln \frac{4\pi\mu^2}{s}, \quad (5.6)$$

that appear in the one-loop corrections to the hard cross section in section 4.1. They cancel partly the α_s -dependence, so that the full curves in figures 26 and 27 are much flatter compared to the leading order curves with one- and two-loop α_s . The direct curve varies by only 20% and exhibits a maximum near $\mu/E_T \simeq 1/2$. According to the principle of minimal sensitivity [75], $\mu = 1/2E_T$ would then be the optimal scale. The dependence of the resolved photoproduction cross section is also weakened and amounts to a factor of two in NLO. It meets the one-loop LO result at $\mu \simeq 1/2E_T$. This scale is sometimes preferred since the NLO corrections are small in its vicinity.

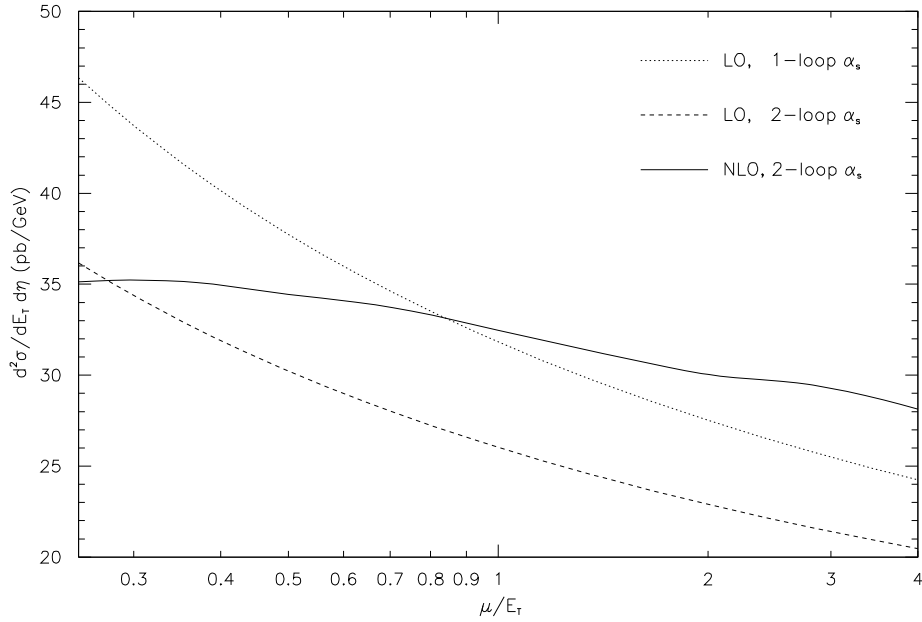


Figure 26: *Inclusive single-jet cross section $d^2\sigma/dE_T d\eta$ for direct photons at $E_T = 20$ GeV and $\eta = 1$, as a function of μ/E_T . From $\mu = 1/4E_T$ to $\mu = 4E_T$, the leading order predictions drop by one half. The two-loop curve (dashed) is 20% smaller than the one-loop curve (dotted). The next-to-leading order (full) curve only varies by 20%.*

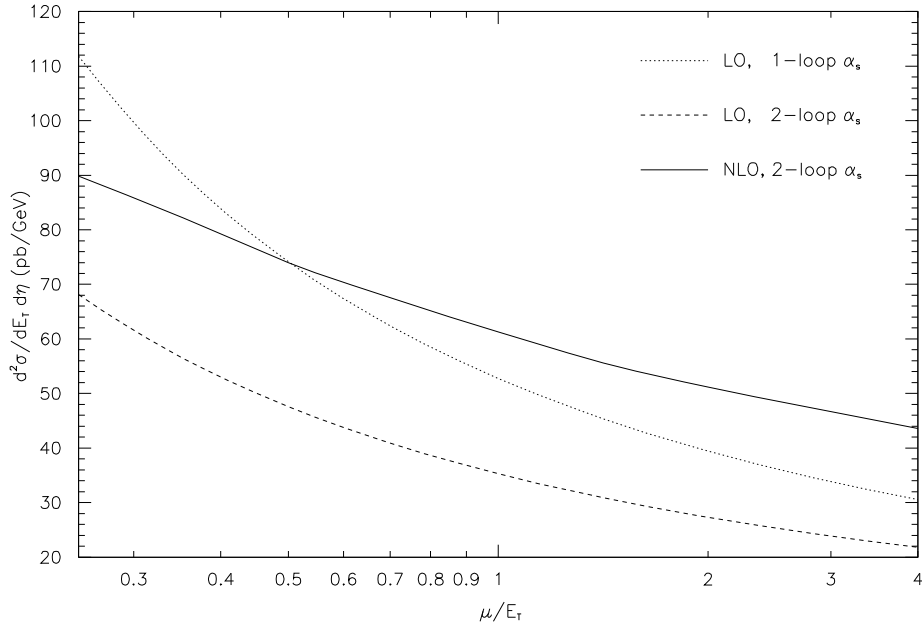


Figure 27: *Inclusive single-jet cross section $d^2\sigma/dE_T d\eta$ for resolved photons at $E_T = 20$ GeV and $\eta = 1$, as a function of μ/E_T . From $\mu = 1/4E_T$ to $\mu = 4E_T$, the leading order predictions drop by a factor of four. The two-loop curve (dashed) is 40% smaller than the one-loop curve (dotted). The next-to-leading order (full) curve only varies by a factor of two.*

The next scale that we will study is the factorization scale in the photon M_a . It separates the soft parton content in the photon given by the parton distribution function $F_{a/\gamma}(y_a, M_a^2)$ from the hard partonic cross section $d\sigma_{ab}(ab \rightarrow \text{jets})$. As discussed in section 2.3, direct and resolved processes are only separable in leading order. The direct parton distribution is then simply a δ -function $\delta(1 - y_a)$ and does not depend on any scale. This can be seen from the dotted curve in figure 28. The resolved part depends, however, strongly on the scale M_a as could already be inferred from e^+e^- -data on the F_2^γ structure function. We expect the M_a -dependence to be dominated by the asymptotic pointlike contribution to F_2^γ

$$F_2^\gamma(x_B, M_a^2) = \alpha \left[\frac{1}{\alpha_s(M_a^2)} a(x_B) + b(x_B) \right] \quad (5.7)$$

that behaves like $\ln M_a^2$. Clearly we see this behavior in the leading order dot-dashed curve in figure 28, which is identical to the dotted curve in figure 29 and is obtained with the GRV photon distributions. As the GRV distributions are fitted in the DIS_γ -scheme, we transform them into the $\overline{\text{MS}}$ scheme by adding the correct finite terms independent of M_a . The renormalization scheme dependence was studied by Bodeker, Kramer, and Salesch [76] and will not be studied here again. The main result is that the dependence disappears in next-to-leading order, because the transformation of the resolved part is compensated through scheme dependent terms in the initial state singularities of the direct photon. The renormalization of the singularities in section 4.2.5

$$F_{a/\gamma}(y_a, M_a^2) = \int_{y_a}^1 \frac{dz_a}{z_a} \left[\delta_{a\gamma} \delta(1 - z_a) + \frac{\alpha}{2\pi} R_{q\leftarrow\gamma}(z_a, M_a^2) \right] F_{\gamma/\gamma} \left(\frac{y_a}{z_a} \right) \quad (5.8)$$

gave also rise to scale dependent terms

$$R_{q\leftarrow\gamma}(z_a, M_a^2) = -\frac{1}{\varepsilon} P_{q\leftarrow\gamma}(z_a) \frac{\Gamma(1 - \varepsilon)}{\Gamma(1 - 2\varepsilon)} \left(\frac{4\pi\mu^2}{M_a^2} \right)^\varepsilon \quad (5.9)$$

through the $1/\varepsilon$ pole

$$-\frac{1}{\varepsilon} P_{q\leftarrow\gamma}(z_a) \left[\left(\frac{4\pi\mu^2}{s} \right)^\varepsilon - \left(\frac{4\pi\mu^2}{M_a^2} \right)^\varepsilon \right] = -P_{q\leftarrow\gamma}(z_a) \ln \left(\frac{M_a^2}{s} \right). \quad (5.10)$$

We can see this negative logarithmic behavior ($-\ln M_a^2$) in the dashed curve in figure 28 for next-to-leading order direct photoproduction. It has the opposite sign than the LO resolved contribution, so that the sum of both will eventually be almost independent of M_a (full curve in figure 28). The next-to-leading order resolved contribution has a similar, but slightly steeper shape than the leading order and is shown as a full curve in figure 29. Therefore, the dependence of the complete NLO calculation on the photon factorization scale is slightly stronger than in the full line of figure 28. The difference will be compensated in next-to-next-to-leading order (NNLO) of direct photoproduction, which is beyond the scope of our calculation. These findings agree with the earlier analysis of the M_a dependence of the inclusive single-jet cross sections in [76] and constitute a nice check of our formalism.

For the proton, we have a similar scale M_b as in the photon case that separates the soft and the hard part of the hadronic and partonic cross sections. Of course, the proton is not point-like and does not have a direct component. The scale dependence of the proton distribution functions $F_{b/p}(x_b, M_b^2)$ is governed by the AP equations. If we solve them iteratively, we can assume that in

$$\frac{dF_{b/p}(x_b, M_b^2)}{d \ln M_b^2} = \frac{\alpha_s^{(0)}}{2\pi} \int_{x_b}^1 \frac{dz_b}{z_b} P_{b\leftarrow b'} \left(\frac{x_b}{z_b} \right) F_{b'/p}^{(0)}(z_b) \quad (5.11)$$

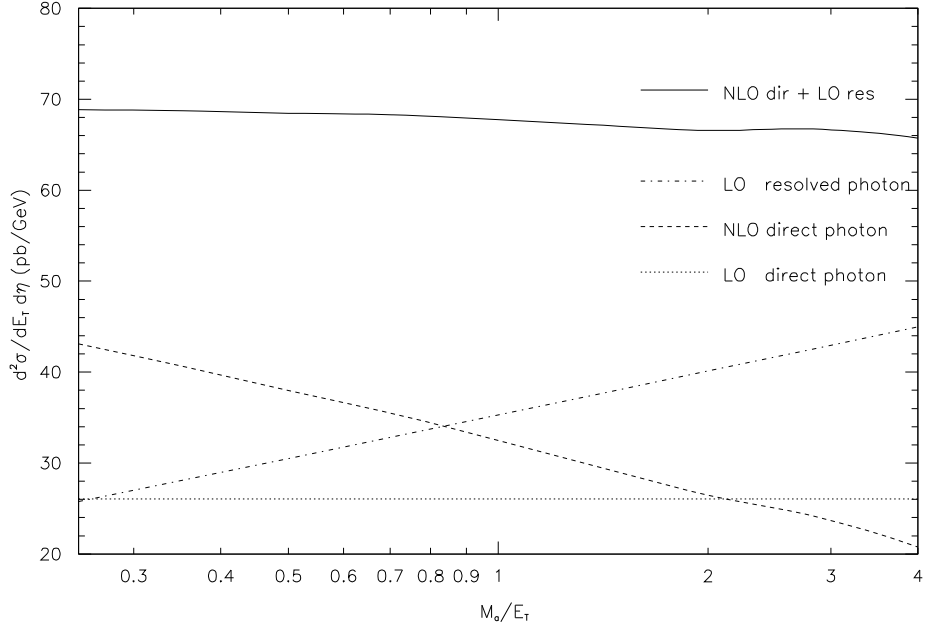


Figure 28: *Inclusive single-jet cross section $d^2\sigma/dE_T d\eta$ for direct photons at $E_T = 20$ GeV and $\eta = 1$, as a function of M_a/E_T . The LO direct curve (dotted) is independent of M_a as is the sum (full curve) of NLO direct (dashed) and LO resolved (dot-dashed) contributions.*

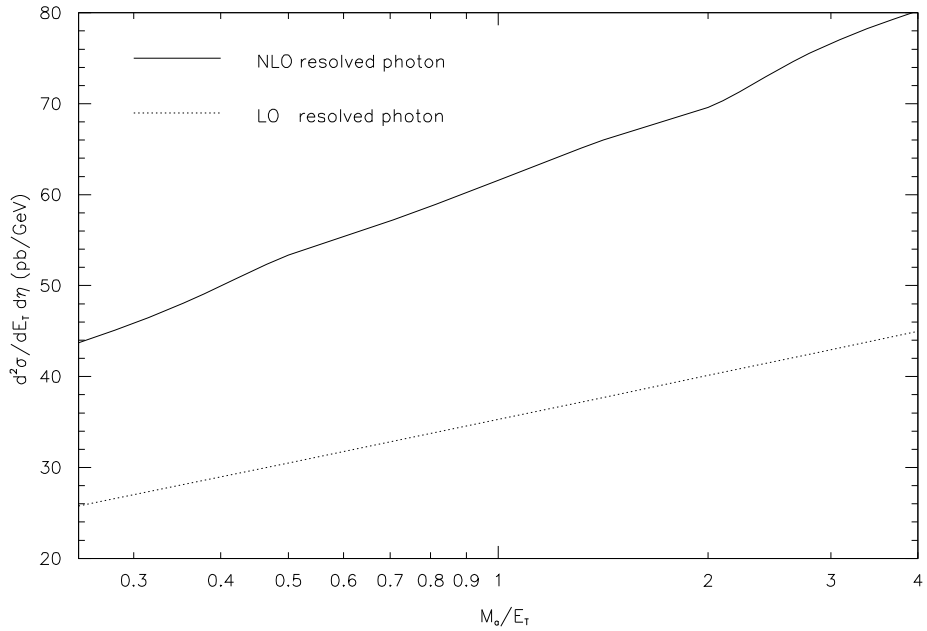


Figure 29: *Inclusive single-jet cross section $d^2\sigma/dE_T d\eta$ for resolved photons at $E_T = 20$ GeV and $\eta = 1$, as a function of M_a/E_T . The logarithmic behavior of the resolved part is slightly steeper in NLO (full curve) than in LO (dotted curve).*

the starting distributions $F_{b/p}^{(0)}(z_b)$ and the coupling constant $\alpha_s^{(0)}$ are scale independent. Then, the integral over $d \ln M_b^2$ can be carried out leading to a simple logarithmic behavior

$$F_{b/p}(x_b, M_b^2) = \frac{\alpha_s^{(0)}}{2\pi} \int_{x_b}^1 \frac{dz_b}{z_b} P_{b \leftarrow b'} \left(\frac{x_b}{z_b} \right) F_{b/p}^{(0)}(z_b) \ln \left(\frac{M_b^2}{s} \right). \quad (5.12)$$

For the LO resolved photon contribution, this approximation is obviously good enough as can be seen from the dotted curve in figure 31. The cross section drops by 20% when going from $M_b = 1/4E_T$ to $M_b = 4E_T$. Of course, the full solution of the AP equations is not so simple, and the LO direct photon contribution in figure 30 deviates slightly from a simply logarithmic graph. The variation of the cross section here amounts only to 6.5%. In next-to-leading order, initial state singularities arise as in the photon case and are absorbed into the proton structure function

$$F_{b/p}(x_b, M_b^2) = \int_{x_b}^1 \frac{dz_b}{z_b} \left[\delta_{bb'} \delta(1 - z_b) + \frac{\alpha_s}{2\pi} R'_{b \leftarrow b'}(z_b, M_b^2) \right] F_{b'/p} \left(\frac{x_b}{z_b} \right). \quad (5.13)$$

Again, finite terms accompany the pole in the $\overline{\text{MS}}$ scheme

$$R'_{b \leftarrow b'}(z_b, M_b^2) = -\frac{1}{\varepsilon} P_{b \leftarrow b'}(z_b) \frac{\Gamma(1 - \varepsilon)}{\Gamma(1 - 2\varepsilon)} \left(\frac{4\pi\mu^2}{M_b^2} \right)^\varepsilon, \quad (5.14)$$

which depend on M_b^2 through

$$-\frac{1}{\varepsilon} P_{b \leftarrow b'}(z_b) \left[\left(\frac{4\pi\mu^2}{s} \right)^\varepsilon - \left(\frac{4\pi\mu^2}{M_b^2} \right)^\varepsilon \right] = -P_{b \leftarrow b'}(z_b) \ln \left(\frac{M_b^2}{s} \right). \quad (5.15)$$

These logarithms cancel the leading logarithmic behavior of the parton distribution functions in the proton. Consequently, the full next-to-leading order curves in figures 30 and 31 depend only very weakly on the renormalization scale M_b in the proton. Finally, we consider the total scale dependence for complete photoproduction in figure 32. The dependence of the inclusive single-jet cross section on $M = \mu = M_a = M_b$ is dominated by the renormalization scale dependence in the one-loop (dotted curve) and two-loop (dashed curve) approximation for α_s . Since resolved photoproduction is more important than direct photoproduction at $E_T = 20$ GeV, figure 32 resembles figure 27 more than figure 26. The total scale dependence is reduced by almost a factor of two in next-to-leading order (full curve).

5.3 One-Jet Cross Sections

In the last section, we have studied the dependence of the inclusive single-jet cross section on the various scales, which cannot be predicted from theory. It was shown that the next-to-leading order cross section is much less dependent on the renormalization and factorization scales than the leading order cross section, due to cancellation mechanisms. We continue to study one-jet cross sections here, but shift the emphasis towards experimentally relevant distributions. The two main experimental observables in the double differential cross section

$$\frac{d^2\sigma}{dE_T d\eta} = \sum_b \int_{x_{a,\min}}^1 dx_a x_a F_{a/e}(x_a, M_a^2) x_b F_{b/p}(x_b, M_b^2) \frac{4E_e E_T}{2x_a E_e - E_T e^{-\eta}} \frac{d\sigma}{dt}(ab \rightarrow p_1 p_2) \quad (5.16)$$

are the hardness or transverse energy E_T of the observed jet and its orientation in the detector, i.e. the angle θ it forms with the beam axis. Instead of this angle, we use the pseudorapidity $\eta = -\ln[\tan(\theta/2)]$ as usual. As the electron is only weakly deflected, it stays in the beam pipe like the proton remnant. Therefore, the jets are homogeneously distributed in the azimuthal angle ϕ , and we have integrated

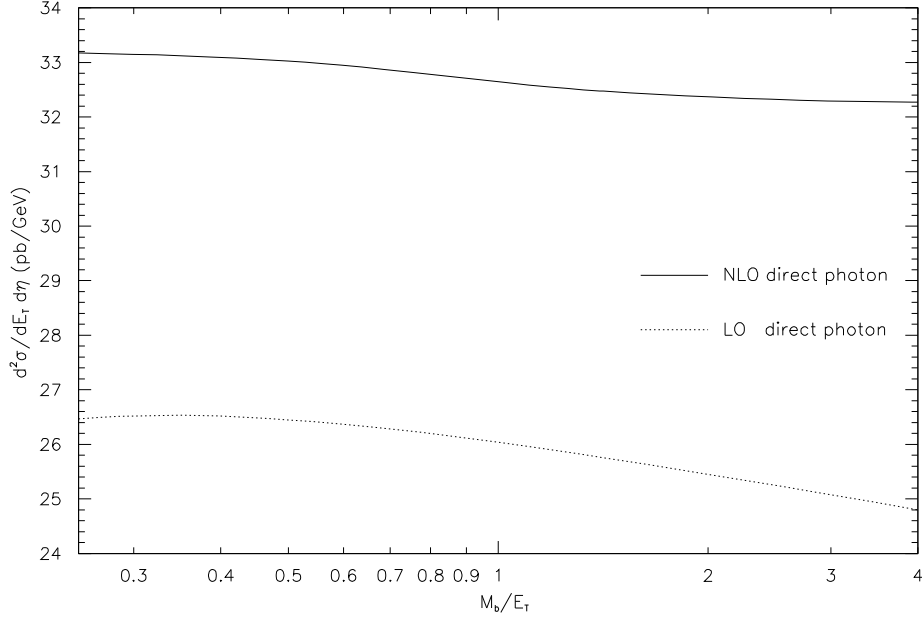


Figure 30: *Inclusive single-jet cross section $d^2\sigma/dE_T d\eta$ for direct photons at $E_T = 20$ GeV and $\eta = 1$, as a function of M_b/E_T . The weak behavior of the LO (dotted) curve is even more reduced in NLO (full curve).*

over ϕ in the theoretical prediction. The single-jet cross sections for direct photoproduction have already been published [8], those for resolved photoproduction are shown here for the first time with our phase space slicing method. Using a different method similar results have been published in [77, 73, 78, 79].

We start with distributions in the jet transverse energy E_T , which is at the same time a measure for the resolution of partons within the photon and the proton. In figure 33, we plot the direct photon contribution for transverse energies between 5 and 70 GeV. In this interval, the cross section drops by almost six orders of magnitude. The next-to-leading order curves are always above the leading order predictions. To separate the curves for three different rapidities, we multiplied those for $\eta = 0$ and $\eta = 2$ by factors of 0.1 and 0.5, respectively. At $\eta = 0$, the phase space restricts the accessible range in E_T to $E_T < 50$ GeV. The so-called k -factor, i.e. the ratio of NLO to LO, drops from 1.8 at 5 GeV to 1.2 at 70 GeV for $\eta = 1$, so that the higher order corrections are more important at small scales, where the strong coupling α_s is large. Had we calculated the leading order with one-loop α_s , the correction would, however, not be so large.

The corresponding curves for resolved photoproduction are shown in figure 34. Here, the curves for $\eta = 1$ and $\eta = 2$ lie closer to each other in spite of the rescaling for $\eta = 2$. This already hints at a broader maximum in the rapidity distribution compared to the direct case (see below). The NLO and LO curves lie further apart due to the large k -factor of about 1.8 over the whole E_T -range. This can be understood from the non-perturbative nature of resolved photons, where higher order corrections are more important at all scales due to the many channels involved.

The rapidity distribution for direct photons is presented in figure 35 at a transverse energy of $E_T = 20$ GeV. In the available phase space of $\eta \in [-1, 4]$, the cross section exhibits a rather broad maximum and steep edges. The k -factor is 1.25 in the central region.

We have already mentioned that the corresponding distribution for resolved photons is expected to have an even broader maximum. This proves to be true in figure 36, where the maximum is also slightly shifted in the proton direction from $\eta = 1$ to $\eta = 1.5$. The reason can be found in the lower longitudinal momentum of photon components with respect to a direct photon. The next-to-leading

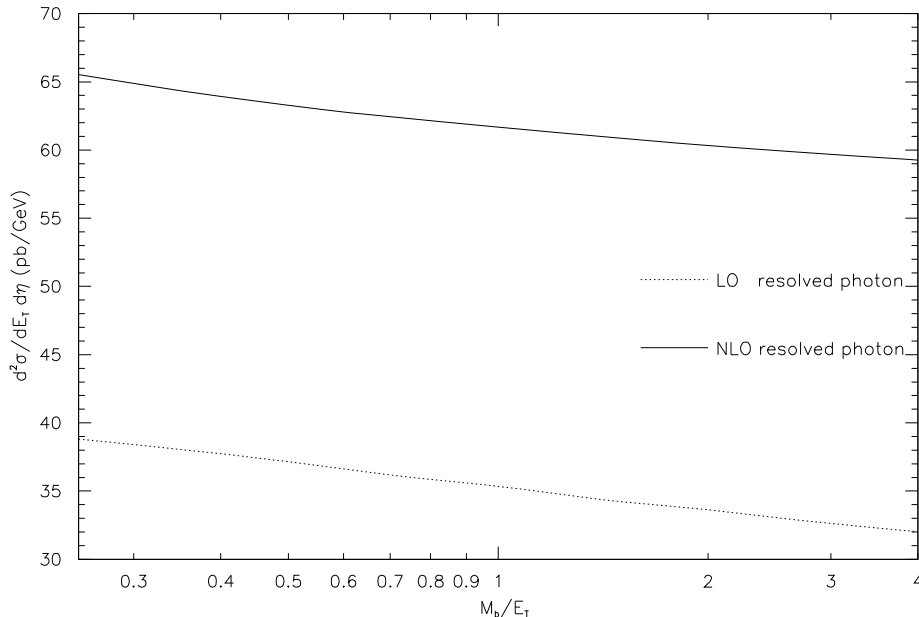


Figure 31: *Inclusive single-jet cross section $d^2\sigma/dE_T d\eta$ for resolved photons at $E_T = 20$ GeV and $\eta = 1$, as a function of M_b/E_T . The approximately logarithmic dependence in LO (dotted curve) is reduced in NLO (full curve).*

order cross section is about 80% larger than the leading order cross section, which is compatible to the observation of a large k -factor from the E_T -distribution above.

We now look at the interplay of direct and resolved photoproduction in inclusive single-jet cross sections. Figures 37 and 38 present the leading order and next-to-leading order predictions for complete photoproduction (full curves), which are the sums of the direct (dotted) and resolved (dashed) curves already presented above. The rapidity of the observed jet is fixed at $\eta = 1$. Obviously, the resolved photon component is dominating at low transverse energies due to the photon structure function and unimportant at large transverse energies, where the perturbative point-like coupling is large. In leading order, the intersection of the resolved and direct curves lies near 26 GeV and is shifted towards 37 GeV in next-to-leading order. The resolved process has larger NLO corrections than the direct process, so that the region, in which the latter is important, moves to higher E_T .

The rapidity distributions for full photoproduction are shown as full curves in figures 39 and 40 for leading and next-to-leading order at a transverse energy of $E_T = 20$ GeV. One expects the direct photon to be important mostly in the electron direction at small or negative rapidities. This behavior can be seen in both figures, but only close to the boundary of phase space below $\eta = 0$.

In figures 41 and 42, we plot the dependence of the single-jet inclusive cross section on the jet cone size R in the Snowmass convention [45]. As discussed in section 2.4, a theoretical definition for jets containing more than one parton is only possible in next-to-leading order. Therefore only the full curves depend on R , whereas the leading order curves are constant. The dependence has the functional form of the next-to-leading order result [73, 77]

$$\frac{d^2\sigma}{dE_T d\eta} = a + b \ln R + cR^2, \quad (5.17)$$

For the direct photon contribution in figure 41, the leading and higher order predictions are equal at $R \simeq 1$ for one-loop α_s (dotted) and at $R \simeq 0.6$ for two-loop α_s (dashed). For the resolved photon contribution in figure 42, the situation is different. The stable points lie at $R \simeq 0.7$ for one-loop (dotted) and $R \simeq 0.12$ for two-loop α_s .

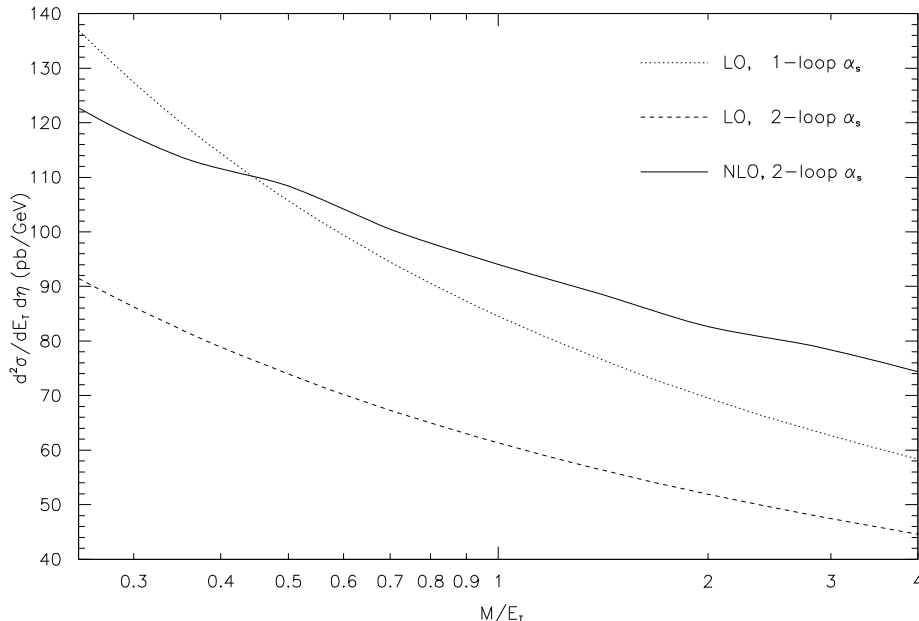


Figure 32: Complete inclusive single-jet cross section $d^2\sigma/dE_T d\eta$ at $E_T = 20$ GeV and $\eta = 1$, as a function of M/E_T for $M = \mu = M_a = M_b$. The strong dependence in LO (dotted and dashed curves) is reduced in NLO (full curve).

5.4 Two-Jet Cross Sections

We now turn to two-jet cross sections, where one does not integrate over the second rapidity η_2 or, alternatively, over the momentum fraction x_a of the parton in the electron. The differential cross section

$$\frac{d^3\sigma}{dE_T^2 d\eta_1 d\eta_2} = \sum_b x_a F_{a/e}(x_a, M_a^2) x_b F_{b/p}(x_b, M_b^2) \frac{d\sigma}{dt}(ab \rightarrow p_1 p_2) \quad (5.18)$$

then yields the maximum of information possible on the parton distributions and is better suited to constrain them than the observation of inclusive single-jets. Since dijet production is a more exclusive process than one-jet production, the cross sections are smaller and require higher luminosity or longer running time in the experiments. This is the reason why H1 and ZEUS have only recently started to analyze dijet data and why we can present here the first theoretical calculation for complete dijet photoproduction.

It is important to note that only in leading order the transverse energies of the two observed jets balance ($E_{T_1} = E_{T_2} = E_T$). In next-to-leading order inclusive cross sections, there may be a third unobserved jet which must have full freedom to become infinitely soft. Therefore, the transverse energies of both jets cannot be observed without spoiling infrared safety. This is an artifact of fixed order perturbation theory and will go away in $\mathcal{O}(\alpha_s^3)$, where one may as well have a fourth jet. We will calculate similar distributions as in the last section, i.e. in the transverse energy of the first jet, E_{T_1} , and in both observable rapidities η_1 and η_2 . Yet, the rapidities η_1 and η_2 always belong to the two jets with largest transverse energy in the event. As in the one-jet case, the direct distributions have already been presented in a recent paper [8], whereas the resolved and complete cross sections are shown here and partly in [12].

First, we look at the distributions in the transverse energy E_{T_1} in figure 43 for direct photons. We fix η_1 at $\eta_1 = 1$ and η_2 at three different values of $\eta_2 = 0, 1, 2$. The curves for $\eta_2 = 0$ and $\eta_2 = 2$ are rescaled by factors of 0.1 and 0.5 as before. We expect the dijet cross sections to be smaller than the single-jet cross sections in figure 33. Indeed, for $E_T, E_{T_1} = 5$ GeV and $\eta, \eta_1, \eta_2 = 1$, the cross section

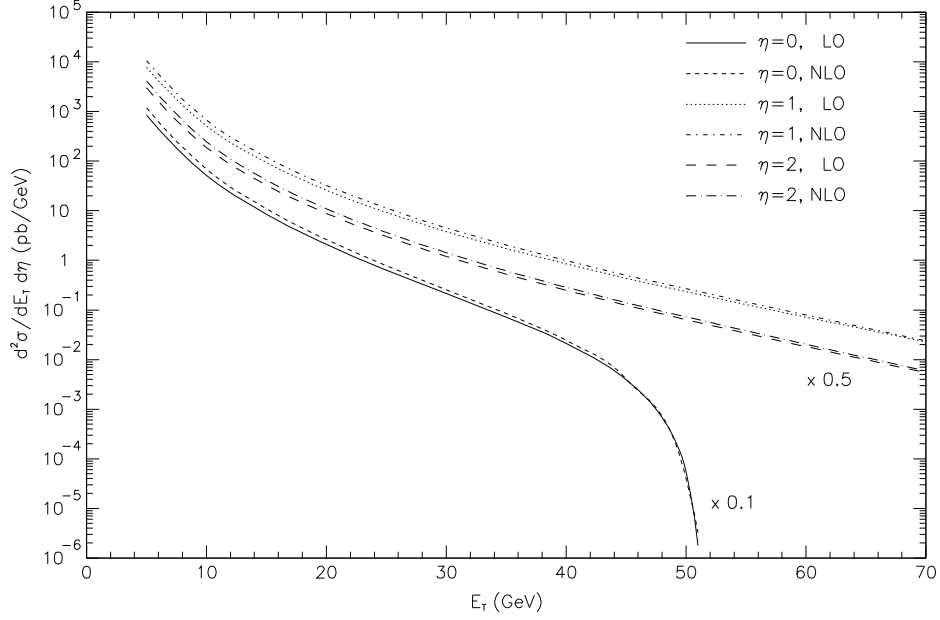


Figure 33: *Inclusive single-jet cross section $d^2\sigma/dE_T d\eta$ for direct photons as a function of E_T for various rapidities $\eta = 0, 1, 2$ in LO and NLO. The cross section for $\eta = 0$ ($\eta = 2$) is multiplied by a factor of 0.1 (0.5).*

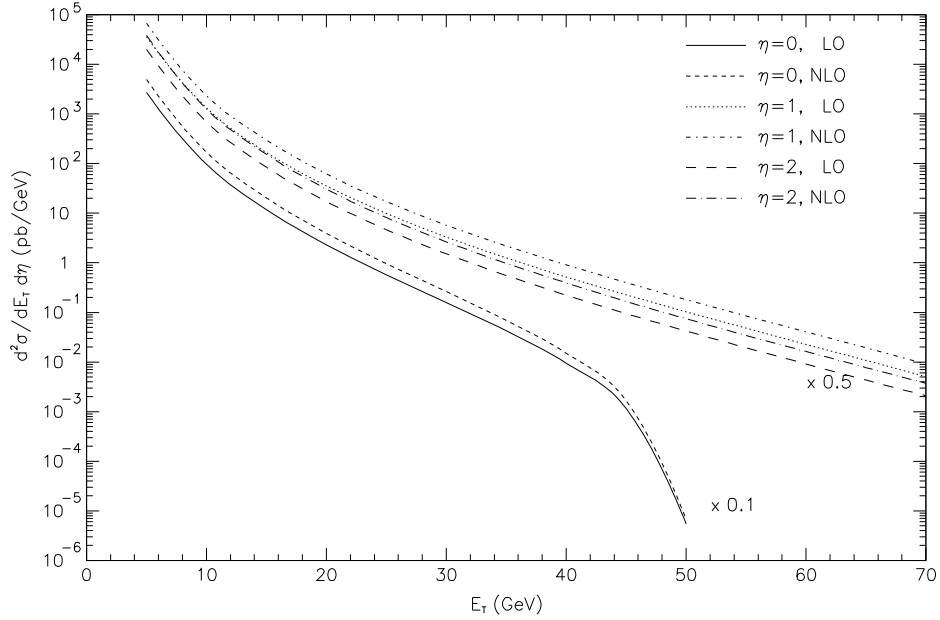


Figure 34: *Inclusive single-jet cross section $d^2\sigma/dE_T d\eta$ for resolved photons as a function of E_T for various rapidities $\eta = 0, 1, 2$ in LO and NLO. The cross section for $\eta = 0$ ($\eta = 2$) is multiplied by a factor of 0.1 (0.5).*

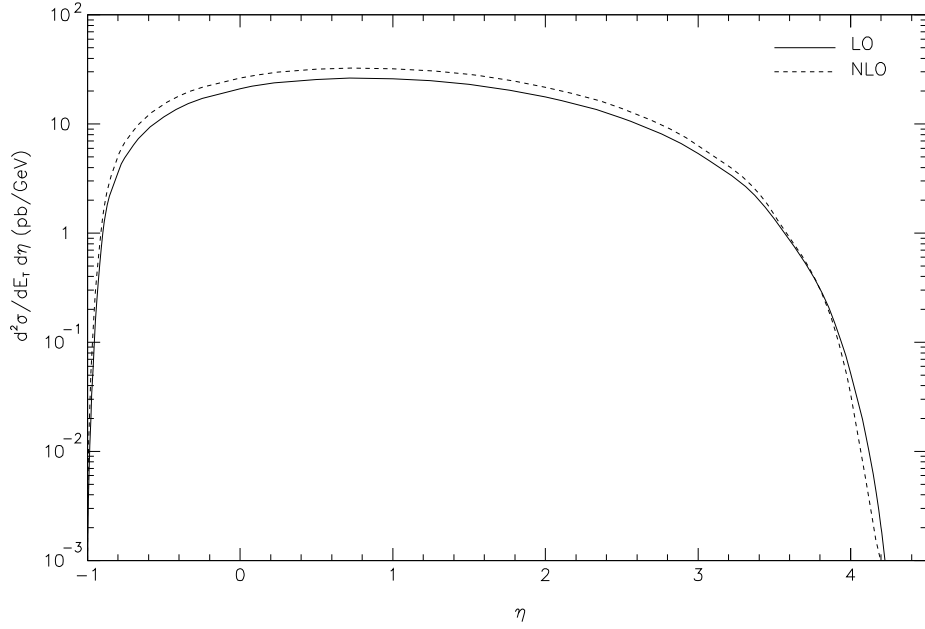


Figure 35: *Inclusive single-jet cross section $d^2\sigma/dE_T d\eta$ for direct photons as a function of η for $E_T = 20$ GeV in LO and NLO.*

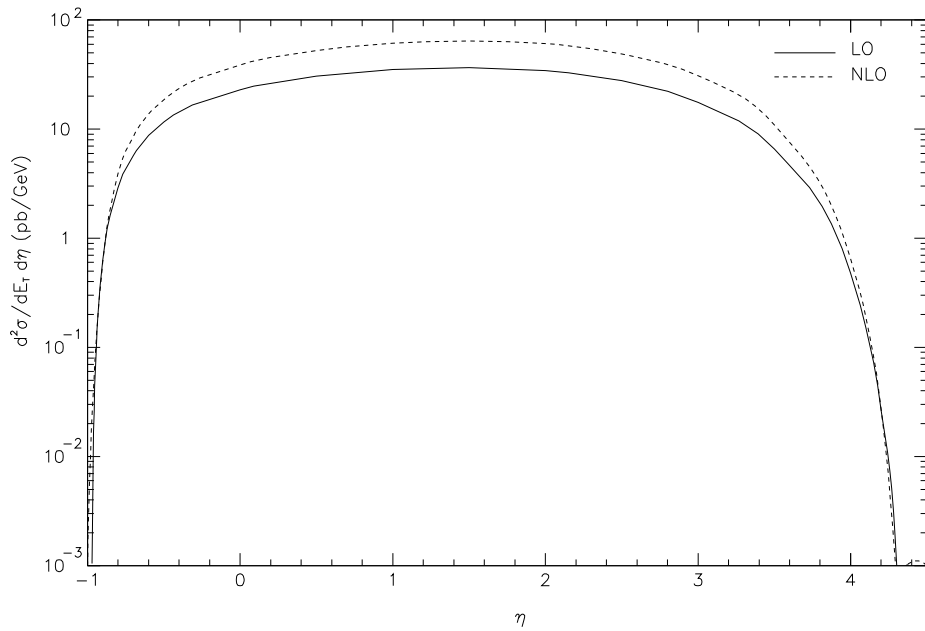


Figure 36: *Inclusive single-jet cross section $d^2\sigma/dE_T d\eta$ for resolved photons as a function of η for $E_T = 20$ GeV in LO and NLO.*

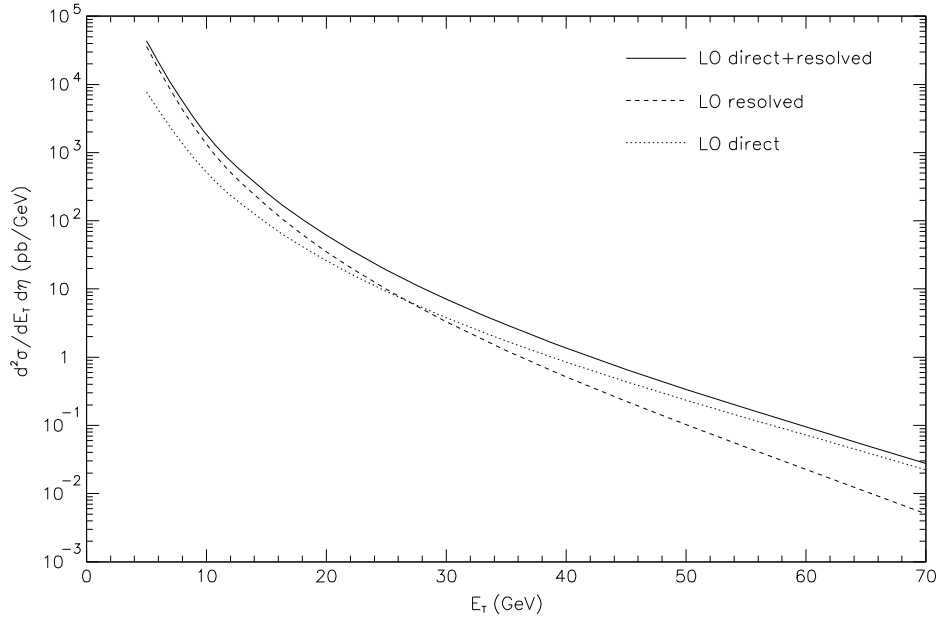


Figure 37: *Inclusive single-jet cross section $d^2\sigma/dE_T d\eta$ for complete photoproduction at $\eta = 1$, as a function of E_T . The full curve is the sum of the LO direct (dotted) and LO resolved (dashed) contributions.*

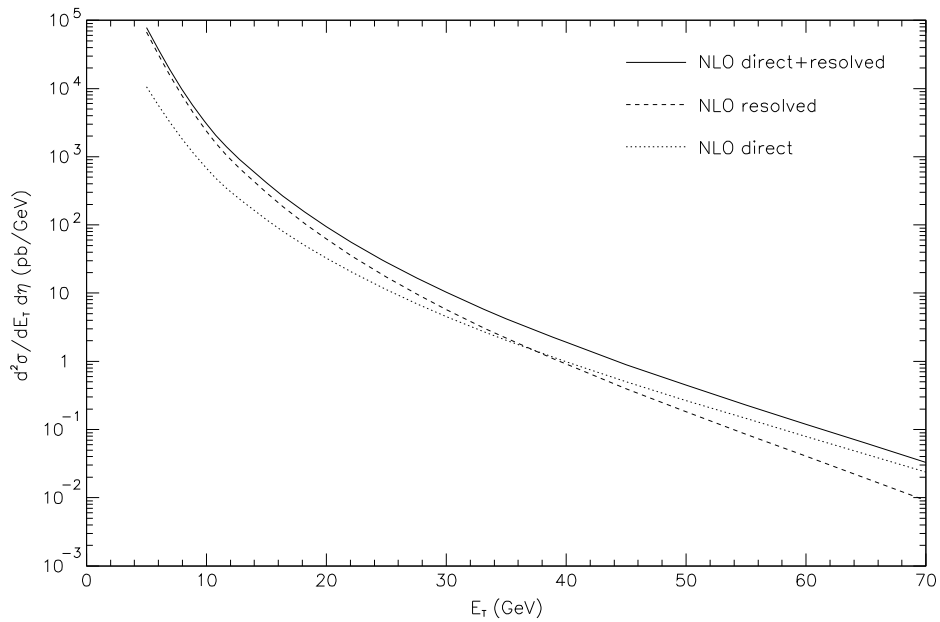


Figure 38: *Inclusive single-jet cross section $d^2\sigma/dE_T d\eta$ for complete photoproduction at $\eta = 1$, as a function of E_T . The full curve is the sum of the NLO direct (dotted) and NLO resolved (dashed) contributions.*

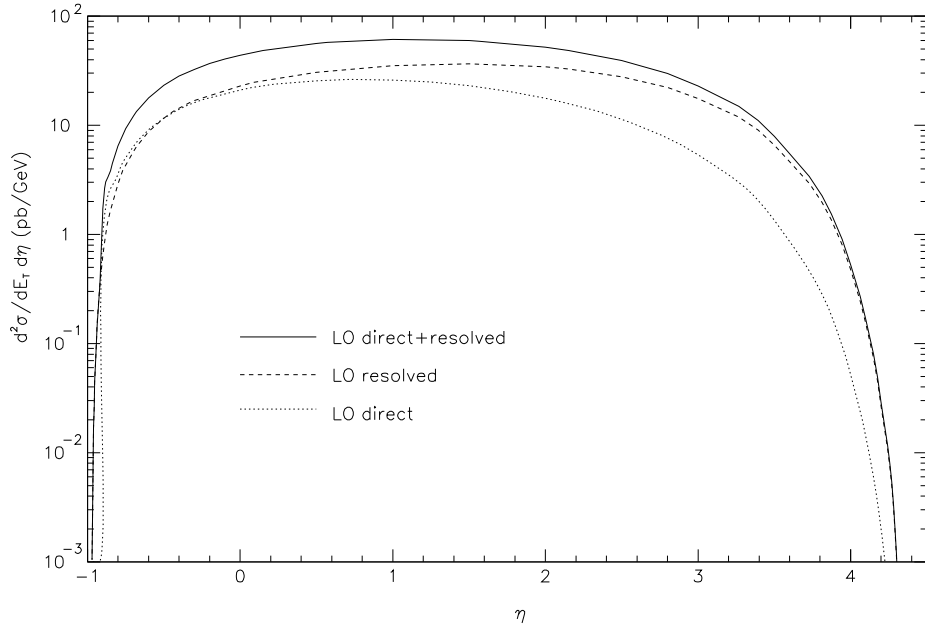


Figure 39: *Inclusive single-jet cross section $d^2\sigma/dE_T d\eta$ for complete photoproduction at $E_T = 20$ GeV, as a function of η . The full curve is the sum of the LO direct (dotted) and LO resolved (dashed) contributions.*

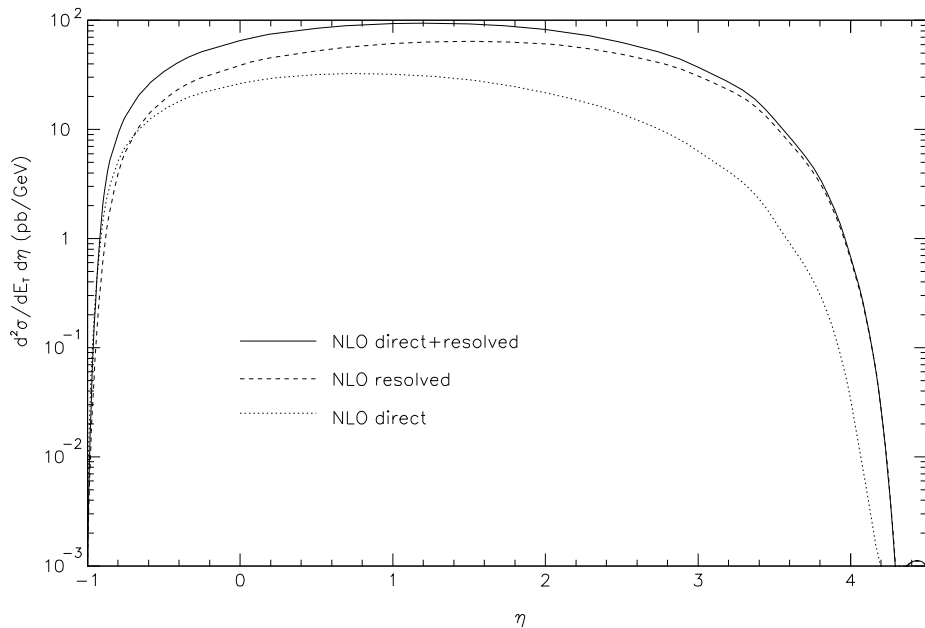


Figure 40: *Inclusive single-jet cross section $d^2\sigma/dE_T d\eta$ for complete photoproduction at $E_T = 20$ GeV, as a function of η . The full curve is the sum of the NLO direct (dotted) and NLO resolved (dashed) contributions.*

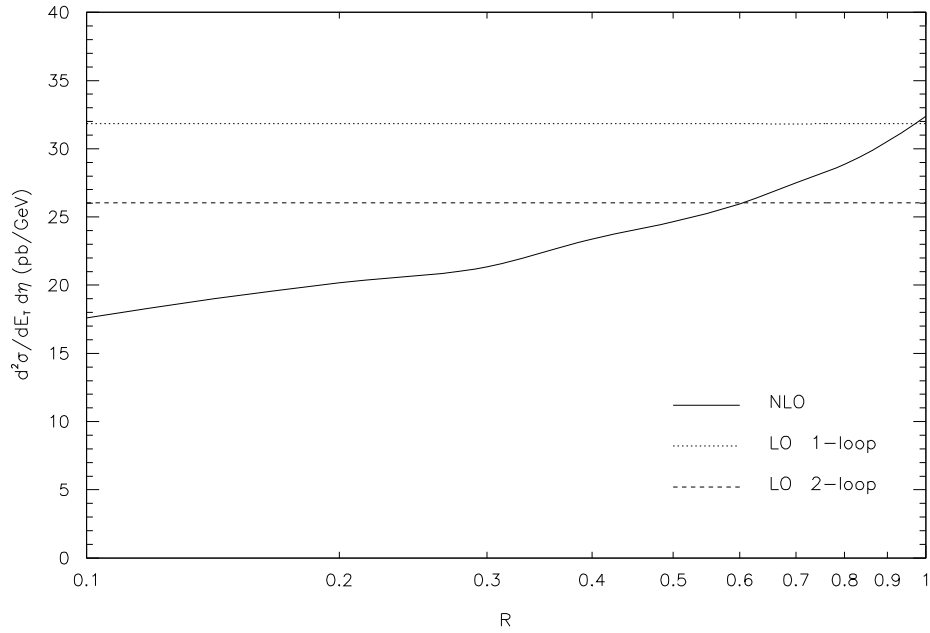


Figure 41: *Inclusive single-jet cross section $d^2\sigma/dE_T d\eta$ for direct photons at $E_T = 20$ GeV and $\eta = 1$, as a function of the jet cone size R . Only the NLO (full) curve and not the LO curves with one- (dotted) or two-loop (dashed) α_s depends on R .*

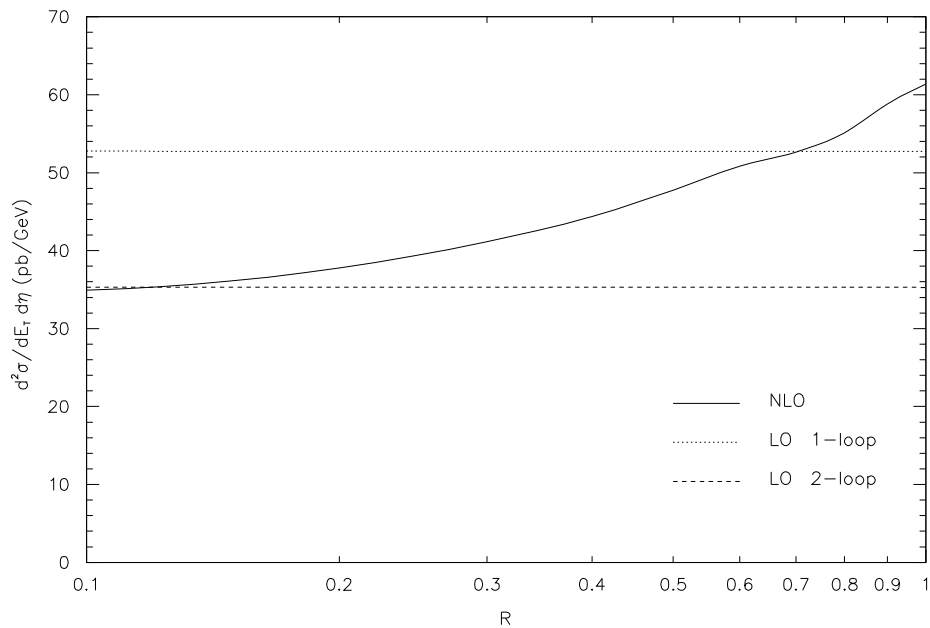


Figure 42: *Inclusive single-jet cross section $d^2\sigma/dE_T d\eta$ for resolved photons at $E_T = 20$ GeV and $\eta = 1$, as a function of the jet cone size R . Only the NLO (full) curve and not the LO curves with one- (dotted) or two-loop (dashed) α_s depends on R .*

drops by almost an order of magnitude from 10.6 nb to 1.29 nb. The k -factors in dijet production are basically the same as in single-jet production. There is, however, one novel feature: for $\eta_2 = 0$, the third jet in next-to-leading order opens up some additional phase space, so that E_{T_1} can go up to $E_{T_1} < 55$ GeV instead of only 39 GeV in leading order.

A similar behavior is seen for resolved photoproduction in figure 44. At the lowest value of $E_{T_1} = 5$ GeV and back-to-back jets ($\eta_1 = \eta_2 = 1$), the two-jet cross section (4.91 nb) is even more than one order of magnitude smaller than the one-jet cross section (67.5 nb). The ratio of NLO to LO is 1.7 for resolved photons over the whole E_{T_1} -range. The phase space for $\eta_2 = 0$ increases from $E_{T_1} = 39$ GeV to $E_{T_1} = 50$ GeV. This slightly smaller value is due to the reduced center-of-mass energy in resolved photoproduction, as some of the energy always goes into the photon remnant.

Next, we present the dependence of the cross sections on the two rapidities in form of the three-dimensional lego-plots 45 and 46. The leading order is always shown on the left side and is completely symmetric in η_1 and η_2 . For the next-to-leading order cross sections on the right hand sides of figures 45 and 46, this is no longer exactly true due to the presence of a “trigger” jet with transverse energy E_{T_1} , which is fixed at $E_{T_1} = 20$ GeV. The next-to-leading order lego-plots are only approximately symmetric. This can best be seen at the bottom of the contour plots, where at least one of the two observed jets is far off the central region. The NLO predictions are considerably larger than the LO predictions, especially in the resolved case.

This becomes even clearer when we plot the projections of the lego-plots for fixed $\eta_1 = 0, 1, 2$ and 3. In figure 47, we plot the leading and next-to-leading order distributions in η_2 for direct photoproduction. It is clearly seen that the second jet tends to be back-to-back with the first jet, since the maximum always occurs at $\eta_2 \simeq \eta_1$. However, at $\eta_1 = 3$ this is no more permitted by phase space. We obtain the same k -factor of 1.25 in the central regions as in single-jet production.

The η_2 -distributions for resolved photons in figure 48 are considerably broader than those in figure 47 due to the smearing of the hard cross sections with the distribution function of partons in the photon. The maxima of the plots are also not so much dominated by kinematics but more by the quark and gluon structure of the photon in different x regimes. They do not lie at $\eta_2 = \eta_1$ any more. Therefore, dijet rapidity distributions are best suited to constrain the photon structure. We will come back to this point in the next section 5.5, when we compare similar plots to data from ZEUS. The k -factors range from 1.65 in the central regions to more than 3 in the proton forward direction. The shapes of the distributions are very similar in LO and in NLO. The absolute values make, however, an important difference.

Direct and resolved contributions are now added to give physical, complete photoproduction results. The dijet cross section is first plotted as a function of the transverse energy E_{T_1} . Figure 49 gives the LO result, figure 50 the NLO result. Like the direct and resolved cross sections alone, the full two-jet cross sections are about an order of magnitude smaller than the one-jet cross sections (see figures 37 and 38). The point where direct and resolved contributions are equally important is lowered towards $E_{T_1} = 20$ GeV in leading order and $E_{T_1} = 30$ GeV in next-to-leading order, so that direct photons are better observed in dijet production.

If one plots the complete two-jet cross sections as a function of η_2 , the different behaviors of direct and resolved photons add up to the full curves in figures 51 and 52. These plots are best suited to decide in which rapidity regions one can look best for the resolved photon structure. We have already seen that this will be in situations where the two jets are not back-to-back, e.g. for $\eta_1 = 0$ and positive η_2 in the upper left plots of figures 51 and 52. On the other hand, the proton structure can best be studied with direct photons, when the cross section is not folded with another distribution. A possible scenario is $\eta_1 = 0$ and negative values of η_2 . This is especially interesting for the small- x components of the proton like the gluons and the quark sea. Another interesting observation is that the relative importance of direct and resolved processes changes dramatically when calculating dijet photoproduction in next-to-leading order $\mathcal{O}(\alpha_s^2)$: resolved processes are much more important at $E_{T_1} = 20$ GeV than one would have guessed from a leading order estimate.

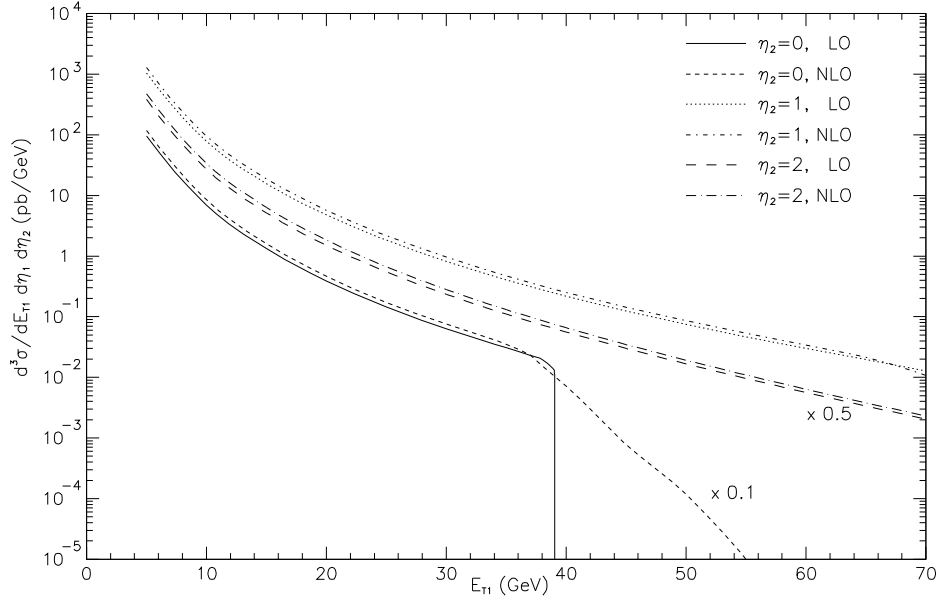


Figure 43: *Inclusive dijet cross section $d^3\sigma/dE_{T_1}d\eta_1d\eta_2$ for direct photons as a function of E_{T_1} for $\eta_1 = 1$ and three values of $\eta_2 = 0, 1, 2$. The cross section for $\eta_2 = 0$ ($\eta_2 = 2$) is multiplied by 0.1 (0.5).*

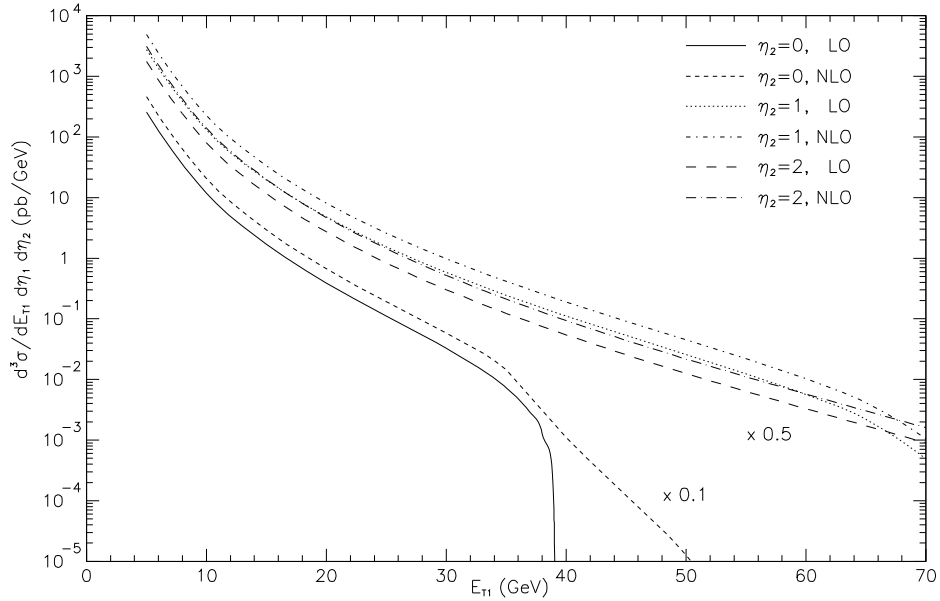


Figure 44: *Inclusive dijet cross section $d^3\sigma/dE_{T_1}d\eta_1d\eta_2$ for resolved photons as a function of E_{T_1} for $\eta_1 = 1$ and three values of $\eta_2 = 0, 1, 2$. The cross section for $\eta_2 = 0$ ($\eta_2 = 2$) is multiplied by 0.1 (0.5).*

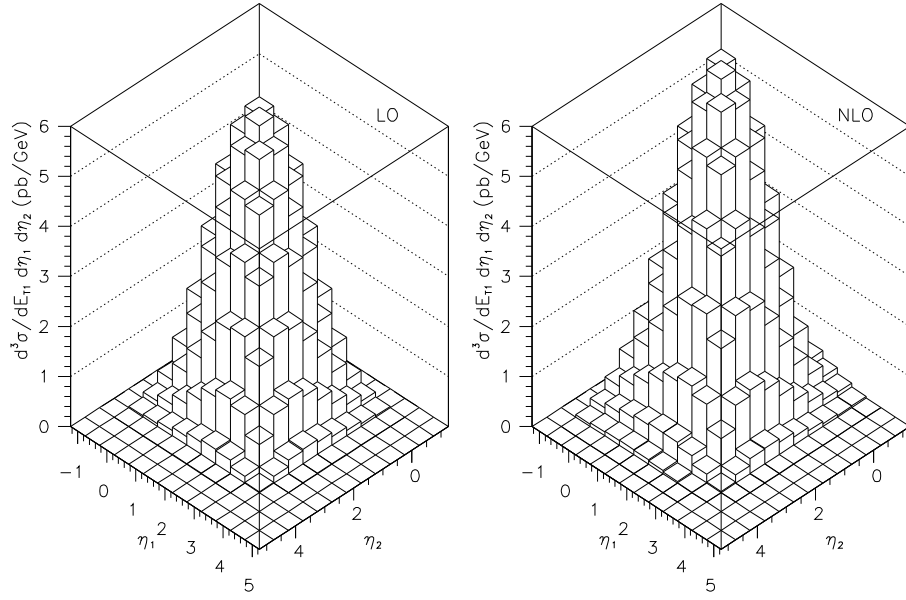


Figure 45: *Inclusive dijet cross section $d^3\sigma/dE_{T_1} d\eta_1 d\eta_2$ at $E_{T_1} = 20$ GeV for direct photons, as a function of η_1 and η_2 . The LO plot (left) is exactly symmetric, the NLO plot (right) only approximately.*

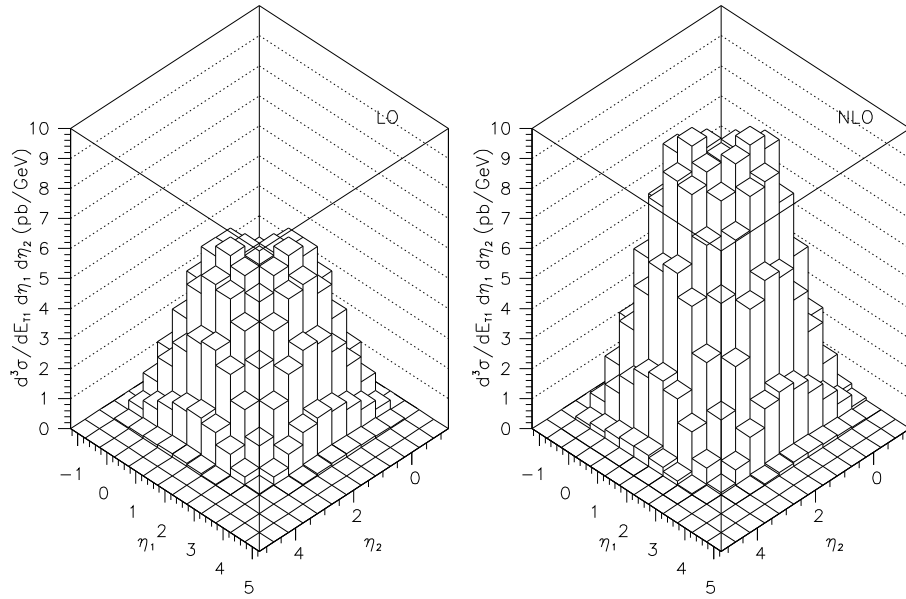


Figure 46: *Inclusive dijet cross section $d^3\sigma/dE_{T_1} d\eta_1 d\eta_2$ at $E_{T_1} = 20$ GeV for resolved photons, as a function of η_1 and η_2 . The LO plot (left) is exactly symmetric, the NLO plot (right) only approximately.*

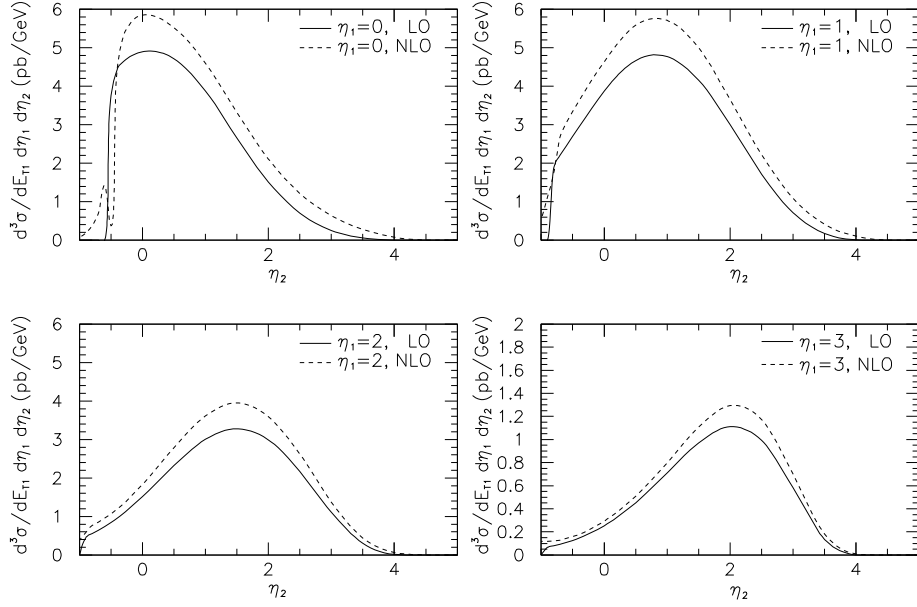


Figure 47: Projections of the LO (full curves) and NLO (dashed curves) triple differential dijet cross section for direct photons at $E_{T_1} = 20$ GeV and fixed values of $\eta_1 = 0, 1, 2,$ and $3,$ as a function of η_2 .

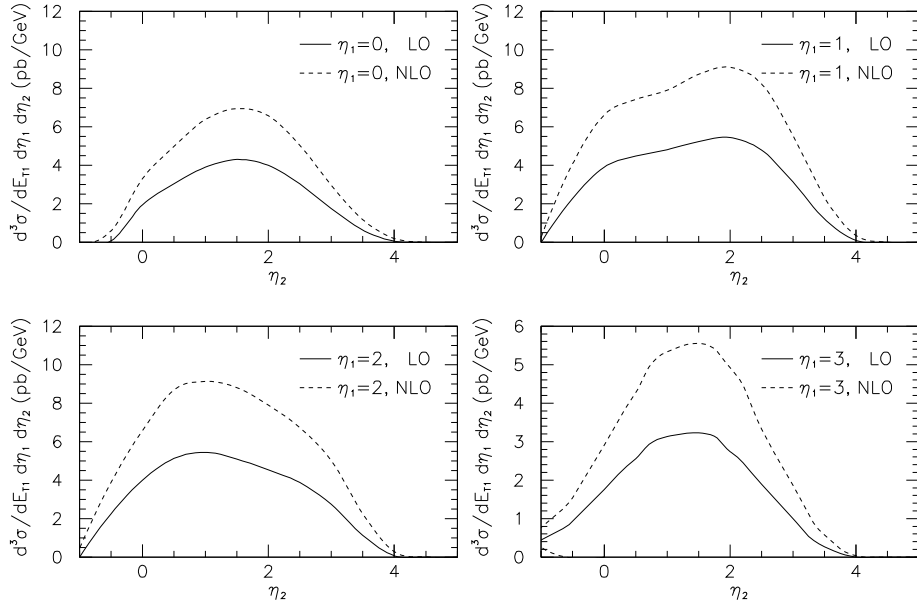


Figure 48: Projections of the LO (full curves) and NLO (dashed curves) triple differential dijet cross section for resolved photons at $E_{T_1} = 20$ GeV and fixed values of $\eta_1 = 0, 1, 2,$ and $3,$ as a function of η_2 .

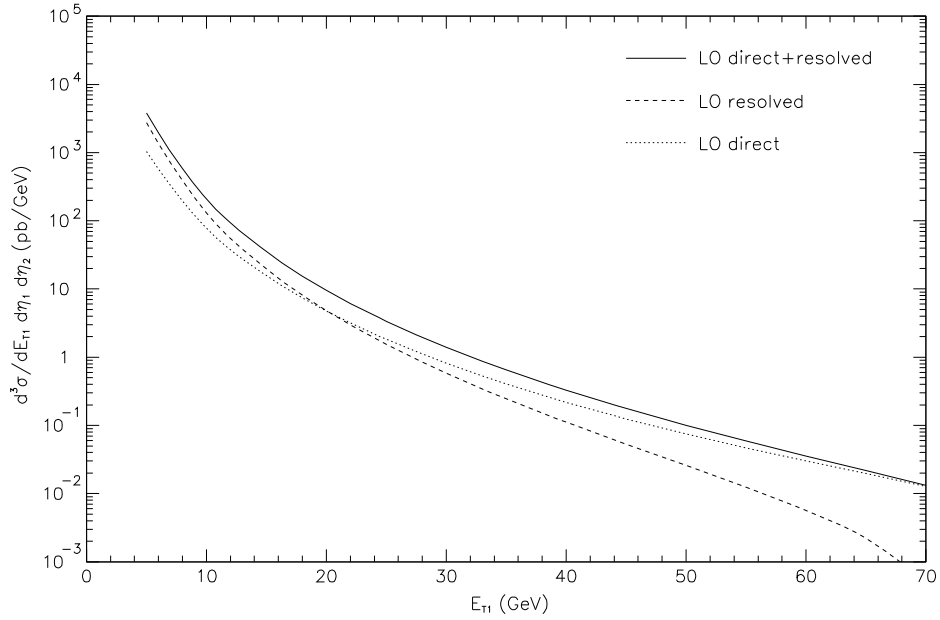


Figure 49: *Inclusive dijet cross section $d^3\sigma/dE_{T_1}d\eta_1d\eta_2$ for full photoproduction at $\eta_1 = \eta_2 = 1$ as a function of E_{T_1} . The full curve is the sum of the LO direct (dotted) and LO resolved (dashed) contributions.*

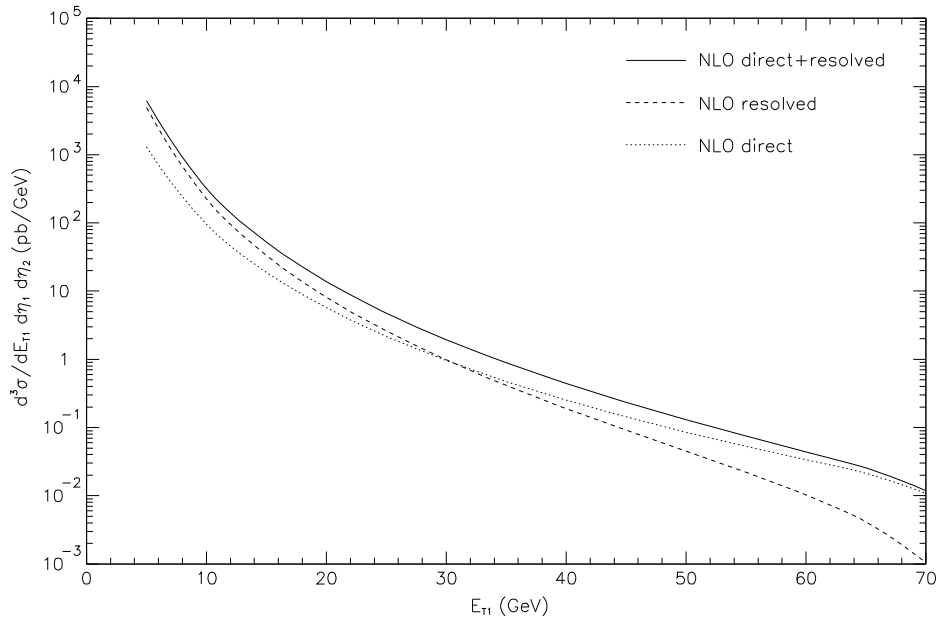


Figure 50: *Inclusive dijet cross section $d^3\sigma/dE_{T_1}d\eta_1d\eta_2$ for full photoproduction at $\eta_1 = \eta_2 = 1$ as a function of E_{T_1} . The full curve is the sum of the NLO direct (dotted) and NLO resolved (dashed) contributions.*

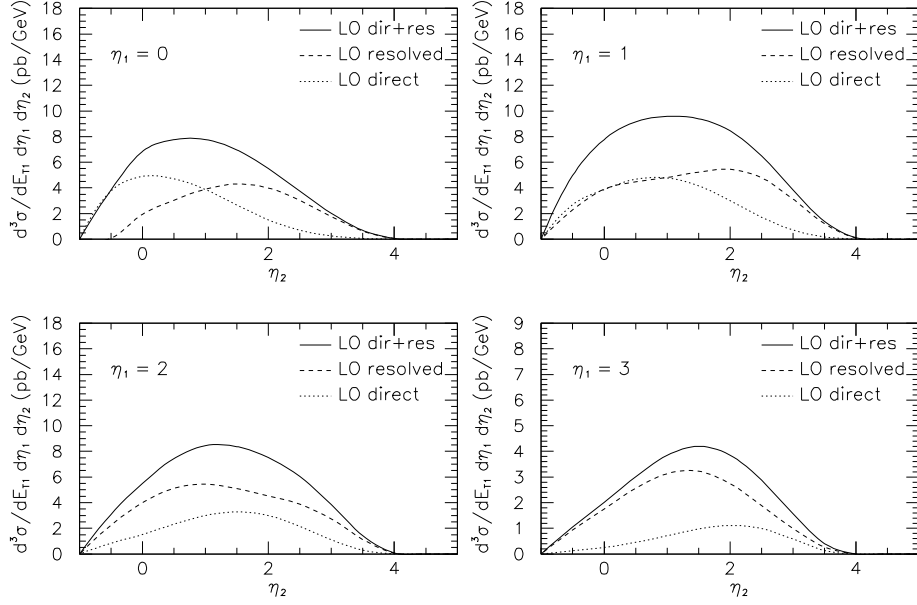


Figure 51: *Projections of the complete triple differential dijet cross section at $E_{T1} = 20$ GeV and fixed values of $\eta_1 = 0, 1, 2,$ and $3,$ as a function of η_2 . The full curve is the sum of the LO direct (dotted) and LO resolved (dashed) contributions.*

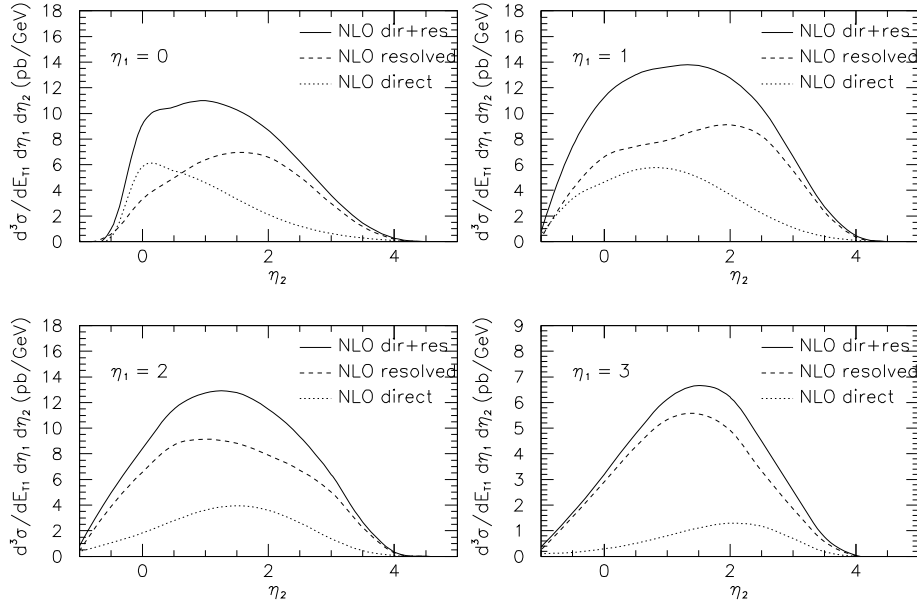


Figure 52: *Projections of the complete triple differential dijet cross section at $E_{T1} = 20$ GeV and fixed values of $\eta_1 = 0, 1, 2,$ and $3,$ as a function of η_2 . The full curve is the sum of the NLO direct (dotted) and NLO resolved (dashed) contributions.*

5.5 Comparison of Photoproduction Results to H1 and ZEUS Data

In this section we compare the next-to-leading order calculation to recent one- and two-jet data from the H1 and ZEUS collaborations at HERA. Both collaborations have continuously measured various cross sections for the photoproduction of jets since HERA started running in 1992. With the increased luminosity in recent years, the data have improved and many aspects of jet production could be studied. In our comparison we restrict ourselves to the measurements of one- and two-jet cross sections just recently published which are based either on 1994 or 1995 data. In particular, we shall compare with the inclusive single-jet data of 1994 from the ZEUS collaboration [82], with the inclusive dijet data of 1994 from ZEUS [83], with inclusive dijet data of 1995 from ZEUS [83], and with inclusive dijet data of 1994 from the H1 collaboration [84].

We start with the single-jet cross section $d^2\sigma/d\eta dE_T$ integrated over $E_T \geq E_{T_{\min}}$ as a function of η . This cross section $d\sigma/d\eta$ has been measured in the η range between -1 and 2 and with the E_T thresholds $E_{T_{\min}} = 14, 17, 21$, and 25 GeV. The cross section $d\sigma/d\eta$ for $E_T > 14$ GeV has also been measured in three different regions of W : $134 \text{ GeV} < W < 190 \text{ GeV}$, $190 \text{ GeV} < W < 233 \text{ GeV}$, and $233 \text{ GeV} < W < 277 \text{ GeV}$. The measurements refer to jets at the hadron level and are performed for two cone radii in the $\eta - \phi$ plane, $R = 0.7$ and $R = 1$ using the iterative cone algorithm PUCCELL. The complete data have already been compared to our next-to-leading order calculations in the ZEUS publication [82]. Therefore, we show only a selection for some specific kinematical ranges and compare them with the data. Our results for $d\sigma/d\eta$ for $E_T > 17$ GeV, $R = 1$ and $R = 0.7$ are shown in figures 53 and 54, respectively, and are compared to the ZEUS data. The error bars in figures 53, 54, 55, and 56 only contain the statistical error. The systematic error and the uncertainty associated with the absolute energy scale is not included, which adds an additional 30% error (see [82]). The theoretical predictions include resolved and direct processes in NLO. For the proton, the CTEQ4M [31] parton densities have been used. For the photon distribution, the GRV-HO [33], converted to $\overline{\text{MS}}$ factorization, and as an alternative set the recent GS96 [38] parametrizations have been chosen as input. The renormalization and factorization scales have been put equal to E_T , and α_s was calculated with the two-loop formula with $\Lambda_{\overline{\text{MS}}}^{(4)} = 296 \text{ MeV}$ as used in the proton parton densities. In figures 53 and 54, two curves are presented for both photon distribution sets labeled as $R_{\text{sep}} = 2R$ and $R_{\text{sep}} = 1R$. They correspond to two choices of the R_{sep} parameter. Since our calculations include only up to three partons in the final state, the maximum number of partons in a single jet is two. Therefore, the overlapping and merging effects of the experimental jet algorithm cannot be simulated in the theoretical calculation [85]. To account for these effects, the R_{sep} parameter was introduced [85]. It has the effect that two partons are not merged into a single jet if their separation in the $\eta - \phi$ plane is more than R_{sep} . Then $R_{\text{sep}} = 2R$ means that no further restriction is introduced and the cone algorithm is applied in its original form. Experimentally, the two extreme values of $R_{\text{sep}} = 2R$ and $1R$ correspond to a fixed cone algorithm (like EUCELL) and to the k_T clustering algorithm (like KTCLUS), whereas an iterative cone algorithm (like PUCCELL) is described by some intermediate value. In both calculation and data analysis, the maximal virtuality of the photon is equal to $Q_{\text{max}}^2 = 4 \text{ GeV}^2$, and the full W range, which corresponds to $0.20 < x_a < 0.85$ in the EPA formula, is used. Looking at figures 53 and 54, we observe that the behavior of the measured cross sections is different for $R = 0.7$ and $R = 1$. For $R = 1$, the shape of the cross section is well described for $-1 < \eta < 0.5$. For higher values of η , the data stay almost constant as a function of η , whereas the theoretical curves decrease as a function of η for both radii $R = 1$ and $R = 0.7$. However, when $R = 0.7$ is used, the shape and magnitude of the NLO results agree quite well with the measured differential cross section in the entire η range. This is also the case in the comparison for the lower E_T threshold, $E_{T_{\min}} = 14 \text{ GeV}$, with $R = 0.7$ shown in [82]. For the higher E_T thresholds, 21 and 25 GeV, the NLO predictions give a good description of the measured cross sections in magnitude and shape for both cone radii $R = 0.7$ and $R = 1$ (see [82]). In general, the choice $R = 0.7$ should be preferred for the comparison between data and theory. Figure 54 shows that the predictions with the GS96 parametrization of the photon parton distributions agree better with the data than the GRV-HO parametrization which is above the data for both R_{sep} parameter values

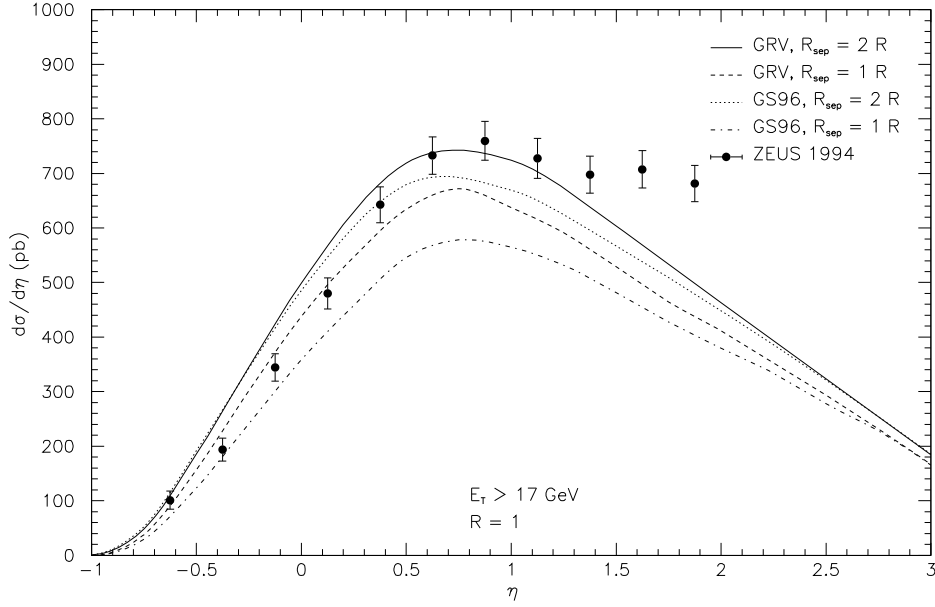


Figure 53: η dependence of the inclusive single-jet photoproduction cross section integrated over $E_T > 17\text{GeV}$ with jet cone size $R = 1$. We compare our NLO prediction with GRV and GS96 photon parton densities and the two extreme R_{sep} values to 1994 data from ZEUS.

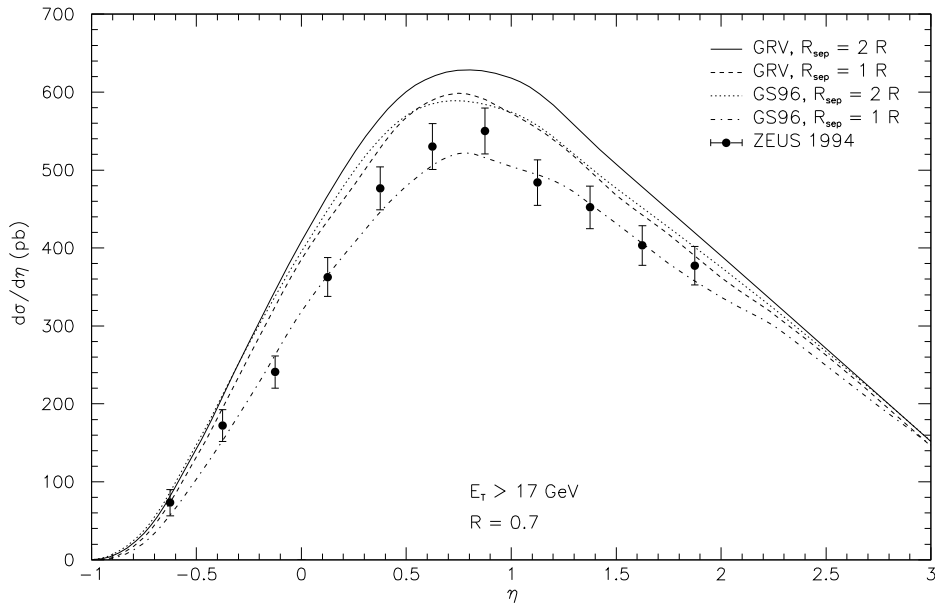


Figure 54: η dependence of the inclusive single-jet photoproduction cross section integrated over $E_T > 17\text{GeV}$ with jet cone size $R = 0.7$. We compare our NLO prediction with GRV and GS96 photon parton densities and the two extreme R_{sep} values to 1994 data from ZEUS.

over the whole η range. Concerning the R_{sep} parameter the curve for $R_{\text{sep}} = 1R$ is in somewhat better agreement than the curve for $R_{\text{sep}} = 2R$. We have checked that a value of $R_{\text{sep}} = 1.4R$ gives the best agreement. This supports a recent study of the jet shape function, which depends sensitively on this parameter [86]. By comparing with recent measurements of this jet shape by the ZEUS collaboration [87], it was found that $R_{\text{sep}} = 1.5R$ gives very good agreement with the jet shape data for PUCCELL in the same η and E_T range [86].

A comparison of $d\sigma/d\eta$ for $E_T > 14$ GeV in different W regions has also been presented. As an example, we show $d\sigma/d\eta$ as a function of η for the largest W range: $233 \text{ GeV} < W < 277 \text{ GeV}$ (corresponding to $0.55 < x_a < 0.85$) in figure 55 ($R = 1$) and in figure 56 ($R = 0.7$). Whereas the $R = 1$ theoretical cross section (figure 55) agrees for low values of η , it disagrees in the high η region with the data. This disagreement shows up particularly in the high W range [82]. The measured differential cross section is again well described by the NLO calculation for $R = 0.7$ (see figure 56).¹

The excess of the measured cross section with respect to the calculations in the high η range and for the smaller E_T thresholds for $R = 1$ is supposed to be due to the presence of the underlying event in the data which yields a larger amount of extra energy lying in the jet cone for $R = 1$ but not for the smaller cone $R = 0.7$. From figure 53 it is clear that the excess occurs only in the large η range where the resolved cross section dominates and where additional interactions of the photon and proton remnants are supposed to occur which are not included in the NLO calculations. These deviations between NLO theory and the data at large η and smaller E_T 's were found earlier [88] when the theoretical predictions were compared with the 1993 ZEUS data [5].

In conclusion, we can say that the NLO calculations describe reasonably well the experimental inclusive single-jet cross section for jets defined with $R = 0.7$ in the entire η range and for $R = 1$, if E_T is large enough.

Next, we compare the NLO predictions with inclusive dijet cross sections measured by ZEUS [83] and H1 [84]. Inclusive two-jet cross sections depend on one more variable as compared to the inclusive one-jet cross sections considered above. Therefore they are supposed to give a much more stringent test of the theoretical predictions than the inclusive one-jet cross sections. For the comparison with the data it is essential that in the theoretical calculations the same jet definitions are introduced as in the experimental analysis. Furthermore it is important that the theoretical calculations contain the same cuts on the kinematical variables as for the measured cross sections. First experimental data for inclusive two-jet production have been published by the ZEUS collaboration in [5] and [89]. The more recent ZEUS analysis based on the 1994 data taking presented in [80] and recently in [83] extends the earlier analysis in [5] based on 1993 data in several ways. The larger luminosity obtained in 1994 lead to a reduction of the statistical errors as well as allowing for the measurement of the cross section at higher E_T , a region, where uncertainties due to hadronization of partons into jets and of underlying event effects are reduced making the comparison with the NLO predictions more meaningful. Furthermore, the ZEUS collaboration applied three different jet definitions: two variations of the cone algorithm [45] called "EUCCELL" and "PUCCELL", and the k_T -cluster algorithm "KTCLUS" as introduced for hadron-hadron collisions [90]. The two cone algorithms treat seed finding and jet merging in different ways. Since the NLO calculations contain only up to three partons in the final state, these experimental seed finding and jet merging conditions cannot be fully reproduced. This ambiguity is largely reduced in the k_T -cluster algorithm. In the NLO calculations, the two cone algorithms can be simulated by introducing R_{sep} already considered for the one-jet cross sections. The EUCCELL definition corresponds to $R_{\text{sep}} = 2R$, whereas PUCCELL is best simulated with $R_{\text{sep}} = 1.4R$ for the E_T range considered in the experimental analysis (see above) [86, 46]. The k_T -cluster algorithm for hadron-hadron collisions is identical to using $R_{\text{sep}} = R$. Therefore by introducing the R_{sep} parameter into the NLO calculations of the two-jet cross sections, all three jet finding definitions used in the experimental analysis can be accounted for. The ZEUS results of the earlier analysis [80] have been compared to the NLO

¹The wiggles in the curves in figures 55 and 56 are due to insufficient numerical accuracy and have no physical significance.

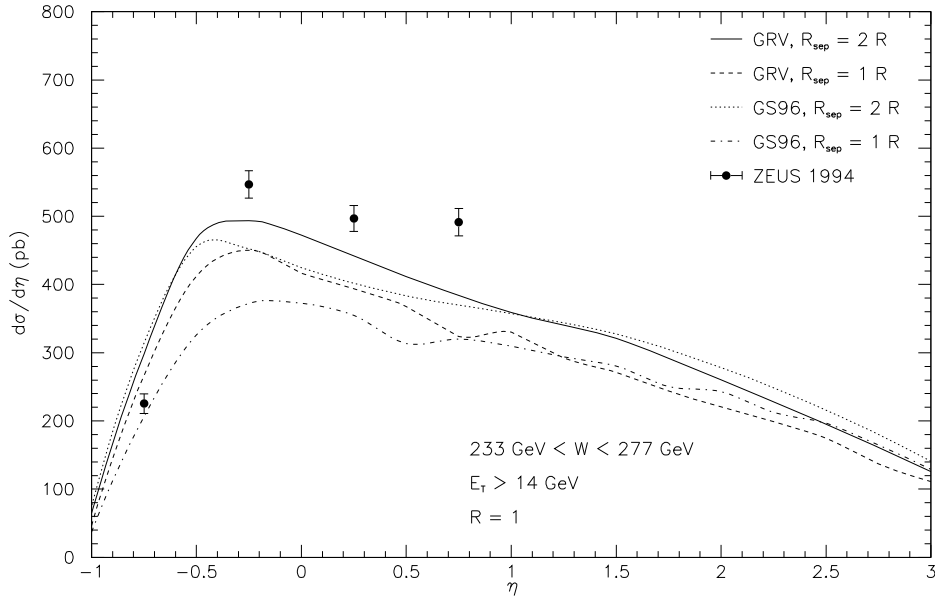


Figure 55: η dependence of the inclusive single-jet photoproduction cross section integrated over $233 \text{ GeV} < W < 277 \text{ GeV}$ with jet cone size $R = 1$. We compare our NLO prediction with GRV and GS96 photon parton densities and the two extreme R_{sep} values to 1994 data from ZEUS.

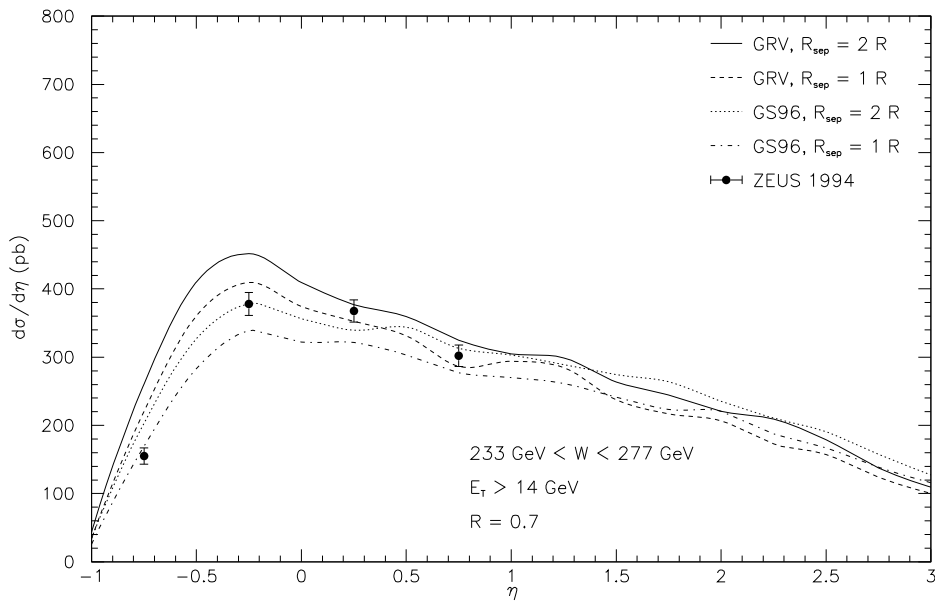


Figure 56: η dependence of the inclusive single-jet photoproduction cross section integrated over $233 \text{ GeV} < W < 277 \text{ GeV}$ with jet cone size $R = 0.7$. We compare our NLO prediction with GRV and GS96 photon parton densities and the two extreme R_{sep} values to 1994 data from ZEUS.

predictions in [12] for the case of the KTCLUS algorithm and in [10] for the EUCELL algorithm. These comparisons were done for the differential cross section $d\sigma/d\bar{\eta}$, where $\bar{\eta} = 1/2(\eta_1 + \eta_2)$ is the average rapidity of the observed jets with E_T larger than $E_{T_{\min}}$ for both observed jets. This common cut on the E_T of both jets causes some theoretical problems as has been noticed already some time ago [81].

The new measurements [83] are for the triple differential cross section $d^3\sigma/dE_T d\eta_1 d\eta_2$ using the k_T -cluster or the PUCELL algorithm. The jet with the highest E_T (leading jet, $E_T = E_{T_1}$) is required to have $E_T > 14$ GeV and the second highest- E_T jet to have $E_{T_2} > 11$ GeV. This cross section is symmetrized with respect to η_1 and η_2 and therefore double counted. By this symmetrization, the experimental ambiguity of determining the leading jet is avoided and the measured cross section corresponds to the calculated cross section where E_T corresponds to the trigger jet which is not necessarily the leading jet with the highest E_T . In order to have a handle to enhance direct over resolved photoproduction, one determines also the variable [5, 91]

$$x_\gamma^{\text{OBS}} = \frac{\sum_i E_{T_i} e^{-\eta_i}}{2x_a E_e}, \quad (5.19)$$

where the sum runs over the two jets of highest E_T and $x_a E_e$ is the initial photon energy. x_γ^{OBS} measures the fraction of the photon energy that goes into the production of the two hardest jets. The LO direct and resolved processes populate different regions of x_γ^{OBS} : $x_\gamma^{\text{OBS}} = 1$ for the direct process and $x_\gamma^{\text{OBS}} < 1$ for the resolved process. In NLO, the direct process populates also the region $x_\gamma^{\text{OBS}} < 1$. To obtain a measurement of the enriched direct photoproduction cross section, the cut $x_\gamma^{\text{OBS}} > 0.75$ is usually introduced.

Figure 57 shows $d\sigma/dE_T$ for six independent regions in the (η_1, η_2) plane. The upper curves in each plot give the dijet cross section for the entire x_γ^{OBS} region, and the lower curves which, to separate the curves, all have been scaled down by a factor of 5, present the cross section for the direct γ region $x_\gamma^{\text{OBS}} > 0.75$. The NLO calculations are performed for $Q_{\max}^2 = 4$ GeV² and 134 GeV $< W < 277$ GeV using the same parton densities for the proton and the photon as in the inclusive one-jet calculations. Furthermore we use $R_{\text{sep}} = 1.4R$ with $R = 1$ to simulate the PUCELL algorithm. We compare with the corresponding data from ZEUS [83] analyzed with the PUCELL algorithm. The agreement between the data and the theoretical predictions is quite reasonable. Except near the backward regions (the last two η_1, η_2 regions), the cross sections for the GRV and GS96 photon densities are very similar. To discriminate between them, the experimental errors must be reduced. We observe that the cross section for $x_\gamma^{\text{OBS}} > 0.75$ increases as compared to the full cross section (all x_γ^{OBS}) as E_T increases in agreement with the prediction from the calculation. This is the effect of the direct component which shows in general a flatter distribution with increasing E_T than the resolved cross section [12, 10]. We emphasize that the magnitude as well as the shape of the measured cross section is well reproduced by the calculations except for the first E_T bin and for the case that both jets are in the region $-1 < \eta_{1,2} < 0$. In this region (the last plot), the predictions lie above the data. The same cross section has been calculated also for the k_T -cluster algorithm. The results for the GS96 photon densities have been presented together with the corresponding experimental data in [83]. The agreement between data and theory is quite similar. In [83] also data for $d\sigma/d\eta_2$ for $E_T > 14$ GeV in three regions of η_1 and the KTCLUS algorithm are compared to our NLO calculations with the GRV-HO and GS96 parametrizations of the photon densities. Both shape and magnitude of the cross sections are roughly reproduced by the calculations except for the small η_1 region. Comparisons for the same cross section with the PUCELL cone algorithm have been done, too, but are not shown here [92].

The comparison between measurements and calculations of the triple differential cross section shown so far covers the dependence of this cross section in all three variables E_T , η_1 and η_2 . Another equivalent set of variables consists of the dijet invariant mass M_{JJ} , the rapidity of the dijet system y_{JJ} , and the scattering angle θ^* in the dijet center-of-mass system. The dijet invariant mass is obtained

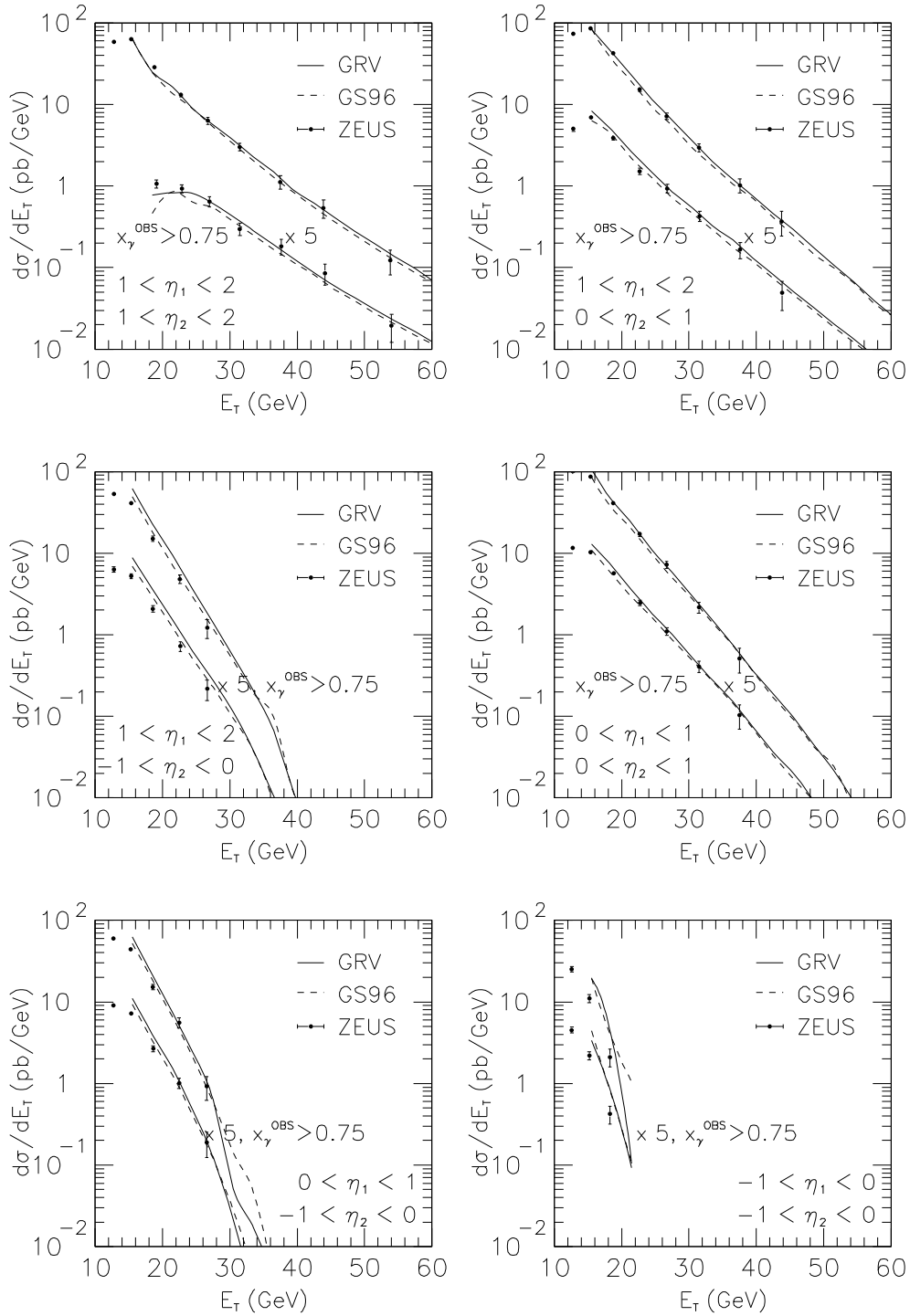


Figure 57: E_T dependence of the symmetrized dijet photoproduction cross section integrated over different rapidity bins. We compare our NLO prediction with GRV and GS96 photon parton densities and the full and upper range of x_γ^{OBS} to preliminary 1995 data from ZEUS.

from the relationship

$$M_{JJ}^2 = 2E_{T_1}E_{T_2} [\cosh(\eta_1 - \eta_2) - \cos(\phi_1 - \phi_2)], \quad (5.20)$$

where ϕ_1 and ϕ_2 are the azimuthal angles of the two jets in the HERA frame. For two jets back-to-back in ϕ and with equal E_T ,

$$M_{JJ} = 2E_T \cosh [(\eta_1 - \eta_2)/2] = 2E_T / \sin \theta^* \quad (5.21)$$

and $\cos \theta^* = \tanh[(\eta_1 - \eta_2)/2]$. For events with more than two jets, the two highest E_T jets are used to calculate M_{JJ} .

The distribution in the dijet mass M_{JJ} provides an additional test and is sensitive to the presence of resonances that decay into two jets. The dijet cross section as a function of $\cos \theta^*$ is sensitive to the parton-parton dynamics in the direct and resolved contributions [52]. Direct processes involve quark propagators in the t and u channels leading to a characteristic angular dependence proportional to $(1 - |\cos \theta^*|)^{-1}$. In the case of the resolved process, t -channel gluon exchange processes dominate which lead to an angular dependence proportional to $(1 - |\cos \theta^*|)^{-2}$. This exchange rises more steeply with increasing $|\cos \theta^*|$ than in the case of the direct processes. This different behavior in the angular dependence for resolved and direct processes was observed for $M_{JJ} > 23$ GeV [89]. We have calculated the NLO cross section $d\sigma/d\cos \theta^*$ for $x_\gamma^{\text{OBS}} < 0.75$ (= “resolved”) and $x_\gamma^{\text{OBS}} > 0.75$ (= “direct”) and have confirmed the different behavior in the two x_γ^{OBS} bins as shown in the data (not shown here).

The cross sections $d\sigma/dM_{JJ}$ and $d\sigma/d\cos \theta^*$ have been measured recently using the sample of dijet events found with the PUCCELL cone and the KTCLUS cluster algorithms. This analysis also includes the 1995 data which have an even higher statistics than used in the previous analysis [89] based on 1994 data. These cross sections have been measured in the kinematic region $Q^2 < 4$ GeV², $0.2 < x_a < 0.85$ as used previously. The two jets with highest E_T are required to have $E_{T_1}, E_{T_2} > 14$ GeV and the rapidities of these two jets are restricted to $-1 < \eta_1, \eta_2 < 2.5$. The cone radius is $R = 1$. The cross section $d\sigma/dM_{JJ}$ has been measured in the M_{JJ} range between 47 GeV and 120 GeV integrated over $|\cos \theta^*| < 0.85$. The cross section $d\sigma/d\cos \theta^*$ has been measured in the interval $0 < |\cos \theta^*| < 0.8$ integrated over $M_{JJ} > 47$ GeV. The experimental results [83, 93] for $d\sigma/dM_{JJ}$ are shown in figure 58 separately for the two jet definitions, where the cross sections for the k_T algorithm have been scaled down by a factor of 10 in order to separate the data obtained for the two jet definitions. Systematic errors are available, but only statistical errors are shown here. In figure 58, two NLO curves are compared to the measurements, the full curve being the result for the GRV-HO and the dashed curve the result for the GS96 parametrization of the photon densities. For the lower M_{JJ} values, the GRV density seems to describe the data better than the GS96 density. However, we have to consider that the data points have an additional systematic error from the energy scale uncertainty [83], which is also not shown in figure 58. It is remarkable that the predictions for both jet algorithms, PUCCELL and KTCLUS, agree well with the data over the full range of M_{JJ} where the cross sections exhibits a fall-off of almost three orders of magnitude.

The cross section $d\sigma/d\cos \theta^*$ as a function of $|\cos \theta^*|$ between 0 and 0.8 is plotted in figure 59. Here only the results for the PUCCELL algorithm are shown. For the KTCLUS algorithm, the corresponding cross section is presented in [83]. Again two curves are shown, for the GRV and GS96 photon densities, respectively. The theoretical curves agree reasonably well in magnitude and shape with the data. If it were not for the systematic error and the energy scale uncertainty, the comparison of data and theory would lead to a preference of the GRV over the GS96 density. We conclude, that the NLO calculations account reasonably well for the shape and the magnitude of the measured $d\sigma/dM_{JJ}$ and $d\sigma/d\cos \theta^*$ as well as the triple differential cross section $d^3\sigma/dE_T d\eta_1 d\eta_2$ as a function of E_T for various bins in η_1 and η_2 .

The last comparison between data and our NLO theory concerns the double-differential inclusive dijet cross section $d^2\sigma/dx_\gamma^{\text{OBS}} dE_T$ published just recently by the H1 collaboration [84]. This H1 analysis is based on 1994 data. The photoproduction events have been selected with the constraint $Q_{\text{max}}^2 = 4$ GeV² and $0.2 < x_a < 0.83$. The jets were constructed with the cone algorithm with cone size $R = 0.7$. The implementation of the cone algorithm in the H1 analysis is using a fixed cone and is

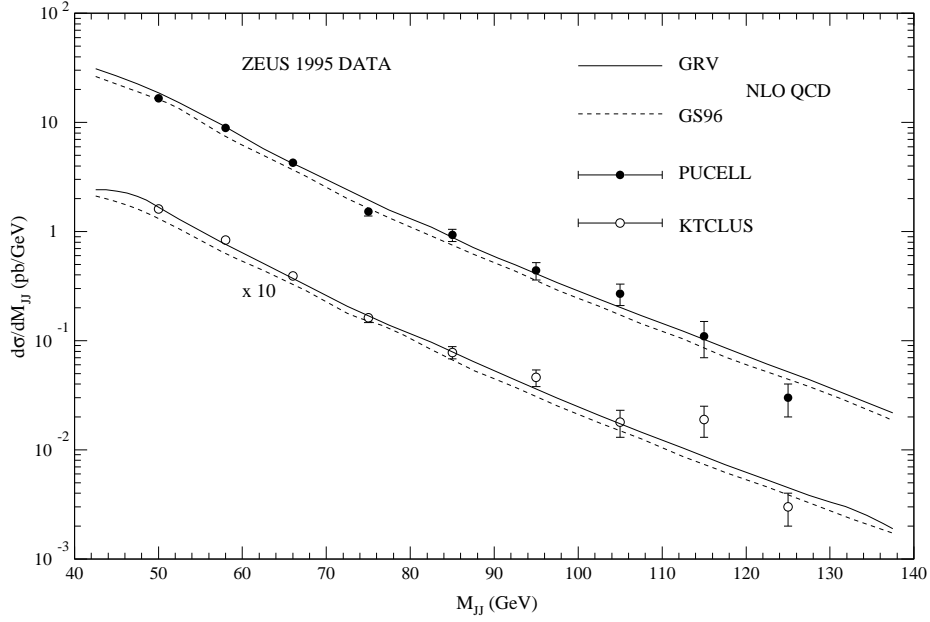


Figure 58: M_{JJ} dependence of the dijet photoproduction cross section integrated over $|\cos \theta^*| < 0.85$. We compare our NLO prediction with GRV and GS96 photon parton densities to 1995 data from ZEUS taken with the PUCCELL and KTCLUS jet algorithms.

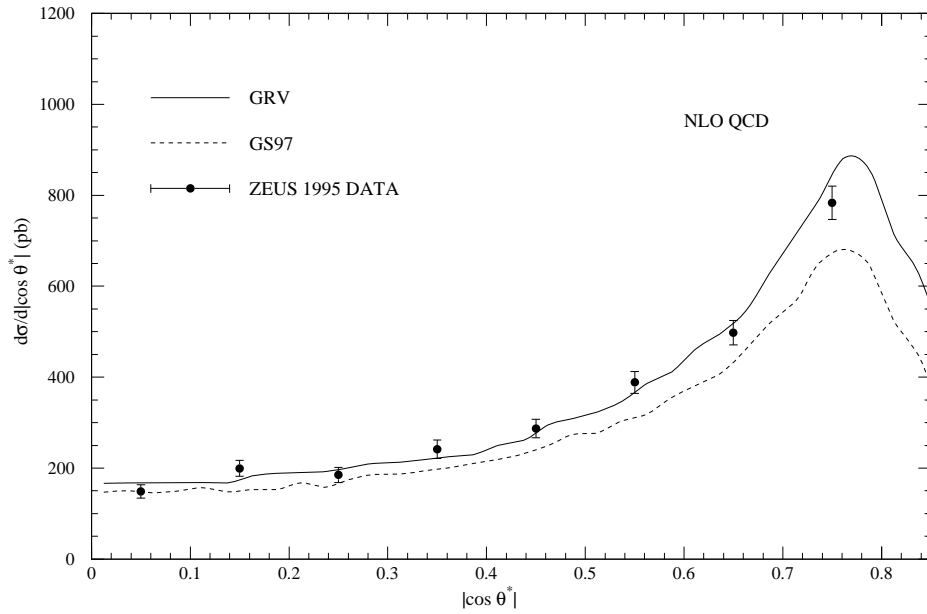


Figure 59: $|\cos \theta^*|$ dependence of the dijet photoproduction cross section integrated over $M_{JJ} > 47 \text{ GeV}$. We compare our NLO prediction with GRV and GS96 photon parton densities to 1995 data from ZEUS using the PUCCELL jet algorithm.

therefore similar to the EUCELL algorithm used by ZEUS. The rapidities of all jets are restricted to the region $-0.5 < \eta < 2.5$. In this specific two-jet analysis, E_T is the average transverse energy of the two jets with the highest E_T . The average rapidities of the two jets were between $0 < (\eta_1 + \eta_2)/2 < 2$ their difference being $|\eta_1 - \eta_2| < 1$, which corresponds to $|\cos \theta^*| < 0.46$. These two cuts on η_1 and η_2 ensured that the jets are in a region with good measurements of the hadronic energy in the detector. The transverse energies of the jets were restricted further to the range

$$\frac{|E_{T_1} - E_{T_2}|}{E_{T_1} + E_{T_2}} < 0.25, \quad (5.22)$$

and E_T was required to lie above 10 GeV. This cut and the cut (5.22) ensure that the transverse energy of both observed jets is above 7.5 GeV (to avoid underlying event problems) without using the same E_T cut for both jets, which would cause problems in the NLO calculations [81]. The observable x_γ^{OBS} was calculated from the same formula (5.19) as in the ZEUS analysis.

The NLO calculations of the inclusive dijet cross section $d^2\sigma/dx_\gamma^{\text{OBS}}d\log_{10}(E_T^2/\text{GeV}^2)$ is based on the same parton distributions for the proton and photon, respectively, as used in the previous sections. The scales are chosen equal to E_T as in the comparisons above. We have chosen $R_{\text{sep}} = 2R$, which we believe simulates best the fixed cone algorithm in the H1 analysis. Otherwise the same cuts on $E_{T_1}, E_{T_2}, \eta_1, \eta_2$ are applied as in the experimental analysis of the two-jet data. Our predictions are shown in figure 60, again for the GRV-HO (full line) and the GS96 (dotted line) photon parton distributions. The curves are compared to the measured cross sections using the statistical and systematic errors added in quadrature. The data and the theoretical cross sections in the various x_γ^{OBS} bins between 0.1 and 1 have been multiplied by factors 10^n ($n = 0, 1, 2, \dots, 6$) in order to separate the results for the seven bins in x_γ^{OBS} . Our calculations give a good description of the data in magnitude and shape as a function of E_T and x_γ^{OBS} , except for some deficiencies in the two highest x_γ^{OBS} ranges. The GRV-HO and the GS96 parton distribution functions each give a satisfactory description of the measured cross sections with slight preference for GS96 in the lowest bin $0.1 < x_\gamma^{\text{OBS}} < 0.2$. It is remarkable that even for $x_\gamma^{\text{OBS}} < 0.3$ the theoretical cross section agrees so well with the data. This region was always a problem in earlier analyses due to the underlying event problems (see for example the inclusive single-jet cross sections for $R = 1$ of the ZEUS collaboration discussed above). These problems are apparently avoided in this analysis by choosing $R = 0.7$ and applying sufficiently large E_T cuts. The deviations of the calculated from the measured cross sections could easily be due to hadronization effects which are not included in the NLO calculations.

The cross section $d^2\sigma/dx_\gamma^{\text{OBS}}d\log_{10}(E_T^2/\text{GeV}^2)$ as a function of x_γ^{OBS} for fixed E_T should show more clearly the dependence on the photon parton distribution sets. Therefore, we have calculated this cross section for $E_T = 11$ GeV and 13 GeV. The result is shown in figures 61 and 62 for the GRV-HO and the GS96 parametrizations and compared to the H1 data [84], again including statistical and systematic errors added in quadrature. The agreement with the data is reasonable for both E_T 's. It seems that the hadronic maximum at $x_\gamma^{\text{OBS}} \simeq 0.3$ is reduced from $E_T = 11$ GeV to $E_T = 13$ GeV, whereas the pointlike/direct peak at $x_\gamma^{\text{OBS}} > 0.8$ is enhanced flattening out the valley in between. This might be due to the QCD evolution of the VMD part of the photon structure function and the increased importance of the anomalous piece and the direct contribution at larger scales. For $x_\gamma^{\text{OBS}} < 0.3$, we see a somewhat better agreement for the prediction with GS96 which we already noticed in connection with the comparison in figure 60. Both parton distribution sets give very similar predictions in the intermediate x_γ^{OBS} range. The different results in the low and high x_γ^{OBS} regions show us clearly how the experimental data must improve in accuracy before we can discriminate between the two alternative parametrizations of the photon distributions used in our calculations.

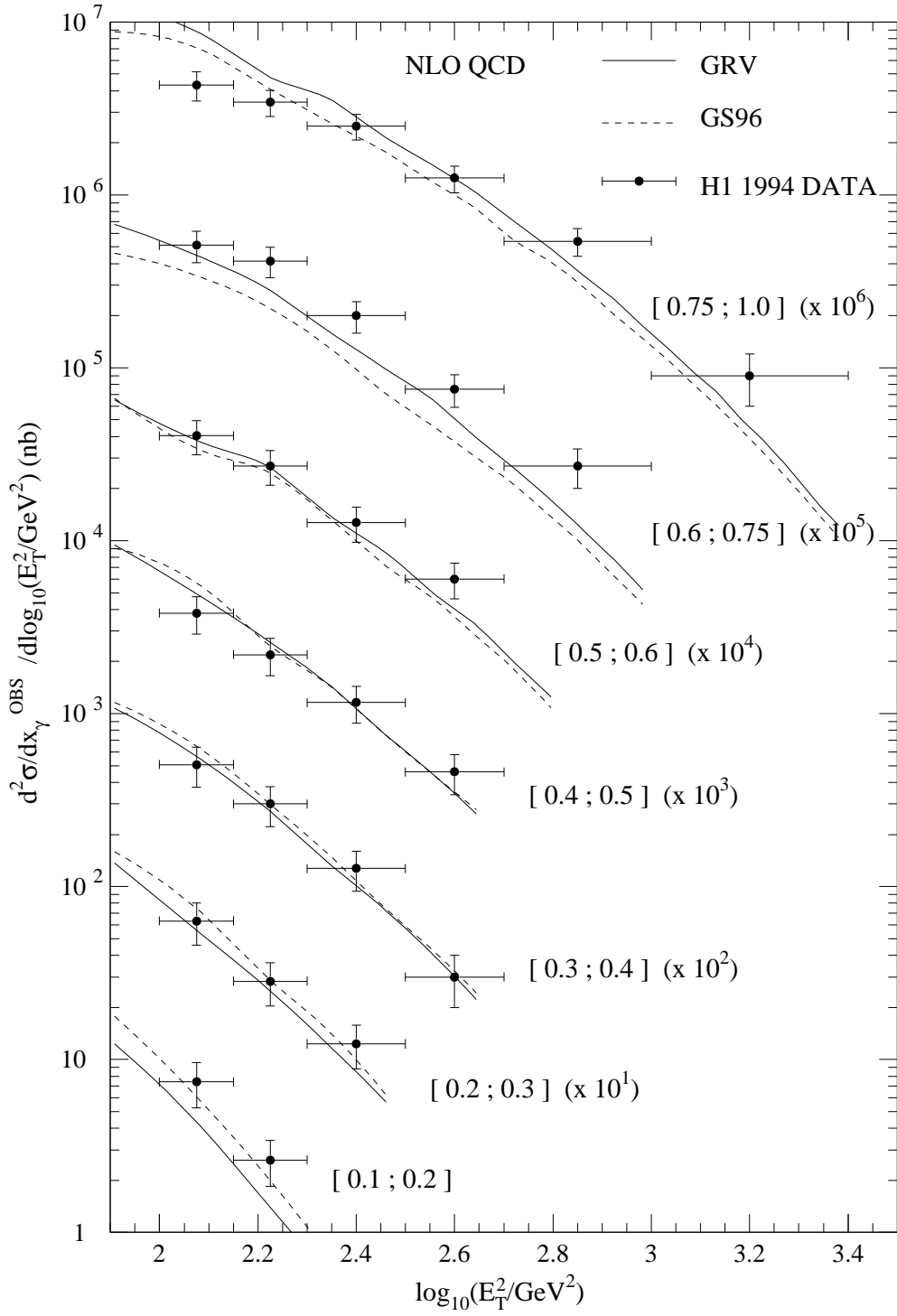


Figure 60: E_T dependence of the symmetrized dijet photoproduction cross section integrated over different x_γ^{OBS} bins. We compare our NLO prediction with GRV and GS96 photon parton densities and $R_{\text{sep}} = 2R$ to 1994 data from H1.

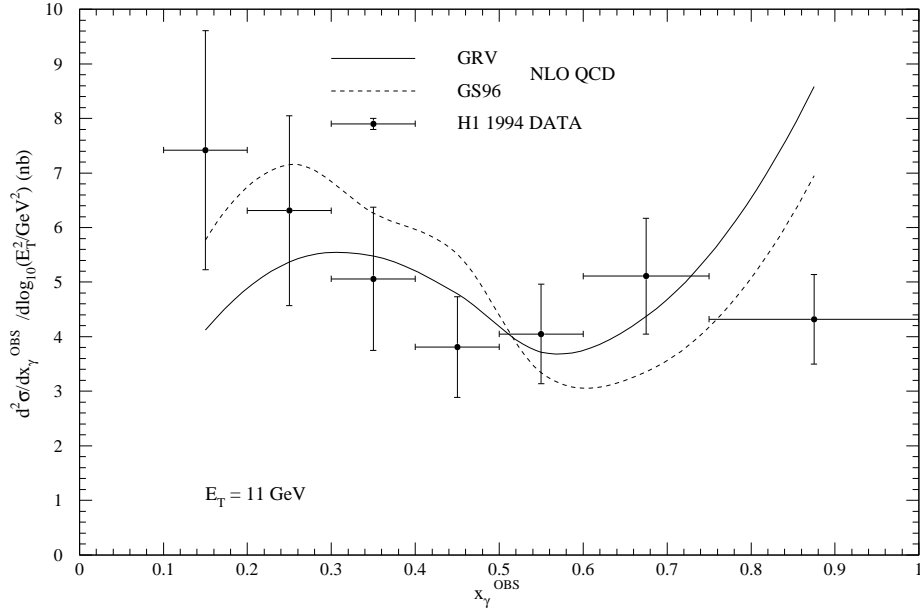


Figure 61: x_γ^{OBS} dependence of the dijet photoproduction cross section at $E_T = 11 \text{ GeV}$. We compare our NLO prediction with GRV and GS96 photon parton densities to 1994 data from H1 using a fixed cone algorithm.

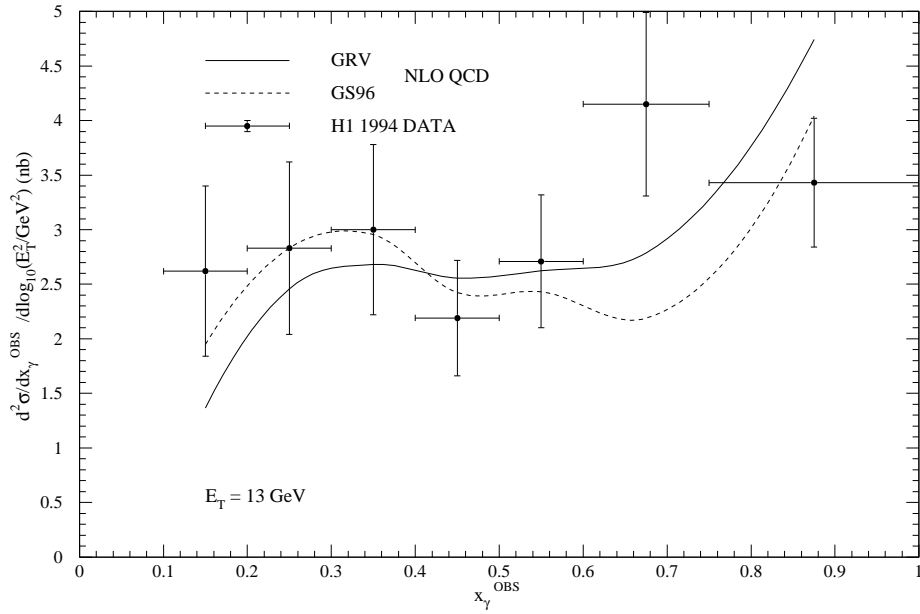


Figure 62: x_γ^{OBS} dependence of the dijet photoproduction cross section at $E_T = 13 \text{ GeV}$. We compare our NLO prediction with GRV and GS96 photon parton densities to 1994 data from H1 using a fixed cone algorithm.

6 Numerical Results for Photon-Photon Scattering

In this section we report on numerical results for inclusive one-jet and two-jet cross sections in $\gamma\gamma$ collisions. We use the analytical results that have been calculated in leading order in section 3 and in next-to-leading order in section 4. The calculation proceeds as in the photoproduction case except that we now have three contributions: (a) the direct contribution, where both virtual photons interact directly with the quarks, (b) the single-resolved contribution, where only one of the photons interacts directly and the other photon is resolved, and (c) the double-resolved contribution, where both photons are resolved. It is clear that (b) and (c) have their analogs in the photoproduction case. For case (a) the analytical results are given in section 3.4 (Born matrix element), in section 4.1.3 (virtual corrections), and in section 4.2.9 (real corrections).

Three partons appear in the final state of all three contributions when we include the NLO corrections. Two of these partons are recombined if they obey the cluster or the jet-cone condition. For the $\gamma\gamma$ process we shall use only the Snowmass jet algorithm already introduced in section 2.4 with $R = 1$ and $R_{\text{sep}} = 2$. This algorithm was applied in the analysis of the TOPAZ, AMY [1], and OPAL [2] data. However, there is no problem to introduce other jet definitions in the calculations, as we have done it for the γp case. Before we compare our results with recent data from the OPAL collaboration [94] obtained at LEP2, we shall present in the next section some general results and discuss some tests of the numerical program.

6.1 Tests and General Results

Similar to the γp case, we have checked that our results are independent of the y -cut when the analytic results are added to the numerical results of the $2 \rightarrow 3$ processes. This has been studied for all $2 \rightarrow 3$ processes separately. As an example, we show in figure 63 the y -dependence of the complete double-resolved two-jet cross section for LEP1 kinematic conditions and at $\eta_1 = \eta_2 = 0$, $E_T = 10$ GeV. As to be expected, the 2-particle contribution is negative and decreases with decreasing y whereas the 3-particle contribution is positive and shows the opposite behavior. The sum of both contributions is independent in the range $10^{-4} < y < 10^{-2}$. For larger y -cuts the independence breaks down because we neglected terms of order y in the analytic contributions. The slight decrease for $y < 10^{-4}$ is caused by insufficient accuracy in the numerical integrations. This could be improved with more CPU time.

For the results in figures 63 to 65, we use the LEP1 center-of-mass energy $\sqrt{s} = 90$ GeV. The photon spectrum is calculated from the formula

$$F_{\gamma/e}(x) = \frac{\alpha}{2\pi} \left[\frac{1 + (1-x)^2}{x} \ln \frac{E^2 \theta_c^2 (1-x)^2 + m_e^2 x^2}{m_e^2 x^2} + 2(1-x) \left(\frac{m_e^2 x}{E^2 \theta_c^2 (1-x)^2 + m_e^2 x^2} - \frac{1}{x} \right) \right] \quad (6.1)$$

where E is the beam energy and $\theta_c = 3^\circ$. The parton distributions are computed with the NLO parametrization of GRV [33] transformed to the $\overline{\text{MS}}$ subtraction scheme. For all scales we set $\mu = M_a = M_b = E_T$ and put $N_f = 5$. $\Lambda_{\overline{\text{MS}}}^{(5)} = 130$ MeV corresponding to $\Lambda_{\overline{\text{MS}}}^{(4)} = 200$ MeV as fixed in the GRV distributions. Inclusive single-jet cross sections have been calculated earlier [7, 95]. In these calculations, the double-resolved contribution has been obtained with a different method for canceling infrared and collinear singularities [73] which, however, can be applied only to the computation of this particular cross section. These results were compared to TOPAZ and AMY [1] jet production data and good agreement was found [95].

The fact that a different method for calculation of the double-resolved contribution to the inclusive one-jet cross section was available was utilized to test the new results based on the y -cut slicing method. Good agreement between the two independent methods was achieved for all double-resolved processes ($qq', q\bar{q}', qq, q\bar{q}, qq, gg \rightarrow$ one jet) separately.

In the following figures we show results for $d^3\sigma/dE_T d\eta_1 d\eta_2$ as a function of E_T for special η values and as function of η_2 for $E_T = 5$ GeV and $\eta_1 = 0$ using LEP1 kinematics. In figure 64 we show the

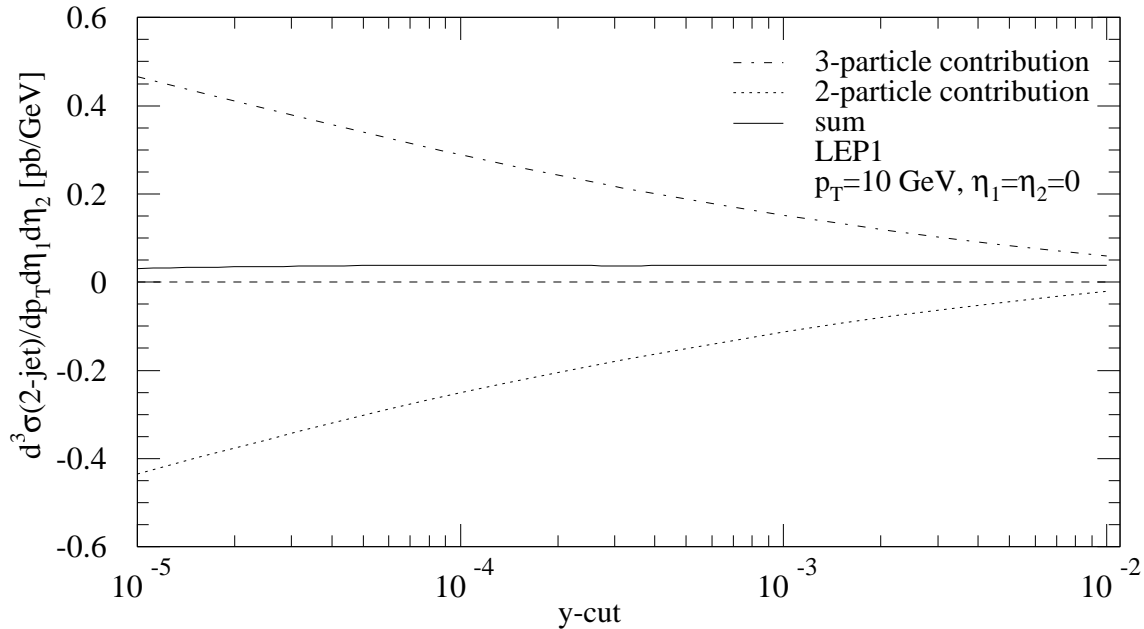


Figure 63: *Dependence of the inclusive dijet cross section on the y -cut, the boundary between analytical and numerical integration. Only the double-resolved part is shown.*

E_T distribution for $\eta_1 = \eta_2 = 0$ in LO and NLO. We plotted the direct, the single-resolved, and the double-resolved contributions separately and show the sum of all three contributions. From the E_T spectrum it is already visible that the direct contribution is reduced by the NLO corrections whereas for the resolved contribution the NLO corrections are positive. The correction in the double-resolved contribution is near 100%. This is seen more clearly in the lower part of figure 64, where we plotted the k -factor as a function of E_T for the three contributions and the sum. We remark that the LO curves are calculated with the two-loop α_s and the same NLO parton distributions of the photon as in the NLO calculation. For a genuine LO prediction, one would choose the one-loop α_s formula and LO parton distributions. This would change the k -factors. In figure 64, the k -factors show just the influence of the NLO corrections to the parton-parton scattering cross sections. The upper part of figure 64 also shows how the contributions of the three components (direct, single-resolved, and double-resolved) sum up to the full inclusive two-jet cross section. For relatively small E_T , this cross section is dominated by the two resolved components. In this region we have a positive NLO correction and a k -factor larger than 1. In the medium E_T range and for large E_T , the direct component dominates, the net NLO correction is negative, and the k -factor is less than 1. It is clear that the importance of the resolved parts for larger E_T increases with increasing center-of-mass energy.

In figure 65, we show the η_2 distribution for $\eta_1 = 0$ and $E_T = 5$ GeV, again for the three components separately and their sum in LO and in NLO. The k -factors corresponding to the upper part of figure 65 are shown in the lower part. The three components show a very distinct behavior as a function of η_2 . The single-resolved contribution does not have a plateau as broad as the other two components. So, by measuring in different η_2 regions, it might be possible to enhance one or two of the three contributions.

An important test of our calculations is the compensation of the factorization scale dependence

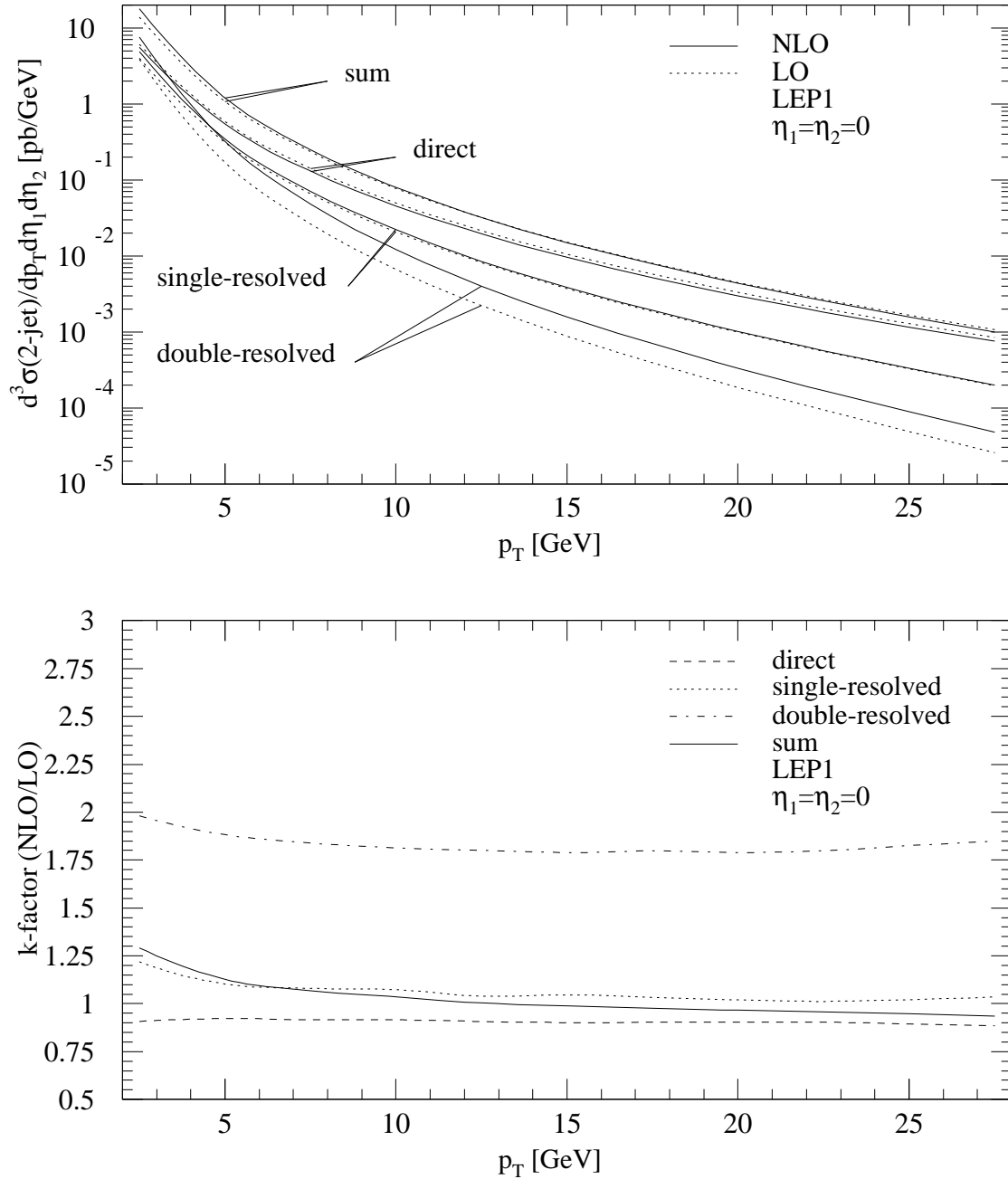


Figure 64: Direct, single-resolved, and double-resolved contributions and their sum in LO and NLO for the inclusive two-jet cross section at LEP1. Upper figure: E_T -spectrum, lower figure: correspondent k -factors.

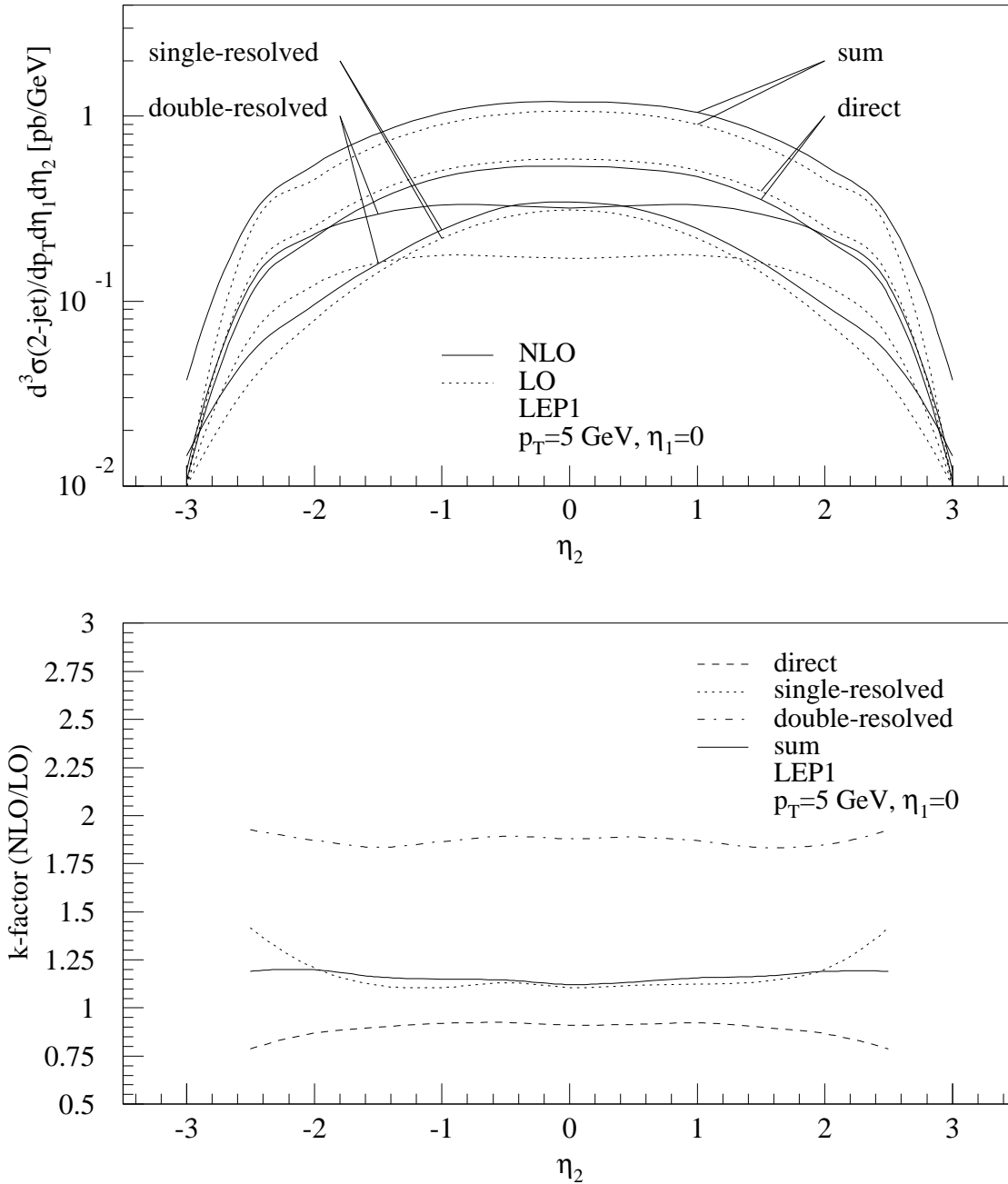


Figure 65: *Direct, single-resolved, and double-resolved contributions and their sum in LO and NLO for the inclusive two-jet cross section at LEP1. Upper figure: η -spectrum, lower figure: correspondent k -factors.*

between the direct and the single-resolved components and between the single-resolved and the double-resolved components. That this compensation works is shown in figures 66 a) and b) for the inclusive two-jet cross section at $E_T = 10$ GeV and $\eta_1 = \eta_2 = 0$. For this test we applied LEP2 kinematics, i.e. $\sqrt{s} = 175$ GeV and $\theta_c = 1.72^\circ$ in the photon spectra. In figure 66 a), the NLO direct and the LO single-resolved cross section, where only the upper photon γ_a is resolved, are plotted as a function of M_a/E_T . The dependence of the NLO direct contribution on M_a is clearly visible. This is opposite to the dependence of the single-resolved contribution originating from the scale dependence of the parton distributions. As one can see, the sum is constant as a function of M_a/E_T . The same compensation occurs between the NLO single-resolved and the LO double-resolved cross section. In the single-resolved cross section, only the lower photon γ_b is resolved. Also in this case (figure 66 b) the sum of both contributions is rather independent of M_a . Another important topic for the NLO theory is the question of the overall scale dependence and whether this is reduced in NLO as compared to the LO cross section. First we show the dependence on the renormalization scale μ alone with the factorization scales $M_a = M_b = E_T$ fixed. In figure 67 a) it is clearly visible that in NLO the dependence on μ is reduced as compared to LO when μ is varied between $\mu = E_T/2$ and $2E_T$. If all scales $\mu = M_a = M_b = M$ are equal and this common scale M varies in the same range for the LO and NLO cross section we obtain the curves in figure 67 b). We see that the dependence in LO is such that the cross section as a function of M increases which is opposite to the behavior as a function of the renormalization scale μ in figure 67 a). This comes from the dependence on the factorization scale which is not compensated (see figures 66 a) and b)). In NLO we have the effect that the dependence on the factorization scale is reduced due to the presence of the NLO corrections, so that in NLO the cross section as a function of M is fairly constant, i.e. it decreases only slightly with increasing M/E_T . In conclusion we can say that the NLO cross section is nearly independent of the scales and therefore presents a much more solid prediction than the LO cross section.

When high statistics data become available, one could test the variation of the jet cross section with changing cone radius R . This has been studied for the dijet cross section for $E_T = 10$ GeV and $\eta_1 = \eta_2 = 0$. The result is displayed in figure 68 where the NLO cross section $d^3\sigma/dE_T d\eta_1 d\eta_2$ is shown as a function of R for $R \geq 0.5$. It increases as a function of R almost like $a + b \ln R$ and somewhat stronger for $R > 1$. With our definition of the LO cross section the NLO result at $R = 0.9$ is equal to the LO cross section, so that the NLO corrections stay moderate if R varies between 0.7 and 1.

6.2 Comparison with Experimental Data

The first measurements of jet production in $\gamma\gamma$ reactions were done by the TOPAZ and AMY [1] collaborations at TRISTAN. They presented data for the inclusive one- and two-jet cross sections as a function of E_T in the range $2.5 \text{ GeV} < E_T < 8 \text{ GeV}$ with different ranges of rapidity in the two experiments. These data were compared to predictions based on the theoretical work presented here in [9]. Good agreement between the data of both experiments and the theoretical results was achieved for the one- and two-jet cross sections. The distribution in E_T and also the absolute normalization agreed when the parton distributions were described by the GRV set. At the energy of the TRISTAN collider ($\sqrt{s} = 58$ GeV), the main contribution to the jet cross sections comes from the direct process. However, the data could not be reproduced by the direct component alone. The resolved contributions were necessary to obtain agreement over the whole E_T range.

In the fall of 1995 the LEP ring was operated at the center-of-mass energy of 133 GeV. During the short run period, the OPAL collaboration collected data for jet cross sections in $\gamma\gamma$ collisions. They measured the inclusive one-jet cross section integrated over $|\eta| < 1.0$ and the inclusive two-jet cross section for $|\eta_1|, |\eta_2| < 1$ as a function of E_T in the range $3.0 \text{ GeV} < E_T < 14 \text{ GeV}$ [2]. These data were compared to our calculated NLO one- and two-jet cross sections in [2, 9], and good agreement between the measurements and the predictions was found. The calculations were done with $N_f = 5$, $\Lambda_{\overline{\text{MS}}}^{(5)} = 130$ MeV and the NLO GRV parton distributions. In [11], also the dependence of the two-jet

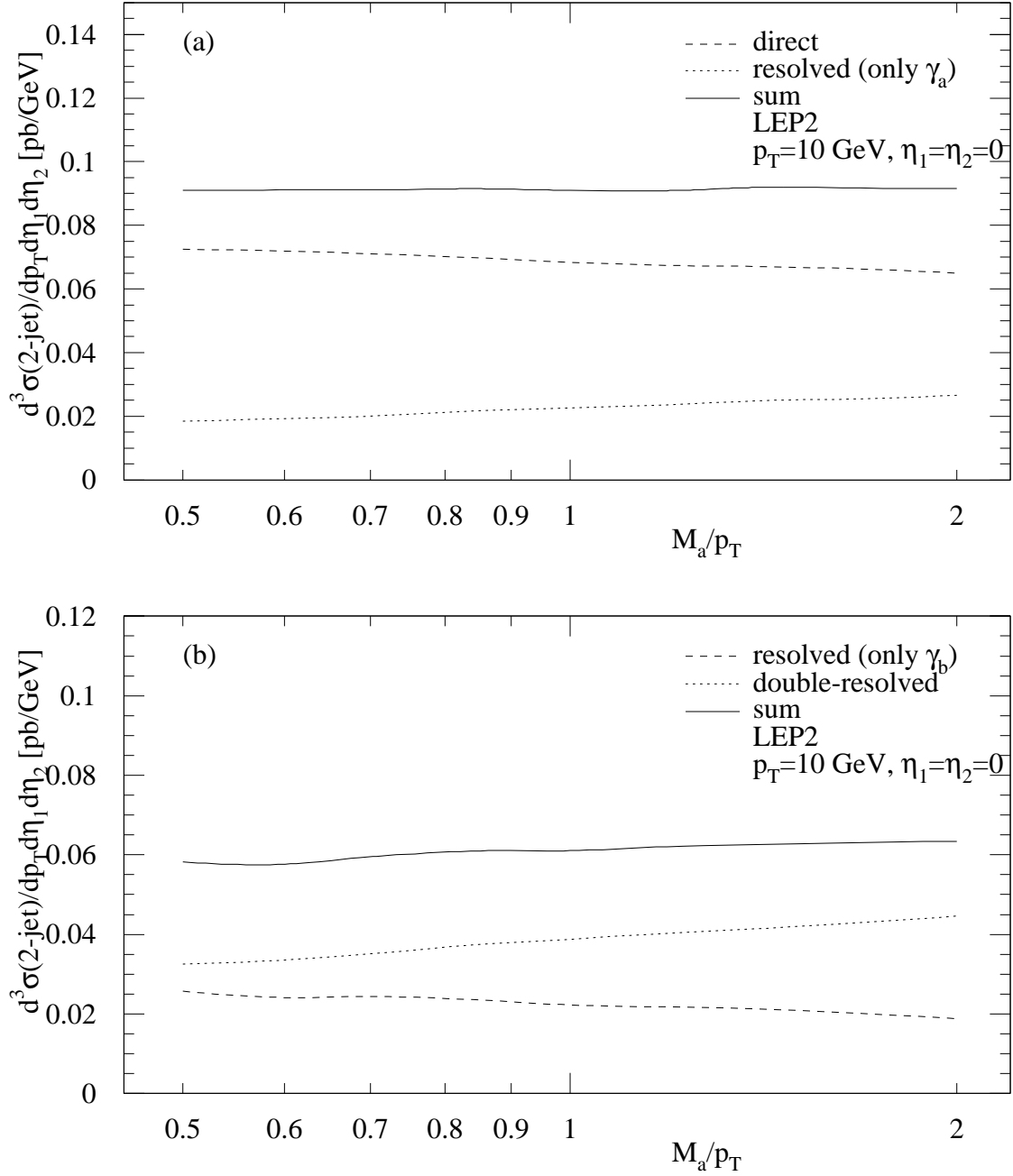


Figure 66: *Dependence of the inclusive two-jet cross section on the factorization scale M_a in the photon γ_a . Upper figure: NLO direct and LO single-resolved photon (only γ_a resolved), lower figure: NLO single-resolved (only γ_b resolved) and LO double-resolved photon.*

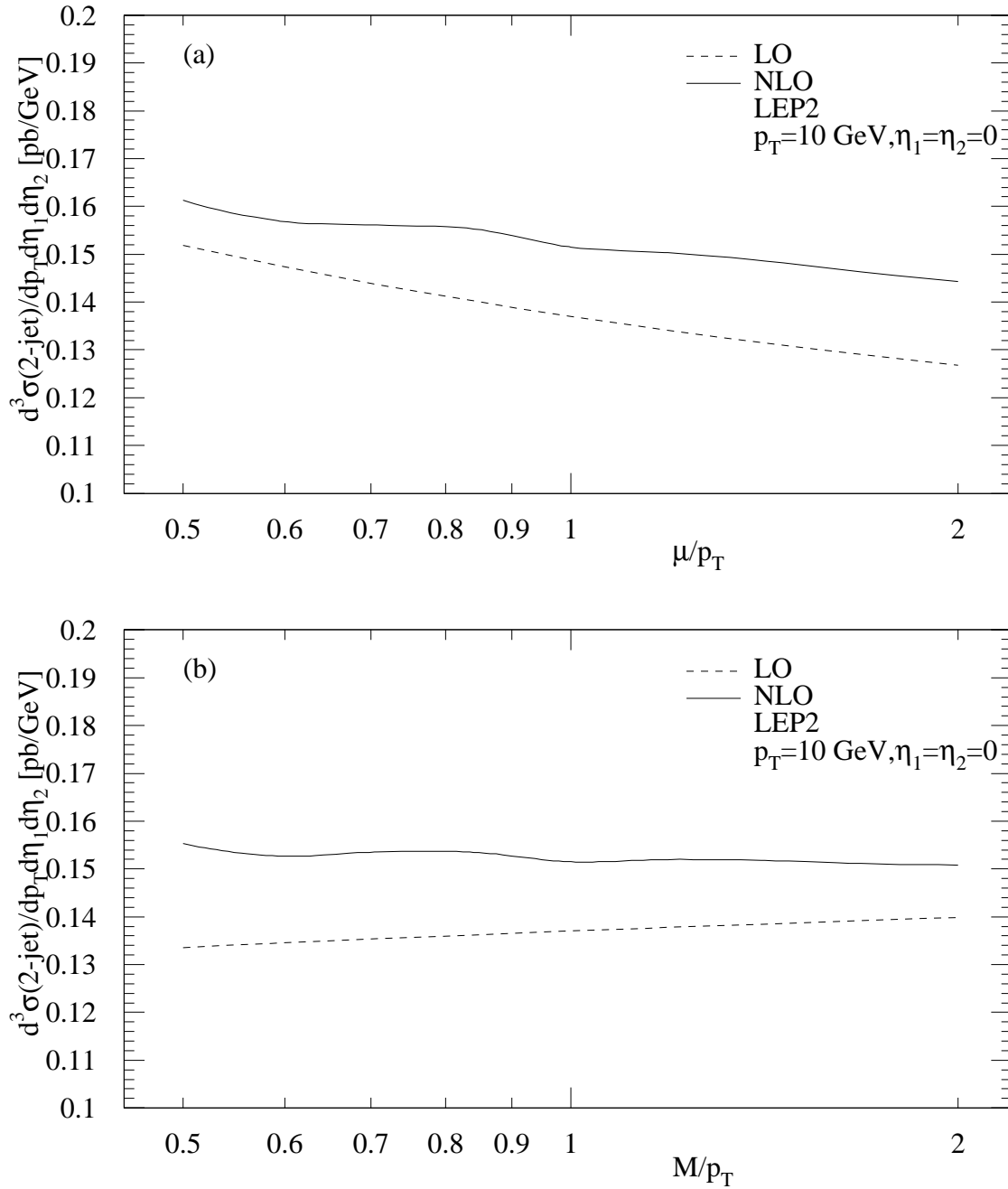


Figure 67: *Dependence of the inclusive two-jet cross section on the renormalization scale μ (a) and on the variation of all scales $\mu = M_a = M_b = M$ (b).*

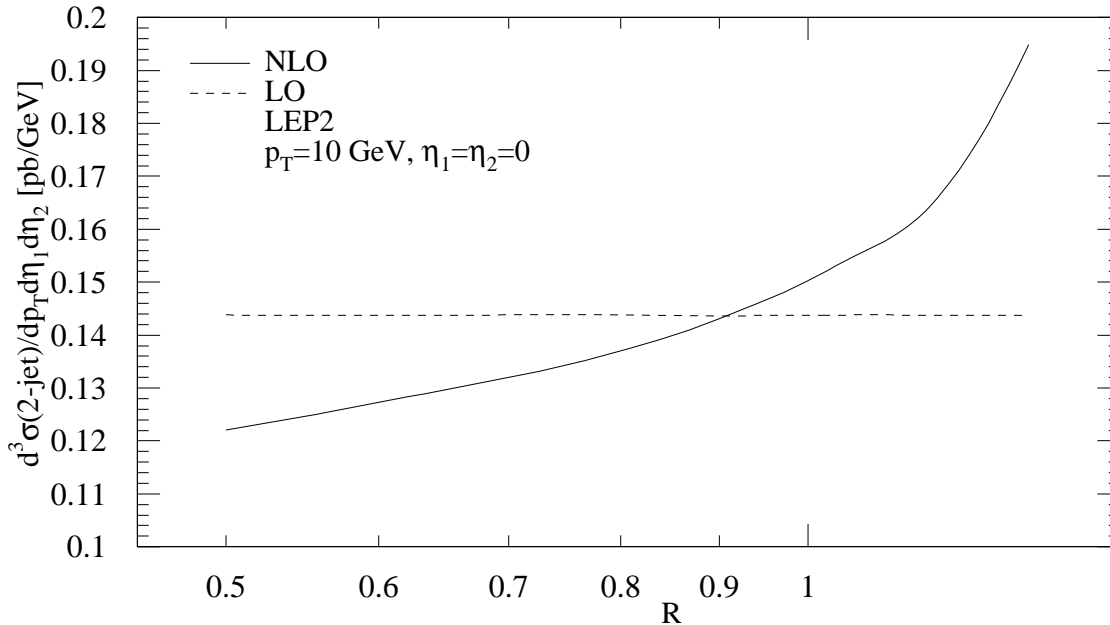


Figure 68: *Dependence of the inclusive two-jet cross section on the size of the jet cone R for LO and NLO.*

prediction on other parton distribution sets was studied with the result that the other NLO sets, GS [37] and ACFGP [34], lead to almost the same results and the OPAL data could not be used to rule out one of these sets. In these calculations, the photon spectra were described by eq. (6.1) with $\theta_c = 1.43^\circ$ as in the experimental setup. The cone radius was $R = 1$ and $R_{\text{sep}} = 2$.

In the meantime the LEP energy was raised and the OPAL collaboration extended their measurements to the center-of-mass energies of $\sqrt{s} = 161$ GeV and 172 GeV [94]. They presented one-jet cross sections for $|\eta| < 1$ and two-jet cross sections for $|\eta_1|, |\eta_2| < 1$ ($\sqrt{s} = 161$ GeV) and two-jet cross sections for $|\eta_1|, |\eta_2| < 2$ ($\sqrt{s} = 161$ GeV and 172 GeV). The latter cross section was compared to our predictions already in [94]. As an example, we show the experimental results of the OPAL collaboration from the $\sqrt{s} = 161$ GeV run. In figures 69 and 70 the inclusive one- and two-jet cross section data as a function of E_T for jets with $|\eta| < 1$ are compared to the NLO calculations with $R = 1$, $R_{\text{sep}} = 2$, and the NLO GRV parametrization for the photon. The parameters were $\theta_c = 33$ mrad, $\Lambda_{\overline{\text{MS}}}^{(5)} = 130$ MeV, and $\mu = M_a = M_b = E_T$. The direct, single-resolved, double-resolved cross sections and their sum (full line) are shown separately. As we can see, the agreement between data and the predictions is good. The resolved cross sections dominate in the region $E_T \leq 7$ GeV, whereas at high E_T the direct cross section dominates. We emphasize that the inclusive two-jet cross section is measured using events with at least two jets. If an event contains more than two jets, only the two jets with the highest E_T values are used. This definition of the inclusive two-jet cross section coincides with what is done in the theoretical calculation. The good agreement between measured and calculated cross section is remarkable, since the NLO calculation gives the cross sections for massless partons, which are combined to jets, whereas the experimental jet cross sections are measured for jets built of hadrons. The good agreement then tells us that in $\gamma\gamma$ jet production, parton-hadron duality is realized to a high degree and no major disturbance due to underlying event energy is present. This

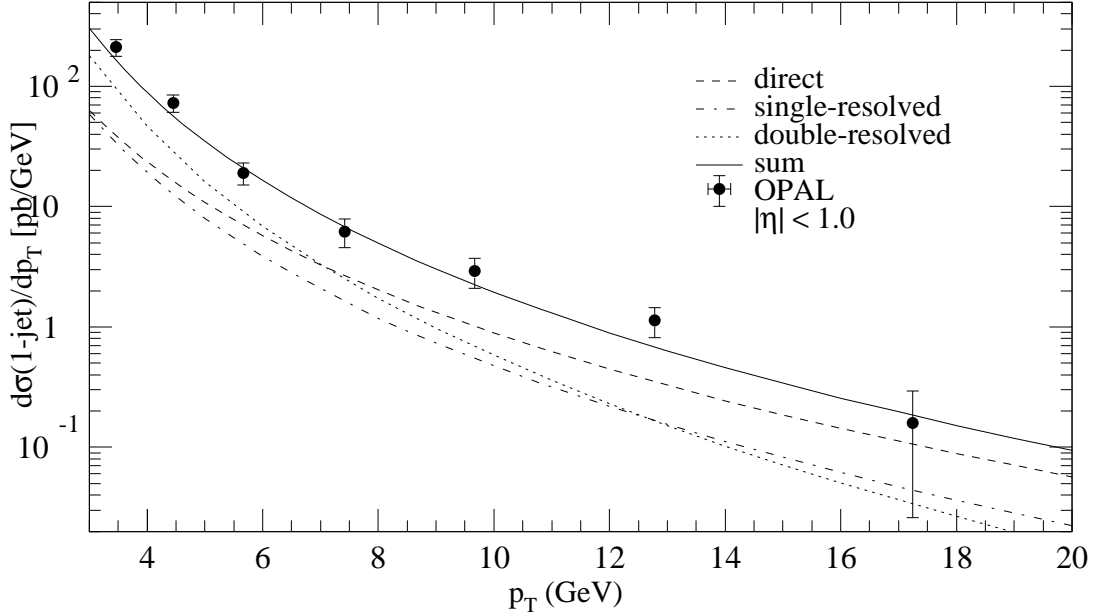


Figure 69: *The inclusive one-jet cross section as a function of E_T with $|\eta| < 1$ compared to our NLO calculation. The direct, single-resolved, and double-resolved cross sections and the sum (full line) are shown separately.*

is in contrast to what we observed for γp jet production at lower E_T where there was disagreement at the larger rapidity values.

As a last point we confront the recently published $|\cos\theta^*|$ distribution of the OPAL collaboration with the theoretical predictions. These data were taken for two x_γ^{OBS} intervals to separate direct and resolved dominated contributions similar as it was done for jet production in ep scattering (see section 5). The selection cuts were $x_\gamma^\pm > 0.8$ (direct-dominated) and $x_\gamma^\pm < 0.8$ (resolved-dominated), where

$$x_\gamma^+ = \frac{\sum_{i=1}^2 E_{T_i} e^{-\eta_i}}{2x_a E_{e^+}} \quad (6.2)$$

$$x_\gamma^- = \frac{\sum_{i=1}^2 E_{T_i} e^{\eta_i}}{2x_b E_{e^-}} \quad (6.3)$$

are in LO equal to the fractions of the photon energies of the upper and lower vertex entering the hard parton-parton scattering process. Thus, in LO the direct process has $x_\gamma^+ = x_\gamma^- = 1$, whereas the double-resolved process occurs only for $x_\gamma^+, x_\gamma^- < 1$. The direct cross section data for $|\cos\theta^*|$ between 0 and 0.85 for the two event classes $x_\gamma^\pm > 0.8$ and $x_\gamma^\pm < 0.8$ are exhibited in figure 71. The data points are normalized to have an average value of 1 in the first three bins and are plotted at the center of the bins. The data with $x_\gamma^\pm > 0.8$ show a small rise with increasing $|\cos\theta^*|$, whereas the data for $x_\gamma^\pm < 0.8$ show a much stronger rise in $|\cos\theta^*|$, similar to the findings in γp scattering, where we pointed out how this qualitative behavior is related to the exchanges of the LO cross sections. The theoretical curves for the cross section in the two x_γ^\pm ranges are also shown using the two sets for the parton distribution functions, NLO GRV and NLO GS96 [38]. In these calculations, $|\eta_1|, |\eta_2| < 1$, $|\bar{\eta}| < 1$, where $\bar{\eta} = \frac{1}{2}(\eta_1 + \eta_2)$, and the invariant two-jet mass $M_{JJ} > 12$ GeV, as in the experimental selection [94]. M_{JJ} is calculated from the two jets with highest E_T . All other parameters are as stated

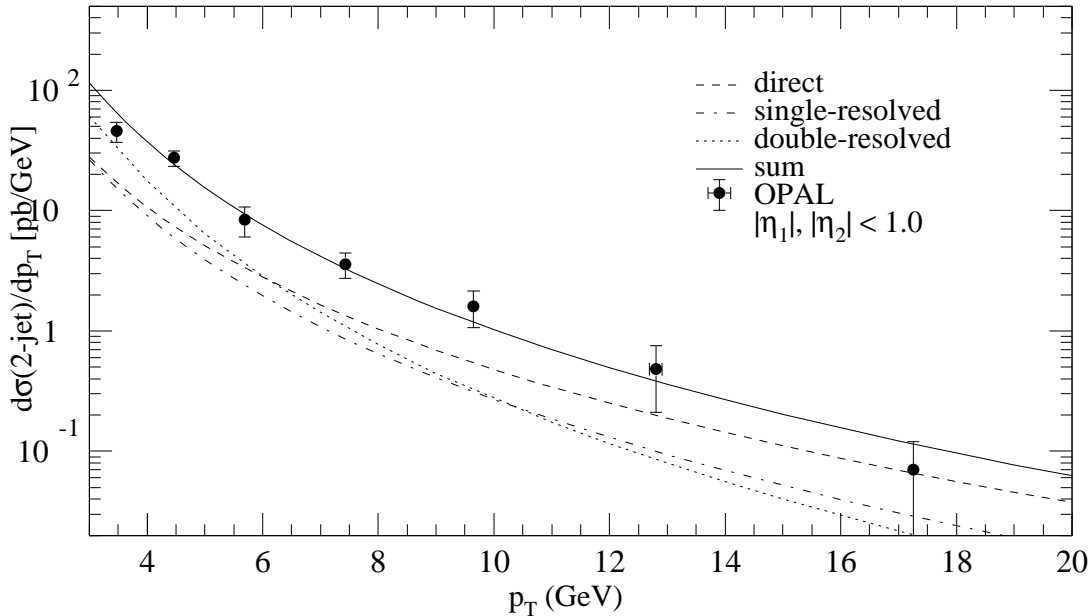


Figure 70: *The inclusive two-jet cross section as a function of E_T with $|\eta_1|, |\eta_2| < 1$ compared to our NLO calculation. The direct, single-resolved, and double-resolved cross sections and the sum (full line) are shown separately.*

previously. The theoretical curves in figure 71 are normalized at $|\cos \theta^*| = 0$. We observe that the shape of the $|\cos \theta^*|$ distributions in the two x_γ^\pm bins is nicely reproduced in comparison with the data. This means that the qualitative behavior known from LO arguments is still present in NLO and agrees with the experimental data. On the quantitative side, the theoretical cross sections seem to increase stronger towards $|\cos \theta^*| = 1$ than the data, both the direct and the double-resolved event sample, indicate. However, a new OPAL analysis shows that the quantitative agreement there is much better for the resolved sample, if the k_T -cluster algorithm is used instead of the cone algorithm. We remark that the data analysis is still going on, i.e. the experimental data are still preliminary and we have to wait for the final analysis before further conclusions can be drawn.

7 Summary and Outlook

In this work we have presented a complete next-to-leading order calculation of direct and resolved photoproduction of one and two jets in γp and $\gamma\gamma$ collisions. Photon-proton and photon-photon scattering were considered simultaneously since the two processes are intimately related to each other. The results are of great importance not only as a test of quantum chromodynamics (QCD), but also for the measurement of the proton and photon parton densities currently performed at HERA and LEP.

First, we embedded the perturbatively calculable photon-parton scattering in the experimentally observable electron-proton scattering process, using the Weizsäcker-Williams approximation and universal structure functions for the proton and the photon. For these structure functions, we chose recent next-to-leading order parametrizations from the CTEQ and GRV collaborations. Special emphasis was given to experimental and theoretical ambiguities in the Snowmass jet definition.

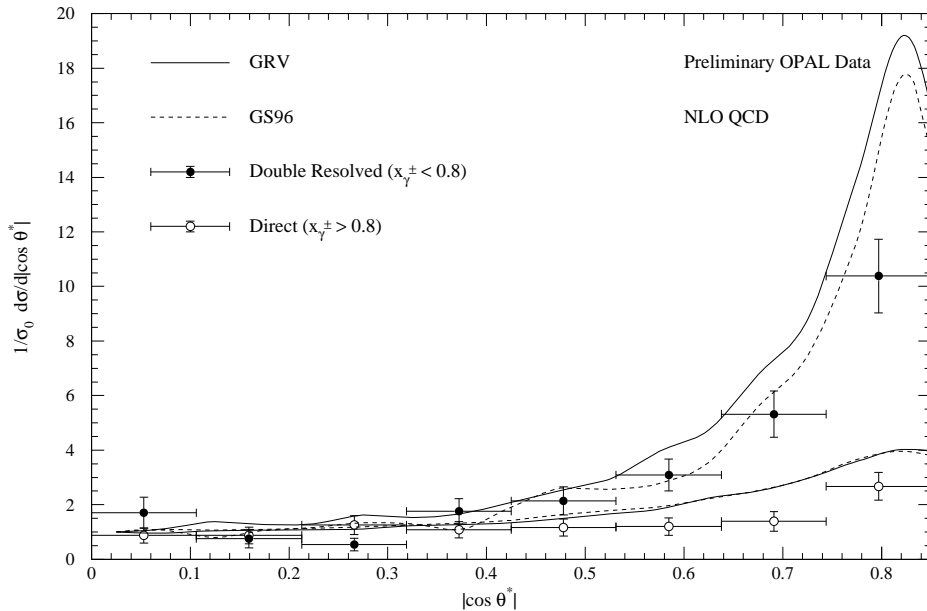


Figure 71: $|\cos \theta^*|$ dependence of the dijet $\gamma\gamma$ cross section for $M_{JJ} > 12 \text{ GeV}$, $|\eta_1|, |\eta_2| < 1$ and $|\bar{\eta}| < 1$. We compare our NLO prediction with GRV and GS96 photon parton densities for direct-enhanced and double-resolved enhanced regions to preliminary data from OPAL.

The hard photon-parton and photon-photon scattering cross section was calculated in leading and in next-to-leading order. The analytical calculation included the tree-level Born matrix elements, the virtual corrections with one internal loop, and the real corrections with the radiation of a third particle in the initial or final states. We integrated the latter over singular regions of phase space up to an invariant mass cut y . This was done in d dimensions in order to regularize the soft and collinear divergencies. All infrared singularities canceled, as they must according to the Kinoshita-Lee-Nauenberg theorem. The ultraviolet poles in the virtual corrections and the collinear poles in the initial state corrections were absorbed into the Lagrangian and the structure functions, respectively.

The cross sections proved to be independent of the technical y -cut and less dependent on the renormalization and factorization scales, when added to the regular three-body contributions and integrated numerically. Excellent agreement was found in inclusive single-jet predictions with the existing programs of Bödeker and Salesch. We extensively studied the direct, resolved, and complete (in the case of γp) and the direct, single-resolved, double-resolved, and complete (in the case of $\gamma\gamma$) one- and two-jet distributions in the transverse energies and rapidities of the observed jets as well as the dependence on the jet cone size R . Finally, we compared similar distributions to inclusive and dijet data from H1 and ZEUS and OPAL and found good agreement in all cases.

It is possible to extend the work presented here in a number of different ways. First, the formalism presented can easily be extended to the calculation of γp and $\gamma\gamma$ collisions, where one of the photons has a virtuality larger than zero, although still small compared to E_T [100]. Second, other observables than those considered in this work will allow to test the theory further and make it easier to isolate the resolved contributions to obtain information on the parton distributions in the photon for various scales. Third, our program can be used to predict single and dijet cross sections in proton-proton and proton-antiproton scattering at the TEVATRON at Fermilab in Chicago or at the designated LHC at CERN in Geneva.

A Phase Space Integrals for Final State Singularities

This appendix contains the formulæ needed to integrate the real $2 \rightarrow 3$ matrix elements in sections 4.2.2 and 4.2.3 over phase space regions with final state singularities. To this aim, we have defined in section 4.2.1 a measure

$$\int d\mu_F = \int_0^{y_F} dz' z'^{-\varepsilon} \left(1 + \frac{z's}{t}\right)^{-\varepsilon} \int_0^1 \frac{db}{N_b} b^{-\varepsilon} (1-b)^{-\varepsilon} \int_0^\pi \frac{d\phi}{N_\phi} \sin^{-2\varepsilon} \phi, \quad (\text{A.1})$$

which contains all variables associated with the phase space of the unobserved subsystem $\bar{p}_1 = p_1 + p_3$. The integral over the azimuthal angle ϕ is trivial, as the matrix elements are independent of ϕ .

We give the results for the four generic types of integrals in the following:

$$\begin{aligned} f_1(a) &= \int d\mu_F \frac{1}{z'} \frac{a}{z' + ab} = \int d\mu_F \frac{1}{z'} \frac{a}{z' + a(1-b)} \\ &= \frac{1}{2\varepsilon^2} + \frac{1}{\varepsilon} \left(-1 - \frac{1}{2} \ln a\right) + \ln a - \frac{1}{2} \ln^2 \frac{y_F}{a} + \frac{1}{4} \ln^2 a - \text{Li}_2\left(-\frac{y_F}{a}\right) - \frac{\pi^2}{6} + \mathcal{O}(\varepsilon), \end{aligned} \quad (\text{A.2})$$

$$\begin{aligned} f_2(a) &= \int d\mu_F \frac{1}{z'} (1-b)(1-\varepsilon) \\ &= -\frac{1}{2\varepsilon} + \frac{1}{2} + \frac{1}{2} \ln y_F + \mathcal{O}(\varepsilon), \end{aligned} \quad (\text{A.3})$$

$$\begin{aligned} f_3(a) &= \int d\mu_F \frac{1}{z'} \\ &= -\frac{1}{\varepsilon} + \ln y_F + \mathcal{O}(\varepsilon), \end{aligned} \quad (\text{A.4})$$

$$\begin{aligned} f_4(a) &= \int d\mu_F \frac{1}{z'} (1-b+b^2) \\ &= -\frac{5}{6\varepsilon} + \frac{5}{6} \ln y_F - \frac{1}{18} + \mathcal{O}(\varepsilon). \end{aligned} \quad (\text{A.5})$$

Terms of order ε have been omitted since they vanish in the limit $d \rightarrow 4$.

B Phase Space Integrals for Initial State Singularities

In this appendix, we calculate the formulæ needed to integrate the real $2 \rightarrow 3$ matrix elements in sections 4.2.5 through 4.2.8 over phase space regions with initial state singularities. The integration measure was defined in section 4.2.4 and is given by

$$\int d\mu_I = \int_0^{y_I} dz'' z''^{-\varepsilon} \int_{X_a}^1 \frac{dz_a}{z_a} \left(\frac{z_a}{1-z_a}\right)^\varepsilon \int_0^\pi \frac{d\phi}{N_\phi} \sin^{-2\varepsilon} \phi \frac{\Gamma(1-2\varepsilon)}{\Gamma^2(1-\varepsilon)}. \quad (\text{B.1})$$

The integration variables are associated with the phase space of the unobserved particle p_3 . The integral over the azimuthal angle ϕ is again trivial, as the matrix elements do not depend on ϕ . The longitudinal momentum fraction z_a is integrated over numerically, since the cross sections still have to be folded with the parton densities. These are contained in the functions $g(z_a)$ below.

We give the results for the four generic types of integrals in the following:

$$i_1(a) = \int d\mu_I g(z_a) \frac{1}{z''} \frac{a}{z'' + a(1-z_a)}$$

$$\begin{aligned}
&= \int_{X_a}^1 \frac{dz_a}{z_a} g(z_a) \left[-\frac{1}{\varepsilon} - \frac{1}{\varepsilon} \frac{z_a}{(1-z_a)_+} + \left(\frac{\ln \left(a \left(\frac{1-z_a}{z_a} \right)^2 \right)}{1-z_a} \right)_+ - \ln \left(a \left(\frac{1-z_a}{z_a} \right)^2 \right) \right. \\
&\quad \left. - \frac{z_a}{1-z_a} \ln \left(1 + \frac{a(1-z_a)}{y_I z_a} \right) + \ln \left(y_I \left(\frac{1-z_a}{z_a} \right) \right) \right] \\
&\quad + g(1) \left[\frac{1}{2\varepsilon^2} - \frac{1}{2\varepsilon} \ln a + \frac{1}{4} \ln^2 a + \frac{\pi^2}{2} \right] + \mathcal{O}(\varepsilon), \tag{B.2}
\end{aligned}$$

$$\begin{aligned}
i_2(a) &= \int d\mu_{I\bar{I}} g(z_a) \frac{1}{z_a''} \\
&= \int_{X_a}^1 \frac{dz_a}{z_a} g(z_a) \left[-\frac{1}{\varepsilon} + \ln \left(y_I \frac{1-z_a}{z_a} \right) \right] + \mathcal{O}(\varepsilon), \tag{B.3}
\end{aligned}$$

$$\begin{aligned}
i_3(a) &= \int d\mu_{I\bar{I}} g(z_a) \frac{1}{z_a''} (1-z_a)(1-\varepsilon) \\
&= \int_{X_a}^1 \frac{dz_a}{z_a} g(z_a) \left[-\frac{1}{\varepsilon} (1-z_a) + (1-z_a) + (1-z_a) \ln \left(y_I \frac{1-z_a}{z_a} \right) \right] + \mathcal{O}(\varepsilon), \tag{B.4}
\end{aligned}$$

$$\begin{aligned}
i_4(a) &= \int d\mu_{I\bar{I}} g(z_a) \frac{1}{z_a''} \left(\frac{z_a^2 - 2z_a + 2 - \varepsilon z_a^2}{z_a} \right) \frac{1}{1-\varepsilon} \\
&= \int_{X_a}^1 \frac{dz_a}{z_a} g(z_a) \left[-\frac{1}{\varepsilon} \frac{z_a^2 - 2z_a + 2}{z_a} + \frac{z_a^2 - 2z_a + 2}{z_a} \ln \left(y_I \frac{1-z_a}{z_a} \right) - 2 \frac{1-z_a}{z_a} \right] + \mathcal{O}(\varepsilon). \tag{B.5}
\end{aligned}$$

Terms of order ε have again been omitted.

References

- [1] H. Hayashi et al., TOPAZ Collaboration, Phys. Lett. **B314** (1993) 149, B.J. Kim et al., AMY Collaboration, Phys. Lett. **B325** (1994) 248.
- [2] K. Ackerstaff et al., OPAL Collaboration, Z. Phys. **C73** (1997) 433.
- [3] T. Ahmed et al., H1 Collaboration, Phys. Lett. **B346** (1995) 415, M. Derrick et al., ZEUS Collaboration, Phys. Lett. **B363** (1995) 201.
- [4] A. Bouniatian, Report DESY FH1K-95-04, S. Aid et al., H1 Collaboration, Z. Phys. **C70** (1996) 17.
- [5] M. Derrick et al., ZEUS Collaboration, Phys. Lett. **B342** (1995) 417, Phys. Lett. **B348** (1995) 665.
- [6] Z. Kunszt, D.E. Soper, Phys. Rev. **D46** (1992) 192, S. Catani, M.H. Seymour, Nucl. Phys. B (Proc. Suppl.) 51 C (1996) 233.
- [7] T. Kleinwort, G. Kramer, Nucl. Phys. **B477** (1996) 3.
- [8] M. Klasen, G. Kramer, Z. Phys. **C72** (1996) 107.
- [9] T. Kleinwort, Report DESY 96-195, September 1996.
- [10] M. Klasen, Report DESY 96-204, September 1996.

- [11] T. Kleinwort, G. Kramer, Z. Phys. **C75** (1997) 489.
- [12] M. Klasen, G. Kramer, Z. Phys. **C76** (1997) 67.
- [13] E. Auge et al., NA14 Collaboration, Phys. Lett **168B** (1986) 163.
- [14] D. Adams et al., E683 Collaboration, Phys. Rev. Lett. **72** (1994) 2337.
- [15] E. Paul, DESY 92-026 (1992).
- [16] E. Fermi, Z. Phys. **29** (1924) 315.
- [17] C.F.v. Weizsäcker, Z. Phys. **88** (1934) 612.
- [18] E.J. Williams, Phys. Rev. **45** (1934) 729, Kgl. Danske Vidensk. Selskab. Mat.-fys. Medd. **XIII** (1935) N4.
- [19] R.B. Curtis, Phys. Rev. **104** (1956) 211.
- [20] R.H. Dalitz, D.R. Yennie, Phys. Rev. **105** (1957) 1598.
- [21] M.-S. Chen, P. Zerwas, Phys. Rev. **D12** (1975) 187.
- [22] P. Kessler, in Proc. of the Workshop on “Two-Photon Physics at LEP and HERA”, edited by G. Jarlskog and L. Jönsson, Lund University (1994), p. 183.
- [23] G.A. Schuler, preprint CERN-TH/96-297, hep-ph/9610406.
- [24] S. Frixione, M.L. Mangano, P. Nason, G. Ridolfi, Phys. Lett. **B319** (1993) 339.
- [25] P. Aurenche, A. Finch, M. Greco, D.J. Miller (eds.), Talks given at 2nd general meeting LEP2 physics workshop, Geneva (1995).
- [26] G. Altarelli, G. Parisi, Nucl. Phys. **B126** (1977) 298.
- [27] H. Plochow-Besch, Int. J. Mod. Phys. **A10** (1995) 2901.
- [28] H.L. Lai, J. Botts, J. Huston, J.G. Morfin, J.F. Owens, J.W. Qiu, W.K. Tung, H. Weerts, Phys. Rev. **D51** (1995) 4763.
- [29] A.D. Martin, W.J. Stirling, R.G. Roberts, Phys. Rev. **D50** (1994) 6734, Phys. Lett. **B354** (1995) 155.
- [30] M. Glück, E. Reya, A. Vogt, Z. Phys. **C67** (1995) 433.
- [31] H.L. Lai, J. Huston, S. Kuhlmann, F. Olness, J. Owens, D. Soper, W.K. Tung, H. Weerts, Phys. Rev. **D55** (1997) 1280.
- [32] A.D. Martin, R.G. Roberts, W.J. Stirling, Phys. Lett. **B387** (1996) 419.
- [33] M. Glück, E. Reya, A. Vogt, Phys. Rev. **D45** (1992) 3986.
- [34] P. Aurenche, P. Chiappetta, M. Fontannaz, J.P. Guillet, E. Pilon, Z. Phys. **C56** (1992) 589, P. Aurenche, M. Fontannaz, J.P. Guillet, Z. Phys. **C64** (1994) 621.
- [35] G.A. Schuler, T. Sjöstrand, Z. Phys. **C68** (1995) 607.
- [36] H. Abramowicz, K. Charchula, A. Levy, Phys. Lett. **B269** (1991) 458, H. Abramowicz et al., J. Mod. Phys. **A8** (1992) 1005.

- [37] L.E. Gordon, J.K. Storrow, *Z. Phys.* **C56** (1992) 307.
- [38] L.E. Gordon, J.K. Storrow, *Nucl. Phys.* **B489** (1997) 405.
- [39] J. Binnewies, B.A. Kniehl, G. Kramer, *Phys. Rev.* **D52** (1995) 4947, *Phys. Rev.* **D53** (1996) 3573.
- [40] R.D. Field, R.P. Feynman, *Nucl. Phys.* **B136** (1978) 1, P. Hoyer, P. Osland, H.G. Sander, T.F. Walsh, P.M. Zerwas, *Nucl. Phys.* **B161** (1979) 349, A. Ali, E. Pietarinen, G. Kramer, J. Willrodt, *Phys. Lett.* **B93** (1980) 155, B. Andersson, G. Gustafson, T. Sjöstrand, *Z. Phys.* **C6** (1980) 235.
- [41] S.D. Ellis, Z. Kunszt, D.E. Soper, *Phys. Rev. Lett.* **62** (1989) 726.
- [42] G. Sterman, S. Weinberg, *Phys. Rev. Lett.* **39** (1977) 1436.
- [43] W. Bartel et al., *Phys. Lett.* **119B** (1982) 239, *Z. Phys.* **C33** (1986) 23.
- [44] G. Kramer, *Springer Tracts in Mod. Phys.*, Vol. 102, Springer, Berlin (1984).
- [45] J.E. Huth et al., *Proc. of the 1990 DPF Summer Study on High Energy Physics, Snowmass, Colorado*, edited by E.L. Berger, World Scientific, Singapore (1992) 134.
- [46] J. Butterworth, L. Feld, M. Klasen, G. Kramer, *Proc. of the DESY Workshop on “Future Physics at HERA”* (1996) 554, hep-ph/9608481.
- [47] S. Catani, Y.L. Dokshitzer, M. Olsson, G. Turnock, B.R. Webber, *Phys. Lett.* **B269** (1991) 432, S.D. Ellis, D.E. Soper, *Phys. Rev.* **D48** (1993) 3160, M.H. Seymour, Talk given at the 10th topical workshop on proton-antiproton collider physics, Batavia, IL (1995), hep-ph/9506421.
- [48] E. Byckling, K. Kajantie, John Wiley & Sons, London (1973).
- [49] P. Aurenche, R. Baier, A. Douiri, M. Fontannaz, D. Schiff, *Nucl. Phys.* **B286** (1987) 553.
- [50] P.B. Arnold, M. Hall Reno, *Nucl. Phys.* **B319** (1989) 37.
- [51] D. Graudenz, Ph.D. thesis, University of Hamburg, Hamburg, DESY T-90-01 (1990).
- [52] H. Baer, J. Ohnemus, J.F. Owens, *Phys. Rev.* **D40** (1989) 2844.
- [53] D. Bödeker, Ph.D. Thesis, University of Hamburg, Hamburg (1992), *Phys. Lett.* **B292** (1992) 164, *Z. Phys.* **C59** (1993) 501.
- [54] R. Cutler, D. Sivers, *Phys. Rev.* **D17** (1978) 196.
- [55] B.L. Combridge, J. Kripfganz, J. Ranft, *Phys. Lett.* **B70** (1977) 234, J.F. Owens, E. Reya, M. Glück, *Phys. Rev.* **D18** (1978) 1501.
- [56] R.K. Ellis, J.C. Sexton, *Nucl. Phys.* **B269** (1986) 445.
- [57] M. Klasen, Diploma Thesis, University of Würzburg, Würzburg (1993).
- [58] S.D. Ellis, Z. Kunszt, D.E. Soper, *Phys. Rev.* **D40** (1989) 2188.
- [59] G. t’Hooft, M. Veltman, *Nucl. Phys.* **B44** (1972) 189, C.G. Bollini, J.J. Giambiagi, *Phys. Lett.* **40B** (1972) 566, J.F. Ashmore, *Lett. Nuov. Cim.* **4** (1972) 289, G. M. Cicuta, E. Montaldi, *Lett. Nuovo Cim.* **4** (1972) 329, W.J. Marciano, A. Sirlin, *Nucl. Phys.* **B88** (1975) 86, G. Leibbrandt, *Rev. Mod. Phys.* **47** (1975) 849.

- [60] G. t'Hooft, Nucl. Phys. **B61** (1973) 455, W.A. Bardeen, A.J. Buras, D.W. Duke, T. Muta, Phys. Rev. **D18** (1978) 3998.
- [61] T. Kinoshita, J. Math. Phys. **3** (1962) 650, T.D. Lee, M. Nauenberg, Phys. Rev. **133B** (1964) 1549.
- [62] R.K. Ellis, D.A. Ross, A.E. Terrano, Nucl. Phys. **B178** (1981) 421.
- [63] K. Fabricius, G. Kramer, G. Schierholz, I. Schmitt, Z. Phys. **C11** (1982) 315.
- [64] A.C. Hearn, Rand Publication CP78 (Rev. 4/85).
- [65] F.A. Berends, R. Kleiss, P. De Causmaecker, R. Gastmans, T.T. Wu, Phys. Lett. **103B** (1981) 124.
- [66] T. Gottschalk, D. Sivers, Phys. Rev. **D21** (1980) 102.
- [67] Z. Kunszt, E. Pietarinen, Nucl. Phys. **B164** (1980) 45.
- [68] R.K. Ellis, M.A. Furman, H.E. Haber, I. Hinchliffe, Nucl. Phys. **B173** (1980) 397.
- [69] G. Altarelli, R.K. Ellis, G. Martinelli, Nucl. Phys. **B143** (1978) 521.
- [70] M.A. Furman, Nucl. Phys. **B197** (1982) 413.
- [71] A. Buras, Rev. Mod. Phys. **52** (1980) 199, G. Altarelli, Phys. Rep. **81** (1982) 1, R.K. Ellis, G. Martinelli, R. Petronzio, Nucl. Phys. **B211** (1983) 106.
- [72] G.P. Lepage, J. Comp. Phys. **27** (1978) 192.
- [73] S.G. Salesch, Ph.D. thesis, University of Hamburg, Hamburg, DESY 93-196 (1993).
- [74] F. Aversa, P. Chiappetta, M. Greco, J.P. Guillet, Phys. Lett. **B210** (1988) 225, Z. Phys. **C46** (1990) 253.
- [75] P.M. Stevenson, Phys. Lett. **100B** (1981) 61, Phys. Rev. **D23** (1981) 2916.
- [76] D. Bödeker, G. Kramer, S.G. Salesch, Z. Phys. **C63** (1994) 471.
- [77] G. Kramer, S.G. Salesch, Z. Phys. **C61** (1994) 277.
- [78] P. Aurenche, J.-Ph. Guillet, M. Fontannaz, Phys. Lett. **B338** (1994) 98.
- [79] L.E. Gordon, J.K. Storrow, Phys. Lett. **B291** (1992) 320.
- [80] M. Derrick et al., ZEUS Collaboration, Talk given at XXVIII International Conference on High Energy Physics, Warsaw (1996), pa 02-040, J. Breitweg et al., ZEUS Collaboration, DESY 97-196, hep-ex/9710018.
- [81] M. Klasen, G. Kramer, Phys. Lett. **B366** (1996) 385.
- [82] M. Derrick et al., ZEUS Collaboration, Talk given at International Conference on High Energy Physics, Jerusalem (1997), N-650.
- [83] M. Derrick et al., ZEUS Collaboration, Talk given at International Conference on High Energy Physics, Jerusalem (1997), N-654.
- [84] C. Adloff et al., H1 Collaboration, Report DESY 97-164.

- [85] S.D. Ellis, Z. Kunszt, D.E. Soper, Phys. Rev. Lett. **69** (1992) 3615.
- [86] M. Klasen, G. Kramer, Phys. Rev. **D56** (1997) 2702.
- [87] M. Derrick et al., ZEUS Collaboration, Talk given at International Conference on High Energy Physics, Warsaw (1996), pa 02-043, J. Breitweg et al., ZEUS Collaboration, DESY 97-191.
- [88] M. Klasen, G. Kramer, S.G. Salesch, Z. Phys. **C68** (1995) 113.
- [89] M. Derrick et al., ZEUS Collaboration, Phys. Lett. **B384** (1996) 401.
- [90] S. Catani, Y.L. Dokshitzer, M.H. Seymour, Nucl. Phys. **B406** (1996) 401.
- [91] M. Derrick et al., ZEUS Collaboration, Phys. Lett. **B322** (1994) 287.
- [92] M. Klasen, Proc. of the Ringberg Workshop on “New Trends in HERA Physics”, Ringberg (1997).
- [93] C. Glasman, private communication.
- [94] OPAL collaboration, OPAL Physics Note 291, May 1997. Contribution submitted to the XVIII International Symposium on Lepton-Photon Interactions, Hamburg, 1997, and International Conference on High Energy Physics, Jerusalem, 1997. S. Söldner-Rembold, Proc. of the Ringberg Workshop on “New Trends in HERA Physics”, Ringberg (1997).
- [95] T. Kleinwort, G. Kramer, Phys. Lett. **B370** (1996) 141.
- [96] W.T. Giele, E.W.N. Glover, D.A. Kosower, Phys. Rev. Lett. **73** (1994) 2019.
- [97] M. Klasen, G. Kramer, Phys. Lett. **B386** (1996) 384.
- [98] S. Frixione, preprint ETH-TH/97-14, hep-ph/9706545, S. Frixione, G. Ridolfi, preprint ETH-TH/97-21, hep-ph/9707345.
- [99] B.W. Harris, J.F. Owens, Phys. Rev. **D56** (1997) 4007.
- [100] B. Pötter, Ph.D. Thesis, University of Hamburg, Hamburg (1997), DESY-97-138, hep-ph/9707319, M. Klasen, G. Kramer, B. Pötter, DESY-97-039 (1997), hep-ph/9703302.